

High Resolution Spectroscopy and Applications

Chad A Povey

Bachelor of Science,

University of Lethbridge, 2008

A Thesis

Submitted to the School of Graduate Studies

Of the University of Lethbridge

in Partial Fulfilment of the

Requirements for the Degree

PHD: EARTH, SPACE AND PHYSICAL SCIENCE

Department of Physics & Astronomy

University of Lethbridge

Lethbridge, Alberta, Canada

© Chad A. Povey, 2013

Dedication Page

I would like to dedicate the work in this Thesis to my father Rodney D. Povey who unfortunately is unable to see me receive my PhD.

“Try not to become a man of success, but rather try to become a man of value.”

A. Einstein

Abstract

With the ever increasing spectral resolution now achievable with modern spectrometers we do not just observe dark lines anymore but molecular absorption features at very high resolution. These features are governed by the kinematics of the molecules and can be examined carefully by using high resolution spectroscopy. A detailed description of the setup and performance of the tunable diode laser spectrometer (TDL) system used in my research is presented. This tunable laser system has been used to complete several high resolution line shape studies on the $\nu_1+\nu_2+\nu_4+\nu_5$ and $\nu_1+\nu_3$ combination bands of acetylene. The major focus of the presented results has been on the temperature dependence of the retrieved parameters and the identification of the best fitting line shape profile used in the present investigation.

Improved spectral resolution also requires better understanding of its effects on the recorded data that could not have been observed on data obtained with low resolution instruments. One of these effects is known as line mixing and it occurs when neighbouring transitions interfere with each other causing a slight asymmetry in the spectral profile. In this Thesis I have examined the line mixing effect in CO_2 spectra and the temperature dependence of these line mixing coefficients. The analysis is performed by using two common line mixing models; (1) the energy correct sudden approximation and (2) the exponential power gap law.

Finally I will present a project based on the application of high resolution spectroscopy that involves monitoring N_2O concentration at remote locations through the use of a long path gas cell and a tunable diode laser spectrometer system. The initial testing and setup of this monitoring system will be presented and discussed.

Acknowledgements

“Learn from yesterday, live for today, hope for tomorrow. The important thing is not to stop questioning.”

A. Einstein

It takes a great number of people to create one PhD candidate. To thank each and every one of them is a monstrous task and possibly out of the scope of this Thesis. However there are more than a handful of people that deserve praise for tolerating me these last few years.

Firstly I would like to thank my supervisor Dr. Adriana Predoi-Cross for her amazing guidance, understanding and patience. I will greatly miss working so closely with her.

I would like to thank my family for their unwavering support. My two sons Gavin and Morgan who helped me unwind at the end of the day and my wife Stephanie for her patience, friendship and caring understanding.

Next I would like to thank my committee members Karl Staenz and Arundhati Dasgupta. Through our meetings they have helped me keep on track and plan this whole project.

I would also like to thank all the graduate and undergraduate students I have worked with these last few years. The ones that come to my mind immediately are Amr Ibrahim who helped me learn more through our discussions of spectroscopy, Hoimonti

Rozario for helping me better understand the science that we did, Robab Hashemi whose enthusiasm is inspiring, Jolene Graber for all her help generating the many transmission spectra we needed, and last but not the least Mileno Guillorel-Obregon for his assistance in the measurements of nitrogen perturbed acetylene data.

I would also like to thank Dr. Malathy Devi for her comments and suggested corrections for my Thesis.

Finally I would like to thank the NSERC CREATE AMETHYST program and the U of L SGS for both the professional and financial support they provided during my studies.

Contents

Dedication Page	iii
Abstract	iv
Acknowledgements.....	v
Contents	vii
List of Tables	xv
List of Figures	xxiv
List of Abbreviations	xxxiv
List of Equations.....	xxxv
List of Mathematical Symbols.....	xli
Chapter 1: Introduction	1
1.1. Overview	1
1.2. Spectroscopy	1
1.2.1. Introduction	1
1.2.2. Laser Spectrometer.....	3
1.3. Acetylene as a constituent of planetary atmospheres	4
1.3.1. Introduction	4
1.3.2. Summary of studies	4
1.4. Improving CO ₂ Concentration Retrievals	7

1.5. Monitoring N ₂ O Levels in Agricultural Areas	8
1.6. Thesis Outline.....	9
Chapter 2: Theoretical Aspects.....	11
2.1. Introduction.....	11
2.2. Fundamentals of Spectroscopy.....	11
2.2.1. Interaction of electromagnetic radiation with atoms and molecules 11	
2.2.2. Pure vibration	14
2.2.3. Pure rotation.....	19
2.2.4. Vibration-rotation.....	21
2.2.5. Vibrational angular momentum	22
2.2.6. Vibration-rotation bands	24
2.2.7. Rovibrational bands reported in this thesis.....	25
2.3. Absorption Spectroscopy	27
2.3.1. Introduction	27
2.3.2. Beer Lambert law.....	27
2.4. Spectral Line Shape Functions.....	30
2.4.1. Introduction	30
2.4.2. Doppler Profile.....	32

2.4.3. Lorentz Profile.....	34
2.4.4. Voigt Profile	35
2.4.5. Speed Dependant Voigt Profile	36
2.4.6. Galatry Profile	37
2.4.7. Hard collision Rautian-Sobelman Profile	40
2.5. Temperature Dependence of Line Parameters.....	41
2.6. Line-mixing	42
2.6.1. Introduction	42
2.6.2. The Energy Corrected Sudden Approximation (ECS).....	48
2.6.3. Exponential Power Gap Law (EPG)	50
2.6.4. Calculating Line-mixing coefficients	51
2.7. Conclusion	52
Chapter 3: Experimental Setup of a Tunable Diode Laser Spectrometer (TDLS)	53
3.1. Overview	53
3.2. Diode Laser Spectroscopy	54
3.2.1. Introduction	54
3.2.2. The tunable diode laser	55
3.2.3. Process of scanning the laser system	58
3.3. Layout of The Tunable Diode Laser Spectrometer.....	59

3.3.1. Schematic and overview.....	59
3.3.2. Vibrational isolation.....	64
3.3.3. Detectors configuration and testing.....	65
3.3.4. The Fabry Perot cavity	70
3.4. Pressure and Temperature Controlled Gas Cell.....	72
3.4.1. Introduction	72
3.4.2. Vacuum performance of the cell	75
3.4.3. Temperature performance and gradients inside the temperature controlled cell	77
3.5. Spectrometer Testing and Calibration	82
3.5.1. Introduction	82
3.5.2. Wavelength calibration and measurements of line positions.....	82
3.5.3. Instrumental line shape function.....	85
3.5.4. Errors in the fit parameters	87
3.6. Conclusion	90
Chapter 4: Software Developed for a Tunable Diode Laser Spectrometer (TDLS).....	91
4.1. Introduction.....	91
4.2. Overview of Labview Software	91
4.2.1. Introduction to Labview.....	91

4.2.2. Structure of the Labview language.....	93
4.3. Spectrometer Control Software.....	96
4.3.1. VelocityController.vi	96
4.3.2. How spectra are measured.....	98
4.3.3. Data generated during scans	101
4.4. Preparing Transmission files	105
4.4.1. Introduction	105
4.4.2. Generating the wavenumber scale.....	105
4.4.3. Generating Transmission Spectra.....	107
4.4.4. Calibrating the spectra.....	110
4.5. Conclusion	112
Chapter 5: Line Mixing Effects in Carbon Dioxide	113
5.1. Introduction.....	113
5.2. Line-mixing analysis.....	113
5.2.1. Introduction	113
5.2.2. Exponential Power Gap calculations for rotational transfer	114
5.2.3. Energy Corrected Sudden calculations for rotational transfer.....	121
5.3. Conclusion	133
Chapter 6: High Resolution Measurements of Acetylene Transitions	134

6.1. Introduction.....	134
6.2. Line Shape Study of Acetylene Transitions in the $\nu_1+\nu_2+\nu_4+\nu_5$ Band Over a Range of Temperatures.....	134
6.2.1. Introduction	134
6.2.2. Line intensities	137
6.2.3. Line broadening and pressure induced line shifts.....	140
6.2.4. Weak line mixing effects.....	148
6.3. Low-Pressure line shape study of acetylene transitions in the $\nu_1+\nu_2+\nu_4+\nu_5$ band over a range of temperatures.....	152
6.3.1. Introduction	152
6.3.2. Analysis and experimental overview	153
6.3.3. Self –broadening.....	156
6.3.4. Self-induced pressure shift	160
6.3.5. Self-collisional narrowing.....	162
6.3.6. Diffusion coefficients	167
6.4. Low pressure line shape study of nitrogen perturbed acetylene transitions in the $\nu_1+\nu_3$ band over a range of temperatures.	169
6.4.1. Introduction	169
6.4.2. Experiment and analysis overview	172

6.4.3. N ₂ -Broadening of acetylene transitions	176
6.4.4. N ₂ -collisional narrowing of acetylene transitions.....	180
6.4.5. Diffusion coefficients	183
6.5. Conclusion	187
Chapter 7: Experimental setup of a Greenhouse Gas Monitoring System (GGMS).....	189
7.1. Introduction.....	189
7.2. System Overview.....	190
7.2.1. Introduction	190
7.2.2. Leak rate	192
7.2.3. Generating air flow	193
7.2.4. Fabry Perot cavity	194
7.3. Measuring Signals.....	195
7.3.1. Introduction	195
7.3.2. Measuring transmission spectra.....	197
7.3.3. Signal averaging	200
7.4. Verifying the Optical Alignment of the cell.....	201
7.5. Spectral Analysis.....	204
7.6. Conclusion	206
Chapter 8: Conclusion.....	208

8.1. Closing Remarks	208
8.2. Future Work	210
Bibliography	212

List of Tables

Table 3-1: Comparison of tunable diode laser technologies [62]. The following are the acronyms from the table: Distributed Bragg Reflector (DBR), Distributed Feedback (DFB), Vertical Cavity Surface Emitting (VCSEL) and Extended Cavity Diode (ECDV).....	56
Table 3-2: Example of average SNRs for a set of recorded spectra based on pressure and temperature.	70
Table 3-3: Average fringe spacing from 5 separate laser piezo scans.....	72
Table 3-4: Summary of the temperature and pressure stability of the temperature controlled cell for several different experimental conditions.	82
Table 3-5: Comparison of retrieved line positions for the P(21) transition in the $\nu_1+\nu_3$ band of acetylene. All spectra were recorded at pressures below 50 mTorr.....	84
Table 3-6: Summary of the analysis completed to determine the instrumental line shape for the tunable diode laser spectrometer.....	86
Table 3-7: Summary of the errors found for the pressure independent coefficients	89
Table 4-1: Example of five measurements of pressure and temperature as they are recorded in the “TPfile”. The grey row indicates what each column denotes but these headings do not actually appear in the written file.	102
Table 4-2: Example of the “Peak” file created in the sub VI “FabryPerot.vi”. Once again the first row in grey indicates what each column represents but is not present in the file when it is written. The file name for this example is “test1P21Peak1537_819415.txt”.	104

Table 4-3: Example of “Spectra” file created in the sub VI “FabryPerot.vi”. The first row in grey indicates what each column represents but is not present in the file when it is written. Here CH 1 refers to the voltage reading on the channel 1 photodiode, CH 2 refers to the voltage reading on the channel 2 photodiode, FP is the voltage of the Fabry Perot cavity, Piezo Voltage is the voltage being applied to the back of the laser system, and BG is the voltage reading from the background photodiode. The name for this example file is “test2P21Peak1537_856453.txt” 104

Table 5-1: Room temperature values for the adjustable Exponential Power Gap law (EPG) parameters for pure CO₂ at 296 K in the 30013←00001 and 30012←00001 bands. 116

Table 5-2: Room temperature values for the adjustable Exponential Power Gap law (EPG) parameters for CO₂ broadened by air at 296 K in the 30013←00001 and 30012←00001 bands. 116

Table 5-3: Temperature dependence coefficient “*n*” of the *a*(T) parameter in Eq. 5-2 calculated using the EPG scaling law. The values were obtained over a range of temperatures between 193 and 323 K for self-broadened CO₂ transitions in the 30013←00001 and 30012←00001 bands. The line parameters were taken from Ref. [109]. The last row contains the average values, *n_{ave}*. 119

Table 5-4: Temperature dependence coefficient “*n*” of the *a*(T) parameter in Eq. 5-2 calculated using the EPG scaling law. The values were obtained over a range of temperatures between 193 and 323 K for self-broadened CO₂ transitions in the 30013←00001 and 30012←00001 bands. The line parameters were taken from HITRAN08 [21]. The last row contains the average values, *n_{ave}*. 119

Table 5-5: Temperature dependence coefficient “ n ” of the $a(T)$ parameter in Eq. 5-2 calculated using the EPG scaling law. The values were obtained over a range of temperatures between 193 and 323 K for air-broadened CO_2 transitions in the 30013←00001 and 30012←00001 bands. The line parameters were taken from Ref. [35]. The last row contains the average values, n_{ave} 120

Table 5-6: Temperature dependence coefficient “ n ” of the $a(T)$ parameter in Eq. 5-2 calculated using the EPG scaling law. The values were obtained over a range of temperatures between 193 and 323 K for air-broadened CO_2 transitions in the 30013←00001 and 30012←00001 bands. The line parameters were taken from HITRAN08 [21]. The last row contains the average values, n_{ave} 120

Table 5-7: Room temperature values for the adjustable ECS parameters for pure CO_2 at 296 K in the 30013←00001 and 30012←00001 bands [88]. The first four rows were obtained from the data in [109] and the last 4 rows from [21]. 122

Table 5-8: Room temperature values for the adjustable ECS parameters for air-broadened CO_2 at 296 K in the 30013←00001 and 30012←00001 bands [88]. The first four rows were obtained from the data in [35] and the last 4 rows from [21]. 122

Table 5-9: Temperature dependence coefficient “ $N1$ ” and “ $N2$ ” of the $A(T)$ and $d_c(T)$ parameters in equations 5-3 and 5-4 calculated using the ECS scaling law. The values were obtained over a range of temperatures between 193 and 323 K for self-broadened CO_2 transitions in the 30012←00001 band. The line parameters were taken from Ref. [109]. The last row contains the average values of the temperature dependence parameters. 124

Table 5-10: Temperature dependence coefficient “ $N1$ ” and “ $N2$ ” of the $A(T)$ and $d_c(T)$ parameters in equations 5-3 and 5-4 calculated using the ECS scaling law. The values were obtained over a range of temperatures between 193 and 323 K for self-broadened CO_2 transitions in the 30013←00001 band. The line parameters were taken from Ref. [109]. The last row contains the average values of the temperature dependence parameters..... 124

Table 5-11: Temperature dependence coefficient “ $N1$ ” and “ $N2$ ” of the $A(T)$ and $d_c(T)$ parameters in equations 5-3 and 5-4 calculated using the ECS scaling law. The values were obtained over a range of temperatures between 193 and 323 K for self-broadened CO_2 transitions in the 30012←00001 band. The line parameters were taken from Ref. [21]. The last row contains the average values of the temperature dependence parameters..... 125

Table 5-12: Temperature dependence coefficient “ $N1$ ” and “ $N2$ ” of the $A(T)$ and $d_c(T)$ parameters in equations 5-3 and 5-4 calculated using the ECS scaling law. The values were obtained over a range of temperatures between 193 and 323 K for self-broadened CO_2 transitions in the 30013←00001 band. The line parameters were taken from Ref. [21]. The last row contains the average values of the temperature dependence parameters..... 125

Table 5-13: Temperature dependence coefficient “ $N1$ ” and “ $N2$ ” of the $A(T)$ and $d_c(T)$ parameters in equations 5-3 and 5-4 calculated using the ECS scaling law. The values were obtained over a range of temperatures between 193 and 323 K for air-broadened CO_2 transitions in the 30013←00001 band. The line parameters were taken

from Ref. [35]. The last row contains the average values of the temperature dependence parameters..... 126

Table 5-14: Temperature dependence coefficient “ $N1$ ” and “ $N2$ ” of the $A(T)$ and $d_c(T)$ parameters in equations 5-3 and 5-4 calculated using the ECS scaling law. The values were obtained over a range of temperatures between 193 and 323 K for air-broadened CO_2 transitions in the 30012←00001 band. The line parameters were taken from Ref. [35]. The last row contains the average values of the temperature dependence parameters..... 126

Table 5-15: Temperature dependence coefficient “ $N1$ ” and “ $N2$ ” of the $A(T)$ and $d_c(T)$ parameters in equations 5-3 and 5-4 calculated using the ECS scaling law. The values were obtained over a range of temperatures between 193 and 323 K for air-broadened CO_2 transitions in the 30013←00001 band. The line parameters were taken from Ref. [21]. The last row contains the average values of the temperature dependence parameters..... 127

Table 5-16: Temperature dependence coefficient “ $N1$ ” and “ $N2$ ” of the $A(T)$ and $d_c(T)$ parameters in equations 5-3 and 5-4 calculated using the ECS scaling law. The values were obtained over a range of temperatures between 193 and 323 K for air-broadened CO_2 transitions in the 30012←00001 band. The line parameters were taken from Ref. [21]. The last row contains the average values of the temperature dependence parameters..... 127

Table 5-17: Temperature dependence coefficient “ $N3$ ” of the $A(T)$ parameter in equation 5-5 calculated using the ECS scaling law. The values were obtained over a range of temperatures between 193 K and 323 K for self-broadened CO_2 transitions in the

30013←00001 and 30012←00001 bands. The line parameters were taken from Ref. [109]. The last row contains the average values of the temperature dependence parameters..... 128

Table 5-18: Temperature dependence coefficient “ N^3 ” of the $A(T)$ parameter in equation 5-5 calculated using the ECS scaling law. The values were obtained over a range of temperatures between 193 K and 323 K for self-broadened CO_2 transitions in the 30013←00001 and 30012←00001 bands. The line parameters were taken from Ref. [21]. The last row contains the average values of the temperature dependence parameters... 128

Table 5-19: Temperature dependence coefficient “ N^3 ” of the $A(T)$ parameter in equation 5-5 calculated using the ECS scaling law. The values were obtained over a range of temperatures between 193 and 323 K for air-broadened CO_2 transitions in the 30013←00001 and 30012←00001 bands. The line parameters were taken from Ref. [35]. The last row contains the average values of the temperature dependence parameters... 129

Table 5-20: Temperature dependence coefficient “ N^3 ” of the $A(T)$ parameter in equation 5-5 calculated using the ECS scaling law. The values were obtained over a range of temperatures between 193 and 323 K for air-broadened CO_2 transitions in the 30013←00001 and 30012←00001 bands. The line parameters were taken from Ref. [21]. The last row contains the average values of the temperature dependence parameters... 129

Table 6-1: Experimental conditions for self-broadened acetylene spectra [111]. The numbers in brackets indicate the statistical error of the measured values..... 136

Table 6-2: Line Intensities $\nu_1+\nu_2+\nu_4+\nu_5$ band of acetylene determined using (A) the Voigt profile and (B) the speed-dependent Voigt profile [111]. Here R^2 is the transition dipole moment squared..... 138

Table 6-3: Self-broadening coefficient in the $\nu_1+\nu_2+\nu_4+\nu_5$ band of acetylene determined using (A) Voigt and (B) speed dependent Voigt profile [111].	142
Table 6-4: Pressure induced line self-shift coefficient in the $\nu_1+\nu_2+\nu_4+\nu_5$ band of acetylene determined using (A) the Voigt and (B) the speed dependent Voigt profile [111].	145
Table 6-5: Temperature dependences for self broadening coefficients (obtained using Eq. 6-5) (\mathbf{n}) and pressure induced self-shift coefficients (obtained from Eq. 6-7 (\mathbf{n}') and 6-8 ($\mathbf{\delta}'$)) in the $\nu_1+\nu_2+\nu_4+\nu_5$ band of acetylene[111]. Numbers in the brackets represent the statistical error associated with the last digit of the determined value.	146
Table 6-6: Calculated and measured self-line mixing coefficient in the $\nu_1+\nu_2+\nu_4+\nu_5$ band of acetylene determined using (A) the Voigt and (B) the speed-dependent Voigt profiles [111].	149
Table 6-7: Empirical fit parameters for the EPG scaling law [111]. Once again the numbers in brackets denote the statistical error in the obtained values.	150
Table 6-8: Experimental conditions (each scan takes approximately 3.5 hrs).	155
Table 6-9: Self Broadening coefficients at 293 K and temperature dependence exponents n for both the Soft and Hard collision line shape models [112].	157
Table 6-10: Self-shift coefficients at 293 K and the corresponding temperature dependent coefficients δ' from both the Soft and Hard collision line shape models [112].	160
Table 6-11: Self-collisional narrowing coefficients at 293 K and their temperature dependence exponents n' for the soft and hard collision line shape models [112].	165
Table 6-12: Summary of prior studies of acetylene bands broadened by N_2 .	171

Table 6-13: Experimental conditions for the R(21) transition [113]. The uncertainties listed in the table in parenthesis are one standard deviation from the average listed..... 173

Table 6-14: N₂-Broadening coefficients for five different temperatures obtained using an uncorrelated hard collision Rautian line-shape model [113]. (The normal convention of $m = -J''$ for the P branch and $m = J''+1$ for the R branch is used). 177

Table 6-15: Comparison of theoretical and experimental results obtained for N₂-broadening coefficients at 296 K and their temperature dependence exponents n_1 [113]. 179

Table 6-16: N₂-Narrowing coefficients for the five recorded temperatures using an un-correlated hard collision Rautian line-shape model. The last column shows the temperature dependence terms obtained from the data in the table and equation 6-14 [113]..... 182

Table 6-17: Estimated N₂-Diffusion coefficients obtained from equation 6-15. For the values obtained at 296 K a percent difference was calculated ((theoretical-experimental)/experimental) [113]..... 185

Table 7-1: Retrieved line positions for P(12), P(13) and P(14) lines of the 4v₁+2v₂ band of N₂O. 195

Table 7-2: Summary of the changes observed in the signal to noise ratio in relation to the number of scans averaged..... 200

Table 7-3: Comparison of retrieved line shape parameters using the Voigt profile in “Wproffit.exe” [87] and “ProfileFit.vi”. The isolated R(19) line of the v₁+v₂+v₄+v₅

band of C₂H₂ was used to compare values.^a For positions the differences between the two
retrieved positions are listed. 206

List of Figures

Figure 2-1: Example of the full electromagnetic spectrum of light. [http://www.widen.com/premediablog/call-me-mr-biv-v1]	12
Figure 2-2: Three possible results in a two level quantum system: (1) Spontaneous emission, (2) Stimulated emission and (3) Induced absorption. Here Ψ_n and Ψ_m represent the two quantum states n and m defined above.....	13
Figure 2-3: Potential energy curve and energy levels of a diatomic molecule. The curved solid lines depict the anharmonic case. The dashed lines indicate the classical harmonic oscillator. Here D_e is the dissociation energy measured relative to the equilibrium potential energy, and D_0 is the dissociation energy relative to the actual ground state level [39].	17
Figure 2-4: Simplified example of a molecule vibrating in a degenerate bending mode. A) shows the two possible planes where the molecule will bend while B) shows the circular path the nuclei trace out along the inter molecular axis. The angle in B represents the angular speed at which it rotates around the axis.	23
Figure 2-5: Three commonly used line shape functions.....	29
Figure 2-6: Example of the speed dependence effects on the spectral line shape when $I(\nu)$ is considered (shown on the left), and $\Delta(\nu)$ is considered (shown on the right) [40, 41].....	36
Figure 2-7: Example of the line mixing effect. Panel (a) shows how the two transition profiles overlap. Panel (b) shows the energy levels and how they can be perturbed (dashed horizontal lines) through collisions.....	42

Figure 3-1: Schematic of Velocity Laser cavity. PZT is the Piezo electric actuator mounted on the back of the HR (High Reflectivity) tuning mirror. Finally AR refers to the anti-reflection coating placed on the diode laser cavity..... 56

Figure 3-2: Drawing of important angles and distances resulting in the optimal pivot point. Once again HR refers to the High Reflectivity of the mirror. 57

Figure 3-3: General block diagram of current spectrometer setup. Legend: 1 Vacuum system; 2 Cooling system NesLab ULT 80 Chiller; 3 Gas sample; 4 & 5 Fabry Perot interferometer and controller; 6 Detector pre-amps and power supplies; 7 WA-1500 EXFO wavemeter; 8, 9 Velocity diode laser head and controller; 10 MKS Baratron pressure gauges; L1, L2 , L3 Focusing lenses; M1 & M2 Directing mirrors; D1, D2 & D3 InGaAs detectors; C1, C2, C3, C4 Collimators; S1, S2, S3, S4 Fiber splitters; Vacuum lines are shown in thick black lines. Coolant lines are shown in blue. Laser path is shown by the red lines. Thin curved lines show fiber optic cables with the percentages denoting the split ratios of the fibers..... 60

Figure 3-4: Three- dimensional view of the temperature controlled gas cell. Legend: 1- MKS Baratron pressure gauge, 2- enhanced pirani pressure gauge, 3- vacuum feed throughs, 4- CaF2 windows positioned at Brewster angle, 5- CaF2 windows for the inner cell, 6- platinum resistor thermometers, 7- inner cell body, 8- gas inlet, 9- vacuum valves, 10- gas outlet and 11-port for de-pressuring the vacuum jacket. 61

Figure 3-5: Side view of the temperature controlled cell. Legend: 1- vacuum port, 2a- gas inlet, 2b- vacuum field-through for platinum resistors, 3- vacuum valve, 4- temperature sensors using platinum resistors, 5- CaF2 windows mounted at Brewster

angle, 6- fins for directing the coolant through the coolant jacket, 7- coolant jacket, 8- outer cell body, 9- cell support and 10- valve for de-pressuring of the outer jacket. 62

Figure 3-6: Left and right side views of the inner chamber. Legend: 1- platinum resistor thermometers, 2a- coolant inlet, 2b- coolant outlet, 3- CaF₂ window, 4- left side flange, 5- fins for directing the coolant, 6- right side flange and 7- mounting rings for windows. 62

Figure 3-7: Example of vibrational noise added to a recorded spectra of the R11e transition in the $\nu_1+\nu_3$ band of acetylene. 64

Figure 3-8: Fine structure of the noise depicted in Figure 3-7. 65

Figure 3-9: Image of two of the three InGaAs detectors used to measure the signals for the tunable diode laser spectrometer. The detectors can be seen just opposite the focusing lenses. 66

Figure 3-10: Comparison of the P(21) transition of the $\nu_1+\nu_3$ band of acetylene using three different detector setups. 67

Figure 3-11: Signal-to-noise ratio for the raw signal obtained on the temperature controlled cell. The upper panel shows the recorded spectrum and the bottom panel shows the baseline region used to determine the signal to noise using equation 3-3. 68

Figure 3-12: Signal-to-noise ratio for the corrected spectra obtained from the temperature controlled cell and the background signal. The top panel shows the transmission spectrum and the bottom panel shows the base line region of the same spectrum used in Figure 3-11 to calculate the signal to noise using equation 3-3. 69

Figure 3-13: Example of the fringe pattern produced by the Fabry Perot interferometer during a laser scan. 71

Figure 3-14: Base pressure of the temperature controlled cell over a 3-day period.	75
Figure 3-15: Leak rate of the temperature controlled cell at 323 K. The equation shows a leak rate of 0.112 mTorr per min.	76
Figure 3-16: Leak rate of the temperature controlled cell at 296 K. The equation indicates a leak rate of 0.09 mTorr per min.	77
Figure 3-17: Schematic of the temperature controlled cell showing the assigned locations of the temperature sensors. 1, 2, 3, 4 and 5 are the platinum resistance temperature sensors mounted within the gas chamber.	78
Figure 3-18: Pressure within the temperature controlled cell maintained at a temperature of 213 K. The pressure changes over the scan time for figures A, B and C are 0.09, 0.04, and 0.21 %, respectively.	79
Figure 3-19: Recorded values of temperature for all 5 thermo resistor sensors with the temperature controlled cell. The pressures of the cell for scans A, B and C are those presented in Figure 3-18. The sensor locations are given in Figure 3-17.	79
Figure 3-20: Pressure within the temperature controlled cell maintained at a temperature of 333 K for A and 293 K for B. The pressures changes over the scan time for figures A and B are 0.02 and 0.06 %, respectively.	81
Figure 3-21: Recorded values of temperature for all 5 thermo resistor sensors with the temperature controlled cell. The pressures of the cell for scans A and B are those presented in Figure 3-20. The sensor locations are given in Figure 3-17.	81
Figure 3-22: The experimentally determined pressure dependent broadening coefficient γ as it varies with the cell pressure.	88

Figure 3-23: The experimentally determined pressure dependent shift coefficient δ as it varies with the cell pressure.	88
Figure 3-24: The experimentally determined pressure dependent narrowing coefficient β as it varies with the cell pressure.	89
Figure 4-1: Example of the Hierarchy produced by Labview VI's.	92
Figure 4-2: Front panel of the program Resample.vi.....	94
Figure 4-3: Example of Resample.vi being used as a sub VI within another program. The inputs and outputs correspond directly to the ones marked in the upper right corner of Figure 4-2.....	94
Figure 4-4: Block diagram of the program Resample.vi.	95
Figure 4-5: Example cluster from VelocityContrller.vi. On the left “Mode Settings” is the control cluster and on the right “Current Settings” is the indicator cluster.	96
Figure 4-6: Front panel of the VI “VelocityController.vi”	100
Figure 4-7: Example of the “Settings” file written after the scan button has been pressed.....	101
Figure 4-8: Example of the file Hierarchy used to complete the analysis of recorded transmission spectra. The purple boxes denote text files that are created during the process.....	105
Figure 4-9: Recorded spectra of the R(19) transistion in the $\nu_1+\nu_2+\nu_4+\nu_5$ band of acetylene.	107
Figure 4-10: Example of how the spectra in Figure 4-9 is edited to remove the spectral features to allow for background correction to be completed.	107

Figure 4-11: Screen shot of the “CorrectionFit.vi” program used to produce transmission files.	108
Figure 4-12: Example of an 8 th order Chebyshev polynomial fit to the residual of the spectra shown in Figure 4-10. (Range here denotes the values between -1 to 1 as defined for a Chebyshev polynomial.).....	109
Figure 4-13: Example of the corrected background relative to the channel 1 spectra recorded.	110
Figure 4-14: Final transmission spectra produced by the “CorrectionFit.vi” program.	110
Figure 4-15: The R(19) Transition in the $\nu_1+\nu_2+\nu_4+\nu_5$ band of acetylene at 213 K showing (A) the channel 1 spectra before being correct by channel 2 fits, and (B) the channel 1 spectra after being corrected by channel 2 fits.	112
Figure 5-1: Overlaid measured and calculated air-broadening parameters using the Exponential Power Gap law (EPG) plotted against the rotational quantum number m for CO ₂ transitions in the 30012←00001 band [88].....	117
Figure 5-2: Overlaid are the measured and calculated air-line mixing parameters using the Exponential Power Gap law (EPG) for CO ₂ transitions in the 30013←00001 band plotted against the rotational quantum number m [88].	118
Figure 5-3: Overlaid measured and calculated air-broadening parameters using the Energy Corrected Sudden (ECS) scaling law plotted against m for CO ₂ transitions in the 30013←00001 band [88].	130

Figure 5-4: Measured and calculated air-line mixing parameters using the Energy Corrected Sudden (ECS) scaling law for CO ₂ in the 30013←00001 band. All results are plotted against m [88].	131
Figure 5-5: Percent differences between experimental air-broadening parameters and calculated ones obtained using the EPG scaling law (A) and calculated values obtained using the ECS scaling law (fit 1) (B). The comparisons are made for datasets available at 217, 234,259 and 296 K [88].	132
Figure 6-1: Ratios between calculated intensities at 296 K and the values from HITRAN08 [21], [111].	139
Figure 6-2: Room temperature self-broadening coefficients retrieved using the Voigt profile (A) and speed-dependent Voigt profile (B) [111].	144
Figure 6-3: Room temperature pressure induced self-shift coefficients obtained using the Voigt and speed-dependent Voigt profiles [111].	146
Figure 6-4: Temperature dependence coefficients for pressure shifts retrieved using equations 6-8 (A) and 6-7 (B) [111].	147
Figure 6-5: (A) Overlaid calculated and measured weak self-line mixing coefficients at room temperature. (B) Calculated line mixing coefficients at the experimental temperatures [111].	151
Figure 6-6: Observed and calculated spectra for the R(13) transition of the $\nu_1+\nu_2+\nu_4+\nu_5$ band of C ₂ H ₂ . Here the residuals have been vertically shifted and magnified for easier comparison [112].	154
Figure 6-7: Self Broadening Coefficients at 293 K [112].	158

Figure 6-8: Comparison of self-broadening coefficients from previous studies [112].	158
Figure 6-9: Temperature dependence coefficients n obtained from equation 6-5 [112].	159
Figure 6-10: Self-shift coefficients obtained from spectra recorded at 293 K [112].	161
Figure 6-11: Temperature dependence term δ' obtained from equation 6-7 [112].	162
Figure 6-12: Plot showing the collisional narrowing vs. temperature for the R(11) transition in the $\nu_1+\nu_2+\nu_4+\nu_5$ band of C_2H_2 [112].	163
Figure 6-13: Collisional narrowing coefficients obtained from multispectral fitting of spectra recorded at 293 K in the $\nu_1+\nu_2+\nu_4+\nu_5$ band of C_2H_2 [112].	164
Figure 6-14: Narrowing temperature dependence coefficient n' obtained from equation 6-10 [112].	166
Figure 6-15: Comparison of diffusion coefficients. The diffusion coefficients determined for R(19), R(13) and R(11) were obtained through the use of equation 6-11. The Theoretical values were calculated from equation 6-12 [112].	168
Figure 6-16: Experimentally determined Diffusion coefficients obtained from retrieved β_o at 293K [112].	169
Figure 6-17: Observed and calculated spectra for the P(16) transition of the $\nu_1+\nu_3$ absorption band of C_2H_2 at a pressure of 40 Torr and temperature of 296 K. The residuals have been shifted vertically and magnified for easier comparison [113].	175

Figure 6-18: Comparison of classically calculated and experimentally determined N ₂ -broadening coefficients for three different temperatures. In each panel, the line depicts the theoretically determined broadening coefficients [113].	177
Figure 6-19: Panel A shows a comparison of the present N ₂ -broadening coefficients with previous studies. Panel B shows a smaller region between m=10 to m=25 where only values, obtained from a narrowing model, are compared [113]......	178
Figure 6-20: Temperature dependence exponents n_I obtained from equation 6-13 [113]......	180
Figure 6-21: The pressure dependent narrowing coefficient β_{N_2} for the P(16) and R(16) transitions at 296 K as they vary with the N ₂ pressure [113].	181
Figure 6-22: Comparison of the N ₂ -Narrowing coefficients obtained at 296 K to previous work [113]......	182
Figure 6-23: Narrowing temperature dependence coefficient n_I' obtained from equation 6-14. The diamonds show the results from Section 6.3.5 [112] with self-narrowing coefficients [113]......	183
Figure 6-24: Estimated diffusion coefficients obtained from retrieved experimental $\beta_{N_2}^o$ and equation 6-15 [113]......	186
Figure 7-1: Visual overview of the experimental setup of the GGMS.	191
Figure 7-2: Schematic overview of the GGMS system. M indicates where mirrors are placed and L indicates a lens.....	191
Figure 7-3: Measured leak rate for the AMAC-200 gas cell.	193
Figure 7-4: Image depicts the reduced conductance along the direct path to the vacuum line.	194

Figure 7-5: Screen shot of the “TriggeredMeasuring.vi” VI used to measure spectra with the GGMS.....	196
Figure 7-6: Example of the signals recorded using the GGMS setup.....	198
Figure 7-7: Spectra generated from a single scan of the GGMS system.	199
Figure 7-8: Example of N ₂ O recorded spectra when (A) single scan is performed and (B) 50 scans are averaged together.	201
Figure 7-9: Visual spot pattern produced from proper alignment, (A) shows the spot pattern provided by Aerodyne Research inc. and (B) shows the spot pattern produced by the HeNe trace beam after completing the alignment.....	202
Figure 7-10: Comparison of N ₂ O gas at 10.7 Torr (one single spectrum) measured with the GGMS against HITRAN [21] simulated spectra.	203
Figure 7-11: Comparison of N ₂ O gas at 140 mTorr measured (one single spectrum) with the GGMS against HITRAN [21] simulated spectra.	203
Figure 7-12: Example spectra of the R(19) line in the $\nu_1+\nu_2+\nu_4+\nu_5$ band of C ₂ H ₂ fit with a Voigt profile from the “ProfileFit.vi” VI.	204
Figure 7-13: Controls and Indicators for the “ProfileFit.vi” VI. Gamma denotes the broadening values, Delta the shift with the F representing foreign. Gamma D is the Doppler width. The Inputs cluster contains the initial values and spectral information like pressure and temperature. The best fit parameters are directly related to the Boolean controls in the cluster select to fit.	205

List of Abbreviations

TDLS	Tunable diode laser spectrometer
GGMS	Greenhouse gas monitoring system
DAQ	Data Acquisition
VI	Virtual Instrument
RMS	Root Mean Squared
SNR	Signal to Noise Ratio
ILS	Instrumental Line Shape
GUI	Graphical User Interface
EPG	Exponential Power Gap
HWHM	Half Width at Half Maximum
ECS	Energy Sudden Corrected Approximation
EPG	Exponential Power Gap Law
IOS	Infinite-Order Sudden Law
PRT	Platinum Resistance Thermometer
ECDL	Extended Cavity Diode Laser
InGaAs	Indium Gallium Arsenide

List of Equations

2-1	11
2-2	11
2-3	12
2-4	15
2-5	15
2-6	16
2-7	16
2-8	16
2-9	16
2-10	18
2-11	18
2-12	18
2-13	19
2-14	19
2-15	19
2-16	20
2-17	20
2-18	20
2-19	20
2-20	21
2-21	21
2-22	22

2-23	22
2-24	22
2-25	23
2-26	23
2-27	24
2-28	24
2-29	24
2-30	25
2-31	25
2-32	27
2-33	28
2-34	28
2-35	29
2-36	30
2-37	31
2-38	31
2-39	31
2-40	31
2-41	31
2-42	32
2-43	32
2-44	33
2-45	33

2-46	33
2-47	33
2-48	34
2-49	34
2-50	34
2-51	34
2-52	35
2-53	35
2-54	35
2-55	37
2-56	37
2-57	38
2-58	39
2-59	39
2-60	39
2-61	40
2-62	40
2-63	41
2-64	43
2-65	43
2-66	43
2-67	43
2-68	44

2-69	44
2-70	44
2-71	44
2-72	44
2-73	45
2-74	45
2-75	46
2-76	46
2-77	46
2-78	47
2-79	47
2-80	47
2-81	47
2-82	49
2-83	49
2-84	49
2-85	50
2-86	50
2-87	50
2-88	51
2-89	51
2-90	51
2-91	52

3-1	57
3-2	58
3-3	67
4-1	109
4-2	109
5-1	115
5-2	116
5-3	121
5-4	121
5-5	121
6-1	137
6-2	139
6-3	140
6-4	140
6-5	140
6-6	140
6-7	140
6-8	140
6-9	148
6-10	163
6-11	167
6-12	167
6-13	175

6-14	175
6-15	184
7-1	197
7-2	198
7-3	199
7-4	199

List of Mathematical Symbols

Unless explicitly described otherwise the symbols in this document have the following representations:

f	Frequency
E	Written as a scalar denotes energy
h	Planck's constant
t	Time
$\Psi, \psi\rangle$	Quantum wavefunction
ν	Vibrational quantum number (Greek nu)
R_ν	Vibrational transition
$\vec{\mu}$	Dipole moment
c	Speed of light
\hbar	Planck's constant over 2π
$\tilde{\nu}$	Frequency in wavenumbers
p	Pressure
T	Temperature
S	Intensity
V	Volume
ρ	Density or density operator
B	Rotational constant
I	Moment of inertia
\vec{E}	Electric field
K	Boltzmann constant
\vec{v} and v	Velocity (v not to be confused with nu)

ω	Angular frequency
M	Mass
Δ	Pressure induced shift
Γ	Collisional broadening
γ	Pressure dependant broadening coefficient
δ	Pressure dependant shift coefficient
β	Pressure dependant narrowing coefficient
γ_o	Pressure independent broadening coefficient
δ_o	Pressure independent shift coefficient
β_o	Pressure independent narrowing coefficient
Y	Line-mixing coefficient

Chapter 1: Introduction

1.1. Overview

This chapter will discuss the benefits of using laser spectroscopy to perform high resolution spectroscopic studies on line shape parameters. A discussion will be given on the presence of acetylene in planetary atmospheres and how the use of a tunable diode laser spectrometer can help improve our understanding of the temperature dependant line shape parameters of acetylene. A brief introduction on CO₂ will also be given with the main focus being on improving accuracy of retrieved concentrations. A discussion on the need for a device to monitor terrestrial N₂O levels will be given. Finally an outline of the thesis will be presented.

1.2. Spectroscopy

1.2.1. Introduction

It all began with the sun. Newton was the first to notice the dispersion of light by a prism in 1666. From this Newton coined the term “spectrum” to describe the resulting colors that originated from a white light source. These properties of light were not fully realized until the 1800’s. In 1800 it was shown by W. Herschel that the sun’s spectrum identified by Newton also contained non-visible light in the infrared region. Furthermore, in 1801 J.W. Ritter observed non-visible light in the ultraviolet region.

One of the largest contributions to the study of the solar spectrum came from Joseph Fraunhofer. He was able to show that if the light from the sun was sufficiently

dispersed, you could see dark lines present in the spectrum. Even though Fraunhofer could not attach any significance to this discovery it was the beginning of modern spectroscopy. From his study of dispersion and interference, Fraunhofer was able to create a grating with many slits which were used in some of the earliest spectrometers.

It was not until shortly after these lines were discovered (1859) that G. Kirchhoff realized that each element and compound has its own unique spectrum or fingerprint. Shortly after this realisation around 1885, J. Balmer developed a simple mathematical formula to predict the wavelength of atomic transitions in hydrogen. Just a few years later, J. Rydberg showed that the Balmer equation was a special case of what is now known as the Rydberg equation. The Rydberg equation offered a mathematical method for determining the wavelength of atomic transitions in not only hydrogen but other atoms as well.

Even though the development of the Rydberg equation was pivotal in predicting the atomic finger prints, it did not offer any explanation as to how these transitions were possible and what made them occur. In 1913, Neils Bohr proposed the “solar system” model, which described the atom as having stationary states that the electrons would orbit in. The change in allowed stationary states would result in the emission or absorption of light. This quantization of the allowed stationary states fueled the works of Schrödinger, Heisenberg and others, and has been a fundamental building block for modern quantum theory.

From this modest early beginning spectroscopy has become an essential tool for examining the universe around us. It allows us to probe the depths of the observable

universe and identify the development of stars and solar systems. It creates an opportunity for us to monitor the impact we have on our own environment. Finally it gives us tools for examining the kinematics and dynamics of the quantum world. All of these developments require a very rigorous understanding of the atomic and molecular finger prints that are observed. These observations have only continued to improve in the last century with the development of laser systems and improved experimental techniques.

1.2.2. Laser Spectrometer

With the invention of the laser in the early 1960's, a light source that is relatively coherent was found. The laser in comparison to conventional black body sources offers the advantage of having a high spectral brightness (the power emitted per unit line width), and a narrower line width which results in improved wavelength resolution. These features make the laser ideal for performing high-resolution measurements.

In 1962, Hall et al. [1] developed the first solid state laser system. Those laser systems are now common place and offer the advantages of being small in size, having excellent power conversion efficiencies, great tunability and the ability to be modulated. Applications of these laser systems range from telecommunications to airborne imaging systems.

The work presented in this thesis is mainly concerned with the use of an extended cavity diode laser (ECDL) system and its implementation with a spectrometer setup (see Chapter 3). Through the use of such a laser system, high resolution measurements can be made by examining absorption spectroscopy.

1.3. Acetylene as a constituent of planetary atmospheres

1.3.1. Introduction

In the past decade, numerous acetylene transitions have been used as frequency standards for fiber optic communications ([2] and references therein). Most spectroscopic studies are dedicated to the astrophysical and planetary applications of acetylene line parameters. For example, spectra of Titan's atmosphere recorded by the Cassini instrument reported that acetylene is one of the most abundant trace constituents after methane [3]. A study by Brooke et al. [4] identified acetylene in the infrared spectrum of the comet Hyakutake. They concluded from the abundance present that the formation of the comet was from ice covered interstellar grains, thus indicating acetylene as an important marker for interstellar processes.

1.3.2. Summary of studies

The first study on record that focused on measuring self- and H₂-broadened line parameters in acetylene was by Varanasi and Bangaru [5]. Those authors have studied acetylene transitions in the 1.525 micron region over a wide range of temperatures below room temperature. Laser spectroscopy was used by Wong [6] to measure the self-broadening coefficients for acetylene transitions in the range of his dye laser. The self-broadening parameters of acetylene in the ν_5 band for 27 R- and P-branch transitions were first studied by Lambot et al. [7] using a diode laser spectrometer. Those authors also reported calculated self-broadening coefficients obtained using two semi-classical impact models by applying a simple intermolecular potential. A follow-up study reported low temperature measurements of 21 transitions in the same band [8]. Semiclassical

theoretical calculations were used to model the low temperature broadening coefficients. The authors noted the agreement with experimental values as satisfactory when the electrostatic contributions due to the hexadecapole moment were taken into account. Pine [9] used a difference frequency laser system to measure the self-, N₂- and Ar-broadening coefficients for acetylene transitions in the $\nu_1 + \nu_5$ band. The author quantified the line mixing effects in the Q-branches using scaling laws. Lucchesini et al. [10] used diode laser spectroscopy to measure self-broadening and self shifts for several weak acetylene transitions belonging to overtone bands located in the 12700 to 11800 cm⁻¹ spectral range. Laser spectroscopy was also used by Georges et al. [11] to measure Ar- and self-broadening for a single transition of the 5 ν_3 band of acetylene.

Biswas et al. [12] have studied self- and nitrogen-broadening for transitions in the $\nu_1 + 3\nu_3$ band using spectra recorded with a diode laser spectrometer operating near 782 cm⁻¹. The measured line profiles were well reproduced by the Voigt model. The authors commented that they did not notice evidence of the effects of velocity changing collisions on the measured line shapes. Transitions in the same band were studied by Herregodts et al. [13] using a titanium sapphire autoscan laser spectrometer. The authors reported seeing the effects of Dicke narrowing in their low pressure spectra due to molecular confinement. The authors used several line profiles to model their data according to the pressure regime. Diode laser spectroscopy was used by Yelleswarapu and Sharma [14] to measure the self-broadening and pressure-induced self- shifts for several transitions in the $\nu_1 + 3\nu_3$ band. The spectra were modelled using the Voigt profile.

Minutolo et al. [15] measured self-, N₂-, O₂- and CO₂-broadening and pressure shifts for transitions of C₂H₂ and H¹³C¹²CH in 4 combination bands located in the 1.54 micron range. Twenty acetylene transitions belonging to the $\nu_1 + 3\nu_3$ band have been studied in detail by Valipour and Zimmerman [16]. The authors have studied the acetylene profiles with numerous broadeners: acetylene, N₂, O₂, air, He, Ne, Ar, Kr, Xe and modeled them using Galatry and Rautian profiles. An extensive study of cold bands located in the 5 micron range was performed by Jacquemart et al. [17]. Fourier transform spectra and a multispectrum fit procedure were used to retrieve self-broadening coefficients for over 120 transitions and about 89 pressure shifts.

Thirty absorption lines in the $\nu_4+\nu_5$ band of acetylene were recorded and studied by Lepere et al. [18]. The authors used the Rautian and Voigt models to retrieve the line intensities and self-broadening coefficients. The experimental broadening coefficients were in good agreement with calculated values obtained using a semiclassical model that took into account the main electrostatic interactions and an anisotropic dispersion contribution.

Lyulin et al. [19] measured line parameters for 550 lines belonging to 13 acetylene bands located between 1.7 and 1.9 microns. A multispectrum procedure was used to retrieve the line parameters from FTIR spectra using the Voigt model. Self-broadening coefficients have also been measured for 10 P-branch transitions located near 1.533 microns. The diode laser spectra were analyzed using both Voigt and Rautian models to account for line narrowing effects. Ten self-broadened P-branch transitions in the $\nu_1+\nu_3$ band of acetylene have been studied by Li et al. [20] using diode laser

spectroscopy. The measured line profiles were modeled using the Voigt and Rautian profiles and the results were compared with corresponding literature values.

1.4. Improving CO₂ Concentration Retrievals

In the context of global carbon cycle research, the Earth's atmosphere is both easily accessible and directly affected by human influences, making it one of the most studied systems. Carbon dioxide is a minor, chemically inactive and relatively well mixed atmospheric constituent with a long lifetime somewhere in the neighbourhood of 100 years. The accurate detection and predictions of spatial and temporal patterns in the global carbon cycle rely on the results of long term monitoring efforts of atmospheric carbon dioxide.

Although they are very different in composition compared to the Earth's atmosphere, planetary atmospheres such as those of Mars and Venus have a high content of carbon dioxide. On Mars, the pressures and temperatures of carbon dioxide are such that during the Martian winters the atmospheric carbon dioxide turns to dry ice, whereas in the summers the dry ice evaporates and the CO₂ is released back into the atmosphere. Venus has a dense, CO₂-rich atmosphere, with an atmospheric pressure at the planet's level that is about 92 times that of our own atmospheric pressure. The high content of carbon dioxide and thick clouds of SO₂ contribute to a very strong greenhouse effect and very high surface temperatures.

Today many complex spectra are being recorded by a variety of high-resolution instruments, mounted on everything from ground-based to space-based platforms. These instruments have been used to measure not just the Earth's atmosphere but also the

atmospheres of other planets and the satellites that orbit them. In order to better understand the complex spectra obtained from these instruments, large datasets like HITRAN [21] and GEISA [22] have been compiled. The information within these datasets has allowed for a more complete understanding of global carbon cycle science, global warming, climate change, and even of whole planetary systems besides that of the Earth.

Accurate predictions of the spectral properties of carbon dioxide are fundamental in furthering our understanding of the radiative properties of planetary atmospheres that contain CO₂. As emphasized by several research groups [23-35], accurate spectroscopic remote sensing retrievals rely on highly accurate calculated or experimental results for spectral line parameters over the range of temperatures and pressures relevant to the atmosphere or source in question and for all atmospheric constituents that absorb in the spectral range of interest.

1.5. Monitoring N₂O Levels in Agricultural Areas

Our understanding of N₂O as a greenhouse gas has become very important in recent years. The main reasons for this are its apparent constant increase of about 0.26% per year. It is also one of the main long-lived greenhouse gases with a life span estimated to be 114 years [36]. N₂O has been determined to be 300 times more powerful than CO₂ as a greenhouse gas [37]. It is important in stratospheric chemistry as N₂O is destroyed by photolysis and forms NO by reaction with O (¹D). This means that N₂O contributes to the concentration and distribution of ozone in the stratosphere. The main sources of N₂O have been found to be human related activities such as fertilizer use, fossil fuel burning

and natural events that happen in soil and oceans. A Large scale study started in 2007 of the European grassland system [38] has been underway for several years now to monitor these influences. The importance of similar related studies in Canada is very important as agriculture is a key component to our economy. Therefore, an instrument designed to monitor concentration of N_2O in remote locations will certainly improve our knowledge of the anthropogenic impact on the production of N_2O .

1.6. Thesis Outline

Chapter 2 will present the important underlying principles of rotation-vibration for polyatomic linear molecules. This chapter will also present the guiding principles behind absorption spectroscopy and give a detailed account of various line shape models used to describe the molecular motion in a gas.

Chapters 3 and 4 will present an overview of the tunable laser spectrometer setup developed in our laboratory, at the University of Lethbridge. Chapter 3 will discuss the physical setup and performance of the system, while Chapter 4 will discuss the acquisition and the processing of spectra obtained.

In Chapter 5, two approaches for calculating line mixing coefficients are implemented for the CO_2 molecule. The retrieved broadening coefficients are compared to the currently available values. The temperature dependence for these line mixing coefficients are also carefully analysed.

Chapter 6 is a compilation of three published studies related to the bands $\nu_1+\nu_3$ and $\nu_1+\nu_2+\nu_4+\nu_5$ of acetylene. In this chapter the analysis of the acetylene line parameters

for the $\nu_1+\nu_3$ and $\nu_1+\nu_2+\nu_4+\nu_5$ bands of acetylene will be presented in detail. Spectral line-shape analyses with the major focus of temperature dependence for the retrieved parameters are presented and discussed. Of special interest is the behaviour of these molecules in the Dicke pressure regime.

In Chapter 7 the setup and preliminary testing of a greenhouse gas monitoring system is presented. The system has been designed to measure the $4\nu_1+2\nu_2$ band of N_2O using a long path (200 m) gas cell. A detailed description of the control software and analysis software written in Labview, are presented. Careful attention is paid to the proper alignment of the system and the results verifying this will also be presented.

Finally Chapter 8 will summarize the conclusions and work presented throughout the thesis. A brief discussion on what can be done with future work will also be given.

Chapter 2: Theoretical Aspects

2.1. Introduction

A complete understanding of molecular spectroscopy is a very difficult thing to achieve. However in this chapter, I will present the fundamentals of rovibrational spectroscopy for linear polyatomic molecules, and discuss the vibrational bands of interest contained in this thesis. This chapter will also cover the topic of absorption spectroscopy and present some possible line shape profiles that can be used to describe the nature of experimentally observed absorption features. Finally a description of the line mixing process will be given showing explicitly how line mixing coefficients can be obtained using several different theoretical approaches.

2.2. Fundamentals of Spectroscopy

2.2.1. Interaction of electromagnetic radiation with atoms and molecules

Light or electromagnetic radiation is a transverse wave that has an amplitude directly related to its constituent parts, the electric field \vec{E} and the magnetic field \vec{H} . These two fields will always propagate in the direction of the travelling wave but will remain perpendicular with respect to each other. A simple plane wave propagating in the x-direction can be described by the following equations:

$$E_y = E_{y0} \sin(2\pi ft - kx) \text{ and} \tag{2-1}$$

$$H_z = E_{z0} \sin(2\pi ft - kx), \tag{2-2}$$

Here E_{y0} and E_{z0} are the maximum electric field strength in the y- and z-directions, t is time, x is position, f is the frequency of the light and k is the wavenumber. These equations show that the simple electromagnetic wave is periodic in both space and time and the electric and magnetic components are always in phase with each other. The frequency f of the light can fall into many different regions of the electromagnetic spectrum. Figure 2-1 shows the complete electromagnetic spectrum and indicates the various wavelength/frequency regimes commonly used.

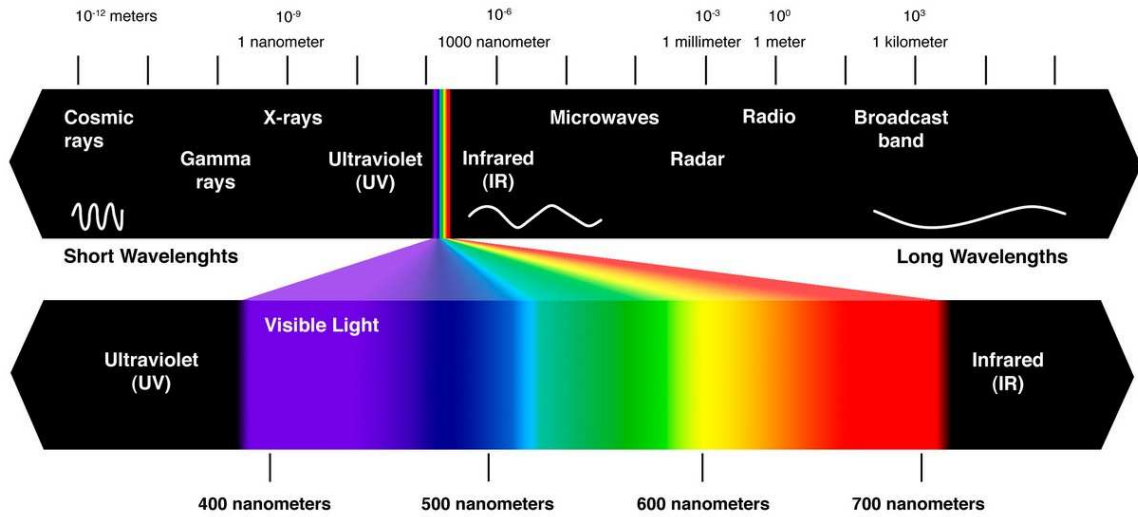


Figure 2-1: Example of the full electromagnetic spectrum of light. [http://www.widen.com/premediablog/call-me-mr-biv-v1]

In order to use light as a probe an understanding of how it will interact with matter is needed. Using a simple two-state quantum system with upper eigenstate m and lower eigenstate n we know that it will have eigenenergies of E_m and E_n . This simple system can undergo a change in energy equal to ΔE that can be written as:

$$\Delta E = E_m - E_n = hf_{mn} , \quad 2-3$$

where f_{mn} is the frequency of the light either absorbed or emitted depending on the process taken and h is the Plank constant. The process by which the energy of this system changes can be any of the three following possible cases:

1. Spontaneous emission: The system spontaneously drops from state m to n and in doing so produces a photon of light with frequency f_{mn} (the frequency f_{mn} is the direct result of the conservation of energy for this system).
2. Stimulated emission: A photon of frequency f_{mn} interacts with an excited system and de-excites it from m to n releasing another photon of frequency f_{mn} . This second photon remains coherent with the original photon. This process in conjunction with population inversion is fundamental to laser systems.
3. Induced absorption: An incident photon is absorbed by the system causing it to go from the lower state n to the upper state m .

Figure 2-2 gives a graphical representation of these three possible processes. When light interacts with atoms or molecules all three of these processes are important.

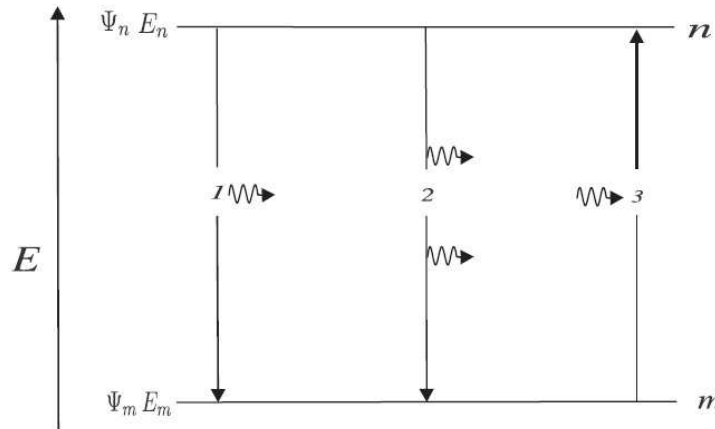


Figure 2-2: Three possible results in a two level quantum system: (1) Spontaneous emission, (2) Stimulated emission and (3) Induced absorption. Here Ψ_n and Ψ_m represent the two quantum states n and m defined above.

When dealing with light interacting with atomic structure only the excitations of electrons around the nucleus are considered, which for the most part is quite straight forward. The discussion of how light interacts with molecules is more complex due to the shape and structure of the molecules under study. In the case of atoms, the electrons are outside the nucleus and arranged on orbitals, and the energy of the system is related to the electrons' angular momentum and spin. Molecules are different in that the energy of the system is dependent on vibration (motion of the atoms relative to each other) and rotation of the molecule as a whole (molecules of certain symmetry types may also contain internal angular momentum as well). This complex motion of molecules will be discussed in the Sections 2.2.2, 2.2.3 and 2.2.4.

2.2.2. Pure vibration

The understanding of the molecular motion is developed by first identifying the degrees of freedom that a polyatomic molecular system will have. The fundamental number of degrees of freedom for any polyatomic molecule is $3N$, now knowing that there are 3 of those degrees associated with the translational motion of the molecule and another 2 to 3 degrees associated with the rotation of the molecule (3 for non-linear molecules and 2 for linear molecules). This means that polyatomic molecules have $3N-5$ (linear molecules) or $3N-6$ (non-linear molecules) degrees of freedom. These remaining degrees of freedom correspond to vibrations of the molecule and are also referred to as the normal modes of vibration. Each of these normal modes is an independent mode of vibration and can be described by a single normal coordinate. The use of normal coordinates to describe a vibrational mode of the molecule is the direct result of having all the atoms vibrating at the same frequency and phase with respect to each other. It is

also possible for two or more modes to be degenerate with each other meaning they will appear to vibrate at the same frequency. This degeneracy in the modes is the direct result of the symmetry of the molecule and is usually associated with bending type modes of vibration for linear molecules.

The energies and thus the frequencies of the normal modes are solutions of the time-independent Schrödinger equation,

$$H|\psi\rangle = E|\psi\rangle, \quad 2-4$$

where H is the Hamiltonian with corresponding eigenenergies E and wavefunctions $|\psi\rangle$. In general, the solution to this equation will give a complete description of the spectroscopic system. However, in practice the complete solution to this equation is not generally possible. Therefore, in order to make progress with this expression, the Born-Oppenheimer approximation must be considered. The use of this approximation allows for the electronic energy ($E_{el} = H|\psi_{el}\rangle$) to be separated from the vibration energy ($E_N = H|\psi_N\rangle$) of the system by making the assumption that the electrons within the system are moving far faster than the nuclei that are present. This separation allows for the wavefunction to be written as a product of the electronic state and the nuclear state as follows.

$$|\psi\rangle = |\psi_{el}\rangle|\psi_N\rangle. \quad 2-5$$

This separation, although only an approximation, still allows for the analysis of the nuclear motion.

For diatomic molecules, in a first approximation the molecule vibrates like a simple harmonic oscillator. We can then solve the Schrödinger equation for a simple harmonic oscillator and obtain the allowed energies of the system as follows.

$$E_n = hf \left(v + \frac{1}{2} \right) \quad 2-6$$

Here f is the vibrational frequency and v is the vibrational quantum number (number of quanta in that mode of vibration i.e. $v = 0, 1, 2, \dots$). This approximation shows that the energy distribution has equidistant levels in it.

The vibrational transitions R_v are connected to a change in the dipole moment and can be examined using the transition moment as follows.

$$R_v = \int \langle \psi'_n | \vec{\mu} | \psi''_n \rangle dx, \quad 2-7$$

where $\vec{\mu}$ is the dipole moment and x refers to the displacement from equilibrium ($x = r - r_e$, where r_e is the equilibrium distance and r is the new displacement). The dipole moment can be written in the form of a Taylor expansion about the equilibrium position as follows.

$$\vec{\mu} = \vec{\mu}_e + \left(\frac{d\vec{\mu}}{dx} \right)_e x + \frac{1}{2!} \left(\frac{d^2\vec{\mu}}{dx^2} \right)_e x^2 + \dots, \quad 2-8$$

where the derivatives are taken with respect to the equilibrium configuration. Substituting equation 2-8 into 2-7 we get the following.

$$R_v = \vec{\mu}_e \int \langle \psi'_v | \psi''_v \rangle dx + \left(\frac{d\vec{\mu}}{dx} \right)_e \int \langle \psi'_v | x | \psi''_v \rangle dx + \dots. \quad 2-9$$

In this expression the first term will be equal to zero because the two wavefunctions are orthogonal to each other (i.e. $\langle \psi'_v | \psi''_v \rangle = 0$). Therefore, if the higher order terms are neglected and only the second term is considered in equation 2-9, a

restriction on allowed transitions results in the following selection rule $\Delta v = \pm 1$. This means that for a harmonic oscillator only transitions that satisfy this condition are allowed, and that all allowed transitions will be at the same frequency f . It is also important to note that the term $\left(\frac{d\bar{\mu}}{dx}\right)$ indicates that the molecule must have a changing dipole moment in order to have an observable transition and its magnitude or intensity is dependent on the size of this term. If this term is zero, as is the case with most homogenous diatomic molecules, no vibrational transition will be observed.

Typically, a diatomic molecule will behave much like a harmonic oscillator only when the internuclear distance is close to the equilibrium distance. At a certain position, far away from the equilibrium position, the molecule will dissociate into its individual atoms. Thus, the typical harmonic oscillator does not describe real molecules. In order to include this dissociation an anharmonic oscillator can be used to describe the vibrational structure of the molecule. Figure 2-3 shows the difference between the potential energy of a harmonic oscillator and that of an anharmonic oscillator. There are two fundamental consequences that result from using an anharmonic oscillator approximation.

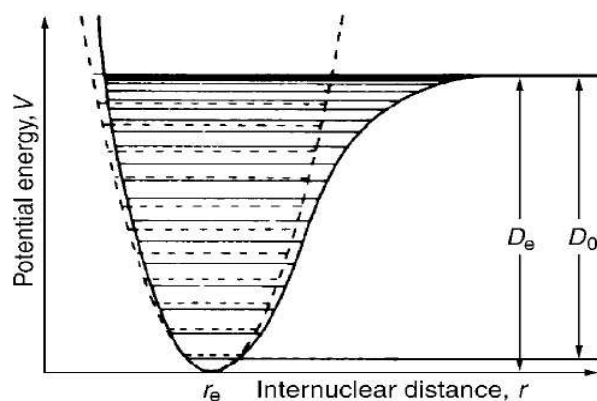


Figure 2-3: Potential energy curve and energy levels of a diatomic molecule. The curved solid lines depict the anharmonic case. The dashed lines indicate the classical harmonic oscillator. Here D_e is the dissociation energy measured relative to the equilibrium potential energy, and D_0 is the dissociation energy relative to the actual ground state level [39].

The first consequence results from the condition that $\Delta\nu = \pm 1$ is no longer the only valid observable transition. The anharmonicity allows for new transitions that follow the selection rule $\Delta\nu = \pm 2, \pm 3 \dots$ where the intensities of these new overtones are related to the anharmonicity of the electronic structure and to the mechanical motion of the molecule. The second consequence is a change in the energy spacing that is now dependent on the vibrational quantum number ν . The following expression describes the energies $G(\nu)$, for the anharmonic case (in terms of the more convenient units of wavenumber).

$$G(\nu) = \tilde{\nu}_e \left(\nu + \frac{1}{2} \right) - \tilde{\nu}_e x_e \left(\nu + \frac{1}{2} \right)^2 + \dots, \quad 2-10$$

where $\tilde{\nu}_e$ is the vibrational wavenumber for a classical oscillator with a small displacement from equilibrium, and x_e is the first order anharmonicity constant.

Using the energy structure of a diatomic molecule the system can be expanded to describe polyatomic molecules. By identifying that the wavefunction ($|\psi\rangle$) that describes the vibrational nuclear motion is the product of the $3N-5$ or $3N-6$ normal vibrational modes (Q_N), to which the wavefunction (for a linear molecule) can be written in the following form;

$$|\psi\rangle = |\psi_1(Q_1)\rangle |\psi_2(Q_2)\rangle \dots |\psi_{3N-5}(Q_{3N-5})\rangle. \quad 2-11$$

The energy for this system will then be the sum of the energy of each normal mode. Therefore for the case of the harmonic oscillator, the vibrational energy of the molecule will be given by:

$$G(\nu_1, \nu_2 \dots \nu_{3N-5}) = \sum_{i=1}^{3N-5} \tilde{\nu}_i \left(\nu_i + \frac{d_i}{2} \right), \quad 2-12$$

where the term d_i as the degeneracy of the i^{th} mode. Once again, this result will only be true for the case when the internuclear distance is close to the equilibrium distance. In order to get a better approximation of the system's energy an anharmonic description is therefore required. The energy of an anharmonic system can be expressed in the following way:

$$G(v_1, v_2 \dots v_{3N-5}) = \sum_{i=1}^{3N-5} \tilde{\nu}_i \left(v_i + \frac{d_i}{2} \right) + \tilde{\nu}_i \sum_i \sum_{k \geq i} x_{ik} \left(v_i + \frac{d_i}{2} \right) \left(v_k + \frac{d_k}{2} \right), \quad 2-13$$

where x_{ik} is the anharmonicity constant associated with i^{th} and k^{th} vibrational modes. When the anharmonicity is taken into account the presence of the x_{ik} constants from equation 2-13 gives rise to what are called combination bands. These bands are the simultaneous excitation of more than one fundamental mode at a time. Though they are weaker than the fundamental transitions, they are still observable.

2.2.3. Pure rotation

As previously discussed, we can use the Born-Oppenheimer approximation to separate the electronic states from the nuclear motion states, and the rotational states from the vibrational states. Hence, the wavefunction can be written as a product of the three components (electronic ($|\psi_{el}\rangle$), rotation ($|\psi_R\rangle$) and vibration ($|\psi_v\rangle$)) as follows:

$$|\psi\rangle = |\psi_{el}\rangle |\psi_R\rangle |\psi_v\rangle. \quad 2-14$$

Writing the wavefunction in this way means that the total energy of the system will be given by the following summation of energies:

$$E = E_{el} + E_R + E_v, \quad 2-15$$

where E_{el} , E_R and E_v are the energies associated with electronic, rotational and vibrational states respectively. The vibrational energy has been discussed in the previous section. Next the energy associated with the rotation of a molecule will be discussed.

To begin, consider a diatomic molecule (a dumbbell shaped molecule) that behaves like a rigid rotor. Using this assumption the Schrödinger equation for a rigid rotor can be written in the following way.

$$\frac{\hat{j}^2}{2I}|\psi\rangle = E_R|\psi\rangle, \quad 2-16$$

where \hat{j} is the total angular momentum operator for a rigid rotor I is the moment of inertia for the rigid rotor molecule. Solving equation 2-16 we obtain the following energies (in wavenumbers) for the rigid rotor as follows:

$$F(J) = \frac{E(J)}{hc} = BJ(J + 1), \quad 2-17$$

where h is the Planck's constant J is the rotational quantum number and can be any positive integer including 0, and B is the rotational constant defined by:

$$B = \frac{h}{8\pi^2 cI}, \quad 2-18$$

here c is the speed of light.

From this the selection rule for the rigid rotor is $\Delta J = \pm 1$ and is the required condition for observable transitions. The frequency of the observable transitions can therefore be calculated by the following expression:

$$\Delta F_{J' \leftarrow J''} = F(J') - F(J'') = 2B(J + 1), \quad 2-19$$

where J' is the rotational quantum number of the upper rotational state and J'' is the rotational quantum number of the lower rotational state. It is easily seen from this

expression that for the case of a rigid rotor there are equidistant transitions with a spacing of $2B$.

To explain what is observed in reality a careful examination of what happens to a diatomic molecule as J increases must be considered. As the molecule begins to rotate with a higher angular momentum, it will experience centrifugal forces causing the bond length to alter slightly. This change in the bond length will then cause the moment of inertia to become slightly different. The net result of this motion is a dependence of the rotational constant B on the vibrational state. Now by incorporating a centrifugal distortion constant (D) into equation 2-19 to account for these small changes in transition spacing we get the following:

$$F(J) = BJ(J + 1) - D[J(J + 1)]^2. \quad 2-20$$

Using this new expression the transition frequencies can be determined in the same way as before, but now with more accurate results as follows:

$$\Delta F_{J \leftarrow J''} = 2B(J + 1) - 4D(J + 1)^3. \quad 2-21$$

Generally $B \gg D$ and therefore it is expected that for small values of J there will be very little difference between the spacing of transitions. However as J starts to get larger, the spacing between the transitions will rapidly decrease.

2.2.4. Vibration-rotation

All experimental spectra correspond to physical states of rotation and vibration. This coupling of excitations requires a slight modification to be made to equation 2-20 obtained in Section 2.2.3. For example, for stretching vibrations the internuclear separation will increase with v . If the spacing is increased, the moment of inertia will also

increase and it will lead to a decrease in both the rotational constant B , and in the centrifugal distortion constant D . This change can be expressed in the following way:

$$B_v = B_e - \sum_i \alpha_i \left(v_i + \frac{d_i}{2} \right) \text{ and} \quad 2-22$$

$$D_v = D_e - \sum_i \beta_i \left(v_i + \frac{d_i}{2} \right), \quad 2-23$$

where α_i and β_i are small compared to B_e and D_e . The subscript “e” in the above equations refers to the constant values at equilibrium and d_i once again refers to the degeneracy of the i^{th} mode. Using equations 2-22 and 2-23 the rotational energy of a molecule undergoing vibration is given by:

$$F(J) = B_s J(J+1) - D_s [J(J+1)]^2, \quad 2-24$$

Here s is the vibrational label of the physical state. It is important to note that the centrifugal distortion constant is a small effect to begin with, thus $D_s \approx D$.

2.2.5. Vibrational angular momentum

As mentioned earlier in Section 2.2.2, linear molecules with bending modes will have a degeneracy associated with them. The degeneracy is the result of two fundamental modes vibrating with the same energy but in two perpendicular planes. Figure 2-4A shows a linear molecule with the red and blue lines, indicating the two planes in which the molecule can vibrate. The net result of the molecule vibrating in both planes with some associated phase gives the appearance of the nuclei rotating about the intermolecular axis. This rotation is labelled as vibrational angular momentum and the degeneracy of the system can be viewed as a rotation in either the clockwise or the counter clockwise direction.

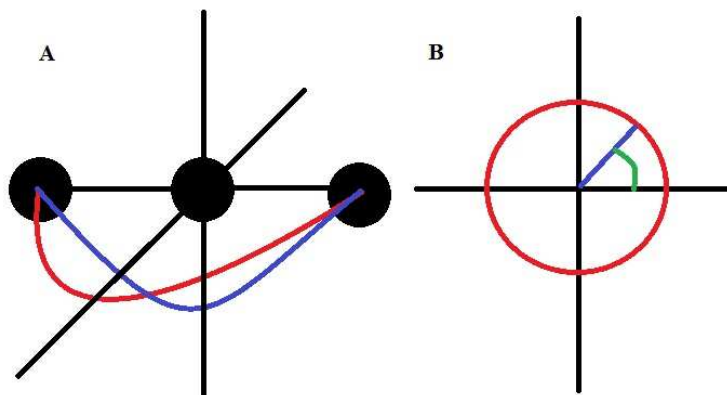


Figure 2-4: Simplified example of a molecule vibrating in a degenerate bending mode. A) shows the two possible planes where the molecule will bend while B) shows the circular path the nuclei trace out along the inter molecular axis. The angle in B represents the angular speed at which it rotates around the axis.

The angular momentum must be quantized in order to be incorporated into the current description of vibration and rotation. The vibrational angular momentum is quantized in packets of $\pm l\hbar$ and l can have the following values:

$$l = \nu_i, \nu_i - 2, \nu_i - 4 \dots - \nu_i, \quad 2-25$$

where ν_i is the vibrational quantum number for the normal bending mode ν . Specific labeling is given to designate the vibrational angular momentum about the inter-nuclear axis (i.e., $\Sigma \rightarrow l = 0$, $\Pi \rightarrow l = 1$, $\Delta \rightarrow l = 2 \dots etc.$).

To determine the total angular momentum of the molecule the contributions from vibration (\vec{l}) and rotation (\vec{M}) need to be considered. The total angular momentum will then be.

$$\vec{j} = \vec{l} + \vec{M}. \quad 2-26$$

For each value of \vec{M} there are two possible values of \vec{l} , resulting in a splitting of rotational levels called l -type doubling. The magnitude of the doubling is given by:

$$\Delta v = qJ(J + 1), \quad 2-27$$

where q is the l -type doubling constant. This doubling will result in a restriction of observable transitions as J can only take the values of $|l|, |l| + 1, |l| + 2, \dots$. Therefore, transitions that do not meet this requirement will be forbidden. A new expression for the rotational energy can be written to include the vibrational angular momentum as follows:

$$F(J, l) = B_v[J(J + 1) - l^2] - D_v[J(J + 1) - l^2]^2. \quad 2-28$$

2.2.6. Vibration-rotation bands

The total energy of the ro-vibrational system will be given by writing the energy in terms of both the rotational and vibrational energy. Combining equations 2-13 and 2-28 an expression for the total energy can be obtained as follows:

$$T = \sum_{i=1}^{3N-5} \omega_i \left(v_i + \frac{d_i}{2} \right) + \omega_i \sum_i \sum_{k \geq i} x_{ik} \left(v_i + \frac{d_i}{2} \right) \left(v_k + \frac{d_k}{2} \right) + \sum_t g_{tt} l_t^2 + B_v J(J + 1) - D_v [J(J + 1)]^2. \quad 2-29$$

The subscript “ t ” denotes the degenerate modes with vibrational angular momentum l_t . This expression indicates that for a single vibrational mode there is a series of allowed rotational energy levels. The spacing for these rotational transitions will vary with the vibrational mode and, thus, it will not be constant.

Polyatomic linear molecules whose spectra are studied and reported in this Thesis have two types of vibrational-rotational bands. One of the two types is known as perpendicular bands. These bands have a dipole moment change that is perpendicular to the molecular axis and are associated with a change in the vibrational angular

momentum. That is $\Delta l = \pm 1$ or transitions of the type $\Pi \leftarrow \Sigma, \Delta \leftarrow \Pi, \dots$. These types of transitions allow for $\Delta J = 0, \pm 1$ thus giving rise to P ($\Delta J = -1$), R ($\Delta J = 1$) and Q ($\Delta J = 0$) branches in the spectra.

The second type of bands are called parallel bands. These bands arise due to the dipole moment changing parallel with the molecular axis. For these transitions $\Delta l = 0$, however this does not mean that $l=0$. When $l=0$, the parallel band will be of the $\Sigma \leftarrow \Sigma$ type with $\Delta J = \pm 1$. Therefore, these bands will have both P ($\Delta J = -1$) and R ($\Delta J = 1$) branches where the transition wavenumbers can be determined by the following expressions:

$$\tilde{\nu}_P = \tilde{\nu}_o - (B'_v + B''_v)J + (B'_v - B''_v)J^2 \text{ and} \quad 2-30$$

$$\tilde{\nu}_R = \tilde{\nu}_o + 2B'_v - (3B'_v + B''_v)J + (B'_v - B''_v)J^2, \quad 2-31$$

where $\tilde{\nu}_o$ is the pure vibration-rotation transition wavenumber, B'_v is the upper state rotational constant, B''_v is the lower state rotational constant, $J = 1, 2, 3, \dots$ for the P branch (eq. 2-30) and $J = 0, 1, 2, \dots$ for the R branch (eq. 2-31). When $l \neq 0$ the transitions are of the type $\Pi \leftarrow \Pi, \Delta \leftarrow \Delta, \dots$. For these transitions, $\Delta J = 0, \pm 1$ will give rise to the same P ($\Delta J = -1$), R ($\Delta J = 1$) and Q ($\Delta J = 0$) branches as seen in the case of perpendicular bands. However, for this case the Q branch is significantly weaker.

2.2.7. Rovibrational bands reported in this thesis

Spectra of three important linear polyatomic molecules are investigated in this work. Acetylene (C_2H_2) molecule belongs to the point group $D_{\infty h}$ and possesses five fundamental vibrational bands with the ν_4 and ν_5 being doubly degenerate. In the present work two combination bands are examined and the first one is the $\nu_1 + \nu_2 + \nu_4 + \nu_5$ band. This

is a parallel band with vibrational angular momentum $l=0$, thus, distinguishing it as a $\Sigma \leftarrow \Sigma$ band with only the P and R branches. The second one is the $\nu_1+\nu_3$ band which is also a $\Sigma \leftarrow \Sigma$ parallel band with $l=0$ as the ν_4 and ν_5 bands are not excited and, therefore, there is no vibrational angular momentum present.

In the case of the $\nu_1+\nu_2+\nu_4+\nu_5$ band only the R branch was measured, as the P branch was hard to observe due to the presence of the stronger $\nu_1+\nu_3$ band. For the $\nu_1+\nu_3$ band both P and R branches were studied. However, simulations were done to determine which lines would be suitable as the lower J valued lines are quite intense inside the 1.5 m path length chamber.

The second polyatomic linear molecule examined is CO_2 . The carbon dioxide molecule also belongs to the $D_{\infty h}$ point group thus has similar symmetry properties as those observed for acetylene. CO_2 however only has three fundamental vibrational modes with the ν_2 mode being doubly degenerate. The $(3\nu_1+\nu_3)_{\text{II}}$ ($30012 \leftarrow 00001$) and $(3\nu_1+\nu_3)_{\text{III}}$ ($30013 \leftarrow 00001$) bands are both $\Sigma \leftarrow \Sigma$ bands thus only having observable P and R branches. Another important feature of these two bands is the selection rule that transitions with J'' that are “even” are only allowed. This selection rule is the result of the symmetry generated from nuclear spin statistics for this molecule (indistinguishable oxygen atoms present).

The third molecule whose infrared spectrum is studied in this investigation is N_2O which belongs to the symmetry point group $C_{\infty v}$. N_2O has the same number of atoms as CO_2 and also possesses three fundamental modes with the ν_2 fundamental mode being doubly degenerate much like CO_2 . The band of interest in this Thesis is the $4\nu_1+2\nu_2$ and

has a vibrational angular momentum of $l=0$. This band is therefore a parallel $\Sigma \leftarrow \Sigma$ band and thus only exhibits P and R transitions.

2.3. Absorption Spectroscopy

2.3.1. Introduction

Over the last 100 years spectrometers have become one of the most important recording instruments used to probe the universe and can be used to examine what makes up the interstellar medium and identify the components of many atmospheres. With the continued growth of the satellites in orbit around Earth and planetary bodies, more and more high-resolution devices are being deployed to study atmospheric chemistry, weather and other physical processes. Understanding these fundamentals gives insight into the physical processes and the type of environment that these gases are exposed to. In the following section, a detailed description of absorption spectroscopy will be presented.

2.3.2. Beer Lambert law

In order to examine the spectral properties of a gas several experimental components are required. These components consist of a source, an absorption cell where the gas under study can be introduced during the data acquisition period and a suitable detector. By measuring the radiation that travels through the cell, one can obtain a spectral fingerprint for the gas inside the cell. The Beer-Lambert law quantifies the properties of the gas that absorbs the radiation as follows:

$$I_t = I_o e^{-\alpha CL}, \quad 2-32$$

where I_t is the transmitted intensity of the light, I_o is the incident intensity of the light, C is the concentration of the gas, L is the path length of the absorption cell and α is the absorption coefficient of the sample gas.

Equation 2-32 can be altered to describe the transmission of a monochromatic source through a medium of length L (cm) as follows:

$$\left(\frac{I_t}{I_o}\right)_{\tilde{\nu}} = e^{-\alpha_{\tilde{\nu}}}. \quad 2-33$$

The variable $\alpha_{\tilde{\nu}}$ is the spectral absorbance as a function of wavenumber and it can be further decomposed into the following form:

$$\alpha_{\tilde{\nu}} = p\chi_{abs}S(T)\varphi_{\tilde{\nu}}L, \quad 2-34$$

where p is the pressure in atmospheres, χ_{abs} is the mole fraction of the absorbing species, T is the gas temperature in Kelvin, S is the line strength in units of $\text{cm}^{-2}\text{atm}^{-1}$, and $\varphi_{\tilde{\nu}}$ is the line shape function.

For an ideal spectrometer the source of the radiation will have no effect on the line shape function and can be assumed to be one of several functions. The choice of the function depends on the physical conditions of the gas being examined, i.e., temperature, pressure, and also on the practical application of the particular measurement. Figure 2-5 shows the three most commonly used line shape functions. The different line shape functions commonly used will be described in greater detail in Section 2.4.

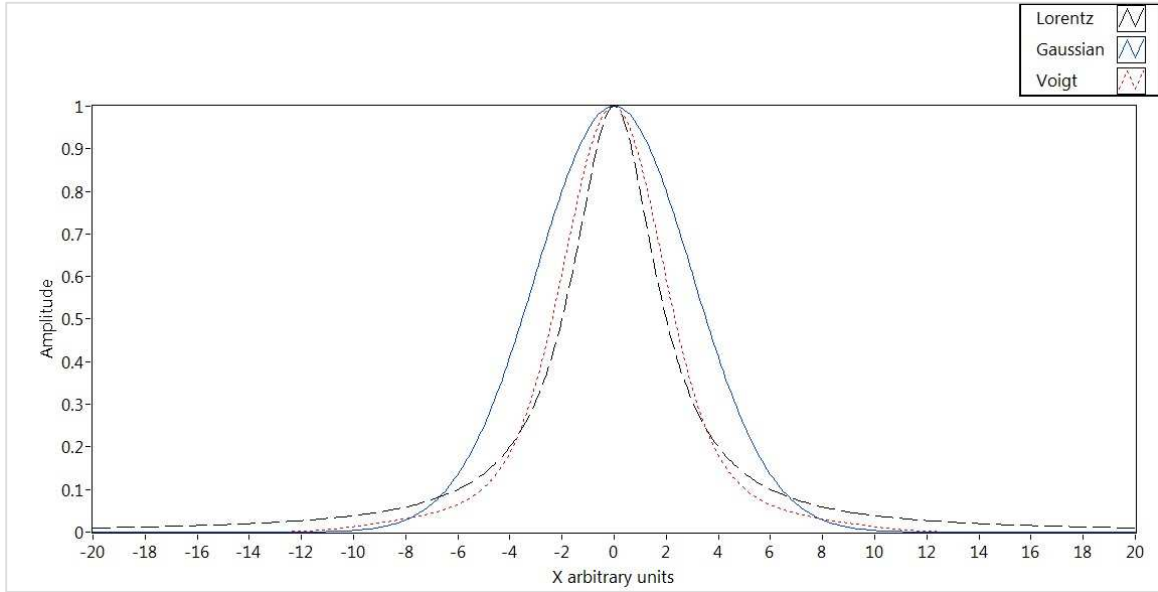


Figure 2-5: Three commonly used line shape functions.

In practice, the finite instrumental line shape (ILS) can alter the overall line shape by adding its own contribution to the measured signal. The result is a small change in the expression of the line shape function ($\varphi_{\tilde{\nu}}$) where it is the convolution of both the natural line shape function (φ_n) and the ILS.

$$\varphi_{\tilde{\nu}} = \varphi_n * ILS = \int_{-\infty}^{\infty} \varphi_n(\tau) ILS(t - \tau) d\tau, \quad 2-35$$

In order to deal with this phenomenon, the line shape function of the instrument must be determined. The instrumental line shape function can be determined by completing a nonlinear least squares fit on measured spectra at low gas pressures. The details of these measurements for the spectra obtained with a tunable diode laser spectrometer used in this work are discussed in Section 0.

2.4. Spectral Line Shape Functions

2.4.1. Introduction

In order to understand the mechanisms that influence the line shape functions used in Equation 2-34, a basic understanding of the physical system is needed. To start with consider a system X which describes a gas or mixture of gases with which an electromagnetic field can interact. The system X can be decomposed into two separate parts. The first labeled X_j , is the portion of the system associated with J^{th} transition (i.e. molecules with rotation-vibration matching this transition) and X_m which is associated with the remaining possible states. From this the Hamiltonian of the system can be written in the following form:

$$H = H_m + H_j + H_{j-m}, \quad 2-36$$

where H_j is the Hamiltonian describing the transition of interest associated with X_j , H_m is the Hamiltonian describing the X_m portion of the system, which contains information about the colliding molecules and their interactions with the electromagnetic field as well as other spectral transitions and H_{j-m} is the interaction Hamiltonian that describes how X_j and X_m influence each other.

In order to examine H_{j-m} closer the system is examined as it evolves in time. That is at time $t = 0$ the system is turned on and at time $t = \tau$ the system is turned off. The result of this is the determination of the average energy of the system, X_j , at $t = 0$ and $t = \tau$. These average energies can then be used to write the absorption coefficient in the following way:

$$\alpha(\omega_j) = \frac{1}{VS(\omega_j)} \lim_{\tau \rightarrow \infty} [\langle E_j(0) \rangle - \langle E_j(\tau) \rangle], \quad 2-37$$

where V is the system volume and $S(\omega_j)$ is the intensity of the j^{th} mode. Therefore by determining $E_j(0)$ and $E_j(\tau)$, a proper expression for the absorption coefficient can be obtained.

$$\langle E_j(\tau) \rangle - \langle E_j(0) \rangle = Tr_X \{ H_j [\rho(\tau) - \rho(0)] \}, \quad 2-38$$

where Tr_X is the trace over all the states within the system X , and ρ is the density operator. This allows for a solution of the absorption coefficient that depends solely on evolution of the density operator from 0 to τ . The evolution of $\rho(\tau)$ is given by the Liouville-Von Neumann equation [40] as follows:

$$i\hbar \frac{\partial}{\partial t} \rho(t) = [H, \rho(t)], \quad 2-39$$

where $[H, \rho(t)]$ denotes the commutator of the Hamiltonian given by equation 2-36 and the density operator $\rho(t)$ at time t . Using the assumption that the system can be divided into individual small cells each with one radiator inside, and a large number of perturbers, then we can define the interaction Hamiltonian using the dipolar approximation [40]:

$$H_{j-m} = -\vec{\mu} \cdot \vec{E}_j(\vec{r}), \quad 2-40$$

where $\vec{\mu}$ is the dipole moment (permanent or induced) with its center of mass located at \vec{r} and $\vec{E}_j(\vec{r})$ is the operator used to describe the incident transverse electric field. Now writing $\rho(0) = \rho_j(0)\rho_m(0)$ and applying a second order iteration to H_{j-m} the absorption coefficient takes on the following form [40]:

$$\alpha(\omega_j) = n_a \frac{4\pi^2 \omega_j}{3\hbar c} (1 - e^{-\hbar\omega_j/KT}) F(\omega_j), \quad 2-41$$

$n_a = \frac{N_a}{V}$ is the number density (N_a) per unit volume (V) of the radiators present, K is the Boltzmann constant and \hbar is Planck's constant divided by 2π . The function $F(\omega_j)$ is the spectral density function and it is the Fourier transform of the dipole autocorrelation function $\Phi(t)$, (the subscript j has been dropped for generality) as follows:

$$F(\omega) = \frac{1}{2\pi} \int_{-\infty}^{\infty} e^{i\omega t} \Phi(t) dt. \quad 2-42$$

The form that the dipole autocorrelation function takes will depend on the molecular motion of the gas. That is, different physical conditions within the gas will give rise to various effects that are observed in measured spectra, and are ultimately defined by the various line shape profiles. The following sections will describe these line shape functions and their impact on the physical description of the system.

2.4.2. Doppler Profile

As a first step, consider the case of a free streaming molecule. This means that the molecule is undergoing no collisions and is travelling in an unrestricted manner with velocity \vec{v} . The position of the molecule can easily be obtained at time t through the expression $\vec{r}(t) = \vec{v}t$. This change in position with time will result in a Doppler shift of the frequency for any scattered or absorbed photons. The amount of shift can be described by the expression as follows:

$$\text{Doppler shift} = \frac{\omega_{fi} v_z}{c}. \quad 2-43$$

In this expression, ω_{fi} is the transition frequency and v_z is the component of the velocity parallel to the direction of propagation for the incident electromagnetic wave vector \vec{k}

$(v_z = \frac{\vec{v} \cdot \vec{k}}{\|\vec{k}\|})$. The Doppler shift in frequency is therefore dependent on v_z through the Maxwell-Boltzmann equilibrium distribution as follows:

$$F_M(v_z) = \left(\frac{M}{2\pi KT}\right)^{3/2} e^{-\left(\frac{v_z}{v_p}\right)^2}, \quad 2-44$$

where M is the mass of the radiator and v_p is the most probable speed defined by $v_p = \left(\frac{2KT}{M}\right)^{1/2}$. The distribution of velocities described by equation 2-44 results in an inhomogenous broadening of the transition that is symmetrical about the transitions frequency ω_{fi} . This allows for a description of the classical dipole autocorrelation function for a free streaming molecule in the following form:

$$C_{ext}(t) = \langle e^{-i(\vec{k} \cdot \vec{v})t} \rangle. \quad 2-45$$

Based on equation 2-44, the thermal equilibrium average of equation 2-45 can be determined resulting in the following expression:

$$C_{ext}(t) = e^{-\left(\frac{\Delta\omega_D t}{2}\right)^2}, \quad 2-46$$

where $\Delta\omega_D = \frac{\omega_{fi} v_p}{c}$ the Laplace transform of this autocorrelation function will give the desired Doppler line shape profile as follows:

$$I_D(\tilde{\omega}) = \frac{1}{\sqrt{\pi}\Delta\omega_D} e^{-\left(\tilde{\omega}/\Delta\omega_D\right)^2}, \quad 2-47$$

where $\tilde{\omega} = \omega - \omega_{fi}$ is the detuning angular frequency, $\Delta\omega_D$ is the $1/e$ Doppler width. The resulting line shape is a Gaussian function that has a half width at half maximum (HWHM) γ_D defined as:

$$\gamma_D = \sqrt{\ln(2)} \frac{\Delta\omega_D}{2\pi c}. \quad 2-48$$

This line shape therefore describes the average thermal motion of the molecules with the exclusion of collisional effects. Therefore, the Doppler profile is only applicable when pressures (at room temperature) are low enough (less than 10^{-3} atm) so that the collisional effects within the gas become negligible.

2.4.3. Lorentz Profile

Now neglecting the thermal motion discussed in Section 2.4.2 the effects of collisions between radiators and perturbers is examined. When collisions occur between radiator and perturber, a phase shift $\varphi(t)$ will be observed in the radiator's dipole moment. These types of collisions are referred to as dephasing collisions. By using an average of the phase shift to describe the correlation function tied to the rovibrational internal degrees of freedom we get the following:

$$C_{int}(t) = e^{i\langle\varphi(t)\rangle}, \quad 2-49$$

where, $\langle\varphi(t)\rangle$ is the classical average of the phase shift that contains both a real part and an imaginary part. The real part Δ describes the shift in frequency that is observed due to collisions and the imaginary part Γ describes the decay rate of the oscillation radiator dipole moment.

Substituting this change into equation 2-49 the following correlation function is obtained:

$$C_{int}(t) = e^{-(\Gamma+i\Delta)t}. \quad 2-50$$

The Laplace transform of equation 2-50 gives the Lorentz profile.

$$I_L(\tilde{\omega}) = \frac{1}{\pi} \frac{\gamma p}{(\tilde{\omega} - \delta p)^2 + (\gamma p)^2}, \quad 2-51$$

where $\gamma p = \Gamma$ is the collisional HWHM, and $\delta p = \Delta$ is the collisional shift at pressure p . The Lorentz profile is most accurate at higher pressures where the main mechanism for broadening is due to inter-molecular collisions.

2.4.4. Voigt Profile

Now that there is a way to describe both the thermal motion and the collisional motion of a gas using two different line shape profiles. These effects can be combined into one line shape profile by multiplying the two dipole autocorrelations functions given by equations 2-46 and 2-50. This multiplication is equivalent to a convolution in the reciprocal space. Therefore, the Voigt profile can be defined as the convolution of the Doppler profile and the Lorentz profile as follows:

$$I_V(x, y) = \int_{-\infty}^{\infty} I_D(\tilde{x}') I_L(x - \tilde{x}', y) d\tilde{x}', \quad 2-52$$

where the following dimensionless parameters have been used: $\tilde{x} = \frac{\tilde{\omega}}{\Delta\omega_D}$, $x = \frac{\tilde{\omega} - \Delta}{\Delta\omega_D}$, and $y = \frac{\Gamma}{\Delta\omega_D}$. Equation 2-52 can then be written in terms of the complex probability function $w(x, y)$ as follows:

$$I_V(x, y) = \frac{1}{\sqrt{\pi}} \text{Re}[w(x, y)] \quad 2-53$$

with

$$w(x, y) = \frac{i}{\pi} \int_{-\infty}^{\infty} \frac{e^{-t^2}}{x - t + iy} dt. \quad 2-54$$

The resulting Voigt profile will contain both the effects of thermal motion and of collisional motion. For intermediate pressures it will represent reasonably well the actual line shape observed for absorption transitions. In the upper and lower pressure limits the Voigt profile will behave as the Lorentz or Doppler profiles respectively, thus making it a

very useful line shape to analyse spectra. Over the years, several fast computational algorithms for the Voigt function have been published.

2.4.5. Speed Dependant Voigt Profile

The thermal motion of the molecules within a gas generally follows the Maxwell-Boltzmann distribution as discussed in Section 2.4.2. Therefore, it is known that not all the molecules travel at the most probable speed as it was assumed until this point. Therefore, to improve the agreement between experimental and modelled line shapes, it is important to consider how the spectral line shift and broadening will be affected by the velocity of the molecules. Figure 2-6 shows how the broadening $\Gamma(\nu)$ and the shift $\Delta(\nu)$ are influenced by the velocity used in calculating the line shape. It can be seen that the speed dependence is going to introduce an asymmetry into the line shape. This asymmetry has been observed in high-resolution measurements and, therefore, must be considered when analysing high-resolution spectra.

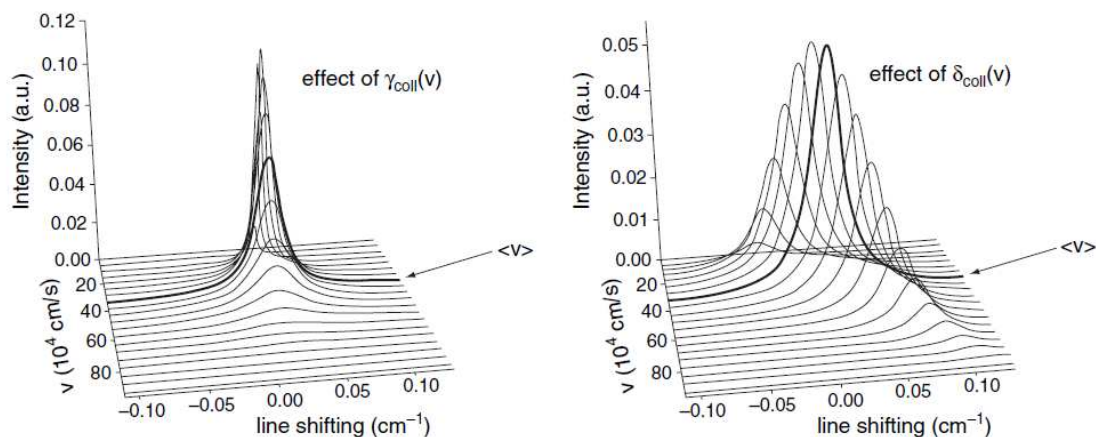


Figure 2-6: Example of the speed dependence effects on the spectral line shape when $\Gamma(\nu)$ is considered (shown on the left), and $\Delta(\nu)$ is considered (shown on the right) [40, 41].

The formulation of the speed dependant Voigt profile was introduced by Berman [42], where the function can be expressed in the following way.

$$I_{sdv} = \frac{1}{\pi} \text{Re} \left\{ \int \frac{F_M(\vec{v})}{[\Gamma(v) - i(\tilde{\omega} - \Delta(v)) - \vec{k} \cdot \vec{v}]} d^3 \vec{v} \right\}, \quad 2-55$$

where $F_M(\vec{v})$ is defined in equation 2-44, and $\Gamma(v)$ and $\Delta(v)$ are the speed dependant broadening and shift, respectively. Most often $\Gamma(v)$ is expressed in the semi-empirical quadratic form of Rohart et al. [43]

$$\Gamma(v) = \Gamma_0 + \Gamma_2 \left[\left(\frac{v}{v_p} \right)^2 - \frac{3}{2} \right], \quad 2-56$$

where v is the radiators speed, v_p is the most probable speed, $\Gamma_0 = \langle \Gamma(v) \rangle$ is the mean relaxation rate, and Γ_2 characterizes the speed dependence of the relaxation rate. Both Γ_1 and Γ_2 vary linearly with pressure.

Equation 2-55 is the Maxwell-Boltzmann average of the speed dependent broadening and shift and describes the absorption of light in the direction of \vec{k} for the ensemble of radiators. It is important to note that if the term $\vec{k} \cdot \vec{v}$ is dropped, this expression will reduce to a weighted sum of Lorentz functions.

2.4.6. Galatry Profile

When fitting recorded laboratory spectra, it becomes very important to choose the appropriate line shape function that will mimic the physical conditions of the gas under examination. Typically, for remote sensing purposes a Voigt line shape function is used. The Voigt profile is a fast and reliable way to examine spectra of this nature. However, with the ever improving advances in signal-to-noise ratios for the new remote sensing

instruments being developed, the more subtle effects that were not noticeable in the past are now influencing the errors in the obtained results.

One such effect is known as “Dicke narrowing” or in general terms the collisional narrowing. This narrowing effect occurs at intermediate pressures when the mean free path of the molecules becomes equal to or less than the wavelength of the incident radiation. When this condition is met, a simple Voigt profile will result in the retrieval of broadening coefficients that are smaller than what would be expected. In order to account for this narrowing, a line shape function that includes the mechanisms of the Dicke narrowing effect needs to be adopted.

Starting from the model of Brownian motion [44] the velocity of the molecule can be defined using the following equation:

$$\frac{d\vec{v}}{dt} = -\beta\vec{v} + \vec{A}(t), \quad 2-57$$

where \vec{v} is the velocity, the $\beta\vec{v}$ term represents the dynamic friction experienced by the molecule and $\vec{A}(t)$ is the characteristic random fluctuating portions associated with the Brownian motion. In the Doppler pressure regime, the velocity of the molecules is defined strictly in terms of a Maxwellian distribution. However, from equation 2-57 it can be seen that outside the Doppler regime, the velocity is dependent on the frictional coefficient β . This dampening effect is the result of velocity changing collisions inside the gas sample. Statistically, it is more likely that the velocity changing collisions inside the gas sample will result in a lower velocity after the collision has taken place. Therefore, the distribution of velocities will be narrower than what is obtained for the Doppler profile.

The Galatry [45] (soft collision model) line shape profile incorporates the Brownian motion model [44] thus allowing for the following expression to describe the velocity changing collision portion of the dipole autocorrelation function.

$$C_{ext}^s(t) = \exp\left\{-\frac{1}{2}\left(\frac{\Delta\omega_D}{V_{VC}^s}\right)^2 [V_{VC}^s t - 1 + e^{-V_{VC}^s t}]\right\}, \quad 2-58$$

where V_{VC}^s is the velocity changing collision rate for a soft collision model. V_{VC}^s is also referred to as the dynamic friction coefficient ($V_{VC}^s \approx \beta$ from equation 2-57) and can be linked to the diffusion coefficient through the following expression:

$$V_{VC}^s = \frac{KT}{MD}, \quad 2-59$$

where D is the diffusion coefficient. It is important to note that D is the optical diffusion coefficient as it does not always have the same value as the more commonly known mass diffusion coefficient.

Now, by taking the product of equations 2-49 and 2-58 the effects due to soft velocity changing collisions can be included, as well as the effects due to dephasing collisions introduced in Section 2.4.3. Taking the Laplace transform of the resulting function gives the following Galatry Profile.

$$I_G(x, y) = \frac{1}{\pi} \text{Re} \left\{ \int_{-\infty}^{\infty} \exp\left[-(ix + y)\tilde{t} + \frac{1}{2z^2}(1 - z\tilde{t} - e^{-z\tilde{t}})\right] d\tilde{t} \right\}, \quad 2-60$$

where x and y are the same as defined in Section 2.4.4, $z = \frac{V_{VC}^s}{\Delta\omega_D}$, and $\tilde{t} = \Delta\omega_D t$.

A simple expression can be used to justify the use of the Galatry profile. The type of collisions present (hard or soft) can be estimated by examining what is known as the mean persistence velocity ratio. This is a ratio of the mean velocity of the radiator

measured post collision and the mean velocity of the radiator measured pre-collision. The mean persistence velocity ratio is expressed in the following way [40]:

$$r_v = \frac{1}{2} \left(\frac{m_a}{m_{ap}} \right) \left[1 + \frac{m_a}{(m_p m_{ap})^{1/2}} \right] \ln \left[\left[\left(\frac{m_p}{M} \right)^{1/2} + 1 \right] \left(\frac{m_{ap}}{m_a} \right)^{1/2} \right]. \quad 2-61$$

Above, m_a is the radiator mass, m_p is the perturber mass and $m_{ap}=m_a+m_p$. When $r_v \approx 1$ (this is equivalent to saying the radiator is heavy compared to the perturber) the bulk of the velocity changing collisions can be considered soft, and therefore the Galatry profile can be used. The case where $r_v \rightarrow 0$ will be discussed in the next section.

2.4.7. Hard collision Rautian-Sobelman Profile

When $r_v \rightarrow 0$ in equation 2-61, the type of collisions that are observed will randomize the velocity of the molecules because it erases the pre-collision velocity information. These types of collisions are usually referred to as hard collisions and are described by V_{VC}^H , which is the hard velocity changing collisional rate. Generally, the hard collisional rate is equal to the kinetic collisional rate. Using this hard collisional rate, Nelkin and Ghatak [46] and independently, Rautian and Sobel'man [47], were able to model a hard collision line shape profile of the following form:

$$I_{NG}(x, y) = \frac{1}{\sqrt{\pi}} Re \left\{ \frac{w(x, y + \varepsilon)}{1 + \sqrt{\pi} w(x, y + \varepsilon)} \right\}, \quad 2-62$$

where $\varepsilon = \frac{V_{VC}^H}{\Delta\omega_D}$, and the parameters x, y and w are the same as defined in Section 2.4.4.

2.5. Temperature Dependence of Line Parameters

To understand how temperature will affect line shape parameters the first thing to do is consider a simple kinetic case where the density of the gas and the mean molecular velocity are examined. To start a simple assumption is made about the collisional frequency. That assumption is that it will increase linearly with density and mean molecular velocity. This means that density will vary as T^{-1} and the mean molecular velocity will vary as $T^{1/2}$. As a first approximation this would suggest that a temperature dependence of the form will result:

$$\frac{\sigma_1}{\sigma_2} = \left(\frac{T_1}{T_2}\right)^{-n}, \quad 2-63$$

where $n=0.5$ for this simple case and σ is the line shape parameter of interest.

The term n , however, is rarely actually found to be 0.5. Therefore, a more rigorous approach must be made. The Anderson-Tsao-Curnette Theory [48, 49] gives a more complete picture of the molecular dynamics. This theory was simplified by Birnbaum [50] by making assumption about the forms of the collisional efficiency and the partial collision cross sections. These assumptions lead to a value of $n = 0.75$ [51] when quadrupole-quadrupole interactions are the dominant factor.

The use of equation 2-63 needs to be handled with care as it has been shown [52] to not only have a rotational dependence (n will vary with the quantum number J) but can also depend on the temperature range of interest. Bonamy *et al.* [53] showed that the assumptions made by Birnbaum begin to break down at higher temperatures when the molecules begin to collide in less than ideal ways. However, for the temperature ranges

considered in the Earth's lower atmosphere the temperature dependence shown in equation 2-63 has been found to work quite well [51, 54].

2.6. Line-mixing

2.6.1. Introduction

The next thing to consider is what happens when transitions interfere with each other. The two adjacent lines as depicted in Figure 2-7 (a) have the same initial and final vibrational states and have overlapping profiles. It is possible that the rotational states become perturbed through inelastic collisions. This perturbation then makes it possible for any of the two coincidental paths (horizontal dashed lines in the Figure 2-7 (b)) to result in the transitional frequency, ν . This creates an interference effect between neighboring features that must be included in the spectral line shape models in order to improve the overall retrieval of line shape parameters.

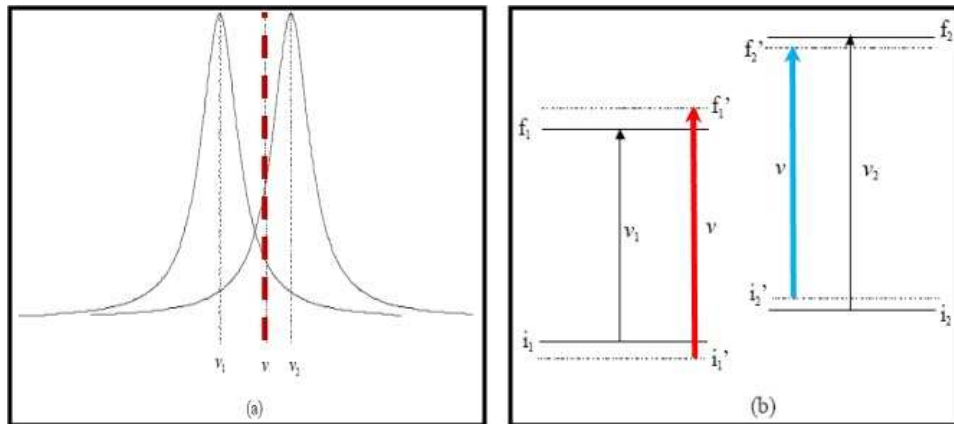


Figure 2-7: Example of the line mixing effect. Panel (a) shows how the two transition profiles overlap. Panel (b) shows the energy levels and how they can be perturbed (dashed horizontal lines) through collisions.

To examine when the effects of line-mixing are non-negligible, further examination of the arguments presented in Section 2.4.1 is required. By starting with

equation 2-42 the autocorrelation function can be defined in terms of the dipole moment and the density operator to get the following expression:

$$\Phi(t) = Tr_{X_m} \left[\rho_m(0) e^{\frac{iH_m t}{\hbar}} e^{-i\vec{k} \cdot \vec{r}} \vec{\mu}^* e^{-\frac{iH_m t}{\hbar}} \vec{\mu} e^{i\vec{k} \cdot \vec{r}} \right], \quad 2-64$$

Here, X_m and H_m are the system and Hamiltonian introduced in Section 2.4.1. Assuming that the gas is in local thermal equilibrium and defining the canonical density operator we have,

$$\rho_m(0) = \frac{e^{-\frac{H_m}{KT}}}{Z_m}. \quad 2-65$$

With $Z_m = Tr_{X_m} \left\{ e^{-\frac{H_m}{KT}} \right\}$, the autocorrelation function becomes

$$\Phi(t) = \frac{1}{Z_m} Tr_{X_m} \left[\rho_m(0) e^{\frac{iH_m(t+i\hbar/KT)}{\hbar}} e^{-i\vec{k} \cdot \vec{r}} \vec{\mu}^* e^{-\frac{iH_m t}{\hbar}} \vec{\mu} e^{i\vec{k} \cdot \vec{r}} \right]. \quad 2-66$$

From Section 2.4.1 it was shown that H_m describes the system of one absorbing molecule and N collisional partners. The perturbers can be considered as statistically independent and the interactions between them will not influence the absorption or emission processes. Hence, we can write H_m as:

$$H_m = V_{a-p} + H_a + K_a + \sum_{i=1}^N [H_p(i) + K_p(i)], \quad 2-67$$

where H_a is the Hamiltonian of the unperturbed radiator describing the internal energy of the system, K_a is the kinetic energy of the perturber associated with its translational motion, $H_p(i)$ and $K_p(i)$ are the Hamiltonian and Kinetic energy of the i^{th} perturber, and

V_{a-p} is the interaction potential between the radiator and all perturbbers. V_{a-p} can be defined as the sum of all binary interactions V_{a-i} as follows:

$$V_{a-p} = \sum_{i=1}^N V_{a-i}. \quad 2-68$$

Now, separating V_{a-p} into V_o and V'_{a-p} where V_o describes the portion of the interactions that will commute with the internal coordinates of the molecules and V'_{a-p} contains the remaining contributions. This decomposition allows for the following Hamiltonian:

$$H_m = H_o + V'_{a-p} \quad 2-69$$

and with H_o given by

$$H_o = V_o + H_a + K_a + \sum_{i=1}^N [H_p(i) + K_p(i)]. \quad 2-70$$

Now, using the “interaction picture” (as defined in Chapter 2 of [40]) we are able to derive the time evolution operator for this system given by:

$$U(z,0) = \exp \left[-\frac{i}{\hbar} \int_0^z \tilde{V}_{a-p}(z') dz' \right]. \quad 2-71$$

In the previous equation, $\tilde{V}_{a-p}(z') = e^{\frac{iH_o z'}{\hbar}} V'_{a-p} e^{-\frac{iH_o z'}{\hbar}}$ and $z = -t - \frac{i\hbar}{KT}$.

The autocorrelation function $\Phi(t)$ can now be written in terms of the time evolution operator to give the following expression:

$$\Phi(t) = \tilde{v} Tr_{Xm} \left[\begin{array}{c} \rho(H_o) e^{\frac{iH_o t}{\hbar}} U(-t - \frac{i\hbar}{KT}, 0) \\ e^{-i\vec{k} \cdot \vec{r}} \bar{\mu}^* U^*(-t, 0) e^{\frac{-iH_o t}{\hbar}} \bar{\mu} e^{i\vec{k} \cdot \vec{r}} \end{array} \right], \quad 2-72$$

where $\rho(H_o) = \frac{e^{-\frac{iH_o t}{\hbar}}}{Z_o}$, $Z_o = Tr_{Sm} \left[e^{\frac{-H_o}{K_b T}} \right]$ and $\tilde{\nu} = \frac{Z_o}{Z_m}$.

Next, separating H_o into two parts, namely H_a and \tilde{H}_o . H_a describes the internal states of the radiator, and \tilde{H}_o describes the remaining states. The density operator can now be written as $\rho(H_o) = \rho(H_a)\rho(\tilde{H}_o) \equiv \rho_a\rho(\tilde{H}_o)$.

By introducing the eigenstates $|i\rangle$ and $|f\rangle$ with corresponding eigenvalues E_i and E_f (that are the eigenfunctions of H_a), we can write the correlation function in the following form:

$$\begin{aligned} \Phi(t) = \tilde{\nu} \sum_{i,f,i',f'} e^{-i\omega_{\beta t}} \langle i | \rho_a | i \rangle \langle f | \bar{\mu} | i \rangle \langle i' | \bar{\mu}^* | f' \rangle \\ \times Tr_{\tilde{H}_o} \left[\rho(\tilde{H}_o) \langle i | U(-t - \frac{i\hbar}{KT}, 0) | i \rangle \langle f | U^*(-t, 0) | f' \rangle \right] \end{aligned} \quad 2-73$$

To go further, the matrix elements of $\bar{\mu}$ need to be solved. This can be done by defining the eigenstates of H_a as $|ajm\rangle$ where j is the rotational quantum number, m is the magnetic quantum number and a represents the other necessary quantum numbers for the radiators states (vibration, electronic, ect ...). With this basis the Wigner-Eckhart Theorem can be used to find the matrix elements of $\bar{\mu}$ as follows:

$$\begin{aligned} \langle a_f J_f m_f | \bar{\mu} | a_i J_i m_i \rangle \langle a'_i J'_i m'_i | \bar{\mu}^* | a'_f J'_f m'_f \rangle = \\ \langle a'_f J'_f | \mu | a'_i J'_i \rangle^* \langle a_f J_f | \mu | a_i J_i \rangle, \\ \times \sum_{q=-1,0,1} \left\{ (-1)^{J_f+m_f+J'_f+m'_f} \sqrt{(2J'_i+1)(2J_i+1)} \right. \\ \left. \times \begin{pmatrix} J'_i & 1 & J'_f \\ m'_i & q & -m'_f \end{pmatrix} \begin{pmatrix} J_i & 1 & J_i \\ m_i & q & -m_f \end{pmatrix} \right\} \end{aligned} \quad 2-74$$

where $\begin{pmatrix} \bullet & \bullet & \bullet \\ \bullet & \bullet & \bullet \end{pmatrix}$ is a 3J symbol.

Substituting equation 2-74 into equation 2-73, the autocorrelation function can then be written in the following way:

$$\Phi(t) = \tilde{v} \sum_{i,f,i',f'} e^{-i\omega_{\tilde{H}} t} (2J_i + 1) \langle a_i J_i | \rho_a | a_i J_i \rangle \langle a'_f J'_f | |\vec{d}| | a'_i J'_i \rangle^* \times \langle a_f J_f | |\vec{d}| | a_i J_i \rangle \text{Tr}_{\tilde{H}_o} \left[\rho (\tilde{H}_o) C_{f'i',fi}(t) \right], \quad 2-75$$

with

$$C_{f'i',fi}(t) = \sum_{\substack{q=-1,0,1 \\ m_i, m_f, m'_i, m'_f}} (-1)^{J_f + m_f + J'_f + m'_f} \frac{\sqrt{(2J'_i + 1)}}{\sqrt{(2J_i + 1)}} \times \begin{pmatrix} J'_i & 1 & J'_f \\ m'_i & q & -m'_f \end{pmatrix} \begin{pmatrix} J_i & 1 & J_i \\ m_i & q & -m_f \end{pmatrix} \times \langle a_i J_i m_i | U(-t - \frac{i\hbar}{KT}, 0) | a'_i J'_i m'_i \rangle \times \langle a'_f J'_f m'_f | U^*(-t, 0) | a_f J_f m_f \rangle. \quad 2-76$$

The term $\text{Tr}_{\tilde{H}_o} \left[\rho (\tilde{H}_o) C(t) \right]$ from equation 2-75 can be simplified by making three simple assumptions: (1) that the perturbers are statistically independent of each other; (2) there is a large number N of perturbers; (3) strong collisions that will not overlap. The combination of these three assumptions leads to the following simplification:

$$\text{Tr}_{\tilde{H}_o} \left[\rho (\tilde{H}_o) C(t) \right] = \exp_t \left[-n_p V \times \text{Tr}_{\tilde{H}_o^1} \left[\rho (\tilde{H}_o^1) (I_d - q(t)) \right] \right], \quad 2-77$$

where \tilde{H}_o^1 is the Hamiltonian of a single perturber, I_d is the identity matrix, and $q(t)$ contains the information generated in $C(t)$.

Next consider only small deviations from the line center defined by $|\omega - \omega_{fi}| \tau_c \ll 1$ where τ_c is a collisional relaxation time. By defining the average time between collisions as τ_o and assuming that $\tau_c < \tau_o$ then equation 2-77 can be simplified to the following [40] expression:

$$\exp_t \left[-n_p V \times Tr_{\tilde{H}^1_o} \left[\rho (\tilde{H}^1_o)(I_d - q(t)) \right] \right] \rightarrow e^{-(n_p W^* + iL_a)t} e^{iL_a}, \quad 2-78$$

where L_a is a Liouville operator created from H_a and W is the impact density normalized relaxation matrix operator. This simplification allows the spectral density function to be written in the following way:

$$F(\omega) = \sum_{\substack{a_i, J_i \\ a_f, J_f}} \rho_{a_i, J_i} \langle a_f J_f | \bar{\mu} | a_i J_i \rangle \sum_{\substack{a'_i, J'_i \\ a'_f, J'_f}} \langle a'_f J'_f | \bar{\mu} | a'_i J'_i \rangle^* \times \frac{1}{\pi} \text{Im} \left[\left\langle \left\langle a'_f J'_f a'_i J'_i \left| [\omega I_d - L_a - i n_p W]^{-1} \right| a_f J_f a_i J_i \right\rangle \right\rangle \right], \quad 2-79$$

where ρ_{a_i, J_i} is the population of $a_i J_i$ states and the Liouville operators have the following definitions.

$$\langle \langle f i' | \omega I_d | f i \rangle \rangle = \omega \times \delta_{i, i'} \delta_{f, f'} \text{ and} \quad 2-80$$

$$\langle \langle f i' | L_a | f i \rangle \rangle = \frac{\langle f | H_a | f \rangle - \langle i | H_a | i \rangle}{\hbar} \delta_{i, i'} \delta_{f, f'} = \omega_{fi} \times \delta_{i, i'} \delta_{f, f'}. \quad 2-81$$

The relaxation matrix that shows up in equations 2-78 and 2-79 contains within it properties of the spectral transitions. The diagonal elements of this matrix define the collisional broadening in the real domain and the collisional induced shift in the imaginary domain. The off-diagonal elements contain within them the interference effects between the various transitions. This interference effect is known as line-mixing

as it adds an asymmetry to the line shape profile associated with interaction between neighbouring transitions.

Methods for the calculation of the relaxation matrix W will be discussed in Sections 2.6.2 and 2.6.3. In Section 2.6.2 the energy corrected sudden approximation (ECS) method used to find the relaxation matrix will be discussed. In Section 2.6.3 a second approach named the exponential power gap law (EPG) will be presented. In Section 2.6.4 a brief discussion of how line mixing is calculated and included in the fitting software will be given.

2.6.2. The Energy Corrected Sudden Approximation (ECS)

The Energy Corrected Sudden (ECS) expression is a dynamically-based fitting law in which the main variable is the angular momentum transferred during molecular collisions. Hence, the collisional rates and basis rate constants depend on the total angular momentum L of the active molecules. The Energy Corrected Sudden fitting law is an extension of the Infinite-Order sudden law (IOS) [55] to the case where molecular collisions are not sudden anymore [27, 40, 55]. If the molecular collisions are not sudden, then the wings of isolated lines are not Lorentzian. The off-diagonal relaxation matrix elements that connect two “downward” transitions ($J'_f \leftarrow J'_i$ ($J'_i < J'_i$) and $J_f \leftarrow J_i$) of the $\nu_{1f}\nu_{2f}^{l_f}\nu_{3f} \leftarrow \nu_{1i}\nu_{2i}^{l_i}\nu_{3i}$ vibrational band at a given temperature T are:

$$\begin{aligned}
 & \left\langle \left\langle J'_i l_i J'_f l_f \left| W(T) \right| J_i l_i J_f l_f \right\rangle \right\rangle = (2J'_i + 1) \\
 & \quad \times \sqrt{(2J_f + 1)(2J'_f + 1)} (-1)^{l_i + l_f} \\
 & \quad \times \sum_{L \text{ even} \neq 0} \begin{pmatrix} J_i & L & J'_i \\ l_i & 0 & -l_i \end{pmatrix} \begin{pmatrix} J_f & L & J'_f \\ -l_f & 0 & l_f \end{pmatrix} , \quad 2-82 \\
 & \quad \times \begin{Bmatrix} J_i & J_f & 1 \\ J'_f & J'_i & L \end{Bmatrix} (2L + 1) \frac{\Omega(J_i, T)}{\Omega(L, T)} Q(L, T)
 \end{aligned}$$

where $\begin{pmatrix} \bullet & \bullet & \bullet \\ \bullet & \bullet & \bullet \end{pmatrix}$ and $\begin{Bmatrix} \bullet & \bullet & \bullet \\ \bullet & \bullet & \bullet \end{Bmatrix}$ are 3J and 6J coefficients. The corresponding off-diagonal relaxation matrix elements that connect two upward transitions are obtained from the detailed balance equation. The expression for the adiabaticity factor at a given temperature T is [40]:

$$\Omega(J, T) = \left\{ 1 + \frac{1}{24} \left[\frac{\Delta E_{J, J-2} d_c}{\bar{v}(T)} \right]^2 \right\}^{-2} , \quad 2-83$$

where $\Delta E_{J, J-2}$, \bar{v} , d_c are the energy difference between levels J and $J-2$ in wavenumber units, the mean relative velocity, and the scaling length, respectively. The basic rates are expressed through an exponential power law dependence [40]:

$$Q(J, T) = A(T) [L(L+1)]^{-\lambda(T)} \exp \left[-\beta(T) \frac{hc E_J}{KT} \right] , \quad 2-84$$

where E_J is the rotational energy of level J . This type of scaling law depends on the adjustable parameters d_c , A , λ , and β .

Once the off-diagonal elements of the relaxation matrix are calculated using the ECS implementation, the diagonal elements can be calculated using the expression [37] as follows:

$$W_{kk} = -\sum_{j \neq k} \frac{d_j}{d_k} W_{jk}, \quad 2-85$$

where μ_k is the dipole matrix element of the optical transition k .

2.6.3. Exponential Power Gap Law (EPG)

The EPG law describes the relaxation matrix through state to state collisional transfer rates. By introducing a probability rate, namely the collisional transfer rate κ_{jk} from the lower rotational level k to a higher rotational level j a description of the system can be given. κ_{jk} is assumed to be independent of the vibrational level. Following observations from isotropic Raman spectra [56], it has been shown that the off-diagonal elements of the relaxation matrix can be expressed as

$$W_{jk} = -\beta \kappa_{jk}, \quad 2-86$$

where β is a constant. The work presented within in this Thesis uses $\beta = 0.56$. This was verified by making sure that the relaxation matrix elements obey a sum rule: the sum of the relaxation elements from any column adds to zero.

Because the gas is in thermodynamic equilibrium, the rate of transfer from state k to j must be equal to the rate of transfer from j to k . This is referred to as detailed balance and as with the relaxation matrix can be expressed as follows:

$$\rho_k \kappa_{jk} = \rho_j \kappa_{kj}, \quad 2-87$$

where ρ_k is the population of the rotational level k .

The equations 2-86 and 2-87 and the sum rule mentioned above are not sufficient to determine the relaxation matrix elements. One approach to finding these elements is to

determine the collisional transfer rates, κ_{jk} , using a parameterized gap or scaling law to calculate the rates as a function of the difference in energy levels [33, 34]. The Exponential Power gap (EPG) law calculates the collisional transfer rates from the lower rotational level k to a higher rotational level j as follows:

$$\kappa_{jk} = a \left[\frac{|\Delta E_{jk}|}{B_0} \right]^{-b} \exp\left(\frac{-c |\Delta E_{jk}|}{B_0} \right), \quad 2-88$$

where ΔE_{jk} is the energy gap between the two rotational states, B_0 is the rotational constant and a , b , and c are the parameters to be optimized.

The line widths (which are the assumed diagonal elements of the relaxation matrix W) are calculated as follows:

$$W_{kk} = \frac{1}{2} \left[\sum_j \kappa_{jk} \right]_{upper} + \frac{1}{2} \left[\sum_j \kappa_{jk} \right]_{lower}. \quad 2-89$$

2.6.4. Calculating Line-mixing coefficients

The elements of the relaxation matrix describe the physical state of the molecule at any given time. However, the main obstacle to the inclusion of line mixing in line shape calculations is a lack of knowledge about the relaxation matrix itself. The real part of the diagonal elements α_{Li} are the broadening coefficients, whereas their imaginary parts are the pressure-induced line shift coefficients δ_i :

$$W_{ii} = \alpha_{Li} + i\delta_i. \quad 2-90$$

The off-diagonal matrix elements W_{jk} and the components of the dipole matrix element of the optical transition μ_k are used to express the weak line mixing coefficients for transitions between any pair j and k of energy levels as follows:

$$Y_{ok}(T) = 2 \sum_{j \neq k} \frac{\mu_j}{\mu_k} \frac{W_{jk}}{\nu_k - \nu_j}. \quad 2-91$$

Therefore, experimentally line mixing coefficients can be obtained by incorporating equation 2-91 into the line shape profile of choice. These experimental results can then be compared to theoretical results obtained through calculating line-mixing coefficients using either of the two approaches described in Sections 2.6.2 and 2.6.3 to obtain the relaxation matrix from the known broadening coefficients.

2.7. Conclusion

To complete the analysis of any high-resolution spectroscopic data a firm grasp on the concepts presented in this chapter is required. In Chapters 5, 6 and 7 it will be seen that every attempt to utilize this knowledge has been taken, and that a careful analysis with these concepts in mind has been performed.

Chapter 3: Experimental Setup of a Tunable Diode Laser Spectrometer (TDLS)

3.1. Overview

As mentioned in section 1.2.1 spectroscopy allows for the examination of the fingerprints of molecules. However, with the advancements in detection techniques and the quest to understand stars and atmospheres, better information is required to develop understanding of the physical principles of the line shapes that are measured. It is not enough to just know where lines from a certain gas will appear, accurate predictions of what the width of the line is going to be, as well as other features like intensity or mixing effects that alter the symmetry of the line need to be understood as well. This becomes even more complex when considering gases in the atmosphere as the consideration of how temperature, pressure and concentration are going to change the profile of the line being examined is important. It is therefore vital that quality spectra be recorded in the laboratory for many of these unique conditions so that better models may be developed for future analysis. It is with this goal in mind that the following tunable diode laser spectrometer system was developed. In this Chapter the setup and performance of the tunable diode laser spectrometer system that has been developed at the University of Lethbridge and used in the present measurements will be discussed.

3.2. Diode Laser Spectroscopy

3.2.1. Introduction

Since the development of the first functioning laser on May 16, 1960 by Theodore H. Maiman [57], the laser and its applications have continued to grow in size. Used now for telecommunications, data storage, and industrial applications as well as in research, the laser has evolved into an invaluable tool. There are many different types of lasers available in the current market place. Examples of these lasers include dye lasers, chemical lasers and solid state lasers, but there are many other unique systems also in use today. In order to choose the laser that will best meet the needs of the application, several key properties of the laser system must be considered. The first of these properties is the line width of the laser emission itself. The line width determines how narrow in the frequency domain the laser appears. The restriction to the line width arises from the Heisenberg uncertainty principle. Lasers with very narrow line widths offer high quality frequency references and can allow accurate measurements and standards. Another important feature of a laser system is its tunability. Tunability refers to the laser's ability to tune over large wavelength regions, however not all lasers are able to provide such large tunability. Lasers with large tuning range can be useful for many applications and come in a variety of styles. Some of these lasers can be tuned mode hop free while others can be tuned through multiple modes. The power and operating frequency are also very important properties for a laser system. Most lasers can only operate in certain narrow spectral regions, however with the number of materials being used today, there are many

to choose from depending on the spectral region of interest. The output power of the laser is also important when it comes to its particular application. The lasers must be able to function properly without losses affecting the desired end results.

To perform high resolution spectroscopy experiments, we need a laser system that has a moderately high power output. The system should also provide a wide mode hop free tuning range and offer a narrow stable line shape. That is why for our system a New Focus™ Velocity laser system has been incorporated. This system offers a tunable range from 1500 to 1570 nm with an output power of approximately 9 mW. The system has a very narrow line width on the order of only a few KHz. The details of the laser's performance and operation will be discussed in the following Section 3.2.2.

3.2.2. The tunable diode laser

The semiconductor laser was first demonstrated in the early 1960s by many groups [1, 58-61]. These first diode lasers were not that practical due to the need for a high injection current and a very low operating temperature (77 K). With the advancements in solid state technology and new fabrication procedures most diodes created today no longer need to be cooled or require high injection currents. Table 3-1 presents an example of several different types of laser systems.

Table 3-1: Comparison of tunable diode laser technologies [62]. The following are the acronyms from the table: Distributed Bragg Reflector (DBR), Distributed Feedback (DFB), Vertical Cavity Surface Emitting (VCSEL) and Extended Cavity Diode (ECDV)

Devices	Tuning Range	Spectral Purity	Mode Control	Tuning Speed	Modulation Speed
DBR	8~80nm	>40dB	Fair	Fast (μ s)	Fast (GHz)
DFB Array	3~4nm X #of DFBs	>55dB	Very Good	Slow (ms)	Fast (Multi-GHz)
VCSEL	>12nm	~45dB	Hard	Fast (μ s)	Slow (<GHz)
ECDL	>32nm	>50dB	Fair	Slow (ms)	Slow (<GHz)

The tunable diode laser offers a very fine line shape and is optimal for creating a coherent source that can be used to measure spectra. The New Focus Velocity laser system has been designed with a modified Littman-Metcalf cavity that is based on previously published studies [63-69]. The cavity depicted in Figure 3-1 offers a wide range of tunability.

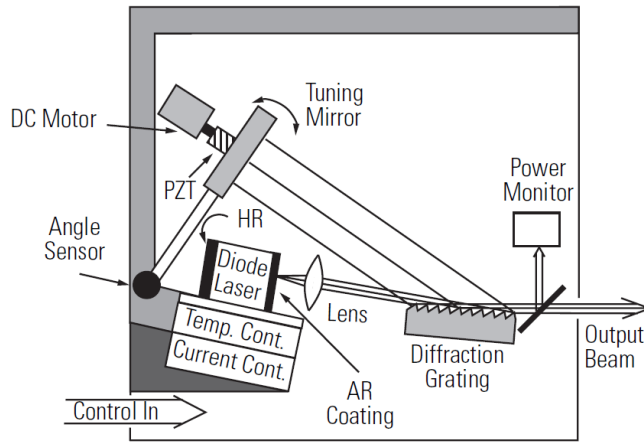


Figure 3-1: Schematic of Velocity Laser cavity. PZT is the Piezo electric actuator mounted on the back of the HR (High Reflectivity) tuning mirror. Finally AR refers to the anti-reflection coating placed on the diode laser cavity.

The laser system works by expanding the diode laser beam onto a diffraction grating at a near grazing incidence angle. The laser light is then diffracted off the grating onto the tuning mirror which reflects the light back to the grating. A small portion of the

light from the tuning mirror is then reflected from the grating surface and forms the output beam. This design acts as a narrow spectral filter and only allows for single longitudinal mode to form inside the cavity.

The selectivity of the wavelength results from the fundamental fact that resonance of the cavity will only be achieved by light with a wavelength that is perpendicular to the tuning mirror. This wavelength is therefore determined by the angle of the tuning mirror relative to the diffraction grating. However in order to avoid any mode hops during the tuning of the laser, the laser cavity must maintain the same number of waves within it as the mirror is rotated.

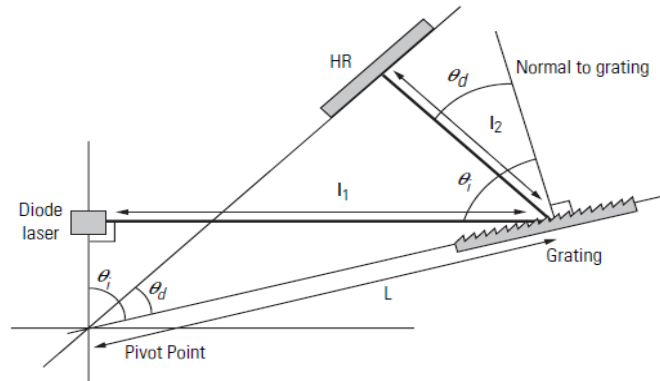


Figure 3-2: Drawing of important angles and distances resulting in the optimal pivot point. Once again HR refers to the High Reflectivity of the mirror.

To maintain the laser mode while tuning the wavelength therefore requires the rotation of the mirror about a special pivot point. This pivot point generates a relationship between the cavity length and the wavelength of the light inside the cavity. The wavelength of the laser is given by the law of diffraction as follows:

$$\lambda = \Lambda[\sin\theta_i + \sin\theta_d], \quad 3-1$$

where Λ is the grating spacing, θ_i and θ_d are the incident and diffracted angles, respectively (Figure 3-2).

The total length of the cavity is given by $D = l_1 + l_2$ as shown in Figure 3-2. Using this Figure the length can be written in terms of the angles of diffraction and reflection to get the following expression:

$$D = L [\sin\theta_i + \sin\theta_d]. \quad 3-2$$

Now taking the cavity length and dividing it by the wavelength of the laser light within the cavity it is clear that L/λ which is a constant. This result shows that by selecting a special pivot point at a distance L from the diffraction grating the rotation of the mirror can achieve mode hop free tuning of the lasers wavelength.

3.2.3. Process of scanning the laser system

Using the Labview programming language (described in Section 4.3) to control the laser system, scans of the piezoelectric device inside of the laser are completed in the following way. First, the general purpose interface bus (GPIB) communication port is used to tell the laser system to adjust the central frequency of the laser to a wavelength that is close to the transition of interest (note that the laser's piezo is maintained at its central position). Once the central frequency is set, the NI-DAQ card starts to send an incremented voltage to the back of the laser controller telling the laser to adjust the piezo's voltage and, thus, tune the output wavelength. High resolution is achieved by ramping the voltage from -3 to 2.7 V in increments of 0.001 V. The voltage increment size can be changed; however, 0.001 V provides the optimal scan time with high enough resolution.

3.3. Layout of The Tunable Diode Laser Spectrometer

3.3.1. Schematic and overview

The overall design of the system is presented in Figure 3-3. The first channel contains the temperature and pressure controlled cell. The second channel contains a room temperature reference cell of similar path length. The third channel records the background of the laser system. By measuring all three channels simultaneously accurate line shape analysis including pressure-induced line shift measurements can be performed.

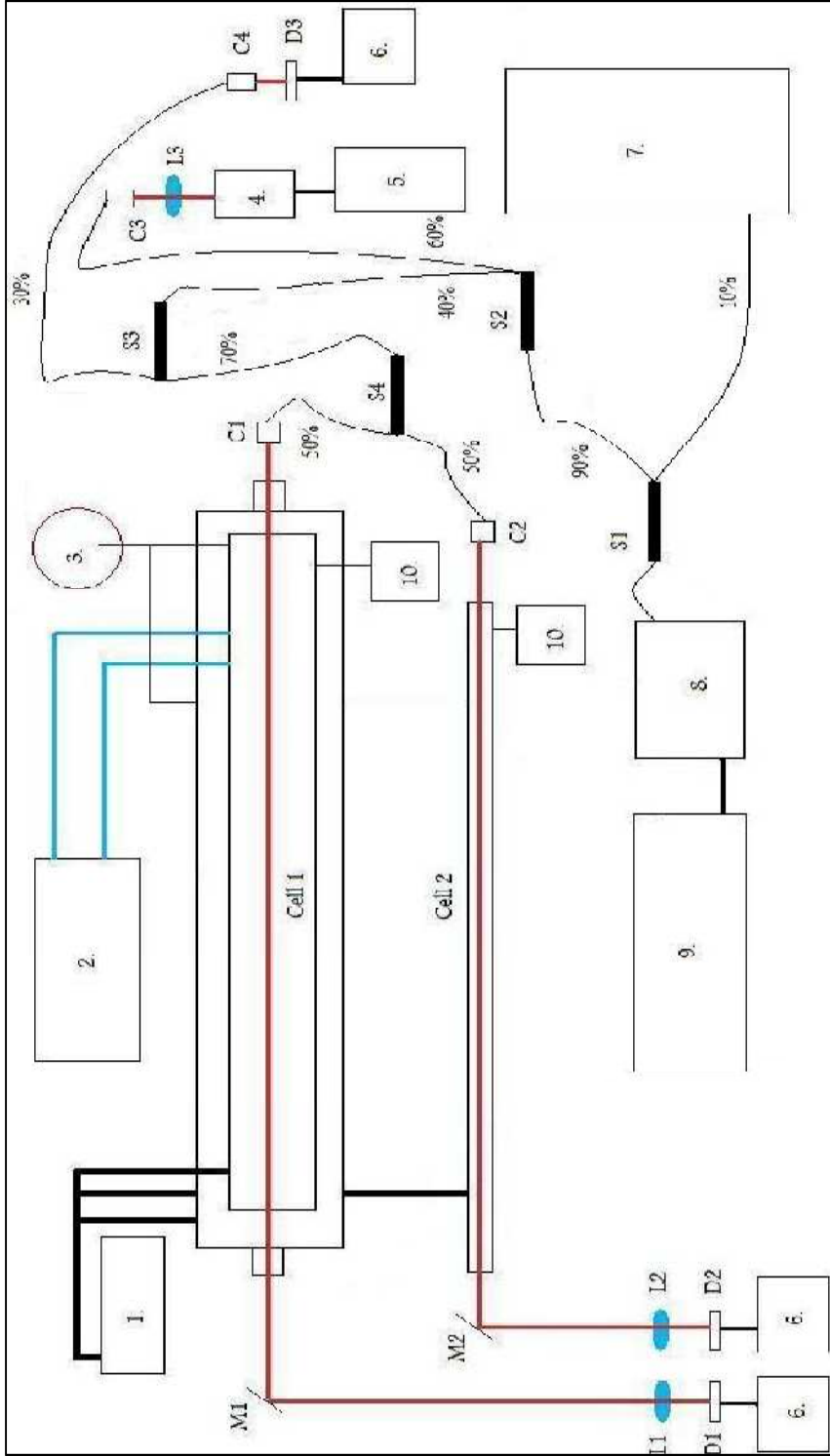


Figure 3-3: General block diagram of current spectrometer setup. Legend: 1 Vacuum system; 2 Cooling system NesLab ULT 80 Chiller; 3 Gas sample; 4 & 5 Fabry Perot interferometer and controller; 6 Detector pre-amps and power supplies; 7 WA-1500 EXFO wavemeter; 8, 9 Velocity diode laser head and controller; 10 MKS Baratron pressure gauges; L1, L2, L3 Focusing lenses; M1 & M2 Directing mirrors; D1, D2 & D3 InGaAs detectors; C1, C2, C3, C4 Collimators; S1, S2, S3, S4 Fiber splitters; Vacuum lines are shown in thick black lines. Coolant lines are shown in blue. Laser path is shown by the red lines. Thin curved lines show fiber optic cables with the percentages denoting the split ratios of the fibers.

The pathlength of the variable temperature cell presented here is 1.54 m. The 3D layout of the temperature controlled cell is presented in Figure 3-4. Two main design features have been employed: i) the absorption cell is centered inside a vacuum jacket to minimize the thermal conductive/convective coupling to the outside cell and ii) heating/cooling is handled by flowing a temperature-controlled fluid around and in contact with almost the whole cell body, ensuring that the temperature gradients are minimized. The mechanical and optical components have been selected to accommodate both stable and flammable gas samples.

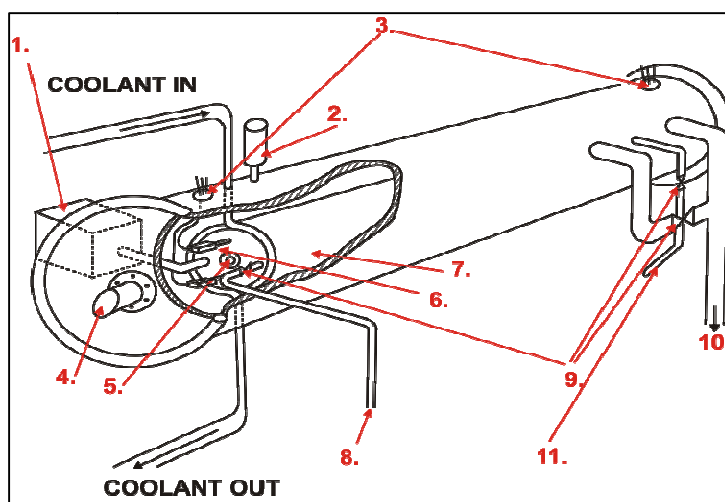


Figure 3-4: Three-dimensional view of the temperature controlled gas cell. Legend: 1- MKS Baratron pressure gauge, 2- enhanced pirani pressure gauge, 3- vacuum feed throughs, 4- CaF₂ windows positioned at Brewster angle, 5- CaF₂ windows for the inner cell, 6- platinum resistor thermometers, 7- inner cell body, 8- gas inlet, 9- vacuum valves, 10- gas outlet and 11- port for de-pressuring the vacuum jacket.

The inner chamber shown in Figure 3-5 and Figure 3-6 is a single-pass cell and is made up of a nominal 4" schedule 40 stainless steel pipe that is 5' long. Both ends have a welded custom designed stainless steel flange, which has four ports each where both flanges have the same diameter as the pipe. One of the flanges has two temperature ports, one pressure port, and a gas inlet port (Figure 3-6 left side). The other flange has

three temperature ports and one gas outlet port (Figure 3-6 right side). Platinum resistor thermometers are mounted on rods and attached to the cell flanges by 1/8" diameter fittings. The 6", 18", and 30" long rods are mounted as shown in Figure 3-4 (legend -4) to ensure that we are able to monitor the temperature at various depths of the cell with an additional sensor being mounted within the vacuum jacket.

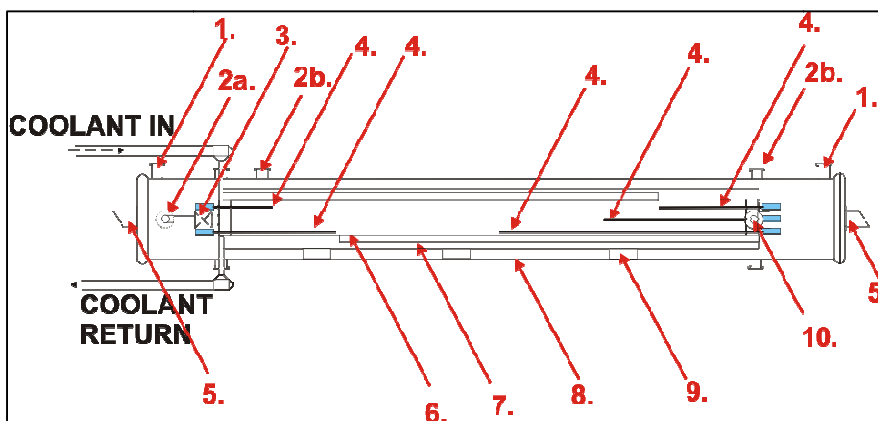


Figure 3-5: Side view of the temperature controlled cell. Legend: 1- vacuum port, 2a- gas inlet, 2b- vacuum field-through for platinum resistors, 3- vacuum valve, 4- temperature sensors using platinum resistors, 5- CaF2 windows mounted at Brewster angle, 6- fins for directing the coolant through the coolant jacket, 7- coolant jacket, 8- outer cell body, 9- cell support and 10- valve for de-pressuring of the outer jacket.

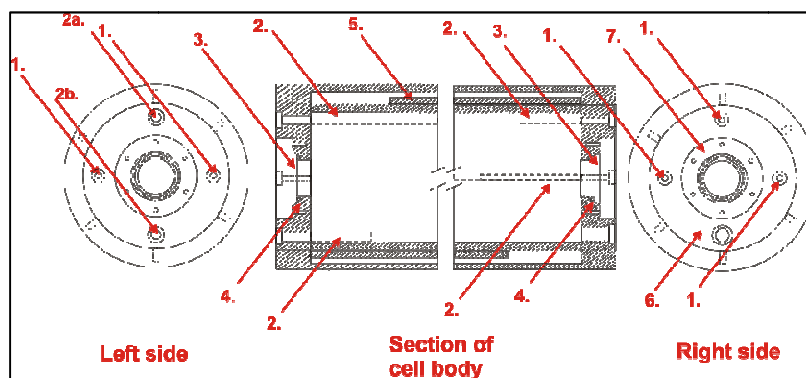


Figure 3-6: Left and right side views of the inner chamber. Legend: 1- platinum resistor thermometers, 2a- coolant inlet, 2b- coolant outlet, 3- CaF2 window, 4- left side flange, 5- fins for directing the coolant, 6- right side flange and 7- mounting rings for windows.

The gas pressure inside the inner cell is measured using a MKS pressure measuring unit with a signal conditioner Model 670 which is monitored via LabVIEW

software. The center counterbore in the end flanges house crystal windows that can be interchanged for the desired spectral range. At the moment the cell is provided with CaF_2 windows that are anti-reflection coated. To suppress channel spectra caused by multiple reflections of the sample beam between the surfaces of the windows, the windows are also wedged. Fluorosilicone O-rings are used on the inner sides of the crystal to seal the CaF_2 windows to the inner test chamber. The chamber is completely sealed from the outside. A stainless steel compression ring is applied to the outer side of each window to hold the window and O-ring assembly together.

The coolant fluid is supplied through a second chamber of 6" diameter shown in Figure 3-4, Figure 3-5 and Figure 3-6. This chamber is configured with 6 fins positioned as shown in Figure 3-5 (legend -6) and Figure 3-6 (legend -5) that allow the fluid to flow uniformly across the length of the cell. The heating/ cooling of the gas inside the temperature controlled cell is provided by a Neslab ULT-80 thermal bath using ethanol or methanol as coolant. The thermal bath is needed to vary the temperature of the gas between 193 and 353 K inside the temperature-controlled cell. The entire inner chamber rests on adjustable support stands to provide alignment of the inner chamber once placed inside the outer chamber.

The outer chamber is made up of nominal 8" schedule 10 stainless steel pipe that is 8' long. This larger chamber houses the inner chamber and is held under constant vacuum. Weld stubs have been specifically placed to allow points of entry for the temperature sensors, sample gas inlet and outlet, pressure monitoring lines, heated or cooled fluid inlet and outlet, and for pressure equalizing. Both ends of the outer chamber are removable to allow access to the inner chamber gas supply/outlet valves and

thermocouples. The center of the end flanges has an interchangeable piece, which houses an additional crystal and is set at a desired angle. This outer chamber is pressure monitored to ensure an adequate seal has formed.

3.3.2. Vibrational isolation

Early experiments indicated the need to vibrationally isolate the optical components of the system from the pumps and mechanical vibrations within the laboratory. Figure 3-7 and Figure 3-8 show spectra recorded with and without the vacuum pump running. It is very clear from the two figures that there is a vibrational dependence with the noise. The formation of the beat pattern within the noise is the direct result of the diaphragm pump, which is used as a backing pump for the turbo molecular pump.

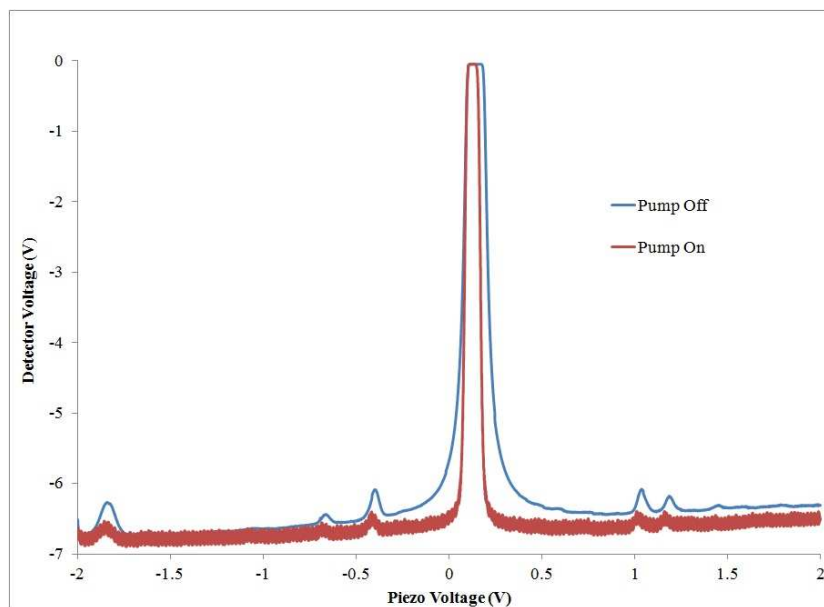


Figure 3-7: Example of vibrational noise added to a recorded spectra of the R11e transition in the $\nu_1+\nu_3$ band of acetylene.

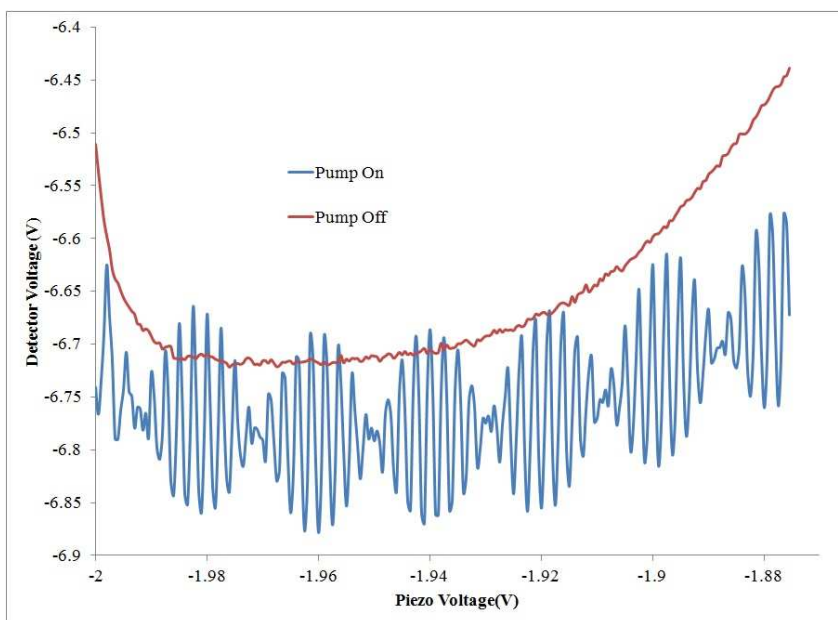


Figure 3-8: Fine structure of the noise depicted in Figure 3-7.

In order to isolate the system from this mechanical vibration noise, a Kinetic Systems 5100H series optical table with active supports was purchased and setup. The dimensions of the table are 48” wide by 144” long and 12” thick. This is a slightly thicker table than the standard 8’, and was purchased to further minimize any low frequency vibrations along the table top itself. The table top “breadboard” pattern was selected to be a ¼-20 tapped holes with 1” spacing between them, to allow for the proper mounting of optical components.

3.3.3. Detector configuration and testing

The optical design of the tunable diode laser spectrometer uses three InGaAs (indium gallium arsenide) photodiode detectors with preamps and power control boxes. Figure 3-9 shows the two detectors setup to record the light coming from the temperature controlled cell (on the left) and the reference cell (on the right). A third detector is used to

monitor the laser's output power. Several experiments were performed to ascertain the repeatability and performance of these detectors with the tunable diode laser system.



Figure 3-9: Image of two of the three InGaAs detectors used to measure the signals for the tunable diode laser spectrometer. The detectors can be seen just opposite the focusing lenses.

In an effort to determine the consistency between all three photodiodes, a set of spectra were recorded with the three detectors being rotated around their locations on the optical table. The three locations are: the optical channel containing the reference cell, the optical channel containing the temperature controlled cell and the channel for the background signal. Figure 3-10 shows the spectra recorded by each detector. It is very clear from the figure that there is almost no variation in the quality or repeatability of recorded spectra using any one of the three photodiodes in any of the three locations. This observation indicates that the photodiodes perform the same, regardless of the location.

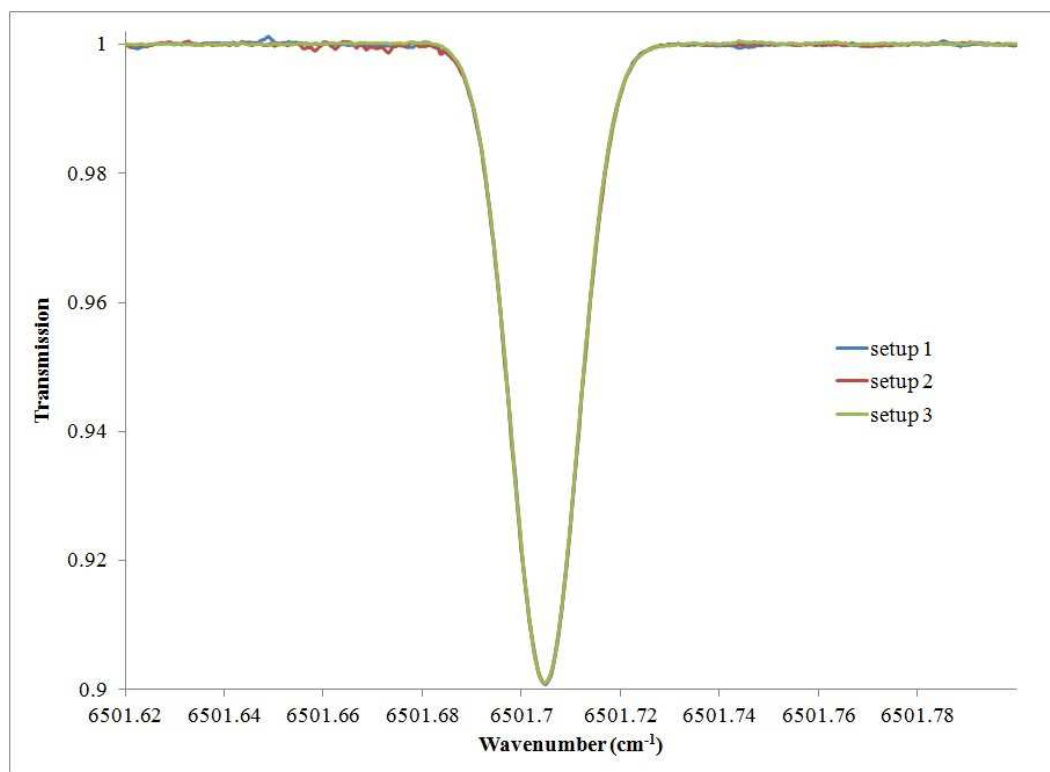


Figure 3-10: Comparison of the P(21) transition of the $\nu_1+\nu_3$ band of acetylene using three different detector setups.

The signal-to-noise ratio (SNR) of the data recorded by the detectors was also examined. For this purpose, the average signal for a data subset of the spectra was calculated and then divided by the RMS noise for the same subset of data using the following equation:

$$SNR = \frac{X_{avg}}{\sqrt{\frac{1}{N} \sum_1^N (X_i - X_{avg})^2}}, \quad 3-3$$

where X_{avg} is the average signal and X_i is the i^{th} data point.

The upper graph of Figure 3-11 shows an example of raw spectrum recorded using the temperature controlled cell channel. The lower graph in the figure shows the data subset used to calculate the SNR. For this particular spectrum, the SNR of the signal on the temperature controlled cell channel is roughly 445:1.

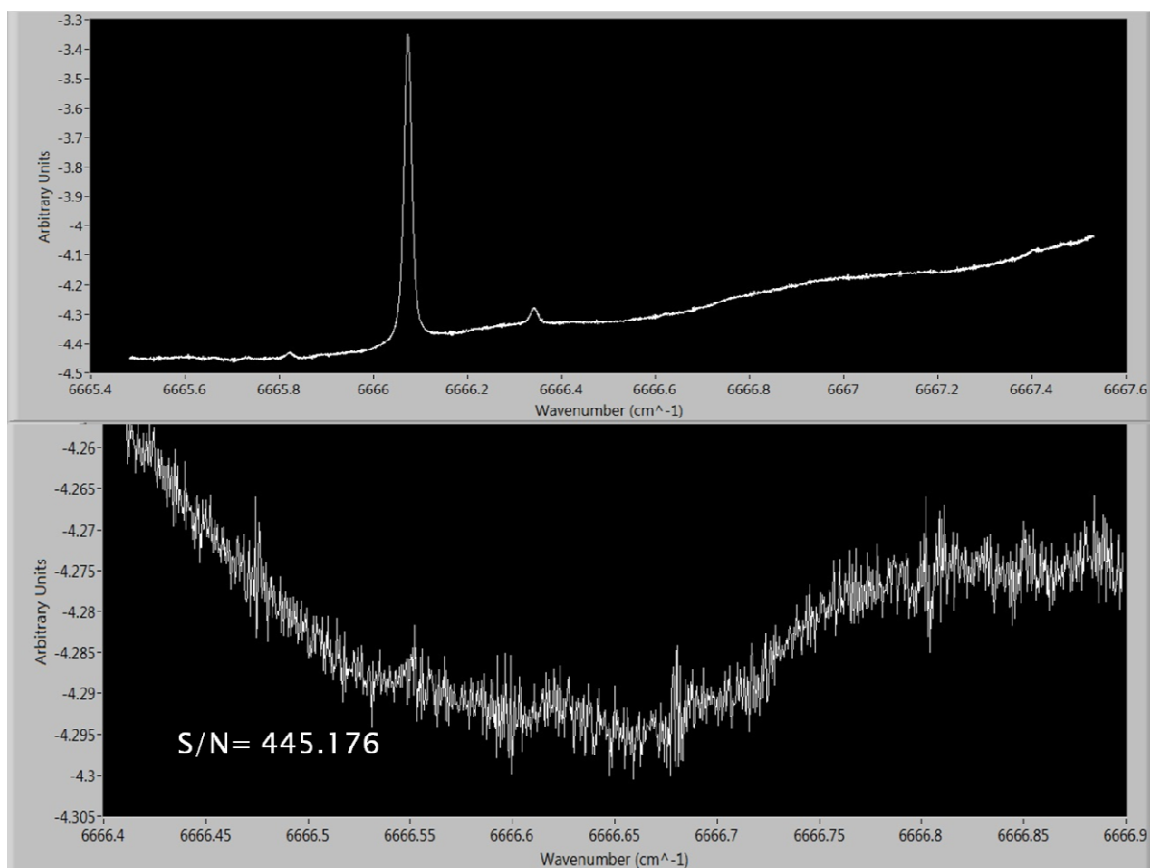


Figure 3-11: Signal-to-noise ratio for the raw signal obtained on the temperature controlled cell. The upper panel shows the recorded spectrum and the bottom panel shows the baseline region used to determine the signal to noise using equation 3-3.

This SNR is actually quite low, however a background channel was recorded simultaneously with the other signals. When used to correct the raw spectra there is a large improvement to the SNR (correction of the spectra is discussed in detail in Section 4.4.3). Figure 3-12 shows the corrected transmission spectra and the calculated SNR for the same baseline region. From the figure it is easy to see that there is a large improvement in the SNR from 445:1 to 2338:1. By measuring the background signal with an identical photodetector the same physical noise can be recorded on each channel and when performing the correction of the spectra to create the transmission spectrum, there is an elimination of most of the mechanical noise present in the spectra.

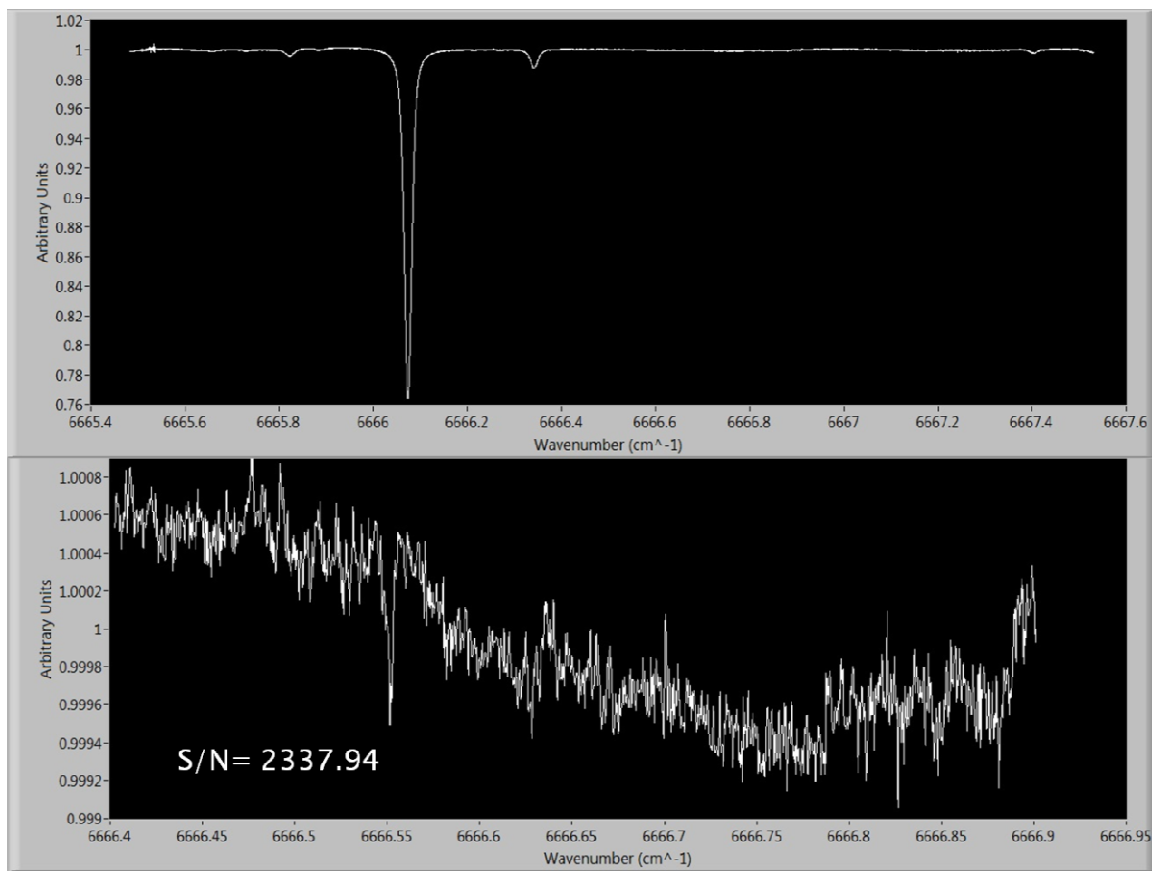


Figure 3-12: Signal-to-noise ratio for the corrected spectra obtained from the temperature controlled cell and the background signal. The top panel shows the transmission spectrum and the bottom panel shows the base line region of the same spectrum used in Figure 3-11 to calculate the signal to noise using equation 3-3.

A summary of the average SNR for a subset of spectra recorded is presented in Table 3-2 with the intent to show the general quality of the recorded spectra. The averages presented are the average of 2 to 4 spectra depending on the availability of good recorded data. For each calculation of the SNR, a region of the baseline corresponding to approximately 0.3 cm^{-1} was selected for the subset. This corresponds to about 3000 data points at a resolution of 0.0001 cm^{-1} and represents about 15 % of the baseline in the recorded spectra. From the Table it can be noticed that at lower temperatures the average SNR is lower. This result is not surprising as the compressors in the thermal bath are working hard producing additional mechanical vibration at low temperatures. Overall, the

results presented in Table 3-2 allow for the confident statement that the instrument can measure spectra with a SNR over 1000:1.

Table 3-2: Example of average SNRs for a set of recorded spectra based on pressure and temperature.

Pressure (Torr)	Temperature (K)	Average SNR	Standard Deviation of SNR
100	213	1221	154
500	213	1070	206
700	213	1240	117
100	293	1492	126
500	293	1725	8
700	293	1336	80

3.3.4. The Fabry-Perot cavity

The tunable diode laser spectrometer incorporates a Thor Labs SA200-14A Fabry Perot interferometer to allow for wavelength calibration. The Fabry Perot cavity offers a 1.5 GHz (0.05 cm^{-1}) free spectral range and has a high finesse. An example of the fringe pattern produced during a laser scan is shown in Figure 3-13. Two important aspects went into testing the Fabry Perot cavity: (1) was examining the fringe spacing to confirm the free spectral range of 0.05 cm^{-1} ; and (2) was to compare our measurements of line positions to other published studies to confirm the accuracy of the wavelength scale obtained using the Fabry Perot cavity. Details regarding the wavelength scale and accuracy testing will be discussed in Section 3.5.2.

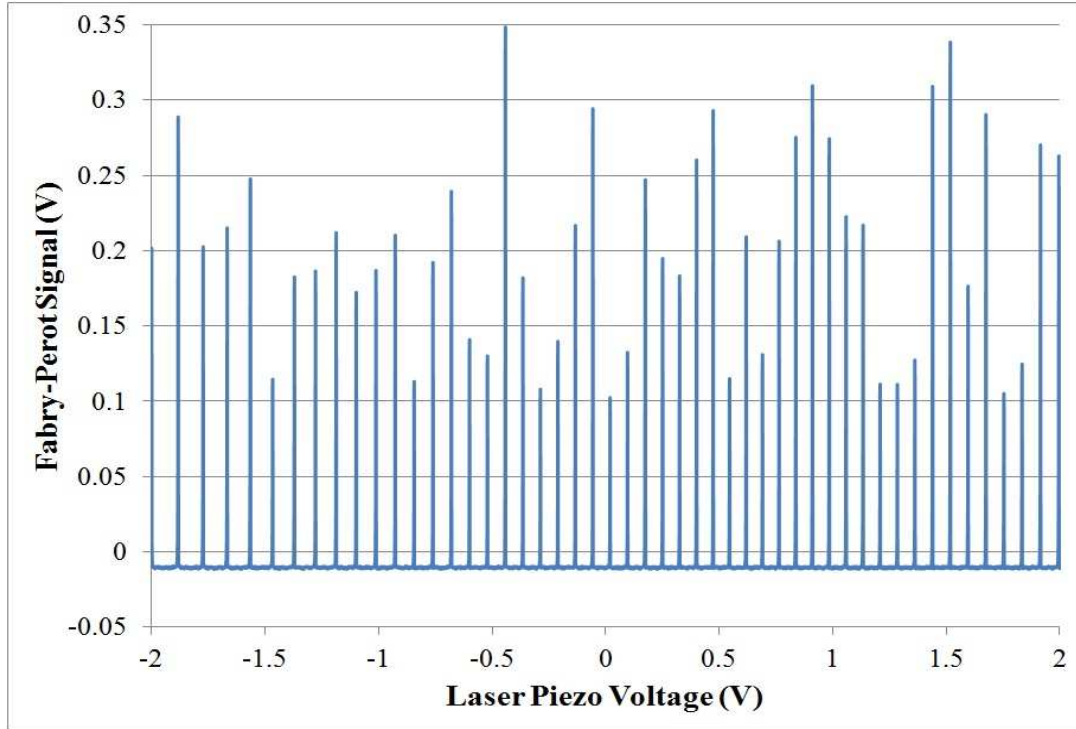


Figure 3-13: Example of the fringe pattern produced by the Fabry Perot interferometer during a laser scan.

In order to confirm the size of the free spectral range of the Fabry Perot cavity, a small experiment was setup. For the test, the laser piezo voltage was scanned from -2 to 2 V in a very slow manner with 3 s between samples. This was done to enable the measurement of three wavelengths from the WA1500 EXFO wavemeter. The sampling time was very important as the wavemeter can only sample in 1 s intervals. The average and standard deviation of the wavelengths was calculated for each laser piezo voltage recorded. The average error in the position recorded was approximately 0.0006 cm^{-1} . After a complete laser piezo scan had been recorded the positions associated with each peak were found and subtracted from each other to find the average free spectra range for that scan. Table 3-3 shows the results of five separate scans that were completed and the overall average spacing as determined from the five scans. From Table 3-3 it can be seen that the free spectral range for the Fabry Perot cavity is $0.0496 \pm 0.0007 \text{ cm}^{-1}$. This

experiment confirms that the Fabry Perot cavity is within the stated free spectral range of 0.05 cm^{-1} . This result confirms the use of 0.05 cm^{-1} as the correct fringe spacing for any analysis completed with this system (0.05 cm^{-1} has been chosen since the manufacturer has confirmed this value to a higher degree of precision than what is presented here).

Table 3-3: Average fringe spacing from 5 separate laser piezo scans.

Calibration Test	Average Fringe Spacing (cm^{-1})	Fringe Spacing Error (cm^{-1})
Test 1	0.0484	0.0015
Test 2	0.0500	0.0010
Test 3	0.0499	0.0012
Test 4	0.0499	0.0012
Test 5	0.0499	0.0010
Average	0.0496	
Standard Deviation	6.6381×10^{-4}	

3.4. Pressure and Temperature Controlled Gas Cell

3.4.1. Introduction

For atmospheric research, long pathlengths are required for absorption cells operating at various temperatures [70] and pressures that are relevant to atmospheric conditions. White type cells typically meet the prerequisite for path length due to their multi-pass configurations [71]. Ref. [17] reports on a long path cell (16-96 m) that operates between 215 and 470 K at gas pressures ranging from vacuum to 10 atm. A temperature controlled White type long path cell was built by McKellar [72, 73] to enable studies of weakly bound complexes at low temperatures. The cell has a base path of 5 m

and allows the users to achieve up to 100 m pathlength. Another example of a variable temperature absorption cell (White design) that can accommodate path lengths up to 512 m and pressures up to 5 atm was built for laboratory spectroscopic studies of gases found in terrestrial and planetary atmospheres [74-78]. A large fraction of the published results are restricted to temperatures near room temperature. Ref. [79] provides a good example at the other end of the temperature range using the concept of collisional cooling in the cell. The minimum temperature that can be maintained in the cell is reported as 10-12 K.

Over the last few decades many papers featuring the use of variable temperature cells have been published, but the key concern in the operation of such cells has been the temperature gradient along the length of the cell. Short-term stability is necessary for the efficient use of any cell as it reduces the time for experiments in the laboratory. In 2004, Valentin et al. [80] reported on a stabilized low temperature infrared absorption cell cooled by an open cycle refrigerator, which can run with liquid nitrogen from 250 to 80 K or with liquid helium from 80 K to only a few Kelvin. The authors have reported temperature stability better than 0.1K over 4 hours for a 300 to 4.5 K temperature spread. Three years later, Mondelain et al. [70] achieved temperature stability better than 0.005 K for their long path cell with a transition from 296 to 20 K taking approximately an hour. The long path cell had a Herriott design and was made completely from copper. Other absorption cells reported in the literature deviate little from this range of temperatures and stability values.

Thermal gradients are often impossible to completely remove from the design of absorption cells but improvements have been made in this area. Multiple temperature sensors are often used to monitor the temperature variability of the cells over their base

length. Smith et al. [81] mounted six thermocouples in contact with their coolant along the length of their cell and have measured an agreement of ± 2 K between them. Eight thermocouples are distributed evenly along another cell built by Cann [82] and three were employed in Schaeffer et al. [83] multipass high temperature cell with an accuracy of ± 1 K. Temperature gradients less than 0.1 K/m have also been shown by the authors of Ref. [84]. The presence of thermal gradients is obvious and is highly dependent upon the base length of the cell. Accordingly, a compromise between a desired optical pathlength and thermal congruence is often necessary.

A 147.5 cm long variable-temperature absorption gas cell was designed [85] and built for spectroscopic measurements of gases of atmospheric interest using a Bomem DA8.3 Fourier transform spectrometer. The heating/cooling system enveloping the cell allows spectroscopic studies of gas samples at temperatures ranging from 205 to 350 K and up to atmospheric pressure. The temperature stability inside the cell are within ± 0.31 K, highlighting the very good performance of this system.

A short coolable gas cell designed for lineshape studies was presented by Lambot et al. [8]. The temperature can be stabilized to within ± 2 K for temperatures between 120 K and room temperature and accommodates any absorption pathlength between 0 and 3 cm. An experimental setup that integrates a low-temperature optical cell working in the UV-visible (UV-Vis) with a liquid X-ray absorption spectroscopy (XAS) cell is reported in Ref. [86]. The proposed gas cell is suitable for the measurement of gases at variable temperatures from room temperature to 195 K.

3.4.2. Vacuum performance of the cell

When completing high accuracy spectroscopic measurements it is important to maintain a pure known sample within the chamber. This requires the system to be vigorously tested for any potential leaks. These leaks will lead to drifts in concentrations of the gas samples with time. Therefore, the temperature controlled cell used in present measurements has been tested to ensure its capability to hold high vacuum.

In order to assess the quality of the vacuum present within the system several tests were completed at room temperature (296 K) and at 323 K to monitor the changes in the base pressure with time. For this purpose the system was pumped down for 3 days with a turbo molecular pump while the Neslab ULT 80 chiller maintained a temperature of 323 K. Figure 3-14 shows a plot of the base pressure during this initial pump down phase.

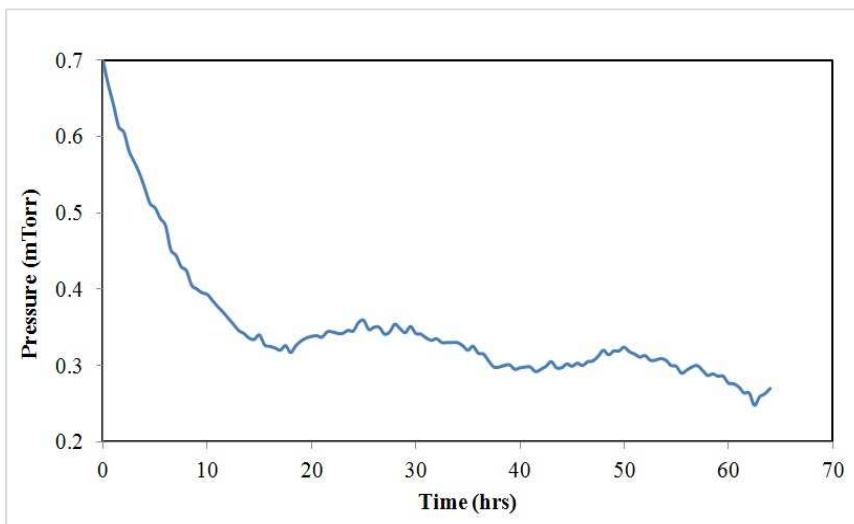


Figure 3-14: Base pressure of the temperature controlled cell over a 3-day period.

Once the base pressure was obtained, the vacuum line was shut off and the pressure monitored over time to determine the leak rate of the system. Two leak rates were determined and are shown in Figure 3-15 and Figure 3-16. With the system being

maintained at 323 K, a leak rate of approximately 0.112 mTorr /min or 1.86×10^{-6} Torr/ s and when maintained at 296 K there is a leak rate of approximately 0.09 mTorr/ min or 1.50×10^{-6} Torr/ s were observed. It is believed that this is the outgassing limit of the system as the chamber has a large surface area and is not made from a highly polished stainless steel. Further baking of the chamber could potentially improve this result, but this is hazardous as our cooling liquid is ethanol. Therefore, any temperatures above 348 K could cause ethanol vapours to form in the cooling jacket which could pose a serious safety hazard.

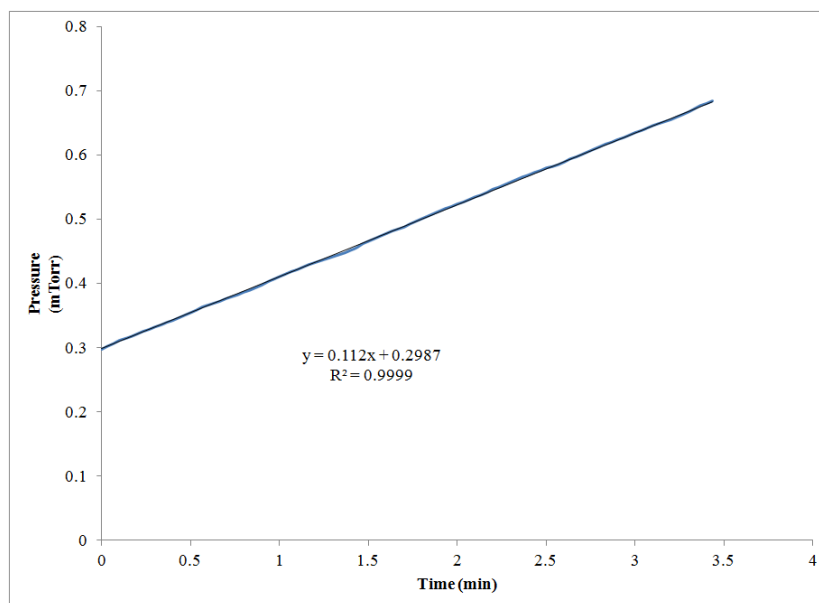


Figure 3-15: Leak rate of the temperature controlled cell at 323 K. The equation shows a leak rate of 0.112 mTorr per min.

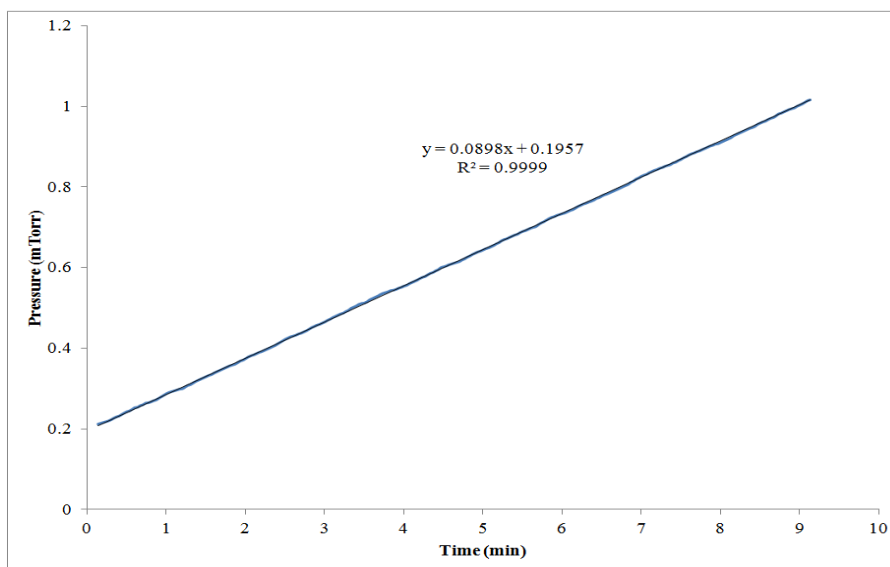


Figure 3-16: Leak rate of the temperature controlled cell at 296 K. The equation indicates a leak rate of 0.09 mTorr per min.

3.4.3. Temperature performance and gradients inside the temperature controlled cell

The overall performance of the system had to be examined to estimate what kind of errors and tolerances were present for the pressure and temperature of the temperature controlled cell. When recording spectra, the system actively monitors both the gas pressure and temperature. Normally, a set of 10 measurements of both temperature and pressure of the gas are obtained for each molecular transition scanned. Five are recorded before the transition is scanned and another five after the scan is completed. During analysis an average of these 10 measurements are used. Within this section several sets of complete experimental measurements are examined to show the pressure and temperature stability of the system with time. A diagram of the temperature sensor setup is given in Figure 3-17.

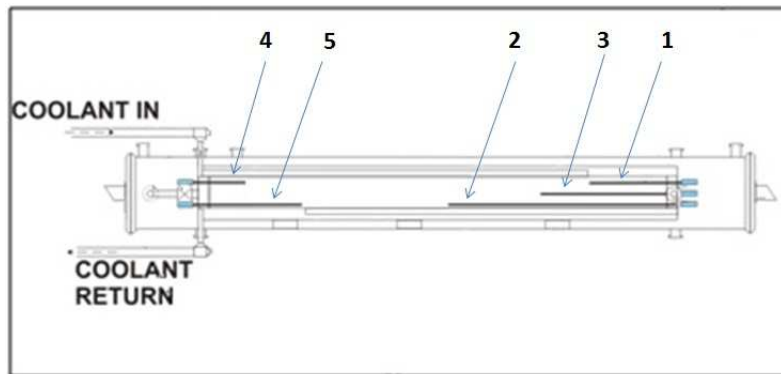


Figure 3-17: Schematic of the temperature controlled cell showing the assigned locations of the temperature sensors. 1, 2, 3, 4 and 5 are the platinum resistance temperature sensors mounted within the gas chamber.

The lowest operating temperature used to date for the system is 213 K. This temperature is most ideal for examining the stability of the system as it is the most extreme operating temperature used in the lab to date. In most cases, the system is left for several hours until it reaches thermal equilibrium which is evident from Figure 3-19. This Figure and Figure 3-18 show the pressure and temperature stability of the system for three separate experiments carried out at 213 K. The overall stability of the temperature for the system is really good. However, it is observed in Figure 3-18 that there is still some drift in the overall pressure with time. In most cases this drift is the result of local temperature instability in the laboratory itself and insufficient long-scale wait times (on the order of a day or two to obtain the optimal thermal equilibrium).

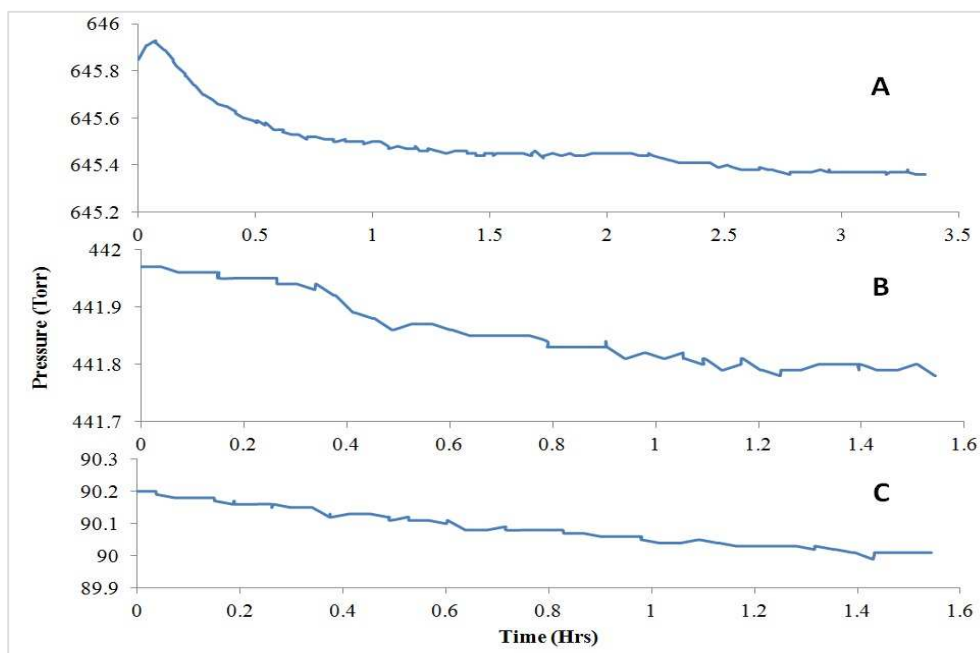


Figure 3-18: Pressure within the temperature controlled cell maintained at a temperature of 213 K. The pressure changes over the scan time for figures A, B and C are 0.09, 0.04, and 0.21 %, respectively.

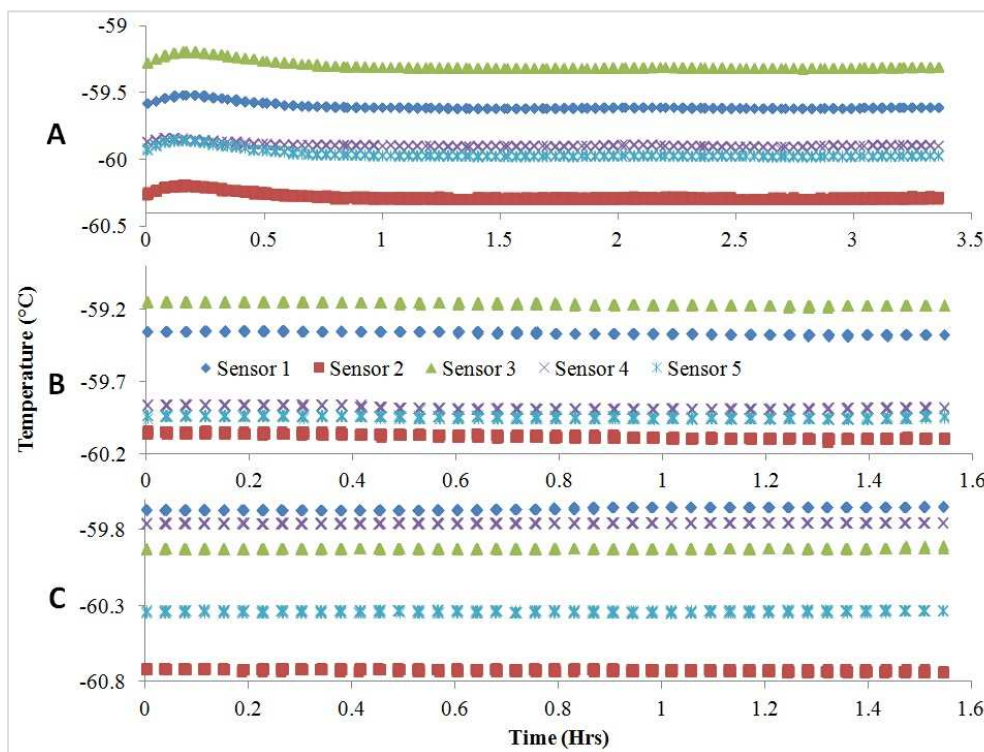


Figure 3-19: Recorded values of temperature for all 5 thermo resistor sensors with the temperature controlled cell. The pressures of the cell for scans A, B and C are those presented in Figure 3-18. The sensor locations are given in Figure 3-17.

The results for two other temperatures were also examined to see how they relate to the low temperature case. Shown in Figure 3-20 and Figure 3-21 we see that the stability of the system at 293 and 333 K is also very good with only small drifts in pressure and very consistent temperatures. A complete summary of all the experiments performed is given in Table 3-4. The values listed in this table show the average pressure and temperature of the system during the measurement time along with the associated errors. The arrangement of the sensors as shown in Figure 3-17 also allowed for the calculation of the thermal gradient inside the cell. End 1 refers to the end of the cell with the three sensors 1, 2 and 3, and End 2 is the opposite side where the sensors 4 and 5 are located. From Table 3-4 it is clear that larger gradients are formed at the lower temperatures, but the pressure inside the cell also influences the degree of change across the length of the chamber. From the values listed in the table below, the largest gradient observed is $2.42 \times 10^{-3} \text{ }^\circ\text{K/cm}$. This means that for the 1.54 m length of the cell, there is a 0.37 K change in the temperature which is quite small (approximately a 0.62 % change across the length of the chamber), and it is the main contributor to the error in the temperature measurement.

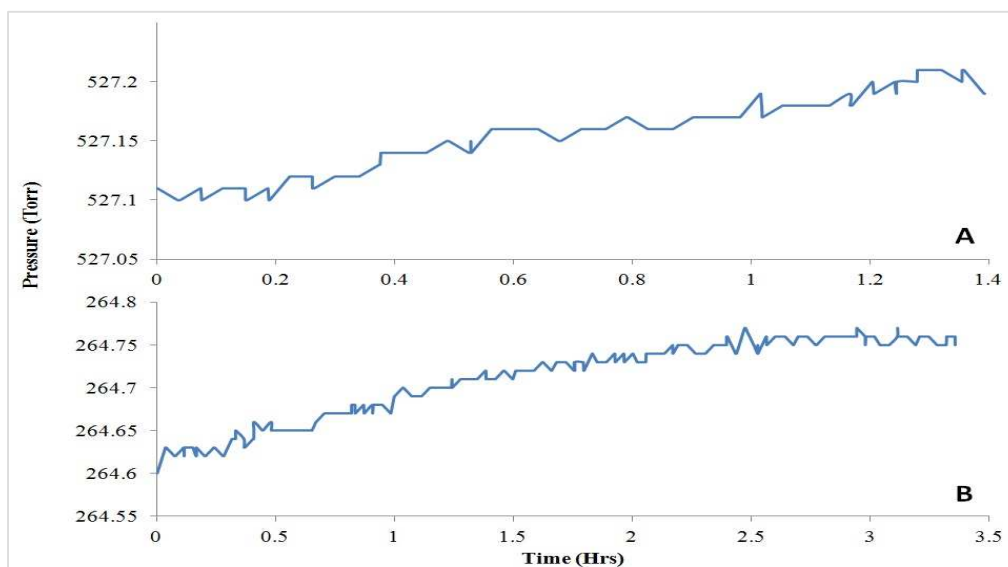


Figure 3-20: Pressure within the temperature controlled cell maintained at a temperature of 333 K for A and 293 K for B. The pressures changes over the scan time for figures A and B are 0.02 and 0.06 %, respectively.

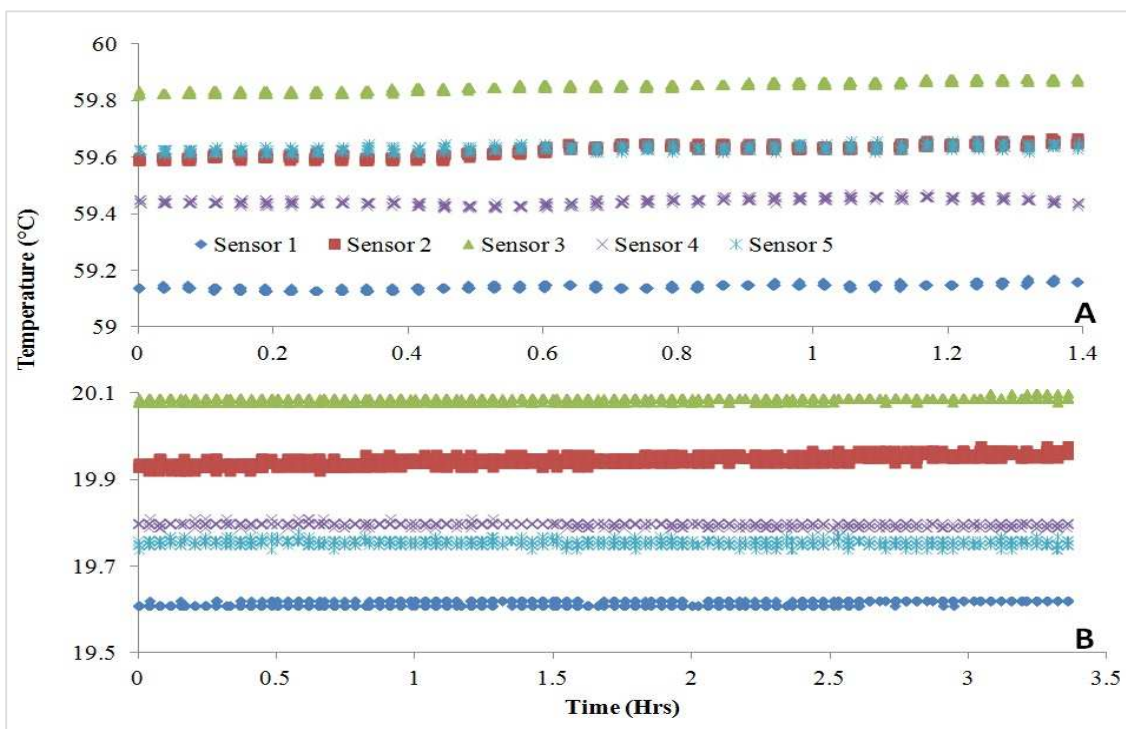


Figure 3-21: Recorded values of temperature for all 5 thermo resistor sensors with the temperature controlled cell. The pressures of the cell for scans A and B are those presented in Figure 3-20. The sensor locations are given in Figure 3-17.

Table 3-4: Summary of the temperature and pressure stability of the temperature controlled cell for several different experimental conditions.

Chiller Set Point (°C)	Average Pressure (Torr)	% Error	Average Temp. (K)	% Error	Average Temp. End1 (K)	Average Temp. End2 (K)	Cell Gradient (End1 - End2) (K/cm)
-60	441.86	0.014	213.46	0.594	213.612	213.239	2.42×10^{-3}
-60	645.48	0.020	213.35	0.559	213.428	213.232	1.28×10^{-3}
-60	90.09	0.064	213.07	0.661	213.049	213.107	-3.75×10^{-4}
60	527.15	0.006	332.69	0.399	332.691	332.690	1.06×10^{-5}
20	264.71	0.017	292.99	0.820	293.033	292.927	6.89×10^{-4}

3.5. Spectrometer Testing and Calibration

3.5.1. Introduction

With the integration of all these parts, the completed system needed to be tested to ensure the high quality of the spectroscopic results obtained. Several important aspects of these tests are presented in the following sections. Firstly, it will be shown that the calibration procedure completed using the Fabry Perot cavity highly agrees with results found in both HITRAN and other sources in the literature. Secondly, a careful examination of the instrumental line shape of the spectrometer will be shown. Finally, a discussion of the errors associated with all the various fit parameters that are determined will be given to justify the quality of the data collected with this instrument.

3.5.2. Wavelength calibration and measurements of line positions

As stated in the introduction, the ability to calibrate the wavelength scale of the spectra is extremely important, even more so because a multispectral fitting software is used in the analysis of the spectroscopic data, and therefore the reproducibility of line

positions is a key component to obtaining high-precision results. Therefore, a short but careful study was performed to ensure the accuracy of the frequency scale produced by the wavemeter and Fabry Perot cavity.

For this study, 23 room temperature (296 K) spectra of the P(21) transition in the $\nu_1+\nu_3$ band of acetylene were recorded at pressures below 50 mTorr (low pressures were used in order to minimize the influence of pressure shifts). For each fit, only the intensity and line position were the floated parameters, while the remaining parameters such as pressure broadening and shift coefficients were fixed to the HITRAN08 [21] values.

The values obtained for line positions have been compared to those in HITRAN08 [21] and to those reported by Madej *et al.* [2] and are presented in Table 3-5. The table shows an average error of 0.002288 cm^{-1} when compared to HITRAN08 [21] and 0.002275 cm^{-1} when compared to the results of Madej *et al.*[2]. This level of agreement is very good as it is within the combined error associated with both the wavemeter (0.001 cm^{-1}) and the Fabry Perot cavity (0.001328 cm^{-1}).

The dual chamber set-up allowed for the simultaneous measurement of line positions inside both the reference cell and the temperature controlled cell. In Table 3-5 the column “Physical Channel” notes in which chamber the spectra were recorded, CH1 refers to the results obtained on the temperature controlled cell and CH2 refers to results obtained for the reference chamber. After recording the spectra simultaneously, each spectrum was fit separately as discussed above in order to find if there were any time delay or sampling issues that may cause a noticeable drift in the line positions measured using spectra recorded by both channels. After taking the difference between each of the

retrieved line positions in Table 3-5 it was found that the line position between the two channels differs by an average of $0.00001645 \text{ cm}^{-1}$. This difference is in the limit of the fitting software error (as can be seen in Table 3-5) and therefore indicates that both spectra are indeed recorded simultaneously.

Table 3-5: Comparison of retrieved line positions for the P(21) transition in the $\nu_1+\nu_3$ band of acetylene. All spectra were recorded at pressures below 50 mTorr.

Laser Center Wavelength (nm)	Physical Channel	Measured Line Position (cm^{-1})	Fitting Error ($\times 10^{-6}$)	HITRAN [21] Position (cm^{-1})	Difference From HITRAN ($\text{cm}^{-1} \times 10^{-4}$)	Madej [2] Position (cm^{-1})	Difference From Madej ($\text{cm}^{-1} \times 10^{-4}$)
1537.877818	CH1	6501.700696	4.96	6501.7047	40.037	6501.70458	38.810
1537.877818	CH2	6501.700704	5.60	6501.7047	39.961	6501.70458	38.733
1537.927818	CH1	6501.704561	3.37	6501.7047	1.3868	6501.70458	0.1593
1537.927818	CH2	6501.704544	4.44	6501.7047	1.5568	6501.70458	0.3293
1537.977818	CH1	6501.704486	3.07	6501.7047	2.1406	6501.70458	0.9131
1537.977818	CH2	6501.704471	4.35	6501.7047	2.2861	6501.70458	1.0585
1538.027818	CH1	6501.699425	4.52	6501.7047	52.750	6501.70458	51.522
1538.027818	CH2	6501.699450	5.42	6501.7047	52.498	6501.70458	51.270
1537.927273	CH1	6501.705515	3.65	6501.7047	8.1533	6501.70458	9.3808
1537.927273	CH2	6501.705518	4.90	6501.7047	8.1808	6501.70458	9.4083
1537.977273	CH1	6501.705404	3.65	6501.7047	7.0424	6501.70458	8.2699
1537.977273	CH2	6501.705394	4.96	6501.7047	6.9433	6501.70458	8.1708
1538.027273	CH1	6501.705158	9.26	6501.7047	4.5820	6501.70458	5.8095
1538.027273	CH2	6501.705150	6.03	6501.7047	4.5021	6501.70458	5.7296
1537.876291	CH1	6501.699756	1.74	6501.7047	49.442	6501.70458	48.214
1537.876291	CH2	6501.699793	1.81	6501.7047	49.069	6501.70458	47.841
1537.877982	CH1	6501.701715	3.99	6501.7047	29.848	6501.70458	28.620
1537.877982	CH2	6501.701728	4.88	6501.7047	29.721	6501.70458	28.493
1537.927982	CH1	6501.704663	3.20	6501.7047	0.3710	6501.70458	0.8565
1537.927982	CH2	6501.704677	4.47	6501.7047	0.2288	6501.70458	0.9987
1537.977982	CH1	6501.703665	2.74	6501.7047	10.345	6501.70458	9.1175
1537.977982	CH2	6501.703684	4.25	6501.7047	10.160	6501.70458	8.9321
1538.027982	CH1	6501.702459	8.59	6501.7047	22.415	6501.70458	21.187
1538.027982	CH2	6501.702486	9.27	6501.7047	22.136	6501.70458	20.908
1537.865294	CH1	6501.701452	7.86	6501.7047	32.483	6501.70458	31.255
1537.865294	CH2	6501.701454	8.67	6501.7047	32.456	6501.70458	31.228
1537.915294	CH1	6501.702267	3.70	6501.7047	24.332	6501.70458	23.104

Laser Center Wavelength (nm)	Physical Channel	Measured Line Position (cm ⁻¹)	Fitting Error (x10 ⁻⁶)	HITRAN [21] Position (cm ⁻¹)	Difference From HITRAN (cm ⁻¹ x10 ⁻⁴)	Madej [2] Position (cm ⁻¹)	Difference From Madej (cm ⁻¹ x10 ⁻⁴)
1537.915294	CH2	6501.702261	4.81	6501.7047	24.391	6501.70458	23.163
1537.965294	CH1	6501.708331	7.22	6501.7047	36.312	6501.70458	37.540
1537.965294	CH2	6501.708312	7.30	6501.7047	36.120	6501.70458	37.347
1538.015294	CH1	6501.706157	4.85	6501.7047	14.569	6501.70458	15.796
1538.015294	CH2	6501.706134	5.28	6501.7047	14.338	6501.70458	15.565
1537.862376	CH1	6501.705545	4.55	6501.7047	8.4537	6501.70458	9.6812
1537.862376	CH2	6501.705556	5.09	6501.7047	8.5570	6501.70458	9.7845
1537.912376	CH1	6501.702522	3.98	6501.7047	21.777	6501.70458	20.549
1537.912376	CH2	6501.702524	4.54	6501.7047	21.755	6501.70458	20.527
1537.962376	CH1	6501.707482	6.20	6501.7047	27.816	6501.70458	29.043
1537.962376	CH2	6501.707526	6.47	6501.7047	28.257	6501.70458	29.485
1538.012376	CH1	6501.710246	6.81	6501.7047	55.456	6501.70458	56.683
1538.012376	CH2	6501.710305	7.16	6501.7047	56.055	6501.70458	57.282
1537.844992	CH1	6501.701675	5.37	6501.7047	30.250	6501.70458	29.022
1537.844992	CH2	6501.701679	12.90	6501.7047	30.211	6501.70458	28.983
1537.894992	CH1	6501.708498	7.83	6501.7047	37.983	6501.70458	39.210
1537.894992	CH2	6501.708496	7.93	6501.7047	37.962	6501.70458	39.189
1537.944992	CH1	6501.704747	4.22	6501.7047	46.790	6501.70458	1.6954
1537.944992	CH2	6501.704735	4.35	6501.7047	35.220	6501.70458	1.5797
1537.994992	CH1	6501.701578	4.99	6501.7047	31.221	6501.70458	29.993
1537.994992	CH2	6501.701592	5.59	6501.7047	31.079	6501.70458	29.851
				Average	22.884		22.756

3.5.3. Instrumental line shape function

In order to optimize the quality of future line parameters measurements, a careful analysis of the spectrometer's instrumental line shape (ILS) function was carried out. To examine the ILS, several transitions in the $\nu_1+\nu_3$ band of acetylene were used and are listed in Table 3-6. The choice to use several transitions was made to rule out any frequency dependence that might exist for the laser system. The spectral features were measured at very low pressures (around 30 mTorr) and were fit with Doppler profile holding all other line parameters constant except the ILS and intensity. The fitting

software also allowed different ILS functions to be used and, therefore, both the Gaussian and Lorentzian ILS functions were tested for each of the recorded spectrum.

Table 3-6: Summary of the analysis completed to determine the instrumental line shape for the tunable diode laser spectrometer.

Laser Center Wavelength (nm)	Transition	Gaussian ILS ($\times 10^{-4}$)	Fit Error ($\times 10^{-5}$)	Lorentzian ILS ($\times 10^{-5}$)	Fit Error ($\times 10^{-6}$)	Best Fit
1531.241616	P11	7.68	0.99	8.70	0.98	LORENTZ
1531.341616	P11	5.72	1.27	6.22	1.18	Either
1531.391616	P11	6.02	1.18	6.96	1.13	LORENTZ
1537.110569	P20	5.07	3.65	6.80	3.39	Either
1537.210569	P20	8.69	2.97	10.2	4.19	Either
1537.740660	P21	9.64	1.12	11.2	1.67	LORENTZ
1537.790660	P21	7.60	1.12	8.32	1.36	Either
1537.840660	P21	7.20	1.28	8.10	1.47	LORENTZ
1515.636027	R18	1.08	1.26	11.2	2.14	GAUSS
1515.736027	R18	3.13	3.99	1.85	3.23	Either
1515.275750	R19	8.47	0.89	10.4	1.14	LORENTZ

The results of these tests are shown in Table 3-6 with the final column indicating which ILS offered the best agreement with the spectra. It was found that on average both a Lorentzian and Gaussian function could work, however, the Lorentzian function offered a slight improvement of the residuals for some cases. Therefore, the ILS that has been used in the analysis with this system is a Lorentzian function with a value of $8.167 \times 10^{-5} \text{ cm}^{-1}$.

3.5.4. Errors in the fit parameters

For most of the work completed with this spectrometer, the focus is on the retrieval of pressure independent line parameters. The most commonly examined coefficients are the pressure broadening γ_o , pressure induced shift δ_o , and the Dicke narrowing β_o . For these coefficients it was very important to attribute a relative error to the values obtained using this instrument. However, determining the error in a fitted parameter can be very difficult to calculate directly, and the errors reported back from the fitting software are only statistical errors related to the quality of the mathematical fit and do not include any errors associated with pressure and temperature variability. In order to obtain a physical error associated with these line parameters, the pressure dependent coefficients were examined closely.

The relationship of these parameters with pressure is linear, therefore this was exploited to examine how well the pressure independent term could be calculated by performing individual fits on spectra recorded at various pressures (all spectra analysed here were recorded at 293 K). Figure 3-22, Figure 3-23 and Figure 3-24 show the linear relationships for the pressure broadening γ , pressure induced shift δ , and the Dicke narrowing parameter β , respectively. The slopes generated from these figures can be used to determine the pressure independent coefficients but more importantly, using a linear regression model, the error in the slope can also be determined. The error in the slope gives a much more physical representation of the errors associated with each of these parameters.

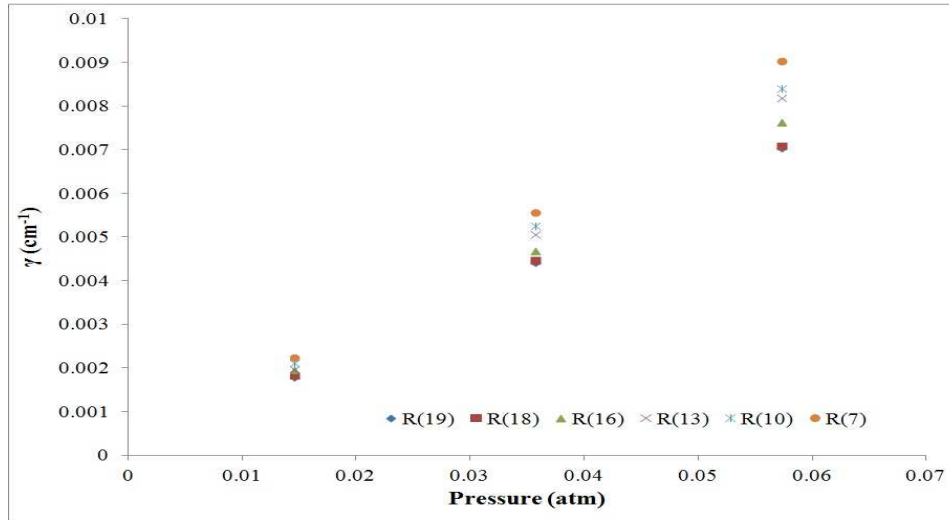


Figure 3-22: The experimentally determined pressure dependent broadening coefficient γ as it varies with the cell pressure.

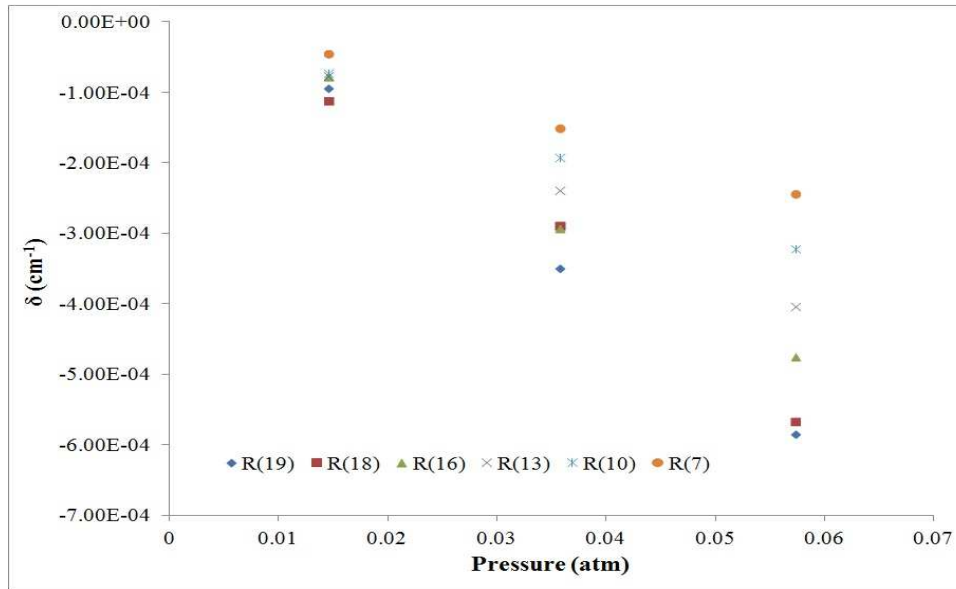


Figure 3-23: The experimentally determined pressure dependent shift coefficient δ as it varies with the cell pressure.

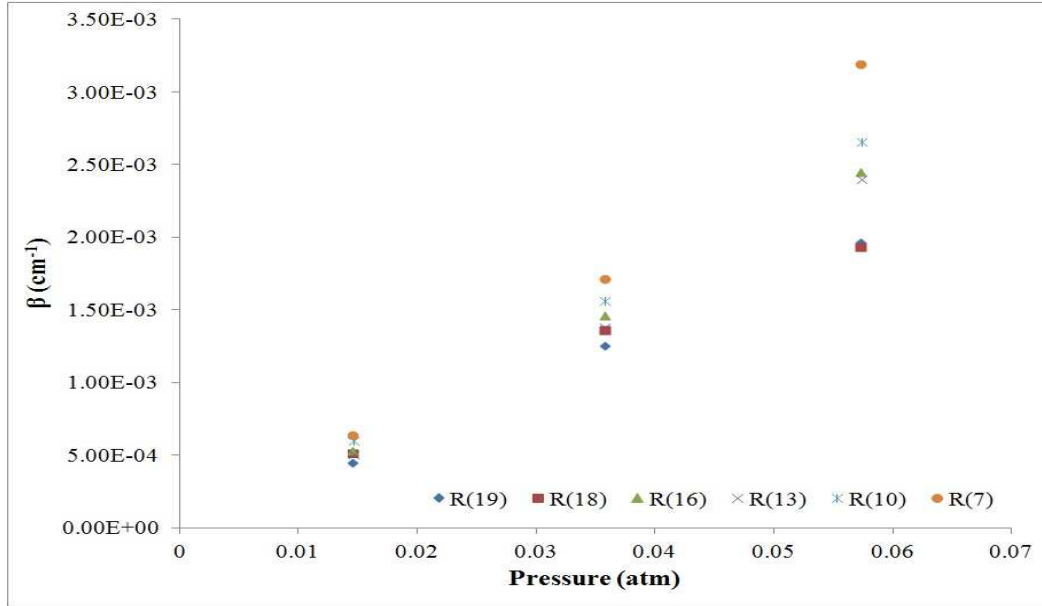


Figure 3-24: The experimentally determined pressure dependent narrowing coefficient β as it varies with the cell pressure.

Table 3-7: Summary of the errors found for the pressure independent coefficients

Variable	Average Error
γ_o	0.43%
δ_o	4.54%
β_o	3.15%

For each transition measured, the slope and error in the slope were calculated for each of the three pressure dependent parameters. Afterwards, an average of the relative error in percentage was calculated and is shown in Table 3-7. The values in Table 3-7 indicate a very high precision in the retrieved broadening and a relatively good precision in the shift and narrowing coefficients. It is important to note that the precision of these parameters also depends on the presence of other local spectral features which in some cases may overlap and ultimately increase the uncertainty in the retrieved parameter values.

3.6. Conclusion

In this chapter the experimental design and setup of the TDLS system has been presented. The overall performance of the system indicates that it can achieve the required accuracy needed to improve our understanding of the spectral parameters for gases of interest. The system offers a high level of control and can generate high quality spectra while maintaining the gas samples pressure and temperature stability.

Chapter 4: Software Developed for a Tunable Diode Laser Spectrometer (TDLS)

4.1. Introduction

In this chapter a detailed discussion of programs used to control the tunable diode laser system will be presented. In Section 4.2 an overview of the software used to control the operation of the spectrometer will be presented followed by a description of the spectrometer control software currently being used (Section 4.3). A detailed account of the data that are produced using this software will be presented with a discussion about how the retrieved data are post processed to generate high-quality spectra for final analysis.

4.2. Overview of Labview Software

4.2.1. Introduction to Labview

The Labview software package provided by National Instruments is the core programming language used to run and handle all of the spectra recorded using the TDLS. The software allows for an easy interface with many different types of data acquisition hardware such as R232, GBIP and data acquisition cards (DAQs). This ease of communication and high-level programming language easily lends itself to a very high level of instrumental control, thus making it ideal to execute experiments in a very precise and automated way.

The programming language works through the creation of what are known as VI's or Virtual Instruments. A single program may be considered a VI; however, it may also contain within it many sub-VIs that are selectively executed. This development of hierarchy allows for complex code to be packaged into a nice organized program with easy to edit functionality. An example of Labview's hierarchy is shown in Figure 4-1. The figure shows the simple first level structure of the main control software for the TDLS spectrometer. By expanding each sub-VI within the main VI "VelocityController.vi", one can then find a complete list of all the sub-VIs that are contained within the main program.

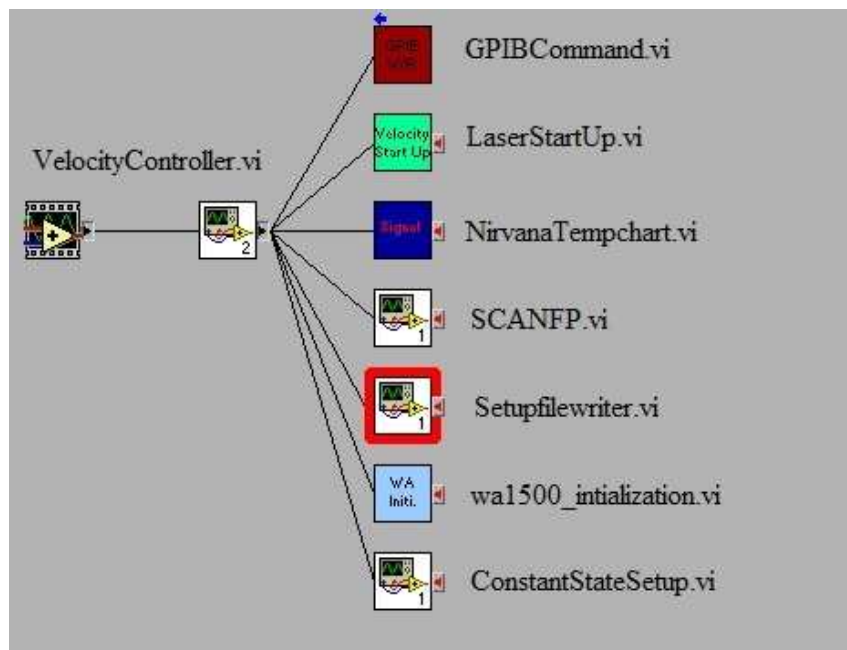


Figure 4-1: Example of the Hierarchy produced by Labview VI's.

4.2.2. Structure of the Labview language

To understand how the various sets of software control the spectrometer operation, some key terms must first be understood. First, Labview is broken into two individual parts, namely the “Block Diagram” and the “Front Panel”. The “Front Panel” shown in Figure 4-2 is the main graphical user interface (GUI) that is operated by the user to control the execution of a given VI while it is running. This view is what the user will operate during execution of the program, and allows them to use “Controls” to input data and then obtain output data through “Indicators”. In the figure the “Controls” are on the right and are generally denoted with a white background, while the indicators (shown here on the left) are generally denoted with a grey background. Another key feature that can be seen in Figure 4-2 is in the top right corner with the coloured boxes. Each colour denotes a connection to either a control or indicator shown on the front panel. The boxes with the thick black borders are outputs while the remaining ones are inputs. This wiring allows for the program to be easily inserted into another program to be executed as a sub-VI; an example of this is shown in Figure 4-3.

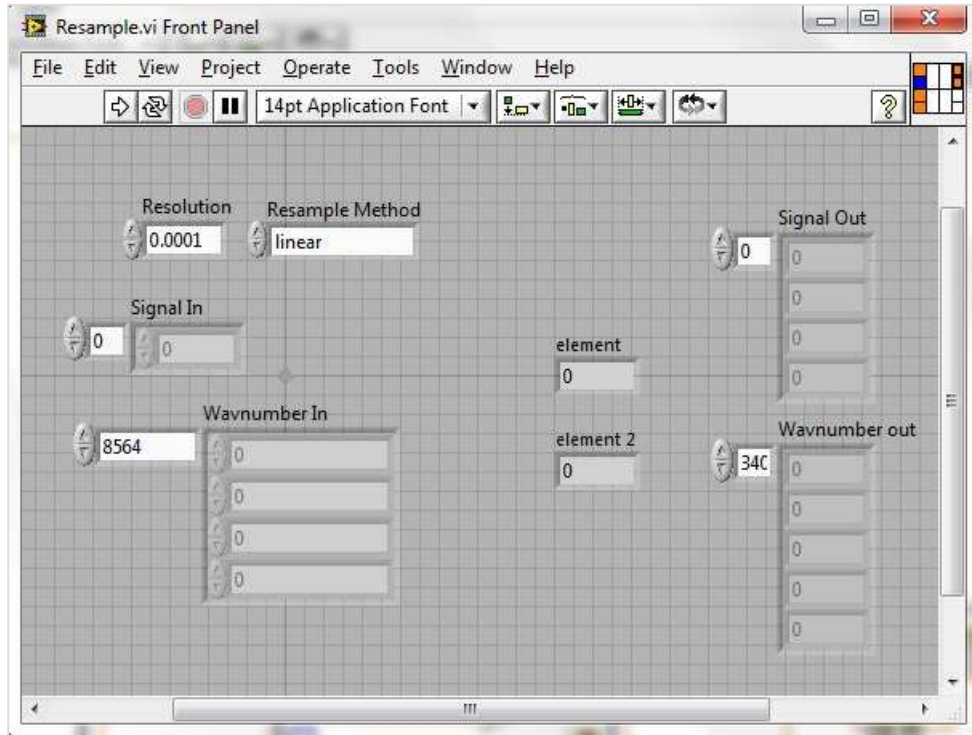


Figure 4-2: Front panel of the program Resample.vi.

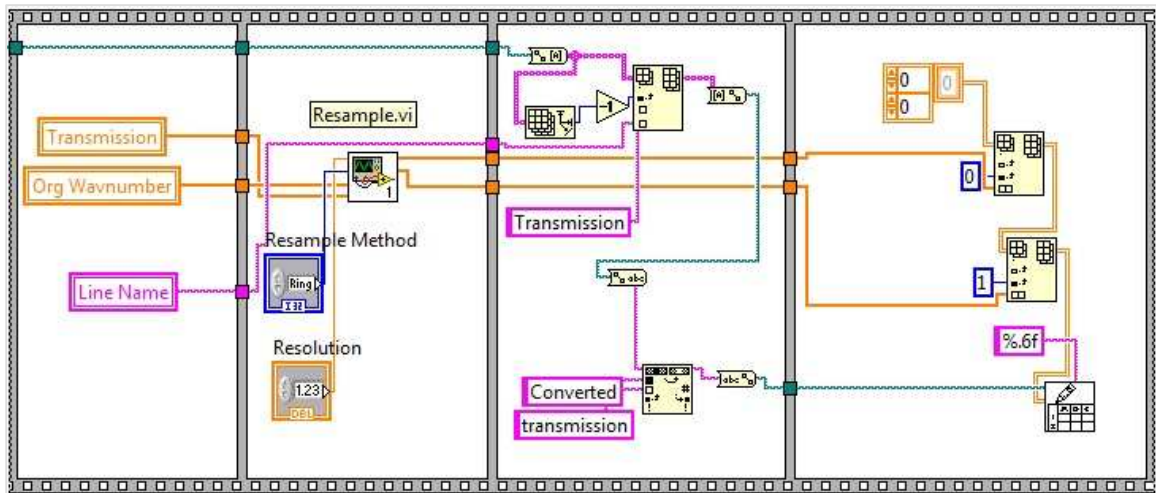


Figure 4-3: Example of Resample.vi being used as a sub VI within another program. The inputs and outputs correspond directly to the ones marked in the upper right corner of Figure 4-2.

The “Block Diagram” of the program Resample.vi is shown in Figure 4-4. The block diagram is the place where the program is executed and edited to function properly. In this view the user can wire up all the controls and indicators to perform the desired operations. This view contains all the programming commands and sequence of code that tells the program what to do. When a program is run, the data will pass in the diagram from left to right executing sub-VIs and program structures once they have received all the necessary data to execute.

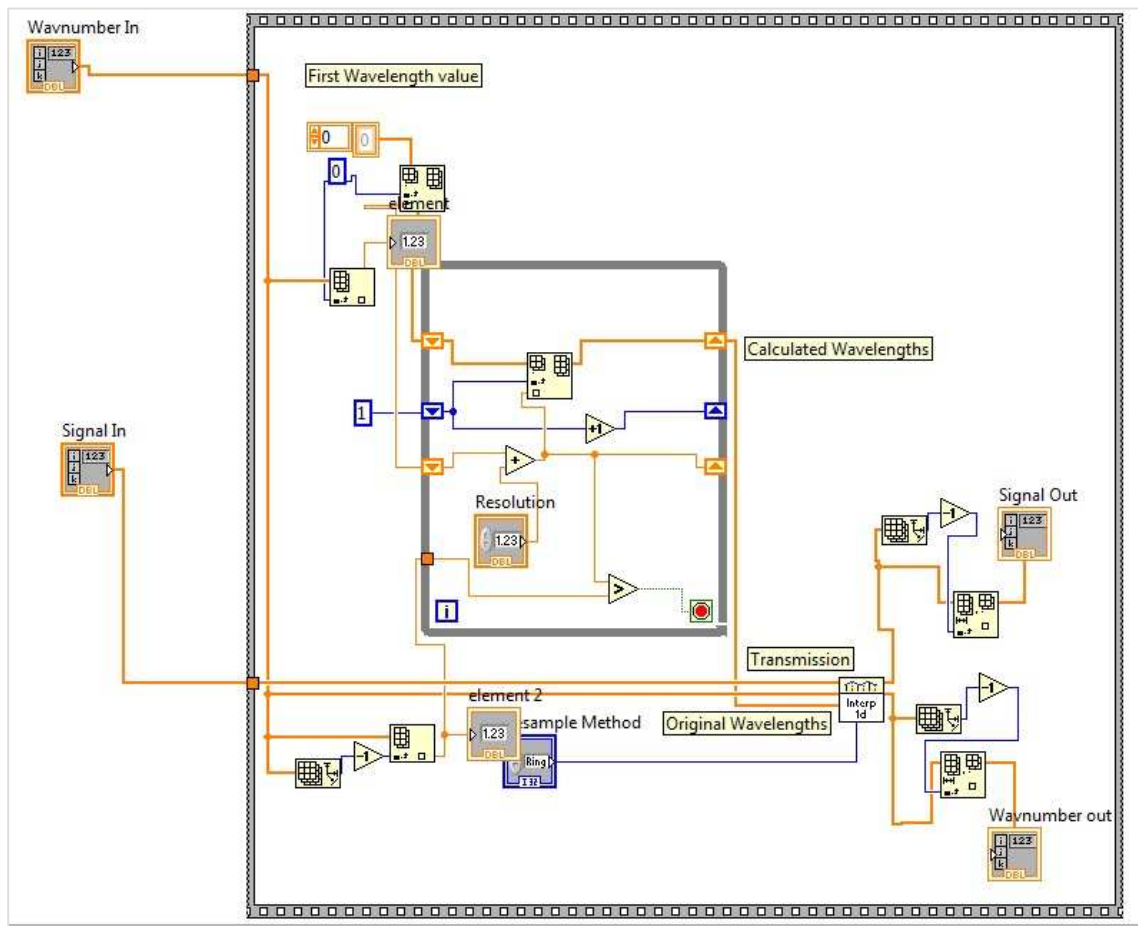


Figure 4-4: Block diagram of the program Resample.vi.

Another unique feature to Labview is the use of what are known as “Clusters”. A cluster can either be an indicator or a control and can contain within it many different data types. This means that it can contain arrays, variables, and Boolean data types. An example of both an indicator and a control cluster is shown in Figure 4-5. Clusters allow for many controls and indicators to be wired or to be passed between other VIs, in a much more efficient way, thus making the block diagram more manageable to work with.

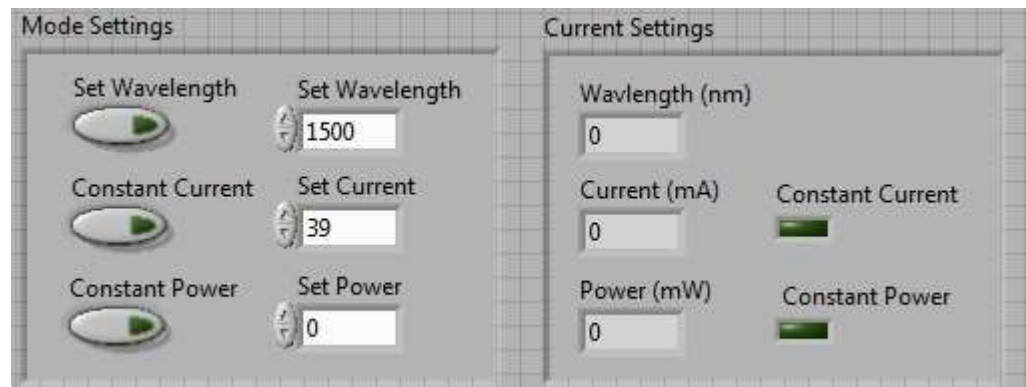


Figure 4-5: Example cluster from VelocityController.vi. On the left “Mode Settings” is the control cluster and on the right “Current Settings” is the indicator cluster.

4.3. Spectrometer Control Software

4.3.1. VelocityController.vi

The main VI used to operate and measure spectra with the tunable diode laser system is labeled “VelocityController.vi”. A screen shot of the front panel is shown in Figure 4-6. This program contains four main control boxes and two methods for scanning spectral features.

The first control box “Laser Startup and Settings” allows the user to turn on the laser using the “Laser Head Power” button. The large green indicator remains lit while the laser is working. The “Scan” button is used to record spectra once an experiment has

been setup and the system is ready. The “Check Signal” button allows the user to read the signal being measured on “Detector Input” located within the “I/O settings” cluster. This feature allows for verification of the instruments alignment prior to completing a scan. The cluster “Mode Settings” allows the user to adjust the current wavelength of the laser system by typing a wavelength in the “Set Wavelength” control then pressing the “Set Wavelength” button once the lasers wavelength has been set. The cluster “Current Settings” will update showing the set wavelength in the “Wavelength” indicator. In much the same way, the user can choose to use either the constant power or constant current mode by first entering a current or power in the appropriate control box then pressing the appropriate button. Upon pressing the button, the current or power will be set and then the readings from the laser will be displayed in the “Current Settings” cluster indicating the wavelength, current, power and operating mode.

The second control box named “Temperature and Pressure” is used to tell the system how many temperature and pressure readings to record before and after each scan of the piezo device inside the laser head. By changing the “Number of Samples”, the user can alter how many readings are obtained before and after a piezo scan (piezo scans are discussed in Section 3.2.3). The “MKS 2 Range” allows the user to properly scale the readings produced by the MKS 270B signal conditioner and Agilent voltmeter.

Next, the control box labeled “Wavelength Scan Settings” is used to setup the range and resolution of the piezo scans that will be performed. The piezo settings are determined by the cluster “Settings”. Within this cluster the control “Voltage Step Size” is used to communicate to the laser system at what voltage interval spacing the piezo will be ramped. Next, the “Max Voltage” and “Min Voltage” controls define the range of the

signal to output to the laser's piezo controller. These three controls together determine the starting voltage of the piezo followed by the number of steps that will be taken to get to the max voltage of the piezo inside the laser head. The end result will be a high precision control over the spectral range and resolution of a completed scan. The control labeled "Fabry Cavity bias" is generally left at zero but is used to make sure that the piezo electric device within the Fabry Perot cavity is always in the same position. Finally, the two controls labeled "Max Wavelength" and "Min Wavelength" are only needed when "Scan Type" is set to "Range" (See Section 4.3.2)

The cluster "I/O Settings" is a control used to set the input/ output channels for all of the analog signals that are read and written during a scan of laser system. The cluster "Channel Inputs" contains RS232 inputs for use with the wavemeter and power meter (though the power meter is very rarely used).

The final section "Wavemeter Settings" is used to control the settings of the wavemeter. Before a scan is performed, the wavemeter is initialized to the settings contained within the "Wavemeter Settings" cluster. After initializing the settings, the wavemeter is queried about its current status which is then returned to the cluster "Display LEDs".

4.3.2. How spectra are measured

The type of scan technique can be selected by the user using the front panel control labeled "Scan Type" on the VelocityController.vi. Two options are available with this control, the first one is called "Range" (shown in Figure 4-6). When "Range" is selected the laser will scan through the range of wavelengths bound between the user-

defined Max and Min wavelength controls found within the settings cluster (shown in Figure 4-6). A single piezo scan will be recorded for each center wavelength starting with the “Min Wavelength”. Once the first scan is completed, the center wavelength of the laser is shifted by 0.25 nm, then another scan is performed. This process is repeated until the “Max Wavelength” has been reached.

The second scan type is called “Line by Line”. For this scan type the user must input a set of spectral lines that they wish to measure. These lines are input by selecting the “Change Lines” button. Once this button has been selected, a sub-VI will open that will allow the user to adjust what spectral lines and line positions are displayed in the “Line Locations” cluster shown in Figure 4-6. Once the user defined lines have been entered the scan button can be pressed. When the scan begins it starts a feedback loop with the laser and the Wavemeter to find the first line position in the list. Once the line position is found, a user defined number of piezo scans are performed. By default, the program is set to complete four piezo scans for one spectral line (this is done with a “for” loop and can be altered by changing the constant wired to the loop within the “SCANFP.vi”). Each one of the four piezo scans is slightly shifted from each other by 0.2 nm (this can also be altered within the “SCANFP.vi”) to guarantee that there is an adequate amount of baseline within the recorded spectra (this feature is more important when completing scans of higher pressure spectra as the lines can become quite broad).

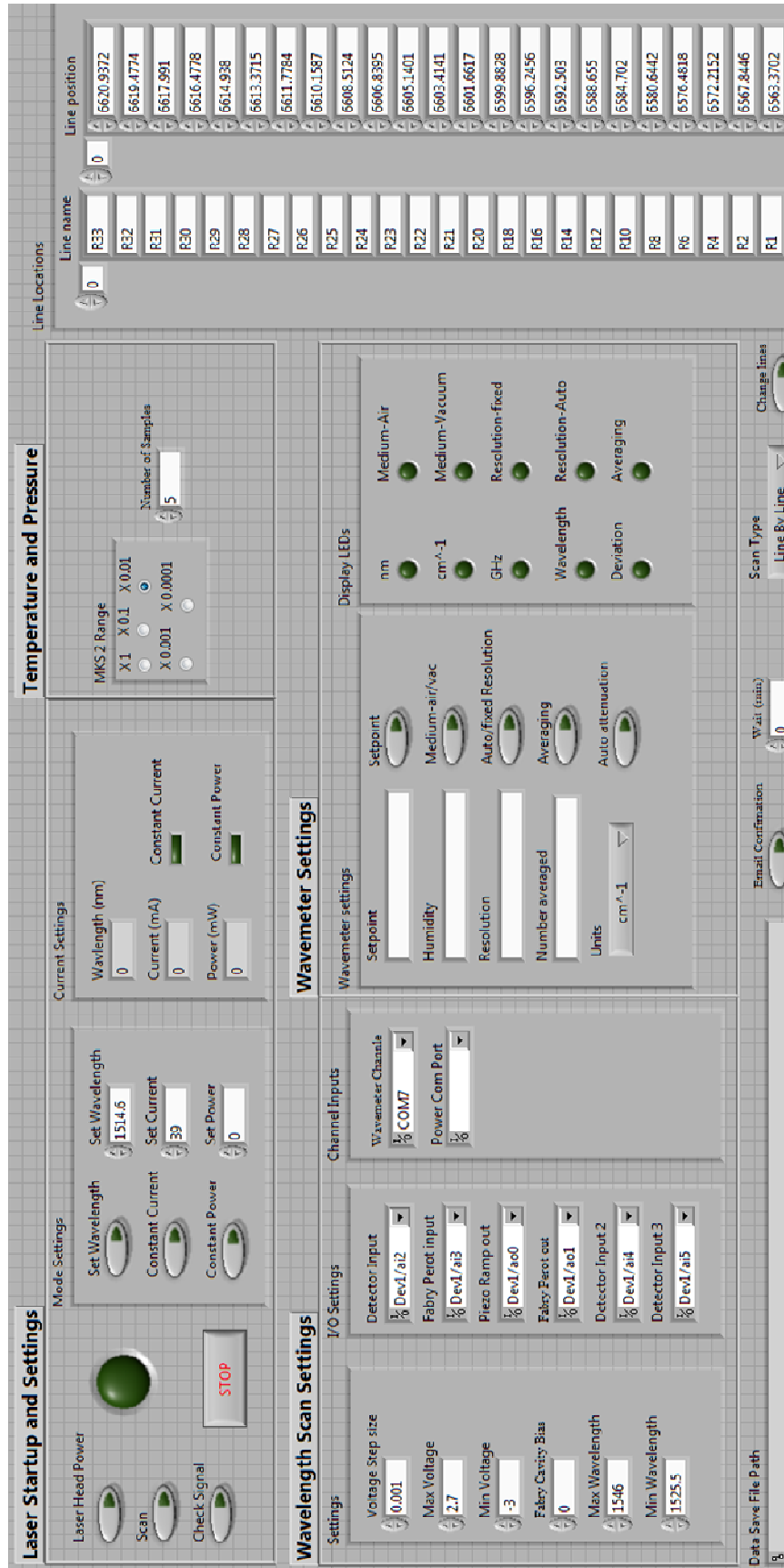
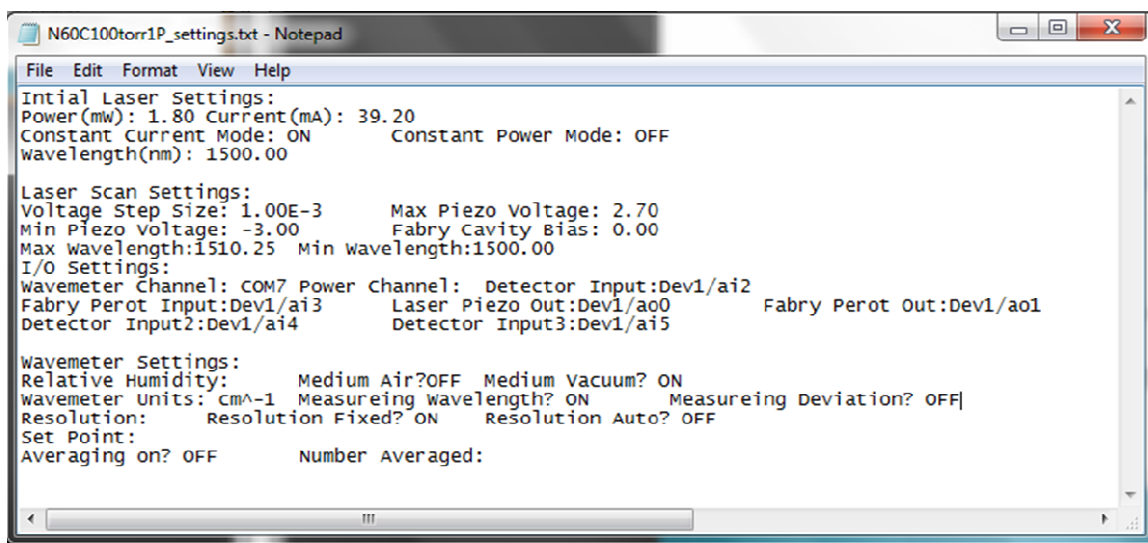


Figure 4-6: Front panel of the VI "VelocityController.vi"

4.3.3. Data generated during scans

When the scan button is pressed, the program will ask for a file name. The user can specify the file name they wish to use, i.e., “user.txt” (the file name “user” will be used throughout the rest of this section to describe what the user has put in for a file name). Most often, the file name will contain the information on the pressure and temperature of the experiment that is performed. After the user defined file name has been entered, a “Settings” file with the name “user_Settings.txt” will be created. The user defined name is a prefix with the tag “Settings” added to it. This technique is employed to simplify file management during the analysis phase. The “Settings” file will contain information about the settings of the scan being performed, an example of the file is shown in Figure 4-7.



```
File Edit Format View Help
Initial Laser Settings:
Power(mw): 1.80 Current(mA): 39.20
Constant Current Mode: ON      Constant Power Mode: OFF
wavelength(nm): 1500.00

Laser Scan Settings:
Voltage Step Size: 1.00E-3      Max Piezo Voltage: 2.70
Min Piezo Voltage: -3.00      Fabry Cavity Bias: 0.00
Max Wavelength:1510.25  Min wavelength:1500.00

I/O Settings:
Wavemeter Channel: COM7 Power Channel: Detector Input:Dev1/ai2
Fabry Perot Input:Dev1/ai3      Laser Piezo Out:Dev1/ao0      Fabry Perot Out:Dev1/ao1
Detector Input2:Dev1/ai4      Detector Input3:Dev1/ai5

Wavemeter Settings:
Relative Humidity:      Medium Air?OFF  Medium Vacuum? ON
Wavemeter Units: cm^-1  Measuring Wavelength? ON      Measuring Deviation? OFF
Resolution:      Resolution Fixed? ON      Resolution Auto? OFF
Set Point:
Averaging on? OFF      Number Averaged:
```

Figure 4-7: Example of the “Settings” file written after the scan button has been pressed.

Once the “Settings” file has been written, the program will start the “SCANFP.vi” sub VI. Inside this VI another file referred to as “user/TPfile.txt” is created to write the pressure and temperature of each individual piezo scans completed (the “/” here denotes a separation of how the name is written and does not appear in the actual name of the file). Normally the program is setup to record 5 pressures and temperatures before the piezo scan and 5 temperatures and pressures after the piezo scan is completed. If the default value of 5 is changed, this may cause problems in the analysis software and should be done with caution. In this file, the before and after measurements are denoted as “Before: center wavelength” and “After: center wavelength” where the center wavelength refers to the current central wavelength that the laser system is set to. This step is very important as the center wavelength is also used to define the file names of the spectral files recorded, thus providing a reference to the recorded data. An example of the “TPfile” is shown in Table 4-1 (as a note the column for Pirani contains no information as this function is no longer used). In the table, the temperature sensors 1, 2 and 3 directly match the sensors 1, 2 and 3 seen in Figure 3-17, and sensors 5 and 6 from the table match sensors 4 and 5 respectively from Figure 3-17. The sensors 4, 7 and 8 from Table 4-1 are not currently in use and the value of 22.46 °C seen on sensor 7 is just the default value.

Table 4-1: Example of five measurements of pressure and temperature as they are recorded in the “TPfile”. The grey row indicates what each column denotes but these headings do not actually appear in the written file.

Before: 1500.000000

Time stamp	Pressure CH1 (Torr)	Temperature Sensors (°C)								Pirani (V)	Pressure CH 2 (Torr)
		1	2	3	4	5	6	7	8		
01/08/2010 16:12	90.93	-59.56	-60.58	-59.75	0	-59.54	-60.13	22.46	0	-0.98	5.105
01/08/2010 16:12	90.93	-59.56	-60.57	-59.75	0	-59.54	-60.14	22.46	0	-1.05	5.105
01/08/2010 16:12	90.93	-59.56	-60.57	-59.75	0	-59.54	-60.14	22.46	0	-1.08	5.105
01/08/2010 16:12	90.93	-59.56	-60.58	-59.75	0	-59.54	-60.13	22.46	0	-0.72	5.105
01/08/2010 16:12	90.93	-59.56	-60.57	-59.75	0	-59.54	-60.13	22.46	0	-0.02	5.105

Once the 5 values have been recorded for the pressure and temperature of the scan, the sub-VI “FabryPerot.vi” executes and generates two other files. The first “user/linename/Peak/wavelengthcenter.txt” file records the peak positions observed with the Fabry Perot cavity. For the very first Peak detected, the wavenumber is recorded. An example of the “Peak” file is given in Table 4-2. Only the first wavenumber in the file is correct and the remaining peaks have to be corrected during the analysis phase (see Section 4.4.2).

The second file generated is the “user/linename/Spectra/wavelengthcenter.txt” file (the line name will only be added when the scan type “line by line” is used). This file contains the recorded signal for all the incoming signals recorded as the piezo is ramped. Table 4-3 shows a small section of a “Spectra file”. The errors that appear in the table are the standard deviations of the recorded signals as 100 measurements on each channel are made, then they are averaged.

Using these four files allows a comprehensive analysis to be completed. The next section will discuss how these files are processed into transmission spectra that can be analyzed with spectroscopic software.

Table 4-2: Example of the “Peak” file created in the sub VI “FabryPerot.vi”. Once again the first row in grey indicates what each column represents but is not present in the file when it is written. The file name for this example is “test1P21Peak1537_819415.txt”.

Fabry Perot Voltage (V)	Wavenumber (cm ⁻¹)	Wavenumber error
0.545633	6502.96	0.0005
0.424167	6502.96	0
0.114282	6502.96	0
0.606192	6502.96	0
0.324634	6502.96	0
0.454532	6502.96	0
0.57236	6502.96	0
0.349399	6502.96	0
0.335056	6502.96	0
0.392093	6502.96	0
0.285577	6502.96	0
0.647052	6502.96	0
0.111749	6502.96	0

Table 4-3: Example of “Spectra” file created in the sub VI “FabryPerot.vi”. The first row in grey indicates what each column represents but is not present in the file when it is written. Here CH 1 refers to the voltage reading on the channel 1 photodiode, CH 2 refers to the voltage reading on the channel 2 photodiode, FP is the voltage of the Fabry Perot cavity, Piezo Voltage is the voltage being applied to the back of the laser system, and BG is the voltage reading from the background photodiode. The name for this example file is “test2P21Peak1537_856453.txt”

Piezo Voltage	CH 1 (V)	error	FP (V)	error	CH 2 (V)	error	BG (V)	error
-2.885	-6.795	0.012	-0.008	0.002	-5.549	0.011	-5.763	0.012
-2.884	-6.798	0.015	-0.001	0.003	-5.548	0.013	-5.765	0.013
-2.883	-6.791	0.014	0.002	0.003	-5.547	0.012	-5.761	0.012
-2.882	-6.798	0.016	0.013	0.008	-5.550	0.013	-5.766	0.013
-2.881	-6.799	0.016	0.035	0.007	-5.551	0.013	-5.767	0.014
-2.880	-6.797	0.018	0.050	0.005	-5.551	0.016	-5.765	0.015
-2.879	-6.798	0.014	0.070	0.021	-5.549	0.013	-5.767	0.012
-2.878	-6.797	0.017	0.151	0.118	-5.552	0.014	-5.767	0.014
-2.877	-6.794	0.015	0.232	0.172	-5.547	0.014	-5.763	0.014
-2.876	-6.801	0.015	0.510	0.168	-5.551	0.014	-5.769	0.013
-2.875	-6.799	0.015	0.619	0.114	-5.552	0.013	-5.766	0.013
-2.874	-6.800	0.012	0.266	0.174	-5.549	0.011	-5.767	0.011
-2.873	-6.798	0.017	0.026	0.025	-5.553	0.015	-5.767	0.014
-2.872	-6.800	0.014	-0.003	0.007	-5.552	0.013	-5.768	0.013
-2.871	-6.796	0.017	-0.010	0.002	-5.549	0.015	-5.766	0.015

4.4. Preparing Transmission files

4.4.1. Introduction

Figure 4-8 shows the general process for recording and processing spectra using the tunable diode laser spectrometer. The upper portion of the figure was discussed in the previous section defining the four files “Peak”, “Spectra”, “TPfile” and “Settings”. In this section the focus will be on describing what takes place for the remaining steps shown in the figure and a discussion of the subsequent VIs that are used to process the raw data.

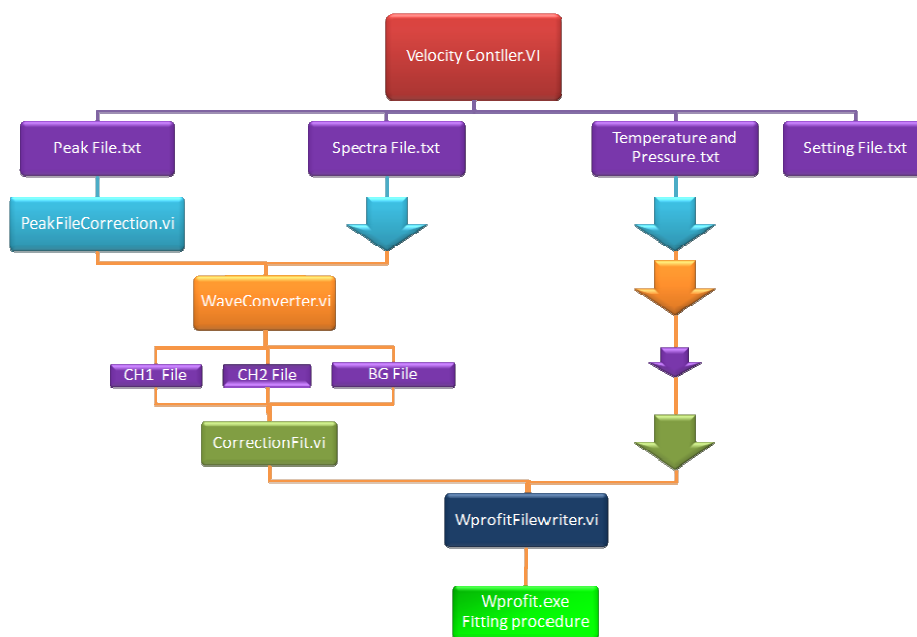


Figure 4-8: Example of the file Hierarchy used to complete the analysis of recorded transmission spectra. The purple boxes denote text files that are created during the process.

4.4.2. Generating the wavenumber scale

There are two programs required to generate a wavenumber scale that can be used to analyse the spectra. The first one is the program “PeakFileCorrection.vi” and is shown in Figure 4-8. This program will take the “Peak” file and correct it by using the first peak

recorded in it (The first peak is recorded from the wavemeter directly) along with the known fringe spacing of the Fabry Perot cavity (0.05cm^{-1} Section 3.3.4) and will assign a wavenumber to each peak in the file..

The second program, “WaveConverter.vi”, then uses the corrected “Peak” file and the “Spectra” file to create three new files called “Converted_CH1”, “Converted_CH2” and “Converted_BG” for the spectra recorded on channel 1, channel 2 and the background, respectively. For each file, the program uses the information in the “Peak” file and the Fabry Perot signal from the “Spectra” file to identify the number of data points between successive peaks. Once the number of data points is known, then the fringe spacing divided by the number of points will give the resolution for that portion of the file. Knowing the wavenumber spacing between each data point and the starting wavenumber, the program then generates all the wavenumbers for that region of the spectra. The program will iteratively do the same for each set of fringes in the file, until it has calculated a wavenumber for each data point.

This approach will generate a wavenumber scale with varying resolution as the sampling rate remains constant. The number of points between peaks changes with the piezo voltage (nonlinear correlation between wavenumber and piezo voltage). However, the analysis software used requires evenly spaced data points (constant resolution). Therefore, in the next step a resampling technique that was used in the generation of the transmission spectra is discussed.

4.4.3. Generating Transmission Spectra

The next step shown in Figure 4-8 uses the “CorrectionFit.vi” shown in Figure 4-11. This program will generate a “Transmission” file out of the “Converted” files described in the previous section. To create the transmission file the baseline is compared between the spectra recorded on channel 1 or 2 with that of the background channel. An example of an original channel 1 and background are shown in Figure 4-9. From the figure it can be seen that the background channel that is recorded has a slightly different signal as compared to what is observed on channel 1. To correct for this, the spectral features are cut from the channel 1 data. An example of how this looks like is presented in Figure 4-10. Next, using these two signals, a residual is calculated between the two spectra as follows:

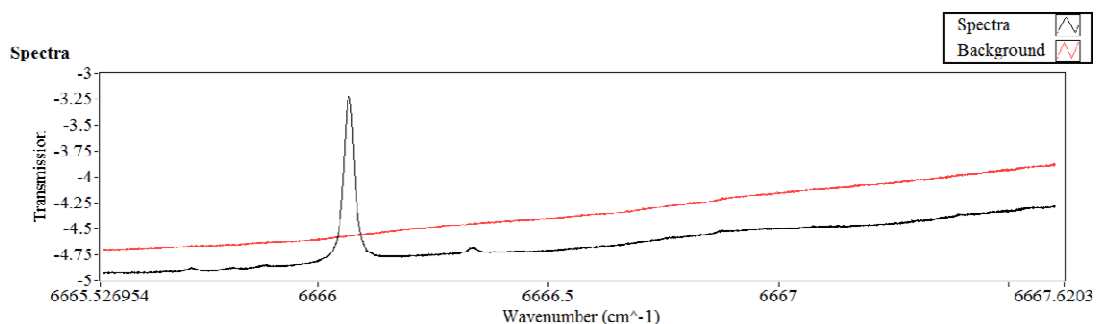


Figure 4-9: Recorded spectra of the R(19) transition in the $\nu_1+\nu_2+\nu_4+\nu_5$ band of acetylene.

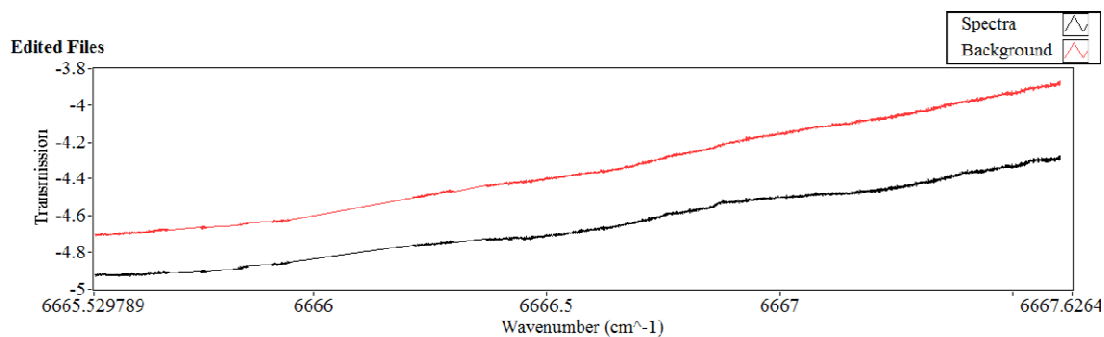


Figure 4-10: Example of how the spectra in Figure 4-9 is edited to remove the spectral features to allow for background correction to be completed.

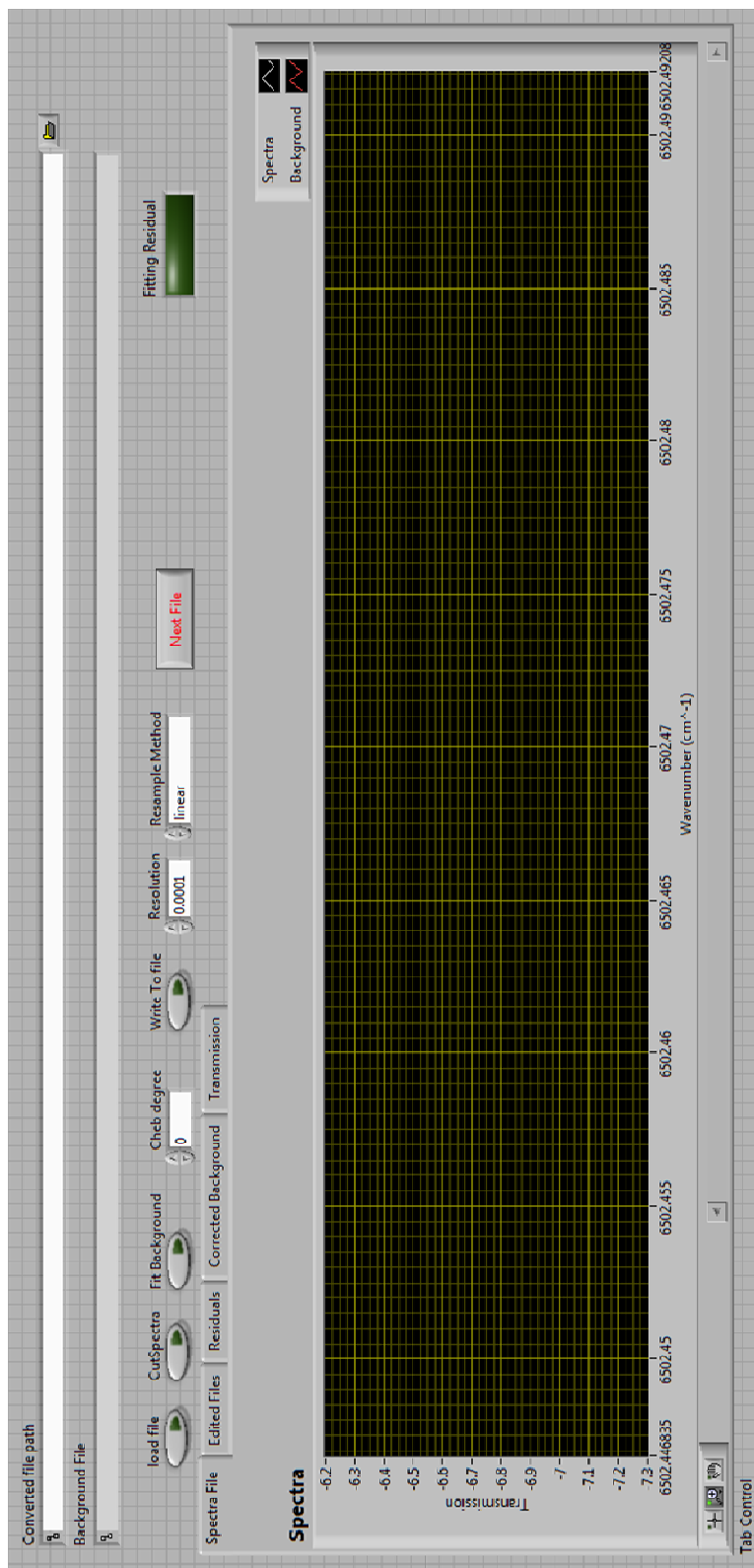


Figure 4-11: Screen shot of the “CorrectionFit.vi” program used to produce transmission files.

$$\text{residual} = \text{Channel1 baseline} - \text{Background}. \quad 4-1$$

The *Channel1 baseline* refers to the spectra measured in channel 1 with the lines cut from the file. An example of what this residual looks like is shown in Figure 4-12.

Next, a *Chebyshev* polynomial (the degree of the polynomial is determined by the user) is fit to the residual. Figure 4-12 shows an example of this type of fit being completed on the residual signal generated from Figure 4-10. Once the best order of Chebyshev polynomial is identified, it is used to correct the channel 3 background signal in the following way.

$$\text{Cheb Poly} + \text{background} = \text{Corrected baseline}. \quad 4-2$$

Figure 4-13 shows the corrected baseline in relation to the recorded spectra on channel 1. Finally, the corrected baseline is then used to divide the channel 1 or 2 raw spectra by the background to obtain a transmission spectral file. Figure 4-14 shows the final result of this process.

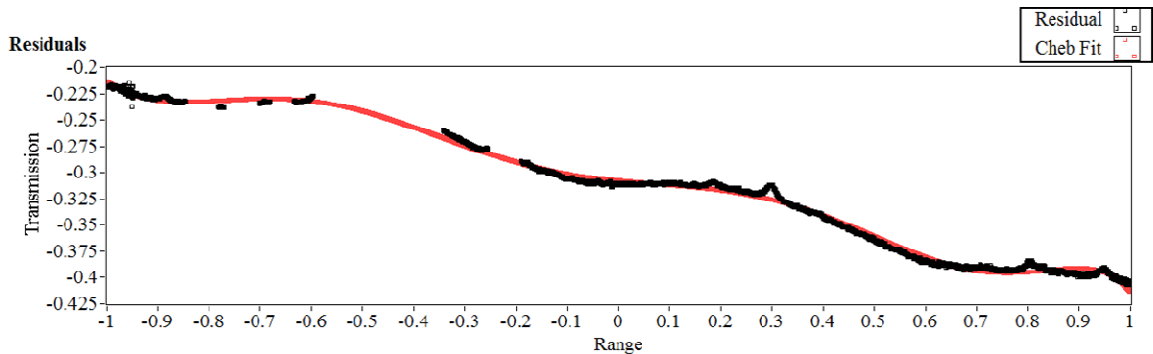


Figure 4-12: Example of an 8th order Chebyshev polynomial fit to the residual of the spectra shown in Figure 4-10. (Range here denotes the values between -1 to 1 as defined for a Chebyshev polynomial.)

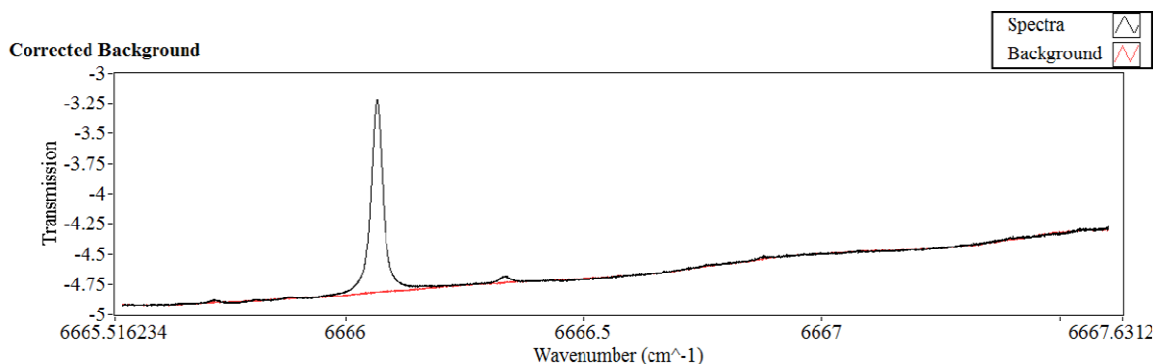


Figure 4-13: Example of the corrected background relative to the channel 1 spectra recorded.

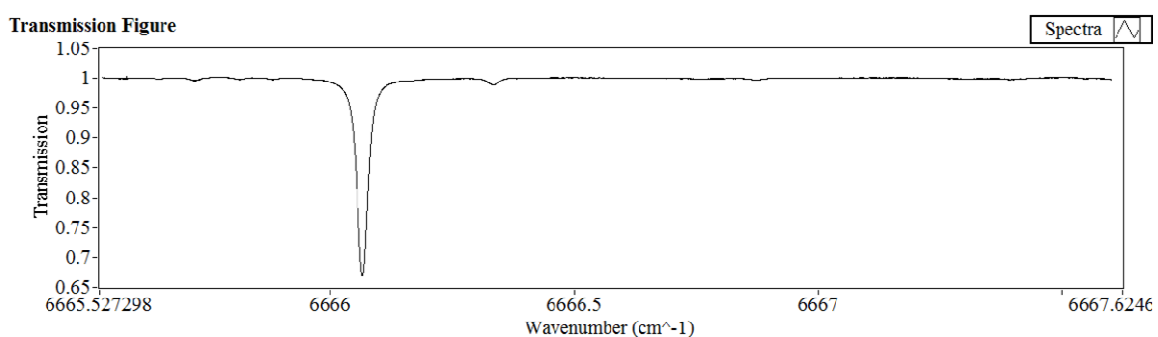


Figure 4-14: Final transmission spectra produced by the “CorrectionFit.vi” program.

Once the correction has been made and verified to be adequate by the user it can be saved by clicking on the “write to file” button shown in Figure 4-11. When this button is pressed, a new file called “Transmission” is created. The original spectrum in the file is re-sampled using a linear interpolating function in order to produce a transmission spectrum with equally spaced points in the wavenumber domain, as it is required by the analysis software used.

4.4.4. Calibrating the spectra

To allow for the use of multispectral analysis each spectrum must be guaranteed to be similar. This similarity is obtained by calibrating each spectra’s wavenumber scale. Figure 4-15 A shows three spectra recorded at the same temperature but different pressures. It is clear from the figure that each piezo scan of the laser system has generated

its own unique wavenumber scale. Therefore, to correct this scale, the wavenumber scale must be calibrated in some way. The process of calibrating the wavenumber scale is completed by performing a spectral analysis on the channel 2 spectra. These spectra are recorded at room temperature and at lower pressures to reduce the effects of pressure induced shifts. By fitting the line positions for the transitions of interest, a simple difference calculation can be made with the line positions found in HITRAN08 [21]. This difference is then used to shift the channel 1 spectra accordingly. The shifting of the spectra is handled by the VI “ShiftCall.vi” and requires the channel 1 transmission file and an output file from the “Wprofit.exe” program for channel 2 (which will contain within it the fit line position obtained for channel 2) to complete the calibration. This procedure guarantees that each spectrum recorded is centered to the same calibrated line position, allowing for the use of multispectral analysis. Figure 4-15 B shows the same spectra in A after they had the wavenumber scale corrected in this way. It is clear from this figure that the spectra are now centered about the calibration point. It is important to note that this technique guarantees that the measurements of pressure-induced shifts are accurate but at the expense of being able to determine individual line positions with a high accuracy.

The accuracy of the line positions obtained from channel 1 is completely dependent upon the accuracy for transitions of interest in HITRAN08. This makes this technique not very useful for obtaining accurate line positions.

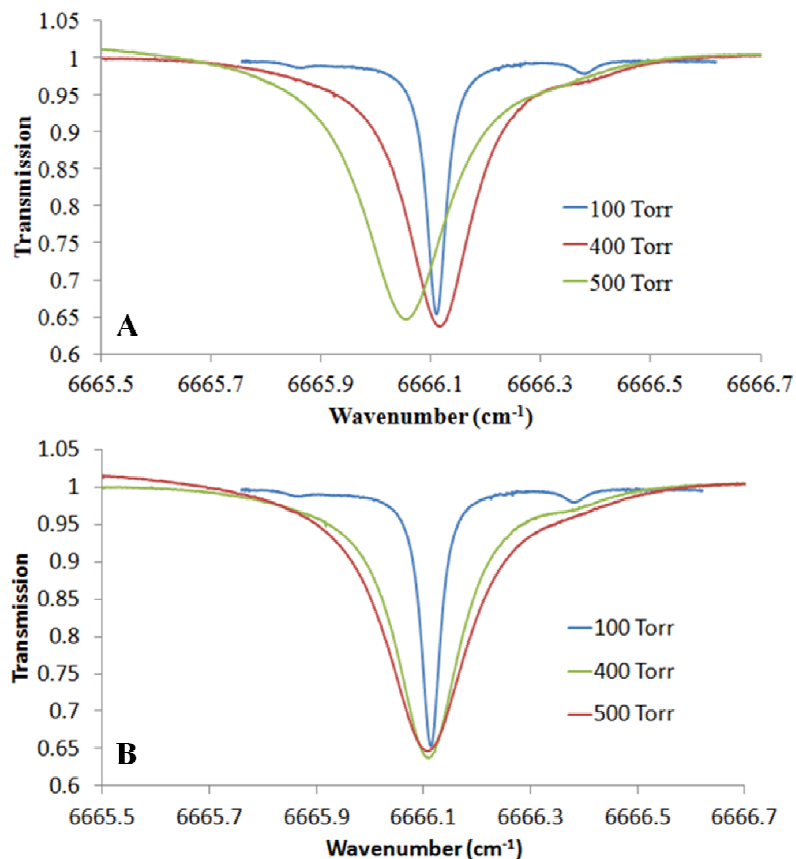


Figure 4-15: The R(19) Transition in the $\nu_1+\nu_2+\nu_4+\nu_5$ band of acetylene at 213 K showing (A) the channel 1 spectra before being corrected by channel 2 fits, and (B) the channel 1 spectra after being corrected by channel 2 fits.

4.5. Conclusion

The detailed description of the software used in these investigations and given in this Chapter was to show the various steps required to obtain a transmission spectrum for later analysis. In order to perform high-resolution studies on spectral line parameters it is important that multiple spectra be processed simultaneously. First correcting the background spectrum and then calibrating the wavenumber scale ensures that each unique spectrum recorded by the laser system can be analysed using the weighted multispectrum analysis software developed by Dr. Daniel Hurtmans [87] and made available to our group.

Chapter 5: Line Mixing Effects in Carbon Dioxide

5.1. Introduction

In this chapter the results from the study “*Computations of temperature dependences for line shape parameters in the 30012 <- 00001 and 30013 <- 00001 bands of pure CO₂*” published in the Journal of Molecular Spectroscopy [88] will be presented. The following sections will discuss the results reported in Ref. [88] with editorial changes for clarity and flow of the text.

5.2. Line-mixing analysis

5.2.1. Introduction

Currently, most of the laboratory spectral retrieval models are based on the sum of independent Voigt profiles describing each transition. Recent studies [31-35], have suggested the need to go beyond this approach, even for vibrational bands such as the two Fermi bands presented here. Therefore, speed-dependent broadening and line mixing effects of the spectral lines should be taken into consideration [31-34].

Prior to the spectroscopic studies presented in [31-35], the primary focus on most studies involving line mixing in carbon dioxide was on the Q-branches [89-97], because of the great difficulties in the retrievals of atmospheric temperature profiles. Several different theoretical models have been used to model line mixing, including semi-classical calculations [92], empirical models [98], first principle computations based on models for the intermolecular potential [99], models based on fitting laws [93, 100],

models based on a formalism for adjustable inter-branch coupling for line mixing effects [101, 102], and models based on scaling laws [33, 35, 93, 95-97, 103]. The line shape modeling based on the Energy Corrected Sudden approximation (ECS) has been used in several previous studies of line mixing in CO₂ [27, 33, 35, 94, 97, 104-108].

In this study the broadening and first order line mixing parameters for over 100 transitions in the 30012←00001 and 30013←00001 bands of carbon dioxide were calculated. The calculations were performed over the 193 to 323 K temperature range for pure CO₂ and lean mixtures of CO₂ and air. The elements of the relaxation matrices were calculated at the appropriate physical conditions using the Exponential Power Gap (EPG) and Energy Corrected Sudden (ECS) scaling laws as presented in Section 2.6. The calculated low pressure line-mixing parameters and the broadening coefficients have been compared with experimental results from two previous studies [33, 35] available at 217, 234, 258 and 296 K. At all temperatures, the calculated broadening coefficients were also compared with those available in the HITRAN08 database [21].

5.2.2. Exponential Power Gap calculations for rotational transfer

The spectroscopic analysis was completed using two different datasets. The first set was based on self- and air-broadened line parameters from the HITRAN08 [21] database calculated in steps of 10 K at temperatures between 193 and 323 K. The second dataset was based on self- and air-broadened experimental line broadening and line mixing results at 217, 234, 258, and 296 K presented in Refs. [35] and [109]. The temperature dependence coefficients for air- and self-broadening reported in these studies were used to extrapolate the broadening coefficients at intermediate temperatures

between 193 and 323 K. In total, there were self- and air-broadening coefficients available at 13 distinct temperatures.

The room temperature self- and air- line parameters from the two datasets were fitted using equations 2-86 and 2-88 to determine the room temperature values for the parameters a_o , b_o , c_o , and β , that best reproduce the broadening coefficients. A non-linear fitting program written in Matlab was used to minimize the difference between the experimental self- and air-broadening coefficients and the calculated ones given by equation 2-89. As suggested in Section 2.6.3, the value $\beta = 0.56$ was used for all calculations. These room temperature adjustable parameters are summarized in Table 5-1 and Table 5-2. It can be noticed that the values obtained for the same parameter for R and P branch transitions are very close. Note that there are very small differences between the adjustable parameters obtained using experimental data and those obtained using line parameters from the HITRAN08 database. The goodness of the fit results was checked over all available transitions [40] using the sum rule:

$$\sum_j S_j * Y_{oj}(T) = 0, \quad 5-1$$

where S_j are the line strength parameters and Y_{oj} are the line mixing coefficients calculated using equation 2-91 and the sum is over all possible transitions. The calculated values for this sum rule are reported in the last columns of Table 5-1 and Table 5-2. The fact that they are not null values indicates that there is a lack of information on line parameters with very high J values.

Table 5-1: Room temperature values for the adjustable Exponential Power Gap law (EPG) parameters for pure CO₂ at 296 K in the 30013←00001 and 30012←00001 bands.

Band	Branch	a ($\times 10^{-2}$)	Error a	b ($\times 10^{-1}$)	Error b	c	Error c	Sum rule ($\times 10^{-25}$)	Ref. #
30013←00001	P	5.32	9.41×10^{-6}	2.77	4.39×10^{-5}	1.21	5.61×10^{-5}	1.30	[109]
30013←00001	R	5.03	8.82×10^{-6}	2.70	3.92×10^{-5}	1.21	5.11×10^{-5}	-1.93	[109]
30012←00001	P	5.47	3.16×10^{-9}	2.85	1.04×10^{-8}	1.20	4.84×10^{-8}	1.31	[109]
30012←00001	R	5.51	1.02×10^{-9}	2.90	3.33×10^{-9}	1.19	1.52×10^{-8}	-2.00	[109]
30013←00001	P	4.94	9.00×10^{-9}	2.61	3.28×10^{-8}	1.22	1.54×10^{-7}	1.28	[21]
30013←00001	R	5.01	9.98×10^{-6}	2.67	4.47×10^{-5}	1.21	5.64×10^{-5}	-1.94	[21]
30012←00001	P	4.94	2.85×10^{-9}	2.61	1.04×10^{-8}	1.22	4.88×10^{-8}	1.30	[21]
30012←00001	R	5.01	9.15×10^{-8}	2.67	3.29×10^{-7}	1.21	1.52×10^{-6}	-1.98	[21]

Table 5-2: Room temperature values for the adjustable Exponential Power Gap law (EPG) parameters for CO₂ broadened by air at 296 K in the 30013←00001 and 30012←00001 bands.

Band	Branch	a ($\times 10^{-2}$)	Error a	b ($\times 10^{-1}$)	Error b	c	Error c	Sum rule ($\times 10^{-25}$)	Ref. #
30013←00001	P	3.97	8.95×10^{-9}	2.90	3.88×10^{-8}	1.07	1.38×10^{-7}	0.95	[35]
30013←00001	R	3.91	8.91×10^{-10}	2.91	3.91×10^{-9}	1.06	1.37×10^{-8}	-1.44	[35]
30012←00001	P	3.97	8.94×10^{-10}	2.90	3.87×10^{-9}	1.07	1.37×10^{-8}	0.96	[35]
30012←00001	R	3.85	8.74×10^{-9}	2.86	3.89×10^{-8}	1.07	1.37×10^{-7}	-1.46	[35]
30013←00001	P	3.98	8.98×10^{-9}	2.91	3.87×10^{-8}	1.07	1.38×10^{-7}	0.95	[21]
30013←00001	R	3.84	2.76×10^{-10}	2.86	1.23×10^{-9}	1.07	4.33×10^{-9}	-1.43	[21]
30012←00001	P	3.98	8.98×10^{-10}	2.91	3.87×10^{-9}	1.07	1.38×10^{-8}	0.96	[21]
30012←00001	R	3.84	8.67×10^{-9}	2.86	3.87×10^{-7}	1.07	1.36×10^{-6}	-1.46	[21]

The temperature dependence of the collisional rates was determined using the following temperature dependence for the parameter a :

$$a(T) = a_0 \left(\frac{T_0}{T} \right)^n \quad 5-2$$

In Table 5-3 and Table 5-4 the self-broadened results are presented for the n parameter obtained by keeping a_0 , b_0 , and c_0 fixed to the values given in Table 5-1. The corresponding air-broadened values obtained keeping the a_0 , b_0 , and c_0 values fixed to the values given in Table 5-2 are reported in Table 5-5 and Table 5-6. The last row of each table contains the average values for n over the range of temperatures 193 to 323 K.

Figure 5-1 shows overlaid measured and calculated air-broadening parameters using the Exponential Power Gap law (EPG) plotted against m , where $m = -J$ for P-branch transitions and $m = J+1$ for R-branch transitions. The results correspond to transitions in the 30012←00001 band of carbon dioxide. As the plots show, the EPG fitting law does not model successfully the entire range of rotational states. For average $|m|$ values it provides a good agreement with the experimental results. However, a quick look at Figure 5-2 shows that the air-line mixing coefficients calculated using the EPG model offer a good agreement with the experimental room temperature line mixing values obtained independently by two different groups [32, 33].

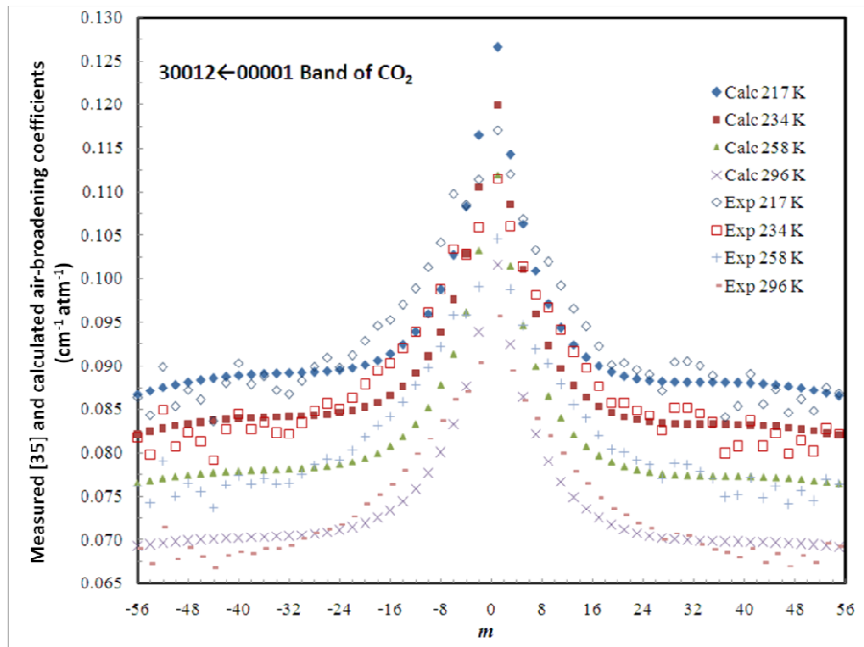


Figure 5-1: Overlaid measured and calculated air-broadening parameters using the Exponential Power Gap law (EPG) plotted against the rotational quantum number m for CO_2 transitions in the 30012←00001 band [88].

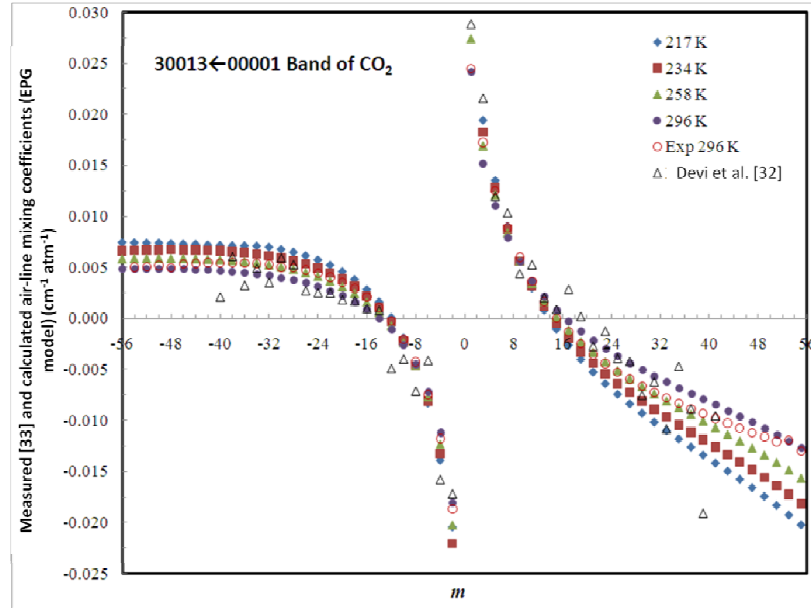


Figure 5-2: Overlaid are the measured and calculated air-line mixing parameters using the Exponential Power Gap law (EPG) for CO₂ transitions in the 30013←00001 band plotted against the rotational quantum number m [88].

Table 5-3: Temperature dependence coefficient “ n ” of the $\alpha(T)$ parameter in Eq. 5-2 calculated using the EPG scaling law. The values were obtained over a range of temperatures between 193 and 323 K for self-broadened CO₂ transitions in the 30013←00001 and 30012←00001 bands. The line parameters were taken from Ref. [109]. The last row contains the average values, n_{ave} .

Temperature (K)	30013 ← 00001 band			30012 ← 00001 band		
	P branch		R branch	P branch		R branch
	n	Error n	n	n	Error n	n
193.15	1.10	3.24×10^{-08}	1.09	1.08	3.27×10^{-05}	1.06
203.15	1.09	1.15×10^{-05}	1.09	1.07	3.83×10^{-05}	1.06
217	1.09	4.81×10^{-07}	1.08	1.07	3.43×10^{-05}	1.05
223.15	1.09	5.38×10^{-05}	1.08	1.07	3.83×10^{-05}	1.05
234	1.09	6.66×10^{-05}	1.08	1.07	6.71×10^{-05}	1.05
243.15	1.08	5.77×10^{-05}	1.06	1.05	6.22×10^{-05}	1.05
253.15	1.08	1.05×10^{-04}	1.07	1.05	1.06×10^{-05}	1.05
258	1.08	1.21×10^{-04}	1.07	1.06	1.22×10^{-04}	1.04
263.15	1.08	1.44×10^{-04}	1.07	1.06	4.36×10^{-05}	1.04
283.15	1.07	2.82×10^{-04}	1.07	1.05	4.01×10^{-05}	1.04
313.15	1.07	1.06×10^{-06}	1.06	1.05	3.37×10^{-07}	1.03
323.15	1.07	6.62×10^{-05}	1.06	1.05	2.20×10^{-06}	1.03
	1.08	7.58×10^{-05}	1.08	1.06	3.96×10^{-05}	1.05
						8.53×10^{-05}

Table 5-4: Temperature dependence coefficient “ n ” of the $\alpha(T)$ parameter in Eq. 5-2 calculated using the EPG scaling law. The values were obtained over a range of temperatures between 193 and 323 K for self-broadened CO₂ transitions in the 30013←00001 and 30012←00001 bands. The line parameters were taken from HITRAN08 [21]. The last row contains the average values, n_{ave} .

Temperature (K)	30013 ← 00001 band			30012 ← 00001 band		
	P branch		R branch	P branch		R branch
	n	Error n	n	n	Error n	n
193.15	1.10	2.31×10^{-05}	1.08	1.10	1.03×10^{-08}	1.08
203.15	1.10	3.82×10^{-05}	1.08	1.10	1.15×10^{-05}	1.08
217.00	1.09	4.82×10^{-05}	1.08	1.09	4.82×10^{-05}	1.08
223.15	1.09	5.39×10^{-07}	1.08	1.09	5.39×10^{-07}	1.08
234.00	1.09	6.68×10^{-07}	1.07	1.09	2.01×10^{-05}	1.07
243.15	1.09	7.80×10^{-03}	1.07	1.09	2.47×10^{-03}	1.07
253.15	1.08	7.46×10^{-05}	1.07	1.08	1.05×10^{-05}	1.07
258.00	1.08	1.21×10^{-05}	1.07	1.08	8.59×10^{-05}	1.07
263.15	1.08	4.33×10^{-05}	1.07	1.08	1.43×10^{-05}	1.07
283.15	1.08	3.80×10^{-04}	1.06	1.08	1.26×10^{-06}	1.06
313.15	1.07	3.35×10^{-07}	1.06	1.07	3.35×10^{-07}	1.06
323.15	1.07	2.19×10^{-06}	1.06	1.07	2.09×10^{-04}	1.05
	1.09	5.84×10^{-05}	1.07	1.09	3.55×10^{-05}	1.07
						4.99×10^{-05}

Table 5-5: Temperature dependence coefficient “ n ” of the $a(T)$ parameter in Eq. 5-2 calculated using the EPG scaling law. The values were obtained over a range of temperatures between 193 and 323 K for air-broadened CO₂ transitions in the 30013←00001 and 30012←00001 bands. The line parameters were taken from Ref. [35]. The last row contains the average values, n_{ave} .

Temperature (K)	30013 ← 00001 band			30012 ← 00001 band		
	P branch		R branch	P branch		R branch
	n	Error n	n	n	Error n	n
193.15	1.06	3.88×10^{-05}	1.04	3.93×10^{-05}	1.06	1.22×10^{-08}
203.15	1.06	4.56×10^{-05}	1.04	4.62×10^{-05}	1.06	3.22×10^{-05}
217.00	1.05	1.75×10^{-05}	1.04	5.60×10^{-05}	1.05	1.74×10^{-05}
223.15	1.05	6.51×10^{-07}	1.04	1.99×10^{-05}	1.05	2.05×10^{-06}
234.00	1.05	2.56×10^{-06}	1.04	2.47×10^{-05}	1.05	8.03×10^{-06}
243.15	1.05	9.90×10^{-06}	1.04	7.12×10^{-05}	1.05	3.14×10^{-06}
253.15	1.05	9.11×10^{-05}	1.04	4.12×10^{-06}	1.05	9.08×10^{-05}
258.00	1.05	4.70×10^{-08}	1.03	1.50×10^{-05}	1.05	1.48×10^{-04}
263.15	1.05	5.57×10^{-06}	1.03	5.63×10^{-08}	1.05	5.55×10^{-06}
283.15	1.05	4.92×10^{-04}	1.03	4.98×10^{-04}	1.04	4.91×10^{-06}
313.15	1.04	1.32×10^{-05}	1.03	1.27×10^{-04}	1.04	1.32×10^{-05}
323.15	1.04	2.74×10^{-04}	1.03	2.77×10^{-04}	1.04	2.73×10^{-06}
	1.05	8.26×10^{-05}	1.04	9.82×10^{-05}	1.05	2.73×10^{-05}
						1.28×10^{-04}

Table 5-6: Temperature dependence coefficient “ n ” of the $a(T)$ parameter in Eq. 5-2 calculated using the EPG scaling law. The values were obtained over a range of temperatures between 193 and 323 K for air-broadened CO₂ transitions in the 30013←00001 and 30012←00001 bands. The line parameters were taken from HITRAN08 [21]. The last row contains the average values, n_{ave} .

Temperature (K)	30013 ← 00001 band			30012 ← 00001 band		
	P branch		R branch	P branch		R branch
	n	Error n	n	n	Error n	n
193.15	1.06	2.74×10^{-05}	1.05	1.24×10^{-06}	1.06	3.87×10^{-05}
203.15	1.06	4.34×10^{-05}	1.04	4.61×10^{-05}	1.06	1.37×10^{-05}
217.00	1.05	5.79×10^{-05}	1.04	5.83×10^{-06}	1.05	5.79×10^{-05}
223.15	1.05	2.05×10^{-06}	1.04	6.56×10^{-07}	1.05	4.59×10^{-05}
234.00	1.05	2.55×10^{-06}	1.04	8.16×10^{-05}	1.05	8.16×10^{-06}
243.15	1.05	9.93×10^{-05}	1.04	3.02×10^{-05}	1.05	9.93×10^{-05}
253.15	1.05	9.10×10^{-05}	1.04	1.29×10^{-05}	1.05	1.29×10^{-04}
258.00	1.05	4.48×10^{-05}	1.04	1.49×10^{-05}	1.05	1.48×10^{-08}
263.15	1.05	1.76×10^{-04}	1.04	5.61×10^{-08}	1.05	1.76×10^{-04}
283.15	1.05	1.55×10^{-05}	1.04	3.50×10^{-04}	1.05	4.92×10^{-04}
313.15	1.04	2.95×10^{-04}	1.03	1.33×10^{-06}	1.04	4.17×10^{-04}
323.15	1.04	2.72×10^{-05}	1.03	8.71×10^{-06}	1.04	2.74×10^{-04}
	1.05	7.35×10^{-05}	1.04	4.61×10^{-05}	1.05	1.46×10^{-04}
						6.58×10^{-05}

5.2.3. Energy Corrected Sudden calculations for rotational transfer

This type of scaling law depends on the adjustable parameters d_c , A , λ , and β as defined in Section 2.6.2 with equations 2-82, 2-83 and 2-84. The room temperature values of the adjustable parameters for self- and air-broadened transitions are presented in Table 5-7 and Table 5-8, respectively.

The temperature dependence of the adjustable parameters was explored using two methods. In the first method (referred to as Fit 1) the parameters A and d_c from equations 2-83 and 2-84 were assumed to have the following temperature relation as defined by.

$$A = A_0 \left(\frac{T_0}{T} \right)^{N1} \text{ and} \quad 5-3$$

$$d_c = d_{co} \left(\frac{T_0}{T} \right)^{N2}, \quad 5-4$$

where A_0 and d_{co} are the values fitted at $T_0 = 296\text{K}$. The same two datasets that were used for the EPG calculations have been used here.

In the second method (referred to as Fit 2) only the parameter A from equation 2-84 is assumed to have temperature dependence, namely:

$$A = A_0 \left(\frac{T_0}{T} \right)^{N3}. \quad 5-5$$

Table 5-7: Room temperature values for the adjustable ECS parameters for pure CO₂ at 296 K in the 30013←00001 and 30012←00001 bands [88]. The first four rows were obtained from the data in [109] and the last 4 rows from [21].

Band	Branch	A_0	Error A_0	d_{cs}	Error d_{cs}	λ	Error λ	β_0	Error β_0	Sum rule
30013 ← 00001	P	2.03×10^{-02}	7.79×10^{-06}	3.73	4.06×10^{-06}	6.12×10^{-01}	6.47×10^{-06}	5.21×10^{-02}	1.71×10^{-05}	-1.82×10^{-25}
30013 ← 00001	R	1.98×10^{-02}	3.98×10^{-06}	4.16	2.63×10^{-06}	6.14×10^{-01}	2.78×10^{-06}	5.10×10^{-02}	1.05×10^{-05}	-3.77×10^{-27}
30012 ← 00001	P	2.03×10^{-02}	5.91×10^{-06}	3.66	2.92×10^{-06}	6.14×10^{-01}	4.82×10^{-06}	5.84×10^{-02}	1.23×10^{-05}	-1.78×10^{-25}
30012 ← 00001	R	2.14×10^{-02}	8.17×10^{-06}	4.19	4.88×10^{-06}	6.27×10^{-01}	5.55×10^{-06}	5.30×10^{-02}	1.92×10^{-05}	-3.65×10^{-27}
30013 ← 00001	P	1.87×10^{-02}	8.38×10^{-06}	3.62	3.84×10^{-06}	5.98×10^{-01}	6.29×10^{-06}	5.60×10^{-02}	1.67×10^{-05}	-1.81×10^{-25}
30013 ← 00001	R	1.94×10^{-02}	5.61×10^{-06}	4.36	3.61×10^{-06}	6.06×10^{-01}	3.29×10^{-06}	5.49×10^{-02}	1.43×10^{-05}	-3.78×10^{-27}
30012 ← 00001	P	1.85×10^{-02}	4.57×10^{-06}	3.72	2.23×10^{-06}	5.92×10^{-01}	3.53×10^{-06}	6.76×10^{-02}	9.51×10^{-06}	-1.79×10^{-25}
30012 ← 00001	R	1.95×10^{-02}	6.63×10^{-06}	4.41	3.95×10^{-06}	6.05×10^{-01}	3.69×10^{-06}	6.28×10^{-02}	1.57×10^{-05}	-3.67×10^{-27}

Table 5-8: Room temperature values for the adjustable ECS parameters for air-broadened CO₂ at 296 K in the 30013←00001 and 30012←00001 bands [88]. The first four rows were obtained from the data in [35] and the last 4 rows from [21].

Band	Branch	A_0	Error A_0	d_{eo}	Error d_{eo}	λ	Error λ	β_0	Error β_0	Sum rule
30013 ← 00001	P	1.38×10^{-02}	1.14×10^{-06}	4.55	1.72×10^{-06}	5.90×10^{-01}	1.56×10^{-06}	3.40×10^{-02}	6.23×10^{-05}	-1.37×10^{-25}
30013 ← 00001	R	1.46×10^{-02}	1.23×10^{-06}	5.45	1.14×10^{-06}	6.05×10^{-01}	1.29×10^{-06}	3.04×10^{-02}	3.56×10^{-05}	-2.84×10^{-27}
30012 ← 00001	P	1.38×10^{-02}	8.93×10^{-07}	4.72	5.32×10^{-07}	5.85×10^{-01}	2.49×10^{-07}	4.37×10^{-02}	1.76×10^{-05}	-1.35×10^{-25}
30012 ← 00001	R	1.47×10^{-02}	1.39×10^{-06}	5.75	1.16×10^{-06}	6.02×10^{-01}	1.56×10^{-06}	3.88×10^{-02}	3.67×10^{-05}	-2.76×10^{-27}
30013 ← 00001	P	1.38×10^{-02}	1.17×10^{-06}	4.58	1.33×10^{-06}	5.90×10^{-01}	1.05×10^{-06}	3.41×10^{-02}	4.67×10^{-05}	-1.37×10^{-25}
30013 ← 00001	R	1.45×10^{-02}	1.18×10^{-06}	5.65	7.67×10^{-07}	6.02×10^{-01}	1.04×10^{-06}	3.22×10^{-02}	2.27×10^{-05}	-2.84×10^{-27}
30012 ← 00001	P	1.39×10^{-02}	1.00×10^{-06}	4.66	9.73×10^{-07}	5.87×10^{-01}	6.98×10^{-07}	4.29×10^{-02}	3.32×10^{-05}	-1.35×10^{-25}
30012 ← 00001	R	1.46×10^{-02}	1.09×10^{-06}	5.66	8.52×10^{-07}	6.02×10^{-01}	1.11×10^{-06}	3.82×10^{-02}	2.64×10^{-05}	-2.76×10^{-27}

The line mixing coefficients were calculated by using equation 2-91 scaled by a factor of 0.5. The results obtained using the first method for self-broadened CO₂ are presented in Table 5-9 to Table 5-12 and for the air-broadened CO₂ they are presented in Table 5-13 to Table 5-16. The results for the second method are presented for self-broadened CO₂ and listed in Table 5-18, with the air-broadened case listed in Table 5-19 and Table 5-20.

The software developed to perform Energy Corrected Sudden calculations was initially written by a former researcher in our group, Ian Schofield and was later revised by me. It had been found in previous work [33, 34] that the Wigner 6J and 3J calculations could not be performed directly in Matlab. Therefore, the computations of Wigner 6J and 3J coefficients were implemented using Mathematica's Wigner functions. A link to Mathematica's kernel from Matlab using the Mathematica Symbolic Toolbox for MATLAB version 2.0 [110] was used to correct this issue. This package provides a dynamically linked library (DLL) that allows Mathematica functions to be called from Matlab.

Table 5-9: Temperature dependence coefficient “N1” and “N2” of the $A(T)$ and $d_c(T)$ parameters in equations 5-3 and 5-4 calculated using the ECS scaling law. The values were obtained over a range of temperatures between 193 and 323 K for self-broadened CO₂ transitions in the 30012←00001 band. The line parameters were taken from Ref. [109]. The last row contains the average values of the temperature dependence parameters.

Temperature (K)	30012 ← 00001 band					
	P branch			R branch		
	N1	Error N1	N2	Error N2	N1	Error N1
193.15	1.26	7.44×10^{-06}	6.55×10^{-03}	1.40×10^{-04}	1.22	1.00×10^{-06}
203.15	1.26	7.42×10^{-06}	6.00×10^{-02}	1.82×10^{-04}	1.21	1.11×10^{-06}
217	1.25	6.96×10^{-06}	5.20×10^{-02}	2.25×10^{-04}	1.20	5.11×10^{-06}
223.15	1.25	6.61×10^{-06}	4.87×10^{-02}	2.41×10^{-04}	1.20	1.38×10^{-05}
234	1.25	5.60×10^{-06}	4.24×10^{-02}	2.63×10^{-04}	1.19	6.41×10^{-06}
243.15	1.24	4.99×10^{-06}	3.65×10^{-02}	2.81×10^{-04}	1.19	1.34×10^{-06}
253.15	1.24	5.01×10^{-06}	3.06×10^{-02}	2.99×10^{-04}	1.18	3.05×10^{-06}
258	1.24	5.35×10^{-06}	2.82×10^{-02}	3.11×10^{-04}	1.18	3.93×10^{-06}
263.15	1.23	2.71×10^{-06}	2.49×10^{-02}	3.22×10^{-04}	1.18	4.07×10^{-06}
283.15	1.23	7.88×10^{-06}	1.51×10^{-02}	3.82×10^{-04}	1.17	1.12×10^{-05}
313.15	1.21	2.89×10^{-06}	-3.04×10^{-03}	1.68×10^{-04}	1.16	2.49×10^{-06}
323.15	1.21	3.51×10^{-06}	-1.09×10^{-02}	1.88×10^{-04}	1.15	6.47×10^{-06}
	1.24	5.53×10^{-06}	3.25×10^{-02}	2.50×10^{-04}	1.18	5.79×10^{-06}
						6.62×10^{-02}
						4.40×10^{-04}

Table 5-10: Temperature dependence coefficient “N1” and “N2” of the $A(T)$ and $d_c(T)$ parameters in equations 5-3 and 5-4 calculated using the ECS scaling law. The values were obtained over a range of temperatures between 193 and 323 K for self-broadened CO₂ transitions in the 30013←00001 band. The line parameters were taken from Ref. [109]. The last row contains the average values of the temperature dependence parameters

Temperature (K)	30013 ← 00001 band					
	P branch			R branch		
	N1	Error N1	N2	Error N2	N1	Error N1
193.15	1.22	7.90×10^{-06}	-6.25×10^{-02}	1.92×10^{-04}	1.21	1.35×10^{-05}
203.15	1.21	6.35×10^{-06}	-6.73×10^{-02}	1.05×10^{-04}	1.20	5.44×10^{-06}
217	1.21	2.42×10^{-05}	-7.39×10^{-02}	1.36×10^{-04}	1.20	1.49×10^{-05}
223.15	1.20	1.22×10^{-05}	-7.71×10^{-02}	1.26×10^{-06}	1.19	2.02×10^{-05}
234	1.20	2.55×10^{-05}	-8.20×10^{-02}	1.81×10^{-04}	1.19	7.38×10^{-06}
243.15	1.20	5.87×10^{-06}	-8.62×10^{-02}	9.85×10^{-06}	1.19	7.69×10^{-06}
253.15	1.19	1.27×10^{-05}	-9.06×10^{-02}	2.41×10^{-04}	1.18	8.03×10^{-06}
258	1.19	1.75×10^{-05}	-9.27×10^{-02}	3.37×10^{-04}	1.18	8.80×10^{-06}
263.15	1.19	3.10×10^{-06}	-9.46×10^{-02}	1.13×10^{-04}	1.18	8.66×10^{-06}
283.15	1.18	2.63×10^{-06}	-1.05×10^{-01}	3.46×10^{-04}	1.17	4.97×10^{-06}
313.15	1.18	6.65×10^{-06}	-1.14×10^{-01}	4.08×10^{-04}	1.16	4.54×10^{-06}
323.15	1.17	1.42×10^{-05}	-1.18×10^{-01}	5.83×10^{-04}	1.16	3.29×10^{-06}
	1.20	1.16×10^{-05}	-8.86×10^{-02}	2.29×10^{-04}	1.18	8.95×10^{-06}
						1.82×10^{-02}
						3.38×10^{-04}

Table 5-11: Temperature dependence coefficient “N1” and “N2” of the $A(T)$ and $d_c(T)$ parameters in equations 5-3 and 5-4 calculated using the ECS scaling law. The values were obtained over a range of temperatures between 193 and 323 K for self-broadened CO₂ transitions in the 30012←00001 band. The line parameters were taken from Ref. [21]. The last row contains the average values of the temperature dependence parameters.

Temperature (K)	30012 ← 00001 band					
	P branch			R branch		
	N1	Error N1	N2	Error N2	N1	Error N1
193.15	1.33	1.45×10^{-05}	2.02×10^{-01}	3.72×10^{-04}	1.28	1.96×10^{-06}
203.15	1.33	6.98×10^{-06}	1.98×10^{-01}	1.43×10^{-04}	1.27	1.46×10^{-05}
217	1.32	2.99×10^{-05}	1.91×10^{-01}	4.03×10^{-04}	1.27	4.52×10^{-06}
223.15	1.32	6.96×10^{-06}	1.87×10^{-01}	1.71×10^{-04}	1.26	2.27×10^{-06}
234	1.32	9.55×10^{-06}	1.81×10^{-01}	2.48×10^{-04}	1.26	1.16×10^{-05}
243.15	1.31	1.18×10^{-05}	1.74×10^{-01}	3.12×10^{-04}	1.25	1.91×10^{-05}
253.15	1.31	1.34×10^{-05}	1.66×10^{-01}	3.71×10^{-04}	1.25	7.44×10^{-06}
258	1.31	1.36×10^{-05}	1.63×10^{-01}	3.97×10^{-04}	1.24	5.73×10^{-06}
263.15	1.30	1.40×10^{-05}	1.59×10^{-01}	4.19×10^{-04}	1.24	6.60×10^{-06}
283.15	1.30	8.45×10^{-06}	1.45×10^{-01}	4.67×10^{-04}	1.23	3.50×10^{-06}
313.15	1.28	2.60×10^{-06}	1.19×10^{-01}	1.52×10^{-04}	1.22	2.33×10^{-06}
323.15	1.28	4.24×10^{-06}	1.08×10^{-01}	1.45×10^{-04}	1.21	3.71×10^{-06}
	1.31	1.08×10^{-05}	1.66×10^{-01}	3.00×10^{-04}	1.25	6.95×10^{-06}

Table 5-12: Temperature dependence coefficient “N1” and “N2” of the $A(T)$ and $d_c(T)$ parameters in equations 5-3 and 5-4 calculated using the ECS scaling law. The values were obtained over a range of temperatures between 193 and 323 K for self-broadened CO₂ transitions in the 30013←00001 band. The line parameters were taken from Ref. [21]. The last row contains the average values of the temperature dependence parameters.

Temperature (K)	30013 ← 00001 band					
	P branch			R branch		
	N1	Error N1	N2	Error N2	N1	Error N1
193.15	1.27	2.70×10^{-05}	8.32×10^{-02}	2.92×10^{-04}	1.26	4.62×10^{-01}
203.15	1.26	9.44×10^{-06}	7.53×10^{-02}	1.56×10^{-04}	1.25	1.45×10^{-05}
217	1.26	2.03×10^{-05}	6.44×10^{-02}	3.16×10^{-04}	1.25	4.29×10^{-06}
223.15	1.25	4.79×10^{-06}	5.93×10^{-02}	1.10×10^{-04}	1.25	3.63×10^{-01}
234	1.25	6.22×10^{-06}	5.10×10^{-02}	1.59×10^{-04}	1.24	8.67×10^{-06}
243.15	1.24	7.87×10^{-06}	4.38×10^{-02}	2.05×10^{-04}	1.24	1.22×10^{-05}
253.15	1.24	8.57×10^{-06}	3.63×10^{-02}	2.55×10^{-04}	1.24	1.48×10^{-05}
258	1.24	9.08×10^{-06}	3.29×10^{-02}	2.82×10^{-04}	1.24	1.49×10^{-05}
263.15	1.24	9.33×10^{-06}	2.94×10^{-02}	3.09×10^{-04}	1.23	1.50×10^{-05}
283.15	1.23	9.95×10^{-06}	1.36×10^{-02}	4.37×10^{-04}	1.23	5.24×10^{-06}
313.15	1.22	8.73×10^{-06}	-4.42×10^{-02}	2.49×10^{-04}	1.22	6.62×10^{-06}
323.15	1.21	6.35×10^{-06}	-1.05×10^{-02}	2.99×10^{-04}	1.21	2.19×10^{-06}
	1.24	1.06×10^{-05}	3.95×10^{-02}	2.56×10^{-04}	1.24	8.89×10^{-06}

Table 5-13: Temperature dependence coefficient “N1” and “N2” of the $A(T)$ and $d_c(T)$ parameters in equations 5-3 and 5-4 calculated using the ECS scaling law. The values were obtained over a range of temperatures between 193 and 323 K for air-broadened CO_2 transitions in the 30013←00001 band. The line parameters were taken from Ref. [35]. The last row contains the average values of the temperature dependence parameters.

Temperature (K)	30013 ← 00001 band					
	P branch			R branch		
	N1	Error N1	Error N2	N1	Error N1	Error N2
193.15	1.20	7.39×10^{-07}	4.94×10^{-05}	1.16	2.37×10^{-06}	-1.55×10^{-01}
203.15	1.19	3.25×10^{-06}	1.57×10^{-04}	1.16	3.63×10^{-06}	-2.12×10^{-01}
217	1.18	2.22×10^{-06}	1.90×10^{-04}	1.15	4.06×10^{-06}	-2.34×10^{-01}
223.15	1.18	3.63×10^{-06}	1.30×10^{-04}	1.15	1.05×10^{-05}	-2.44×10^{-01}
234	1.17	1.78×10^{-05}	2.71×10^{-04}	1.14	1.07×10^{-05}	-2.60×10^{-01}
243.15	1.17	3.90×10^{-06}	1.01×10^{-04}	1.14	1.73×10^{-05}	-2.74×10^{-01}
253.15	1.16	5.49×10^{-06}	1.49×10^{-04}	1.14	4.55×10^{-06}	-2.87×10^{-01}
258	1.16	6.25×10^{-06}	1.74×10^{-04}	1.13	3.83×10^{-06}	-2.93×10^{-01}
263.15	1.16	6.59×10^{-06}	1.99×10^{-04}	1.13	5.07×10^{-06}	-3.00×10^{-01}
283.15	1.15	7.86×10^{-06}	3.06×10^{-04}	1.13	6.80×10^{-06}	-3.25×10^{-01}
313.15	1.13	2.78×10^{-06}	1.17×10^{-04}	1.12	9.01×10^{-06}	-3.59×10^{-01}
323.15	1.13	2.72×10^{-06}	1.32×10^{-04}	1.12	1.22×10^{-05}	-3.66×10^{-01}
	1.17	5.27×10^{-06}	1.65×10^{-04}	1.14	7.50×10^{-06}	-2.79×10^{-01}

Table 5-14: Temperature dependence coefficient “N1” and “N2” of the $A(T)$ and $d_c(T)$ parameters in equations 5-3 and 5-4 calculated using the ECS scaling law. The values were obtained over a range of temperatures between 193 and 323 K for air-broadened CO_2 transitions in the 30012←00001 band. The line parameters were taken from Ref. [35]. The last row contains the average values of the temperature dependence parameters.

Temperature (K)	30012 ← 00001 band					
	P branch			R branch		
	N1	Error N1	Error N2	N1	Error N1	Error N2
193.15	1.28	6.32×10^{-06}	2.67×10^{-04}	1.22	4.31×10^{-06}	1.76×10^{-02}
203.15	1.27	1.18×10^{-05}	3.51×10^{-04}	1.21	4.29×10^{-06}	-1.28×10^{-04}
217	1.26	2.75×10^{-06}	2.78×10^{-04}	1.20	4.07×10^{-06}	-2.48×10^{-02}
223.15	1.25	3.50×10^{-06}	1.58×10^{-04}	1.20	3.89×10^{-06}	-3.55×10^{-02}
234	1.24	1.62×10^{-05}	3.12×10^{-04}	1.20	3.34×10^{-06}	-5.35×10^{-02}
243.15	1.24	4.00×10^{-06}	1.20×10^{-04}	1.19	2.75×10^{-06}	-6.92×10^{-02}
253.15	1.23	4.64×10^{-06}	1.46×10^{-04}	1.19	2.46×10^{-06}	-8.54×10^{-02}
258	1.23	5.34×10^{-06}	1.55×10^{-04}	1.19	2.99×10^{-06}	-9.13×10^{-02}
263.15	1.23	5.75×10^{-06}	1.62×10^{-04}	1.18	3.46×10^{-06}	-9.96×10^{-02}
283.15	1.21	6.87×10^{-06}	1.71×10^{-04}	1.18	2.30×10^{-06}	-1.30×10^{-01}
313.15	1.20	3.24×10^{-06}	1.50×10^{-04}	1.17	5.39×10^{-06}	-1.70×10^{-01}
323.15	1.19	5.15×10^{-06}	1.35×10^{-04}	1.16	8.33×10^{-06}	-1.80×10^{-01}
	1.24	6.30×10^{-06}	2.00×10^{-04}	1.19	3.97×10^{-06}	-7.68×10^{-02}

Table 5-17: Temperature dependence coefficient “N3” of the A(T) parameter in equation 5-5 calculated using the ECS scaling law. The values were obtained over a range of temperatures between 193 K and 323 K for self-broadened CO₂ transitions in the 30013←00001 and 30012←00001 bands. The line parameters were taken from Ref. [109]. The last row contains the average values of the temperature dependence parameters.

Temperature (K)	30012 ← 00001 band			30013 ← 00001 band		
	P branch		R branch	P branch		R branch
	N1	Error N1	N1	Error N1	N1	Error N1
193.15	1.24	1.85 × 10 ⁻⁰⁶	1.18	3.09 × 10 ⁻⁰⁶	1.24	1.44 × 10 ⁻⁰⁶
203.15	1.24	1.42 × 10 ⁻⁰⁶	1.18	2.44 × 10 ⁻⁰⁶	1.23	1.56 × 10 ⁻⁰⁶
217	1.23	1.58 × 10 ⁻⁰⁶	1.17	1.97 × 10 ⁻⁰⁶	1.23	9.38 × 10 ⁻⁰⁷
223.15	1.23	9.38 × 10 ⁻⁰⁷	1.17	1.75 × 10 ⁻⁰⁶	1.23	1.45 × 10 ⁻⁰⁶
234	1.23	7.32 × 10 ⁻⁰⁷	1.17	2.10 × 10 ⁻⁰⁶	1.23	1.46 × 10 ⁻⁰⁶
243.15	1.23	9.60 × 10 ⁻⁰⁷	1.17	1.22 × 10 ⁻⁰⁶	1.23	1.77 × 10 ⁻⁰⁶
253.15	1.23	1.75 × 10 ⁻⁰⁶	1.17	1.54 × 10 ⁻⁰⁶	1.23	1.92 × 10 ⁻⁰⁶
258	1.23	1.25 × 10 ⁻⁰⁶	1.17	1.59 × 10 ⁻⁰⁶	1.22	2.88 × 10 ⁻⁰⁶
263.15	1.22	1.52 × 10 ⁻⁰⁶	1.17	2.83 × 10 ⁻⁰⁶	1.22	1.16 × 10 ⁻⁰⁴
283.15	1.22	2.92 × 10 ⁻⁰⁵	1.16	5.20 × 10 ⁻⁰⁶	1.22	3.04 × 10 ⁻⁰⁵
313.15	1.22	3.80 × 10 ⁻⁰⁵	1.16	3.50 × 10 ⁻⁰⁶	1.22	5.26 × 10 ⁻⁰⁶
323.15	1.21	7.56 × 10 ⁻⁰⁵	1.16	1.29 × 10 ⁻⁰⁴	1.21	7.51 × 10 ⁻⁰⁵
	1.23	1.29 × 10 ⁻⁰⁵	1.17	1.30 × 10 ⁻⁰⁵	1.23	2.00 × 10 ⁻⁰⁵
					1.18	1.53 × 10 ⁻⁰⁵

Table 5-18: Temperature dependence coefficient “N3” of the A(T) parameter in equation 5-5 calculated using the ECS scaling law. The values were obtained over a range of temperatures between 193 K and 323 K for self-broadened CO₂ transitions in the 30013←00001 and 30012←00001 bands. The line parameters were taken from Ref. [21]. The last row contains the average values of the temperature dependence parameters.

Temperature (K)	30012 ← 00001 band			30013 ← 00001 band		
	P branch		R branch	P branch		R branch
	N1	Error N1	N1	Error N1	N1	Error N1
193.15	1.26	1.31 × 10 ⁻⁰⁶	1.20	2.26 × 10 ⁻⁰⁶	1.24	1.71 × 10 ⁻⁰⁶
203.15	1.26	1.04 × 10 ⁻⁰⁶	1.20	1.60 × 10 ⁻⁰⁶	1.24	1.34 × 10 ⁻⁰⁶
217	1.26	3.85 × 10 ⁻⁰⁷	1.20	1.37 × 10 ⁻⁰⁶	1.24	9.13 × 10 ⁻⁰⁷
223.15	1.26	6.58 × 10 ⁻⁰⁷	1.20	9.18 × 10 ⁻⁰⁷	1.23	1.76 × 10 ⁻⁰⁶
234	1.25	9.77 × 10 ⁻⁰⁷	1.20	2.52 × 10 ⁻⁰⁷	1.23	1.35 × 10 ⁻⁰⁶
243.15	1.25	1.84 × 10 ⁻⁰⁶	1.19	1.03 × 10 ⁻⁰⁶	1.23	1.40 × 10 ⁻⁰⁶
253.15	1.25	6.34 × 10 ⁻⁰⁷	1.19	1.09 × 10 ⁻⁰⁶	1.23	1.52 × 10 ⁻⁰⁶
258	1.25	1.95 × 10 ⁻⁰⁶	1.19	3.06 × 10 ⁻⁰⁶	1.23	2.02 × 10 ⁻⁰⁶
263.15	1.25	1.36 × 10 ⁻⁰⁶	1.19	2.09 × 10 ⁻⁰⁶	1.23	1.62 × 10 ⁻⁰⁶
283.15	1.24	2.32 × 10 ⁻⁰⁵	1.19	4.02 × 10 ⁻⁰⁵	1.22	2.83 × 10 ⁻⁰⁵
313.15	1.24	2.91 × 10 ⁻⁰⁵	1.18	5.26 × 10 ⁻⁰⁵	1.22	3.62 × 10 ⁻⁰⁵
323.15	1.24	2.98 × 10 ⁻⁰⁶	1.18	2.53 × 10 ⁻⁰⁶	1.22	3.37 × 10 ⁻⁰⁶
	1.25	5.45 × 10 ⁻⁰⁶	1.19	9.08 × 10 ⁻⁰⁶	1.23	6.79 × 10 ⁻⁰⁶
					1.18	6.78 × 10 ⁻⁰⁶

Figure 5-3 shows overlaid measured and calculated broadening parameters using the ECS law. All results are plotted against m . As it can be seen from Figure 5-1 and Figure 5-3 the ECS scaling law models the measured broadening parameters better than the EPG law, with best agreement for medium m values. When comparing the observed and calculated line mixing coefficients obtained using both the ECS and EPG models plotted in Figure 5-2 and Figure 5-4, it can be concluded that the EPG calculation reproduces better the line mixing coefficients compared to with the ECS model.

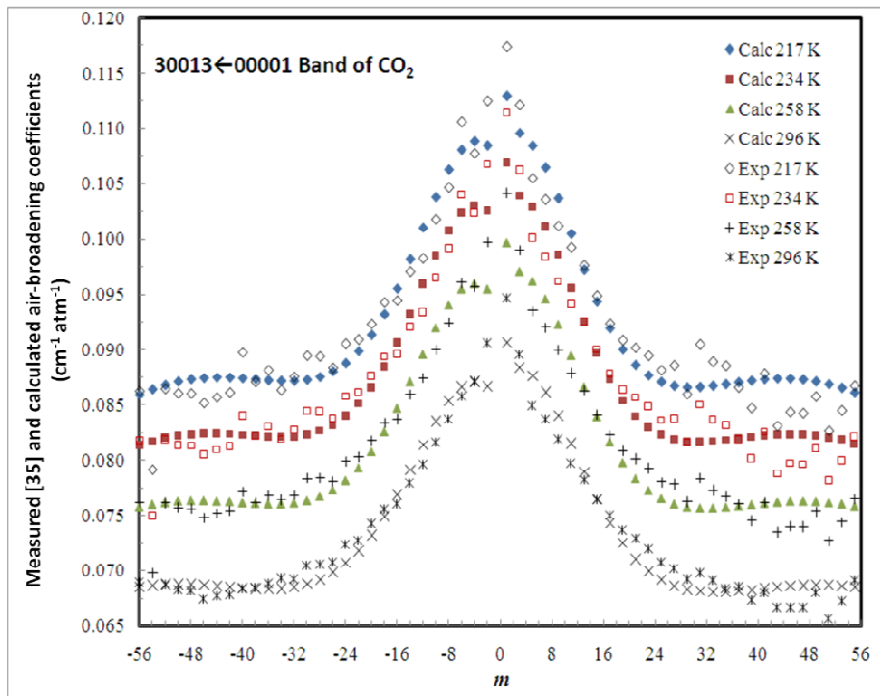


Figure 5-3: Overlaid measured and calculated air-broadening parameters using the Energy Corrected Sudden (ECS) scaling law plotted against m for CO_2 transitions in the 30013←00001 band [88].

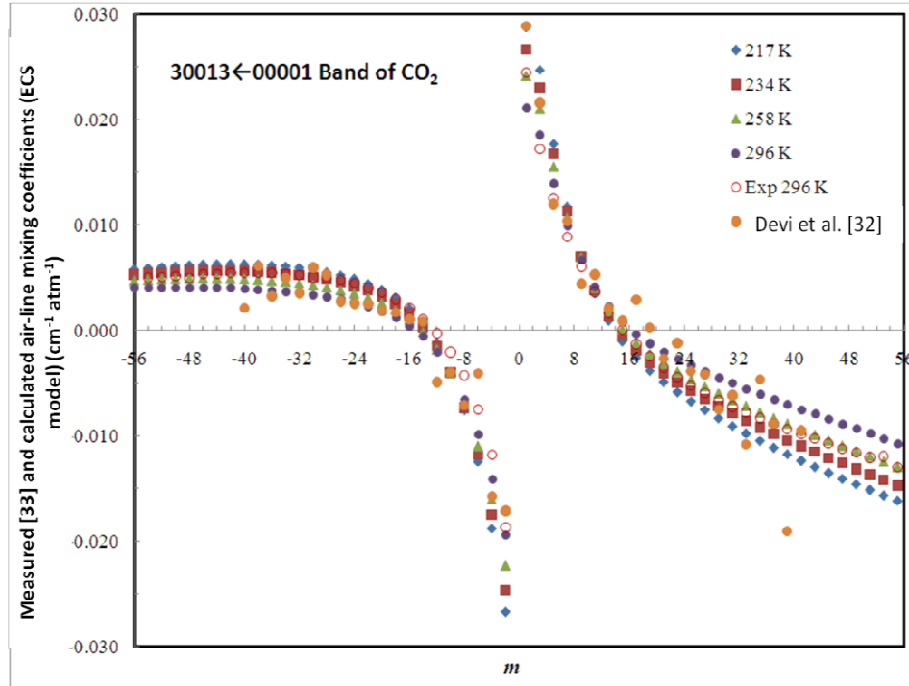


Figure 5-4: Measured and calculated air-line mixing parameters using the Energy Corrected Sudden (ECS) scaling law for CO_2 in the 30013←00001 band. All results are plotted against m [88].

An example of the error found from several of the EPG and ECS fits of the broadening coefficients are shown in Figure 5-5. The error analyses for the different fits performed were similar in that they all appeared to have a periodic nature to them. There are several possible reasons why this could be. It could be caused either by similar inconsistencies that are periodic in the input broadening coefficients or could be from a missing phase term in the calculation of the relaxation matrix elements. It may be necessary to include a sinusoidal type term to account for the loss of phase. However, both these claims need to be supported by more experimental studies over a wider range of temperatures and higher values of m .

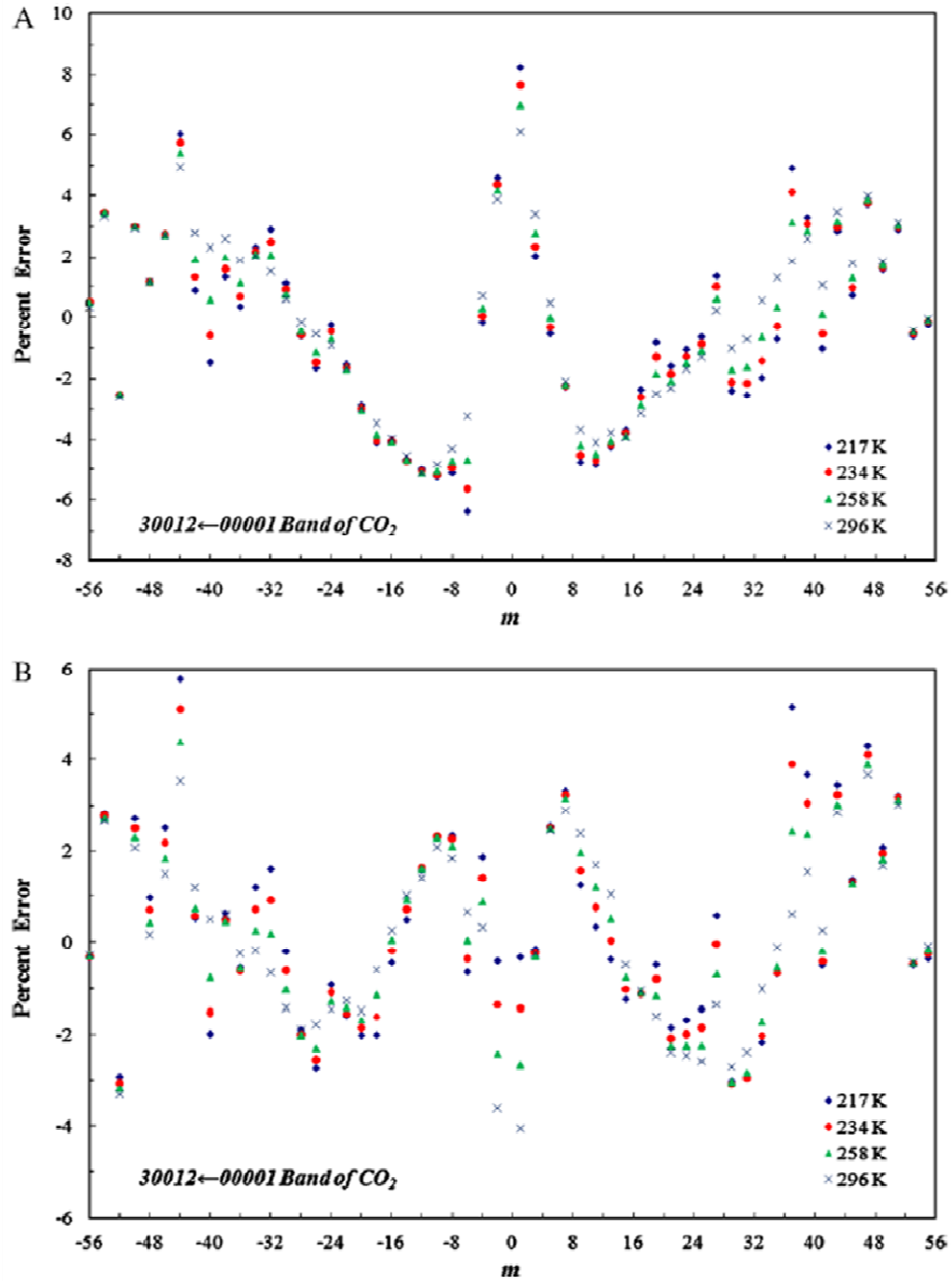


Figure 5-5: Percent differences between experimental air-broadening parameters and calculated ones obtained using the EPG scaling law (A) and calculated values obtained using the ECS scaling law (fit 1) (B). The comparisons are made for datasets available at 217, 234, 259 and 296 K [88].

5.3. Conclusion

A careful examination of the two scaling laws (EPG and ECS) has been shown to suitably model both broadening and line mixing coefficients over the temperature range of 193 to 323 K. All the calculations were performed on the carbon dioxide transitions in the 30012←00001 and 30013←00001 bands. It was determined that the best agreement between theoretical and experimental broadening coefficients is achieved for values of the adjustable parameters that are not unique over a wide temperature range. Also, the values of the best-fit adjustable parameter are slightly different from one band to another. Therefore, it has been proposed that average values for the temperature dependence coefficients for both types of scaling laws should be used.

Chapter 6: High Resolution Measurements of Acetylene Transitions

6.1. Introduction

In this chapter the results of three individual studies of the acetylene molecule that were completed and published during my study period are presented. The first “*Line shape study of acetylene transitions in the $\nu_1+\nu_2+\nu_4+\nu_5$ band over a range of temperatures*” was published in the Journal of Molecular Spectroscopy [111]. The second study “*Low pressure line shape study of acetylene transitions in the $\nu_1+\nu_2+\nu_4+\nu_5$ band over a range of temperatures*” was published in Molecular Physics [112] (This journals website can be located at <http://www.tandfonline.com>). Finally, the third study “*Low pressure line shape study of nitrogen perturbed acetylene transitions in the $\nu_1+\nu_3$ band over a range of temperatures*” was published in the Canadian Journal of Physics [113].

6.2. Line Shape Study of Acetylene Transitions in the $\nu_1+\nu_2+\nu_4+\nu_5$ Band Over a Range of Temperatures

6.2.1. Introduction

The $\nu_1+\nu_2+\nu_4+\nu_5$ upper state in $^{12}\text{C}_2\text{H}_2$ has three sub-states with Σ_u^+ , Σ_u^+ , Π symmetry. The band investigated here is parallel with P and R branches only. The upper sub-state belongs to the $[\text{Nr},\text{Ns},\text{e},\text{u}] = [10,2,\text{e},\text{u}]$ polyad with $\text{Nr}=5$ ν_1+5 ν_3+3 ν_2+ ν_4+ ν_5 and $\text{Ns}= \nu_1+ \nu_2+ \nu_3$. The nuclear spin statistics are either 1 or 3 for even or odd

lower J values, respectively (the opposite for the upper J values). Further details on the ground state structure in acetylene can be found in Ref. [114].

In this study the line intensities, self-broadened widths, self-pressure induced shifts and selected line mixing coefficients for twenty R-branch transitions in the $\nu_1+\nu_2+\nu_4+\nu_5$ band of acetylene were retrieved. The spectra were recorded using the 3 channel diode laser spectrometer described in Chapter 3, a temperature controlled cell of fixed length and a second room temperature cell. The Voigt and speed-dependent Voigt profiles with inclusion of line mixing effects were used to retrieve the line parameters. From the retrieved line parameters the temperature dependences for line broadening and shift coefficients were determined. The line mixing coefficients and their temperature dependence were theoretically modeled using retrieved broadening values. A set of 6 pressures were selected and for each pressure, spectra were recorded at seven temperatures in the 213 K to 350 K range. A summary of the experimental conditions is presented in Table 6-1.

The line parameters of acetylene were retrieved using a weighted multispectrum analysis software [87]. The spectra were divided in smaller sections covering each of the R(0) to R(19) transitions. Batches of spectra recorded at the same set temperature were fitted together. The program minimized the differences between the experimental spectra and the calculated spectra by adjusting various line parameters through non-linear least squares. For the transitions presented in this work, line mixing was needed to fit the spectra within the noise levels. Initial values for the line intensities and self-broadened widths were taken from Ref. [21].

Table 6-1: Experimental conditions for self-broadened acetylene spectra [111]. The numbers in brackets indicate the statistical error of the measured values.

Lines scanned	Average Pressure (Torr)	Average Temperature(K)			
R19-R0	107.08(19)	253.0(2)	R19-R0	483.70(4)	272.9(2)
R19-R0	108.45(3)	253.1(2)	R19-R0	483.70(1)	272.9(2)
R19-R0	265.09(3)	253.1(2)	R19-R0	574.70(3)	272.9(2)
R19-R0	377.88(1)	253.0(2)	R19-R0	700.01(3)	272.9(2)
R19-R0	377.88(1)	253.0(2)	R19-R0	700.09(2)	272.9(2)
R19-R0	538.79(9)	253.1(2)	R19-R0	93.50(8)	293.0(2)
R19-R0	649.07(20)	253.3(3)	R19-R0	93.86(8)	293.0(2)
R19-R0	648.89(2)	253.2(2)	R19-R0	264.71(5)	293.0(2)
R19-R0	780.12(7)	253.0(2)	R19-R0	436.52(1)	293.0(2)
R19-R0	98.42(2)	233.1(3)	R19-R0	436.56(1)	293.0(2)
R19-R0	98.48(2)	233.1(3)	R19-R0	519.22(1)	293.0(2)
R19-R0	244.33(7)	233.3(2)	R19-R0	519.23(1)	293.0(2)
R19-R4	371.70(9)	233.0(3)	R19-R0	616.59(1)	293.0(2)
R19-R0	371.84(1)	233.0(3)	R19-R0	616.57(3)	293.0(2)
R3-R0	371.82(0)	233.0(3)	R19-R0	751.27(1)	293.0(2)
R19-R0	486.50(23)	233.5(3)	R19-R0	751.34(3)	293.0(2)
R19-R0	486.54(3)	233.6(4)	R19-R0	100.41(6)	312.8(2)
R19-R0	595.34(10)	233.7(4)	R19-R0	100.31(1)	312.8(2)
R19-R0	595.48(6)	233.7(4)	R19-R0	230.09(4)	312.8(2)
R19-R0	713.10(17)	233.3(2)	R19-R0	385.03(1)	312.8(2)
R19-R0	90.52(17)	213.1(4)	R19-R0	385.08(1)	312.8(2)
R19-R0	90.09(6)	213.1(4)	R19-R0	496.36(1)	312.8(2)
R19-R0	221.57(5)	213.5(4)	R19-R0	496.38(1)	312.8(2)
R19-R0	337.39(8)	213.9(8)	R19-R0	496.39(1)	312.8(2)
R19-R0	337.11(3)	213.8(8)	R19-R0	496.36(0)	312.8(2)
R19-R0	337.25(1)	213.8(8)	R19-R0	593.06(1)	312.8(2)
R19-R0	337.19(1)	213.8(8)	R19-R0	593.03(1)	312.8(2)
R19-R0	442.08(6)	213.5(4)	R19-R0	679.55(2)	312.8(2)
R19-R0	441.86(6)	213.5(4)	R19-R0	679.47(1)	312.8(2)
R19-R0	541.05(19)	214.7(8)	R19-R0	106.68(4)	332.7(2)
R19-R0	540.83(1)	214.6(8)	R19-R0	106.78(1)	332.7(2)
R19-R0	645.95(22)	213.4(3)	R19-R0	244.43(15)	332.6(2)
R19-R0	645.68(2)	213.3(3)	R19-R0	409.04(1)	332.7(2)
R19-R0	645.48(13)	213.3(3)	R19-R0	409.05(1)	332.7(2)
R19-R0	574.67(1)	272.9(2)	R19-R0	527.04(4)	332.6(2)
R19-R0	115.02(1)	272.8(1)	R19-R0	527.15(3)	332.7(2)
R19-R0	115.58(21)	272.8(1)	R19-R0	630.17(1)	332.6(2)
R19-R0	247.19(23)	272.9(2)	R19-R0	630.15(1)	332.6(2)
R19-R0	434.10(1)	272.4(2)	R19-R0	721.96(4)	332.6(2)
R19-R0	434.12(1)	272.4(2)	R19-R0	721.91(5)	332.6(2)
			R19-R0	107.08(19)	253.0(2)

6.2.2. Line intensities

For each transition from R(0) to R(19) the line intensities were retrieved at all set temperatures by simultaneously analyzing the spectra with the multispectrum fit program [87]. The line intensities retrieved by fitting to Voigt and speed-dependent Voigt are presented in Table 6-2 (A) and (B), respectively. The errors quoted in parenthesis are double the fit errors. Based on consistency tests applied to different lines, the intensities have been found to be accurate to better than 2 %.

For an easy comparison of the presented results with results available in the literature reported at 296 K, the room temperature intensities were converted to intensities at 296 K using the formula:

$$S_{J''}(T_o) = S_{J''}(T_1) \frac{T_1 Z(T_o)}{T_o Z(T_1)} \exp \left\{ -\frac{hcE_{J''}}{K} \left(\frac{1}{T_o} - \frac{1}{T_1} \right) \right\}, \quad 6-1$$

where T_1 is the measured temperature of the spectra, T_o is 296 K and $E_{J''}$ are the lower state energies reported in the HITRAN08 database [21] and the partition functions ($Z(T)$) were assumed to be nearly the same for temperature variations up to 3 K. The converted intensities given in $\text{cm} \times \text{molecule}^{-1}$ are available in Table 6-2 (A) and (B), corresponding to fits with the Voigt or speed-dependent Voigt profiles. In Figure 6-1 the ratios between the converted intensities at 296 K and the HITRAN08 [21] values are shown. With two exceptions, all ratios are below 1. In fact, the average ratio for intensities retrieved using the speed-dependent Voigt profile is 0.99, and for intensities retrieved using the Voigt profile is 0.99. Overall, the intensity measurements are in good agreement with HITRAN08 (with a difference on the order of 2 %).

Table 6-2: Line Intensities $\nu_1+\nu_2+\nu_4+\nu_5$ band of acetylene determined using (A) the Voigt profile and (B) the speed-dependent Voigt profile [111]. Here R^2 is the transition dipole moment squared.

line m		Intensity $\times 10^{24}$ (cm molecule $^{-1}$) retrieved with the Voigt profile									
		213 K	233 K	253 K	273 K	293 K	318 K	350 K	296 K	R^2 (D $\times 10^6$)	
R(0)	1	12.91(1)	12.01(2)	11.10(1)	10.23(1)	9.50(2)	1.38(3)	8.90(2)	8.87(5)	9.41(2)	1.40(3)
R(1)	2	78.80(1)	73.48(1)	67.78(1)	62.12(1)	56.92(2)	1.39(3)	51.72(2)	48.43(4)	56.20(1)	1.41(3)
R(2)	3	38.03(1)	35.68(1)	33.07(2)	30.41(2)	27.86(2)	1.39(3)	25.13(1)	22.90(2)	27.50(1)	1.41(3)
R(3)	4	145.44(1)	136.49(2)	126.70(4)	116.80(3)	107.50(1)	1.39(3)	97.84(2)	90.74(3)	106.20(1)	1.41(3)
R(4)	5	57.18(1)	54.24(1)	50.85(1)	47.26(1)	43.69(1)	1.42(3)	39.62(1)	35.72(1)	43.17(2)	1.44(3)
R(5)	6	191.27(2)	180.60(3)	168.75(2)	156.62(3)	145.09(2)	1.39(3)	132.87(2)	123.39(2)	143.46(2)	1.40(3)
R(6)	7	68.65(1)	65.00(1)	60.93(1)	56.76(1)	52.81(1)	1.39(3)	48.64(1)	45.50(1)	52.25(1)	1.41(3)
R(7)	8	208.93(2)	199.36(2)	188.33(3)	176.69(1)	165.27(1)	1.38(3)	152.61(2)	141.47(1)	163.63(2)	1.39(3)
R(8)	9	70.19(1)	67.42(1)	64.13(1)	60.58(1)	57.02(5)	1.39(3)	52.96(1)	49.13(1)	56.50(1)	1.41(3)
R(9)	10	201.90(3)	195.27(3)	187.11(3)	178.11(3)	168.93(1)	1.37(3)	158.26(2)	147.86(2)	167.58(1)	1.39(3)
R(10)	11	64.61(1)	62.89(1)	60.65(6)	58.09(2)	55.41(3)	1.38(3)	52.19(7)	48.84(6)	55.01(4)	1.39(3)
R(11)	12	179.14(2)	175.57(2)	170.58(7)	164.66(2)	158.31(6)	1.36(3)	150.50(1)	142.18(15)	157.35(3)	1.38(3)
R(12)	13	54.24(1)	53.61(1)	52.56(1)	51.21(2)	49.71(1)	1.36(3)	47.80(2)	45.70(7)	49.48(4)	1.38(3)
R(13)	14	143.64(1)	143.81(1)	142.66(3)	140.41(1)	137.28(4)	1.35(3)	132.50(3)	125.61(5)	136.75(1)	1.36(3)
R(14)	15	42.03(1)	42.47(1)	42.50(1)	42.18(1)	41.55(3)	1.35(3)	40.42(2)	38.52(8)	41.44(1)	1.36(3)
R(15)	16	106.28(2)	109.46(1)	111.41(3)	112.13(3)	111.61(4)	1.34(3)	109.17(1)	103.14(3)	111.42(1)	1.35(3)
R(16)	17	30.42(1)	31.43(1)	32.15(1)	32.56(2)	32.68(1)	1.33(3)	32.41(3)	31.40(3)	32.67(2)	1.35(3)
R(17)	18	74.85(2)	78.56(1)	81.48(2)	83.54(2)	84.71(2)	1.33(3)	84.80(2)	82.60(3)	84.80(2)	1.34(3)
R(18)	19	19.95(1)	21.39(1)	22.62(1)	23.58(2)	24.21(2)	1.32(3)	24.49(1)	23.90(2)	24.28(1)	1.33(3)
R(19)	20	48.93(1)	52.72(1)	56.00(1)	58.67(1)	60.67(2)	1.31(3)	62.05(3)	61.78(2)	60.90(3)	1.32(3)

line m		Intensity $\times 10^{24}$ (cm molecule $^{-1}$) retrieved with the Speed-Dependent Voigt profile									
		213 K	233 K	253 K	273 K	293 K	318 K	350 K	296 K	R^2 (D $\times 10^6$)	
R(0)	1	12.94(1)	12.03(2)	11.09(1)	10.21(1)	9.48(3)	1.38(3)	8.90(2)	8.92(6)	9.39(2)	1.40(3)
R(1)	2	79.03(1)	73.69(2)	67.96(1)	62.28(1)	57.06(1)	1.40(3)	51.85(2)	48.57(4)	56.34(1)	1.41(3)
R(2)	3	38.14(1)	35.77(1)	33.15(2)	30.47(1)	27.92(2)	1.40(3)	25.20(1)	22.99(2)	27.56(1)	1.41(3)
R(3)	4	145.62(3)	136.69(2)	126.92(3)	117.03(3)	107.75(1)	1.39(3)	98.11(2)	91.05(3)	106.45(1)	1.41(3)
R(4)	5	57.45(1)	54.29(1)	50.78(2)	47.19(1)	43.78(1)	1.42(3)	40.17(1)	37.39(1)	43.30(2)	1.44(3)
R(5)	6	191.61(2)	180.89(3)	169.00(2)	156.82(3)	145.25(2)	1.39(3)	133.01(2)	123.52(2)	143.63(2)	1.41(3)
R(6)	7	69.13(1)	65.17(1)	60.57(1)	56.37(1)	52.52(1)	1.38(3)	48.30(1)	44.16(1)	54.05(1)	1.46(3)
R(7)	8	209.36(3)	199.73(2)	188.65(3)	176.96(1)	165.52(1)	1.38(3)	152.84(2)	141.75(1)	163.87(2)	1.40(3)
R(8)	9	70.37(1)	67.59(1)	64.28(1)	60.72(1)	57.14(5)	1.39(3)	53.05(1)	49.19(1)	56.62(1)	1.41(3)
R(9)	10	202.21(3)	195.95(3)	188.07(4)	179.22(4)	170.03(4)	1.38(3)	159.07(2)	147.77(2)	168.67(1)	1.39(3)
R(10)	11	64.70(1)	63.03(2)	60.79(2)	58.17(2)	55.34(2)	1.37(3)	51.80(3)	47.77(2)	54.91(4)	1.39(3)
R(11)	12	179.47(2)	176.11(2)	171.21(3)	165.23(6)	158.64(3)	1.37(3)	150.55(1)	140.55(1)	157.63(3)	1.38(3)
R(12)	13	54.43(1)	53.81(1)	52.75(1)	51.39(1)	49.85(1)	1.36(3)	47.88(2)	45.67(2)	49.61(4)	1.38(3)
R(13)	14	144.08(3)	144.13(3)	142.88(5)	140.57(3)	137.43(4)	1.35(3)	132.71(3)	126.10(4)	136.90(1)	1.37(3)
R(14)	15	42.09(1)	42.59(1)	42.67(1)	42.35(2)	41.69(3)	1.35(3)	40.42(2)	38.22(2)	41.56(1)	1.36(3)
R(15)	16	106.87(3)	109.71(3)	111.37(3)	111.86(3)	111.21(4)	1.34(3)	108.78(3)	103.12(3)	111.01(1)	1.35(3)
R(16)	17	30.59(1)	31.56(1)	32.23(1)	32.61(2)	32.70(1)	1.34(3)	32.44(2)	31.49(3)	32.69(2)	1.35(3)
R(17)	18	75.19(2)	78.65(2)	81.35(2)	83.28(2)	84.39(2)	1.33(3)	84.60(2)	82.86(3)	84.49(2)	1.33(3)
R(18)	19	20.18(1)	21.46(1)	22.54(1)	23.40(1)	24.01(2)	1.31(3)	24.41(1)	24.25(2)	24.08(1)	1.32(3)
R(19)	20	49.30(1)	52.64(1)	55.56(1)	58.01(2)	59.93(2)	1.29(3)	61.33(1)	62.12(2)	60.17(3)	1.30(3)

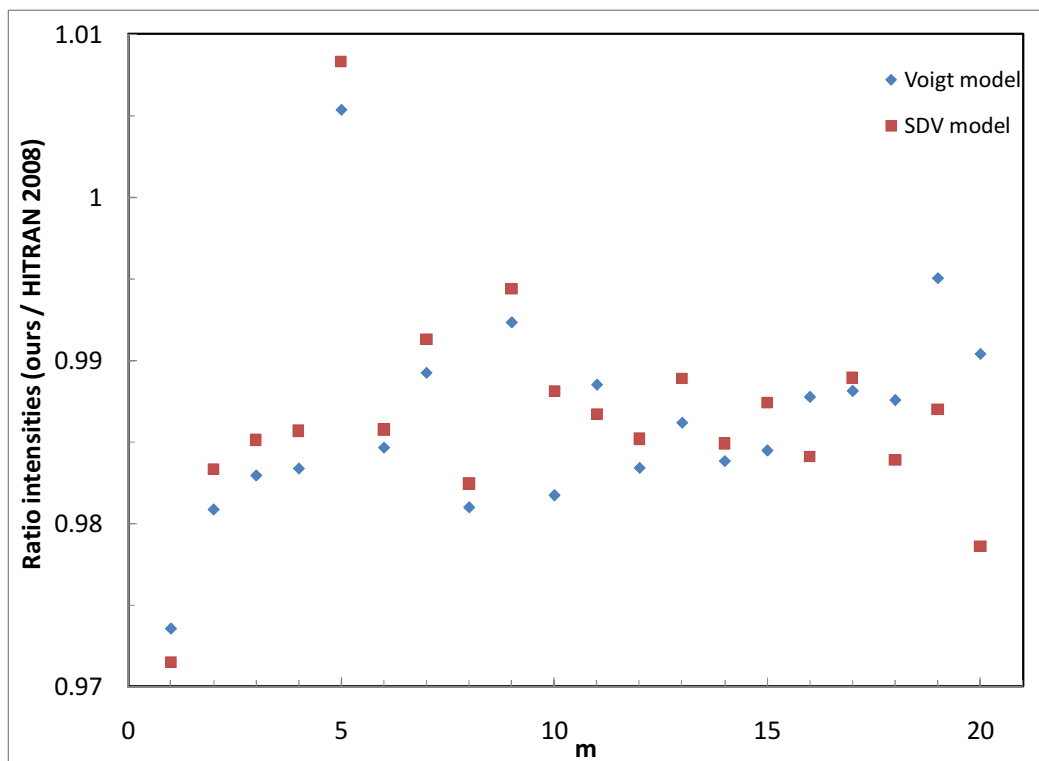


Figure 6-1: Ratios between calculated intensities at 296 K and the values from HITRAN08 [21], [111].

The transition dipole moment squared $|R|^2$ (in Debye²) were calculated using the following expression:

$$S_{J''}(T_0) = \frac{1}{4\pi\epsilon_0} \frac{8\pi^3}{3hc} \frac{\nu}{Z(T)} \exp\left\{-\frac{cE_{J''}}{KT}\right\} \left[1 - \exp\left\{-\frac{hc\tilde{\nu}}{KT}\right\}\right] |R|^2 L(J'', l) \frac{g_s}{g_L}, \quad 6-2$$

where g_s is the statistical weight due to nuclear spin of the lower level, $\tilde{\nu}$ is the transition frequency in cm⁻¹; g_l is a weight introduced in case of bands with ℓ -type doubling; $Z(T_0)$ is the total partition function at temperature T_0 ; $L(J'', l)$ is the Hönl–London factor, J'' being the rotational quantum number of the lower level of the transition, and ℓ its secondary vibrational quantum number ($\ell = |l_4 + l_5|$ for C₂H₂); E'' in cm⁻¹ is the energy of the lower level.

The $\nu_1 + \nu_2 + \nu_4 + \nu_5$ band is a parallel band with $l=0$. For R branch transitions the factor is:

$$L(J,l)=(J+1+l)(J''+1-l)/(J''+1). \quad 6-3$$

The measured values for $|R|^2$ for the 20 lines are next fitted through a least squares procedure to the following equation:

$$|R|^2 = |R_o|^2 F(m) = |R_o|^2 (1 + A_1 m + A_2 m^2)^2, \quad 6-4$$

where $|R_o|^2$ is the vibrational transition dipole moment squared, and $F(m)$ is the empirical Herman–Wallis factor. The Herman-Wallis factor can be expressed using the coefficients A_1 and A_2 and m ($m = J''+1$ for R branch transitions). The values for $|R_o|^2$, A_1 , A_2 for intensities at 293 K are: $1.39 \times 10^{-6} \text{ D}^2$, 5.87×10^{-4} and -9.58×10^{-5} (Voigt model) and $1.39 \times 10^{-6} \text{ D}^2$, 1.21×10^{-3} and -1.33×10^{-4} (SDV model). The values for $|R_o|^2$, A_1 , A_2 for intensities extrapolated to 296 K are: $1.41 \times 10^{-6} \text{ D}^2$, 5.16×10^{-4} and -1.02×10^{-4} (Voigt model) and $1.41 \times 10^{-6} \text{ D}^2$, 1.47×10^{-3} and -1.60×10^{-4} (SDV model).

6.2.3. Line broadening and pressure induced line shifts

The expressions used to retrieve the self-broadened half-width ($\gamma(p, T)$) and pressure-induced shift coefficients ($\delta^o(T)$) and their temperature dependences were derived from Section 2.5 and are as follows:

$$\gamma(p, T) = p\gamma_o(p_o, T_o) \left[\frac{T_o}{T} \right]^n, \quad 6-5$$

$$\nu = \nu_o + p\delta^o(T), \quad 6-6$$

$$\delta^o(T) = \delta^o(T_o) + \delta'_o(T - T_o), \text{ and} \quad 6-7$$

$$\delta^o(T) = \delta^o(p_o T_o) \left[\frac{T_o}{T} \right]^{n'}, \quad 6-8$$

where $p_o = 1 \text{ atm}$ and $T_o = 296 \text{ K}$ are the reference pressure and temperature. γ_o is the retrieved self-broadened halfwidth coefficient at the reference pressure p_o and temperature T_o . $\gamma(p, T)$ is the measured self-broadened half width of the spectral line and p

is the total pressure of the acetylene sample. n is the temperature dependence exponent of the self-broadened half-width coefficient. δ^0 is the pressure-induced line shift coefficient, ν is the line position, ν_0 is the position at zero pressure, and δ' is the temperature dependent coefficient of the self-induced pressure shift coefficients. Note that in this study a second law for temperature dependence of pressure shifts, namely equation 6-8 has been inspected.

Broadening coefficients were retrieved using a multispectrum fitting procedure and the Voigt and speed-dependent Voigt profiles. The values obtained for each temperature and those extrapolated to 296 K are given in Table 6-3 (A) and Figure 6-2 (A) for fits using the Voigt profile and Table 6-3 (B) and Figure 6-2 (B) for fits using the speed-dependent Voigt profile. It can be noticed that the speed-dependent Voigt results are slightly larger than those from using the Voigt. The differences between the two models and the measurements available in the literature for other bands are presented in Figure 6-8. These measurements are in good agreement with previous datasets for self-broadened acetylene.

Table 6-3: Self-broadening coefficient in the $\nu_1+\nu_2+\nu_4+\nu_5$ band of acetylene determined using (A) Voigt and (B) speed dependent Voigt profile [111].

Self-Broadening coefficients ($\text{cm}^{-1} \text{atm}^{-1}$) retrieved with the Voigt profile									
line	m	213 K	233 K	253 K	273 K	293 K	318 K	350 K	296 K
R(0)	1	0.24041(3)	0.22757(9)	0.21656(6)	0.20065(12)	0.19763(7)	0.18406(8)	0.17873(6)	0.1962(2)
R(1)	2	0.23885(3)	0.22476(8)	0.21315(6)	0.20273(11)	0.19292(7)	0.17952(8)	0.17652(6)	0.1933(2)
R(2)	3	0.22201(2)	0.21167(8)	0.20676(6)	0.19084(11)	0.1856(6)	0.17337(7)	0.16471(6)	0.1837(2)
R(3)	4	0.2137(4)	0.20202(7)	0.19362(5)	0.18546(10)	0.17585(6)	0.16829(7)	0.16108(6)	0.1768(2)
R(4)	5	0.21061(2)	0.19837(6)	0.18606(5)	0.1794(9)	0.17155(6)	0.16518(6)	0.15956(6)	0.1728(2)
R(5)	6	0.2028(5)	0.19377(3)	0.18055(4)	0.17263(9)	0.16576(4)	0.15902(4)	0.1513(3)	0.1666(2)
R(6)	7	0.20013(8)	0.18807(10)	0.17704(4)	0.17018(10)	0.16209(6)	0.15604(9)	0.14847(7)	0.1631(2)
R(7)	8	0.19588(4)	0.18278(2)	0.17292(4)	0.16509(4)	0.15722(2)	0.15016(2)	0.14305(3)	0.1584(2)
R(8)	9	0.19301(3)	0.18072(6)	0.16964(6)	0.16203(5)	0.16122(10)	0.14877(5)	0.1415(1)	0.1566(2)
R(9)	10	0.18804(5)	0.17799(1)	0.16725(4)	0.15736(3)	0.15171(5)	0.14499(4)	0.13925(8)	0.1524(2)
R(10)	11	0.18458(2)	0.17251(2)	0.16779(2)	0.15572(2)	0.15096(3)	0.13909(3)	0.13656(2)	0.1503(2)
R(11)	12	0.18271(6)	0.17077(2)	0.16227(2)	0.1542(3)	0.14602(3)	0.14172(2)	0.13737(3)	0.1486(1)
R(12)	13	0.17493(3)	0.16389(2)	0.15691(2)	0.14801(3)	0.14371(3)	0.14254(3)	0.13474(4)	0.1451(1)
R(13)	14	0.16944(3)	0.15934(3)	0.15212(5)	0.14602(2)	0.13909(3)	0.13643(2)	0.12818(3)	0.1402(1)
R(14)	15	0.16775(6)	0.15409(5)	0.14965(3)	0.14373(4)	0.1366(3)	0.13361(5)	0.1258(17)	0.1375(1)
R(15)	16	0.15902(3)	0.15083(3)	0.14527(2)	0.14066(2)	0.13352(3)	0.13022(3)	0.11992(5)	0.1341(1)
R(16)	17	0.15715(3)	0.14965(2)	0.14152(3)	0.1387(1)	0.12698(7)	0.12923(7)	0.12131(6)	0.1325(1)
R(17)	18	0.15179(2)	0.14553(2)	0.13534(3)	0.13222(1)	0.12649(2)	0.12315(2)	0.11805(6)	0.1275(1)
R(18)	19	0.14759(6)	0.13962(7)	0.13348(5)	0.12943(1)	0.12657(4)	0.12037(4)	0.11721(3)	0.1253(1)
R(19)	20	0.14491(3)	0.13633(4)	0.13005(3)	0.12341(3)	0.11723(3)	0.11286(3)	0.11287(5)	0.1201(1)

Self-Broadening coefficients ($\text{cm}^{-1} \text{atm}^{-1}$) retrieved with the Speed-Dependent Voigt profile									
line	m	213 K	233 K	253 K	273 K	293 K	318 K	350 K	296 K
R(0)	1	0.24908(31)	0.23579(43)	0.22312(18)	0.21216(22)	0.20625(44)	0.19029(6)	0.18489(9)	0.2020(2)
R(1)	2	0.24649(6)	0.22866(7)	0.22045(5)	0.20901(6)	0.19632(6)	0.18333(7)	0.17991(13)	0.1957(2)
R(2)	3	0.22913(8)	0.21482(8)	0.21295(16)	0.19622(10)	0.18878(11)	0.17686(8)	0.16799(16)	0.1866(2)
R(3)	4	0.21851(8)	0.20506(6)	0.19814(9)	0.19009(6)	0.17854(3)	0.17124(4)	0.16392(5)	0.1796(2)
R(4)	5	0.21709(8)	0.20156(7)	0.19137(8)	0.18418(7)	0.17450(5)	0.16811(6)	0.15956(6)	0.1733(2)
R(5)	6	0.20713(5)	0.19629(8)	0.18460(4)	0.17635(5)	0.16804(3)	0.16122(4)	0.15329(3)	0.1699(2)
R(6)	7	0.2060(6)	0.19119(5)	0.18246(5)	0.17495(4)	0.16524(4)	0.15896(5)	0.15110(5)	0.1667(2)
R(7)	8	0.19998(5)	0.18504(4)	0.17683(2)	0.16695(2)	0.16077(2)	0.15221(2)	0.14502(2)	0.1610(2)
R(8)	9	0.19845(5)	0.18367(5)	0.17461(5)	0.16685(5)	0.16398(17)	0.15122(4)	0.14374(5)	0.1596(2)
R(9)	10	0.19192(6)	0.18024(6)	0.17099(6)	0.16100(6)	0.15404(6)	0.14723(3)	0.14162(3)	0.1546(2)
R(10)	11	0.18570(0)	0.17602(6)	0.17016(5)	0.15758(6)	0.15207(6)	0.14420(6)	0.13440(0)	0.1515(2)
R(11)	12	0.18675(4)	0.17288(4)	0.16670(4)	0.13500(6)	0.15000(6)	0.14200(3)	0.13610(1)	0.1466(1)
R(12)	13	0.17998(7)	0.16657(6)	0.16212(6)	0.15354(5)	0.14621(4)	0.14260(6)	0.13807(4)	0.1477(1)
R(13)	14	0.17365(6)	0.16313(5)	0.15441(8)	0.14936(5)	0.14309(5)	0.13620(4)	0.13146(5)	0.1428(1)
R(14)	15	0.17176(6)	0.15665(6)	0.15486(5)	0.14827(8)	0.14127(10)	0.13702(9)	0.12494(9)	0.1401(1)
R(15)	16	0.16324(7)	0.15301(7)	0.14955(5)	0.14449(6)	0.13731(7)	0.13089(5)	0.12175(6)	0.1354(1)
R(16)	17	0.16315(5)	0.15216(5)	0.14532(7)	0.14348(8)	0.13123(8)	0.13077(12)	0.12364(15)	0.1349(1)
R(17)	18	0.15614(4)	0.14672(6)	0.13933(5)	0.13596(4)	0.12996(4)	0.12553(4)	0.12057(6)	0.1300(1)
R(18)	19	0.14759(6)	0.14213(6)	0.13806(8)	0.13245(10)	0.13094(12)	0.12272(8)	0.12051(12)	0.1277(1)
R(19)	20	0.14920(4)	0.13853(4)	0.13384(4)	0.12515(5)	0.11912(5)	0.11522(4)	0.11509(5)	0.1223(1)

The multispectrum fitting allowed for the simultaneous retrieval of the pressure-induced line shifts with the two line shape profiles. These results are presented in Table 6-4 (A) for Voigt results and Table 6-4 (B) for speed-dependent Voigt results. Figure 6-3 shows the results obtained for pressure induced shifts at room temperature. From the figure it is seen that there are only small deviations in the values determined from the two sets of shifts. The values for shifts at 296 K were extrapolated using the calculated value

for temperature exponent of the pressure induced shift (n'). These values are also reported in Table 6-4 (A) and (B) in the last column and plotted in Figure 6-3.

The results obtained for the temperature dependences of self-shift coefficients are plotted in Figure 6-4 and reported in Table 6-5. Figure 6-4 presents graphically the results obtained for temperature dependencies of pressure shifts when the empirical law from Eq. 6-8 is used (A) and when the empirical law from Eq. 6-7 is used (B). In the case of equation 6-7 δ_b' becomes negative at very low m values for both the theoretical and measured coefficients. This behavior seems unphysical and is probably due to the fact that this law is of empirical nature.

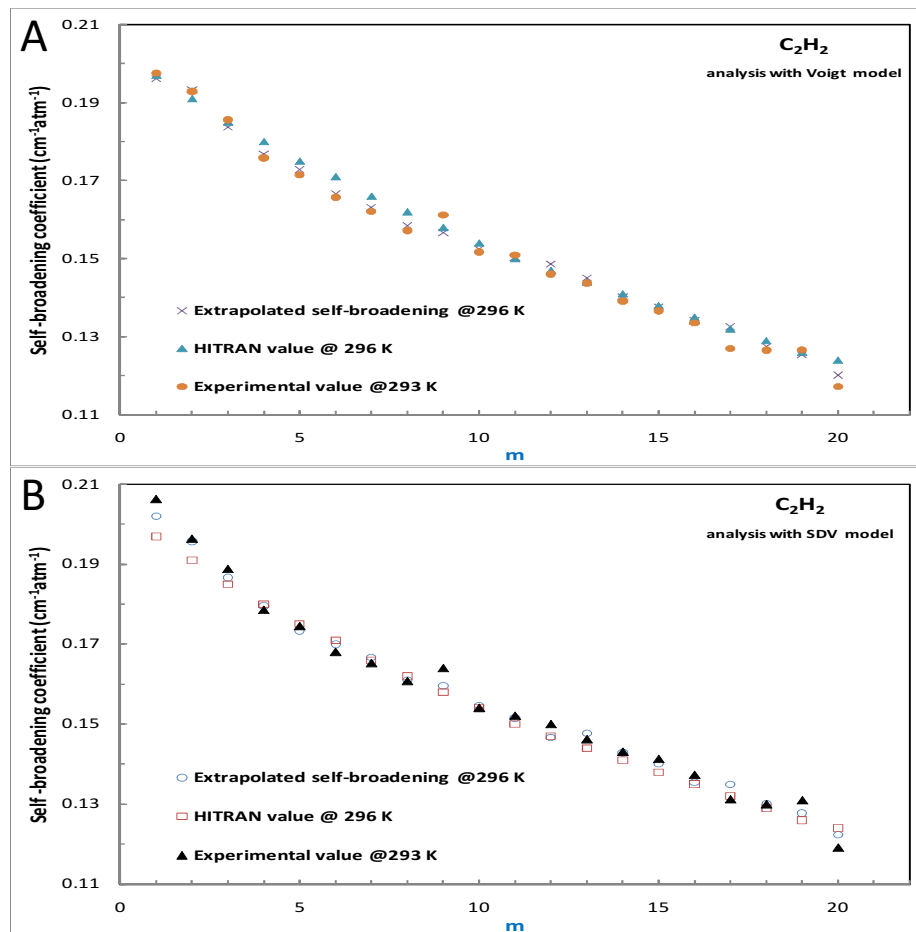


Figure 6-2: Room temperature self-broadening coefficients retrieved using the Voigt profile (A) and speed-dependent Voigt profile (B) [111].

Table 6-4: Pressure induced line self-shift coefficient in the $\nu_1+\nu_2+\nu_4+\nu_5$ band of acetylene determined using (A) the Voigt and (B) the speed dependent Voigt profile [111].

		Self-Shifting coefficients ($\text{cm}^{-1} \text{atm}^{-1}$) retrieved with the Voigt profile							
line	m	213 K	233 K	253 K	273 K	293 K	318 K	350 K	296 K
R(0)	1								
R(1)	2	-0.00147(3)	0.00411(7)	0.00056(3)	-0.00400(10)	-0.00122(5)	0.00077(5)	-0.00071(5)	-0.00108(2)
R(2)	3	0.00166(3)	-0.00042(6)	0.00202(3)	-0.00078(9)	-0.00145(5)	-0.00319(5)	-0.00483(5)	-0.00221(2)
R(3)	4	-0.00261(3)	-0.00112(6)	-0.00027(4)	-0.00202(8)	-0.00157(5)	-0.00283(5)	-0.00332(4)	-0.00214(2)
R(4)	5	-0.00441(3)	-0.00273(5)	-0.00160(4)	-0.00493(7)	-0.00452(5)	-0.00536(4)	-0.00497(4)	-0.00447(4)
R(5)	6	-0.00472(4)	-0.00312(2)	-0.00469(2)	-0.00429(5)	-0.00450(4)	-0.00416(4)	-0.00362(2)	-0.00423(4)
R(6)	7	-0.00563(5)	-0.00607(8)	-0.00422(3)	-0.00796(8)	-0.00501(6)	-0.00660(6)	-0.00413(7)	-0.00570(5)
R(7)	8	-0.00656(4)	-0.00574(2)	-0.00566(3)	-0.00607(3)	-0.00521(2)	-0.00451(2)	-0.00482(2)	-0.00481(4)
R(8)	9	-0.00711(3)	-0.00608(5)	-0.00677(10)	-0.00670(4)	-0.00883(6)	-0.00414(5)	-0.00771(6)	-0.00510(6)
R(9)	10	-0.00550(2)	-0.00488(1)	-0.00725(4)	-0.00805(2)	-0.00518(3)	-0.00601(4)	-0.00687(3)	-0.00617(6)
R(10)	11	-0.00892(2)	-0.00750(2)	-0.00760(2)	-0.00705(2)	-0.00608(3)	-0.00518(2)	-0.00765(2)	-0.00580(6)
R(11)	12	-0.00992(1)	-0.00820(2)	-0.00691(2)	-0.00708(3)	-0.00554(2)	-0.00674(2)	-0.00818(3)	-0.00567(6)
R(12)	13	-0.00914(2)	-0.00853(2)	-0.00637(1)	-0.00730(3)	-0.00759(3)	-0.00361(2)	-0.00505(3)	-0.00578(6)
R(13)	14	-0.01235(3)	-0.01100(2)	-0.01037(4)	-0.00803(2)	-0.00697(2)	-0.00713(2)	-0.00424(3)	-0.00730(8)
R(14)	15	-0.01159(4)	-0.01073(5)	-0.00957(3)	-0.00892(4)	-0.00732(3)	-0.00774(3)	-0.00650(11)	-0.00809(8)
R(15)	16	-0.01270(3)	-0.01130(2)	-0.01059(2)	-0.00918(2)	-0.00925(3)	-0.00833(2)	-0.00506(4)	-0.00890(8)
R(16)	17	-0.01444(7)	-0.01276(3)	-0.01330(1)	-0.01059(1)	-0.01078(3)	-0.01240(3)	-0.00841(2)	-0.01011(10)
R(17)	18	-0.01306(3)	-0.01160(3)	-0.01165(3)	-0.01048(4)	-0.01016(3)	-0.00895(2)	-0.00828(3)	-0.00974(10)
R(18)	19	-0.01419(4)	-0.01377(4)	-0.01179(2)	-0.01174(2)	-0.01155(2)	-0.00972(2)	-0.00881(1)	-0.01062(10)
R(19)	20	-0.01468(2)	-0.01434(36)	-0.01422(2)	-0.01285(3)	-0.01193(2)	-0.01080(2)	-0.01001(-5)	-0.01169(12)

		Self-Shifting coefficients ($\text{cm}^{-1} \text{atm}^{-1}$) retrieved with the Speed-Dependent Voigt profile							
line	m	213 K	233 K	253 K	273 K	293 K	318 K	350 K	296 K
R(0)	1	-0.00396(8)	0.0026(12)	-0.02544(6)	-0.00456(6)	-0.02717(17)	-0.00014(19)	0.00237(24)	-0.01196(4)
R(1)	2	-0.00142(2)	0.00423(2)	0.00069(1)	-0.00415(2)	-0.00123(2)	0.00080(2)	-0.00066(4)	-0.01085(3)
R(2)	3	0.00166(2)	-0.00047(3)	0.00200(5)	-0.00084(3)	-0.00150(3)	-0.00322(2)	-0.00487(4)	-0.01004(3)
R(3)	4	-0.00371(2)	-0.00121(2)	-0.00044(3)	-0.00228(2)	-0.00169(1)	-0.00303(1)	-0.00357(1)	-0.01071(3)
R(4)	5	-0.00464(2)	-0.00278(2)	-0.00169(3)	-0.00521(3)	-0.00461(2)	-0.00546(2)	-0.00497(2)	-0.00905(3)
R(5)	6	-0.00483(1)	-0.00316(2)	-0.00483(1)	-0.00446(2)	-0.00458(1)	-0.00423(1)	-0.00367(1)	-0.00810(2)
R(6)	7	-0.00582(2)	-0.00615(2)	-0.00430(1)	-0.00811(1)	-0.00499(1)	-0.00654(2)	-0.00408(2)	-0.00789(2)
R(7)	8	-0.00675(1)	-0.00584(1)	-0.00586(1)	-0.00621(1)	-0.00548(1)	-0.00457(1)	-0.00494(1)	-0.00615(2)
R(8)	9	-0.00734(1)	-0.00620(1)	-0.00699(2)	-0.00698(2)	-0.00906(5)	-0.00420(1)	-0.00783(2)	-0.00618(2)
R(9)	10	-0.00558(1)	-0.00492(2)	-0.00741(2)	-0.00721(2)	-0.00524(2)	-0.00607(1)	-0.00696(1)	-0.00661(2)
R(10)	11	-0.00960(1)	-0.00906(2)	-0.00772(1)	-0.00902(2)	-0.00406(2)	-0.00596(2)	-0.00357(3)	-0.00626(2)
R(11)	12	-0.01015(1)	-0.00829(1)	-0.00859(1)	-0.00820(3)	-0.00704(1)	-0.01288(3)	-0.00568(3)	-0.00510(2)
R(12)	13	-0.00939(2)	-0.00866(2)	-0.00664(2)	-0.00738(2)	-0.00769(1)	-0.00559(2)	-0.00570(1)	-0.00484(1)
R(13)	14	-0.01125(2)	-0.01053(2)	-0.00960(3)	-0.00872(1)	-0.00743(2)	-0.00384(1)	-0.00468(2)	-0.00487(1)
R(14)	15	-0.01175(2)	-0.01098(2)	-0.01006(1)	-0.00893(3)	-0.00778(3)	-0.00740(3)	-0.00954(3)	-0.00431(2)
R(15)	16	-0.01308(2)	-0.01256(2)	-0.01092(2)	-0.00945(2)	-0.00969(2)	-0.00878(2)	-0.00594(2)	-0.00430(2)
R(16)	17	-0.01602(1)	-0.01302(2)	-0.01523(2)	-0.01123(2)	-0.01142(2)	-0.01177(4)	-0.00871(5)	-0.00205(1)
R(17)	18	-0.01332(1)	-0.01167(2)	-0.01201(2)	-0.01081(1)	-0.01051(1)	-0.00939(1)	-0.00847(2)	-0.00236(1)
R(18)	19	-0.01419(2)	-0.01417(2)	-0.01224(2)	-0.01209(3)	-0.01211(4)	-0.00996(2)	-0.00819(4)	-0.00295(2)
R(19)	20	-0.01519(1)	-0.01461(1)	-0.01471(1)	-0.01240(2)	-0.01222(2)	-0.01102(1)	-0.01017(2)	-0.00220(1)

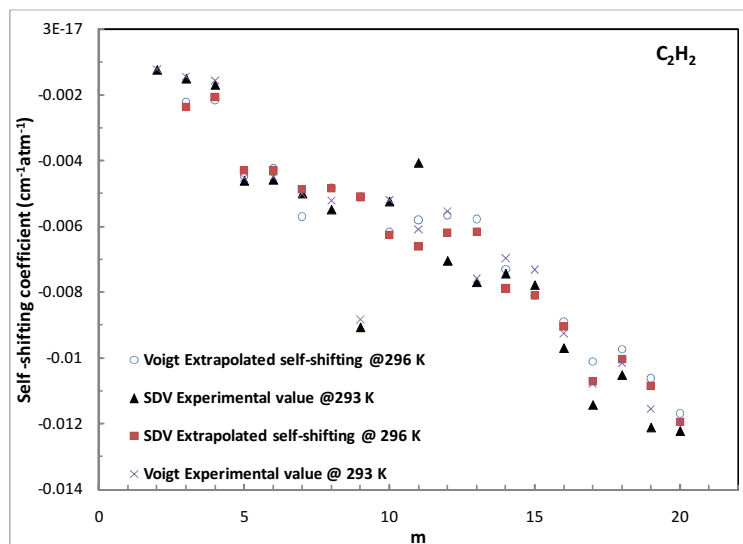


Figure 6-3: Room temperature pressure induced self-shift coefficients obtained using the Voigt and speed-dependent Voigt profiles [111].

Table 6-5: Temperature dependences for self broadening coefficients (obtained using Eq. 6-5) (\mathbf{n}) and pressure induced self-shift coefficients (obtained from Eq. 6-7 (\mathbf{n}') and 6-8 (δ')) in the $\nu_1+\nu_2+\nu_4+\nu_5$ band of acetylene[111]. Numbers in the brackets represent the statistical error associated with the last digit of the determined value.

m	\mathbf{n}		δ'		\mathbf{n}'	
	SDV	Voigt	SDV	Voigt	SDV	Voigt
1	0.60(3)	0.62(3)	0.000033(2)	-	0.97(5)	-
2	0.62(3)	0.63(3)	-0.000004(1)	0.000005(1)	1.19(6)	1.04(5)
3	0.60(3)	0.62(3)	-0.000050(2)	-0.000046(2)	0.98(5)	1.08(5)
4	0.57(3)	0.59(3)	-0.000023(2)	-0.000012(1)	1.04(5)	1.16(6)
5	0.56(3)	0.58(3)	0.000003(1)	-0.000016(1)	1.23(6)	1.19(6)
6	0.59(3)	0.60(3)	0.000008(1)	0.000008(1)	1.19(6)	1.10(5)
7	0.59(3)	0.61(3)	0.000011(1)	0.000006(1)	1.12(6)	1.01(5)
8	0.61(3)	0.63(3)	0.000022(1)	0.000019(1)	1.20(6)	1.14(6)
9	0.60(3)	0.63(3)	0.000029(1)	0.000026(1)	1.15(6)	1.16(6)
10	0.62(3)	0.63(3)	0.000025(1)	0.000028(1)	1.06(5)	1.10(6)
11	0.61(3)	0.63(3)	0.000039(2)	0.000036(2)	1.27(6)	1.27(6)
12	0.58(3)	0.59(3)	0.000026(1)	0.000015(1)	1.20(6)	1.17(6)
13	0.55(3)	0.56(3)	0.000021(1)	0.000016(1)	1.12(6)	1.17(6)
14	0.55(3)	0.56(3)	0.000044(2)	0.000058(3)	1.08(5)	1.10(5)
15	0.55(3)	0.56(3)	0.000044(2)	0.000038(2)	1.12(6)	1.20(6)
16	0.52(3)	0.53(3)	0.000049(2)	0.000041(2)	1.03(5)	1.17(6)
17	0.50(3)	0.51(3)	0.000049(2)	0.000048(2)	1.04(5)	1.06(5)
18	0.51(3)	0.52(3)	0.000035(2)	0.000035(2)	1.04(5)	0.93(5)
19	0.46(2)	0.48(2)	0.000045(2)	0.000042(2)	0.95(5)	0.92(5)
20	0.53(3)	0.54(3)	0.000041(2)	0.000037(2)	0.91(5)	0.95(5)

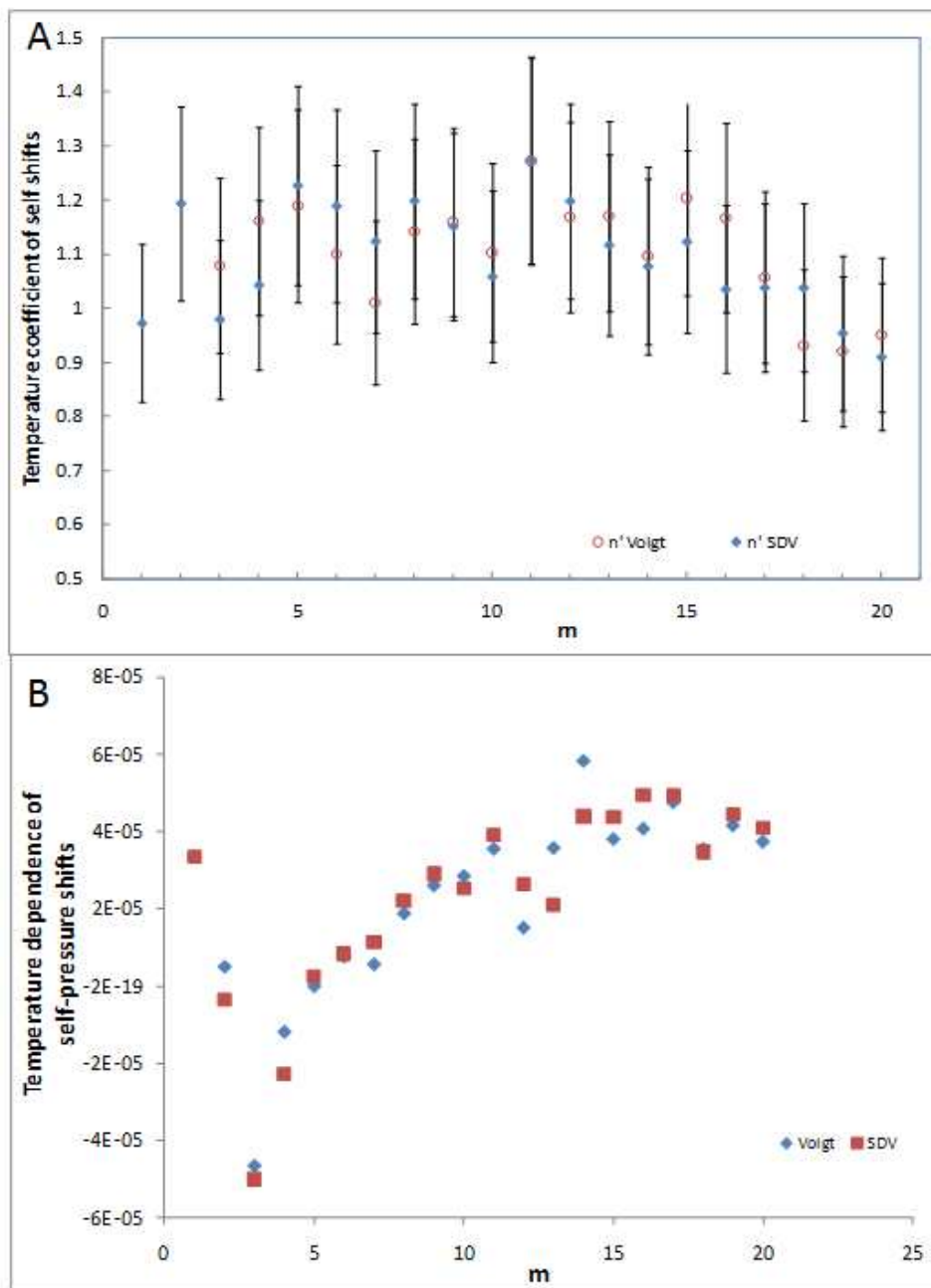


Figure 6-4: Temperature dependence coefficients for pressure shifts retrieved using equations 6-8 (A) and 6-7 (B) [111].

6.2.4. Weak line-mixing effects

In this study it was found necessary to account for weak line mixing effects. The line mixing effects accounting for collisional transfer between pairs of energy levels j and k are modeled within the software by adding an asymmetric profile to the Voigt or speed-dependent Voigt profiles as follows:

$$pY_{ok}(T) = 2p \sum_{j \neq k} \frac{\mu_j}{\mu_k} \frac{W_{jk}}{\tilde{\nu}_k - \tilde{\nu}_j}, \quad 6-9$$

Here p is the gas pressure in atm and $Y_{ok}(T)$ is the weak line mixing coefficient of the transition of interest, μ_k are the elements of the dipole moment matrix, W_{jk} are off-diagonal elements of the relaxation matrix that describes the state of the molecule at a given time, and $\tilde{\nu}_k$ are line positions. Note that the self-broadening coefficients are the real parts of the diagonal elements of the relaxation matrix, W , and the pressure-induced line shift coefficients are the imaginary parts of the diagonal elements.

Line mixing coefficients for the spectra at room temperature were obtained from multispectral fits of spectra recorded in the laboratory. However, for consistency in the multispectrum fits at other temperatures, modeled spectral profiles using calculated line-mixing coefficients obtained from the Exponential Power Gap scaling law (EPG) were used. The calculated and room temperature measured line mixing coefficients are given for the two line shape profiles in Table 6-6 (A) and (B). The calculated sets used in fits with the speed dependent Voigt profile are slightly different (on average about 0.5%) than those obtained for the Voigt profile due to the small differences in line broadening and in the intensities retrieved with the two profiles.

Table 6-6: Calculated and measured self-line mixing coefficient in the $\nu_1+\nu_2+\nu_4+\nu_5$ band of acetylene determined using (A) the Voigt and (B) the speed-dependent Voigt profiles [111].

Self-Line mixing coefficients (atm^{-1}) retrieved with the Voigt profile									
line	m	213 K	233 K	253 K	273 K	293 K	318 K	350 K	293 K experimental
R(1)	1	0.0871(124)	0.0809(115)	0.0755(108)	0.0708(101)	0.0665(95)	0.0621(89)	0.0574(82)	0.0191(12)
R(1)	2	0.0313(16)	0.0296(15)	0.0281(14)	0.0268(13)	0.0256(13)	0.0243(12)	0.0229(11)	0.0243(1)
R(2)	3	0.0204(12)	0.0197(12)	0.0191(11)	0.0185(11)	0.0180(11)	0.0173(10)	0.0166(10)	0.0017(4)
R(3)	4	0.0130(6)	0.0130(6)	0.0130(6)	0.0129(6)	0.0128(6)	0.0125(6)	0.0121(6)	0.0157(1)
R(4)	5	0.0074(1)	0.0079(2)	0.0083(2)	0.0086(2)	0.0088(2)	0.0088(2)	0.0088(2)	0.0048(1)
R(5)	6	0.0030(1)	0.0039(1)	0.0046(1)	0.0052(1)	0.0056(1)	0.0059(1)	0.0060(1)	-0.0003(1)
R(6)	7	-0.0005(1)	0.0007(1)	0.0016(1)	0.0024(1)	0.0030(1)	0.0035(1)	0.0038(1)	-0.0018(1)
R(7)	8	-0.0035(1)	-0.0021(1)	-0.0009(1)	0.0001(1)	0.0008(1)	0.0014(1)	0.0019(1)	0.0002(1)
R(8)	9	-0.0060(1)	-0.0044(1)	-0.0031(1)	-0.0021(1)	-0.0012(1)	-0.0005(1)	0.0001(1)	0.0096(3)
R(9)	10	-0.0082(2)	-0.0065(1)	-0.0051(1)	-0.0039(1)	-0.0030(1)	-0.0021(1)	-0.0014(1)	-0.0007(1)
R(10)	11	-0.0102(2)	-0.0083(2)	-0.0068(2)	-0.0056(1)	-0.0046(1)	-0.0037(1)	-0.0029(1)	-0.0119(2)
R(11)	12	-0.0120(3)	-0.0100(3)	-0.0084(2)	-0.0072(2)	-0.0061(2)	-0.0051(1)	-0.0043(1)	0.0001(1)
R(12)	13	-0.0136(2)	-0.0116(2)	-0.0100(2)	-0.0087(2)	-0.0076(1)	-0.0066(1)	-0.0056(1)	-0.0060(1)
R(13)	14	-0.0152(1)	-0.0132(1)	-0.0115(1)	-0.0102(1)	-0.0090(1)	-0.0080(1)	-0.0070(1)	-0.0160(1)
R(14)	15	-0.0169(1)	-0.0149(1)	-0.0131(1)	-0.0117(1)	-0.0106(1)	-0.0095(1)	-0.0085(1)	-0.0201(2)
R(15)	16	-0.0185(4)	-0.0165(3)	-0.0149(3)	-0.0135(3)	-0.0123(3)	-0.0113(2)	-0.0102(2)	-0.0233(2)
R(16)	17	-0.0206(3)	-0.0186(3)	-0.0170(3)	-0.0156(2)	-0.0145(2)	-0.0134(2)	-0.0123(2)	-0.0411(2)
R(17)	18	-0.0235(7)	-0.0216(6)	-0.0200(6)	-0.0186(5)	-0.0174(5)	-0.0163(5)	-0.0152(4)	-0.0191(1)
R(18)	19	-0.0291(2)	-0.0271(2)	-0.0254(2)	-0.0239(2)	-0.0227(2)	-0.0214(2)	-0.0201(2)	-0.0381(4)
R(19)	20	-0.0467(13)	-0.0438(14)	-0.0414(14)	-0.0392(13)	-0.0373(12)	-0.0354(12)	-0.0333(11)	-0.0132(1)

Self-Line mixing coefficients (atm^{-1}) retrieved with the Speed-dependent Voigt profile								
line	m	213 K	233 K	253 K	273 K	293 K	318 K	350 K
R(1)	1	0.0899(136)	0.0833(126)	0.0776(118)	0.0726(110)	0.0682(103)	0.0635(96)	0.0585(89)
R(1)	2	0.0316(18)	0.0298(17)	0.0283(16)	0.0270(15)	0.0258(15)	0.0245(14)	0.0230(13)
R(2)	3	0.0205(13)	0.0199(12)	0.0192(12)	0.0187(11)	0.0181(11)	0.0174(11)	0.0166(10)
R(3)	4	0.0130(6)	0.0131(6)	0.0130(6)	0.0129(6)	0.0128(6)	0.0126(6)	0.0122(6)
R(4)	5	0.0074(2)	0.0080(3)	0.0084(3)	0.0086(3)	0.0083(3)	0.0089(3)	0.0088(3)
R(5)	6	0.0030(1)	0.0039(1)	0.0046(1)	0.0052(1)	0.0056(1)	0.0059(1)	0.0061(1)
R(6)	7	-0.0006(1)	0.0007(1)	0.0016(1)	0.0024(1)	0.0030(1)	0.0035(1)	0.0038(1)
R(7)	8	-0.0036(1)	-0.0021(1)	-0.0009(1)	0.0001(1)	0.0008(1)	0.0014(1)	0.0019(1)
R(8)	9	-0.0061(2)	-0.0045(1)	-0.0032(1)	-0.0021(1)	-0.0012(1)	-0.0005(1)	0.0002(1)
R(9)	10	-0.0084(2)	-0.0066(1)	-0.0051(1)	-0.0039(1)	-0.0030(1)	-0.0021(1)	-0.0014(1)
R(10)	11	-0.0103(2)	-0.0084(2)	-0.0069(1)	-0.0056(1)	-0.0046(1)	-0.0037(1)	-0.0029(1)
R(11)	12	-0.0121(1)	-0.0102(1)	-0.0086(1)	-0.0072(1)	-0.0061(1)	-0.0052(1)	-0.0043(1)
R(12)	13	-0.0138(3)	-0.0118(3)	-0.0101(2)	-0.0088(2)	-0.0076(2)	-0.0066(2)	-0.0057(1)
R(13)	14	-0.0155(1)	-0.0134(1)	-0.0117(1)	-0.0103(1)	-0.0091(1)	-0.0081(1)	-0.0071(1)
R(14)	15	-0.0171(1)	-0.0150(1)	-0.0133(1)	-0.0119(1)	-0.0107(1)	-0.0096(1)	-0.0086(1)
R(15)	16	-0.0189(5)	-0.0168(4)	-0.0151(4)	-0.0137(3)	-0.0125(3)	-0.0114(3)	-0.0104(3)
R(16)	17	-0.0210(3)	-0.0189(2)	-0.0173(2)	-0.0159(2)	-0.0147(2)	-0.0136(2)	-0.0125(2)
R(17)	18	-0.0240(6)	-0.0220(6)	-0.0203(5)	-0.0189(5)	-0.0177(5)	-0.0165(4)	-0.0154(4)
R(18)	19	-0.0297(2)	-0.0276(2)	-0.0258(2)	-0.0243(2)	-0.0230(2)	-0.0217(2)	-0.0203(2)
R(19)	20	-0.0476(14)	-0.0446(13)	-0.042(12)	-0.0398(12)	-0.0379(11)	-0.0358(11)	-0.0336(10)

Analysis of the EPG law was completed using the expressions outlined in Section 2.6.3. The temperature dependence of the collisional rates and the empirical fit parameters a , b , c , (from equation 2-88) are presented in Table 6-7. It was found that a was slowly decreasing with increasing temperature, b remained almost constant while c slowly decreased with increase of temperature.

Table 6-7: Empirical fit parameters for the EPG scaling law [111]. Once again the numbers in brackets denote the statistical error in the obtained values.

<i>Voigt model</i>			
Temperature (K)	a	b	c
213	0.179308(1)	0.410966(1)	0.963011(1)
233	0.165627(1)	0.414418(1)	0.915323(1)
253	0.15372(4)	0.417081(9)	0.865015(4)
273	0.143115(15)	0.418714(12)	0.813391(13)
293	0.133617(1)	0.419518(1)	0.760618(1)
318	0.123812(1)	0.419669(1)	0.707401(1)
350	0.113519(1)	0.418775(1)	0.652258(1)
<i>Speed Dependent Voigt model</i>			
Temperature (K)	a	b	c
213	0.187117(1)	0.420135(1)	0.943237(6)
233	0.172517(1)	0.423451(1)	0.89383(1)
253	0.159819(15)	0.425945(12)	0.841929(13)
273	0.148527(1)	0.427388(1)	0.78882(3)
293	0.138429(1)	0.427986(1)	0.734671(1)
318	0.127995(1)	0.427853(1)	0.679867(1)
350	0.117044(14)	0.42658(17)	0.622872(12)

Figure 6-5 (A) shows overlaid measured and calculated line mixing coefficients obtained at room temperature. The variation of calculated line mixing coefficients with temperature can be observed in Figure 6-5 (B) (all results plotted against m). The plotted values correspond only to R-branch transitions and cover the range of experimental m values. The EPG scaling law modeled the entire range of rotational states, but it does not fit perfectly the measured broadening parameters. However for $|m|$ values between 4 and 15 the model provides a good agreement with the experimental results.

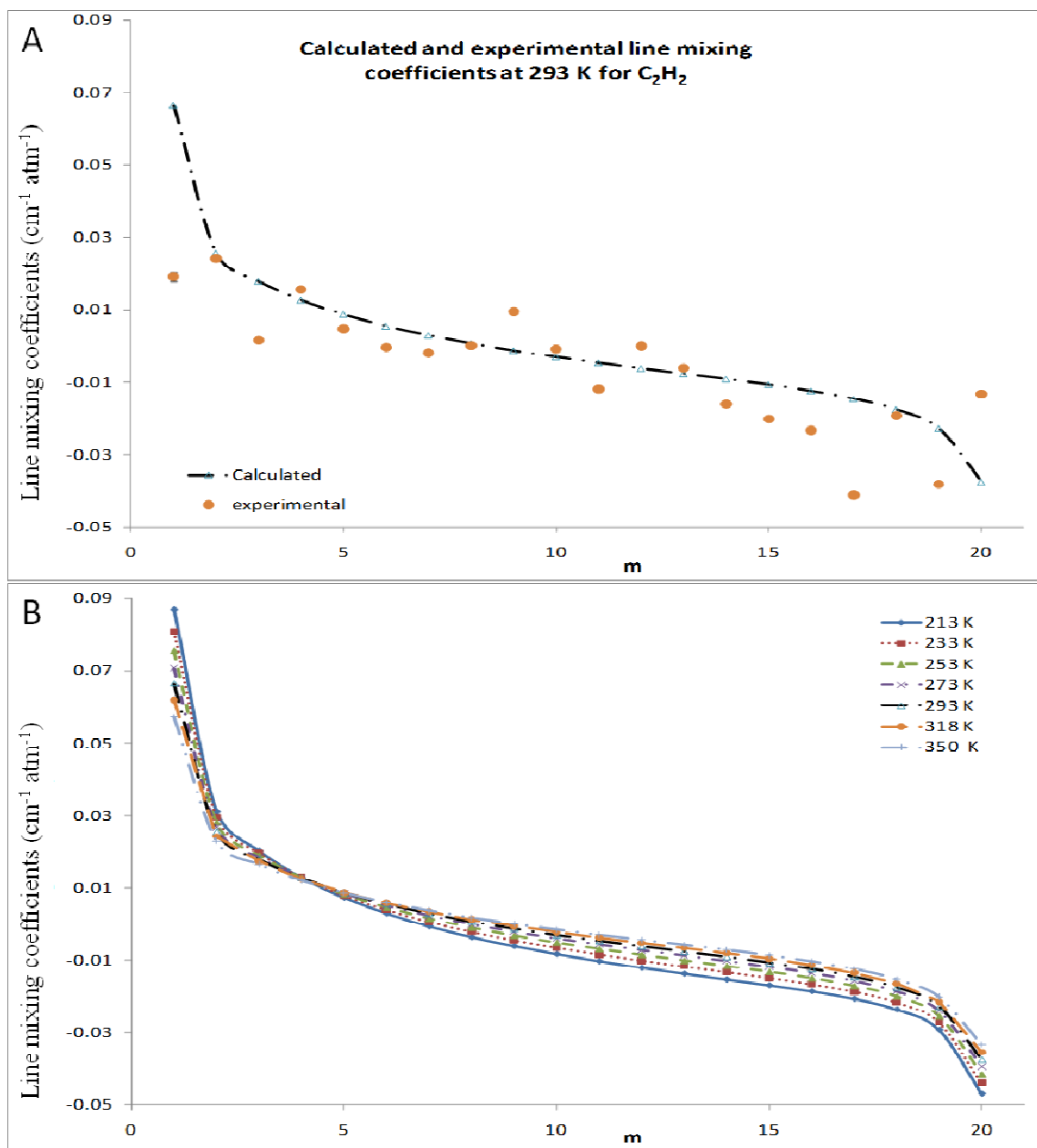


Figure 6-5: (A) Overlaid calculated and measured weak self-line mixing coefficients at room temperature. (B) Calculated line mixing coefficients at the experimental temperatures [111].

6.3. Low-Pressure line shape study of acetylene transitions in the $\nu_1+\nu_2+\nu_4+\nu_5$ band over a range of temperatures

6.3.1. Introduction

This study focused on the retrieval of self-broadened widths, self-pressure-induced shifts, and Dicke narrowing coefficients for twenty R-branch transitions in the $\nu_1+\nu_2+\nu_4+\nu_5$ band of acetylene. The spectra were recorded using the TDLS discussed in detail in Chapter 3. The soft collision (Galatry) and hard collision (Rautian) profiles with inclusion of line mixing effects were used to retrieve the line parameters. The temperature dependences for line broadening, shift, and Dicke narrowing coefficients have been examined.

The motivation for this particular work stems from the lack of temperature dependant studies that have been reported for the acetylene molecule. One of the first studies to investigate low-temperature broadening was the work by Lambot et al. [8]. More recent studies by Dhyne et al. [115] and Povey et al. [111] have ascertained the temperature dependences of both self-broadening and self-shift coefficients. Of the works mentioned above, several authors suggest the need for a diffusion line shape model when examining spectra at pressures below 100 Torr [13, 16, 20, 115, 116]. The measurements by Herregodts et al. [13] and Valipour et al. [16] included the narrowing coefficients for both hard and soft collisions line shape models at room temperature. However, to date there has been no study of the narrowing coefficient and its temperature dependence available in the literature.

6.3.2. Analysis and experimental overview

For intermediate pressures the use of the Voigt function is only effective as long as the mean free path of the molecules is sufficiently large when compared to the wavelength of the incident radiation λ . If the mean free path becomes equal to or less than λ , the resulting motion of the molecules then becomes Brownian in nature and thus the diffusion of the gas becomes relevant. The pressure regime for which this condition applies is known as the “Dicke narrowing” regime and the associated line shapes are narrowed.

The two most common models used to describe the Dicke narrowing regime are the Galatry [45] (soft collision model) and Rautian (hard collision model) [47] line shape functions. These models were discussed in detail in Chapter 2. Figure 6-6 shows the results of fitting the R(13) line of the $\nu_1+\nu_2+\nu_4+\nu_5$ band using a Voigt, Galatry (soft collision) and Rautian (hard collision) line shape models. It is clear from Figure 6-6 that the spectra were recorded in the Dicke narrowing regime as it can be seen that there is a ‘w’ type residual when the spectral feature is fit using a Voigt profile. What is not immediately clear is whether the Soft or Hard collision model is a better choice for modeling these features. Therefore, a complete analysis has been performed using both the Galatry and Rautian line shape models.

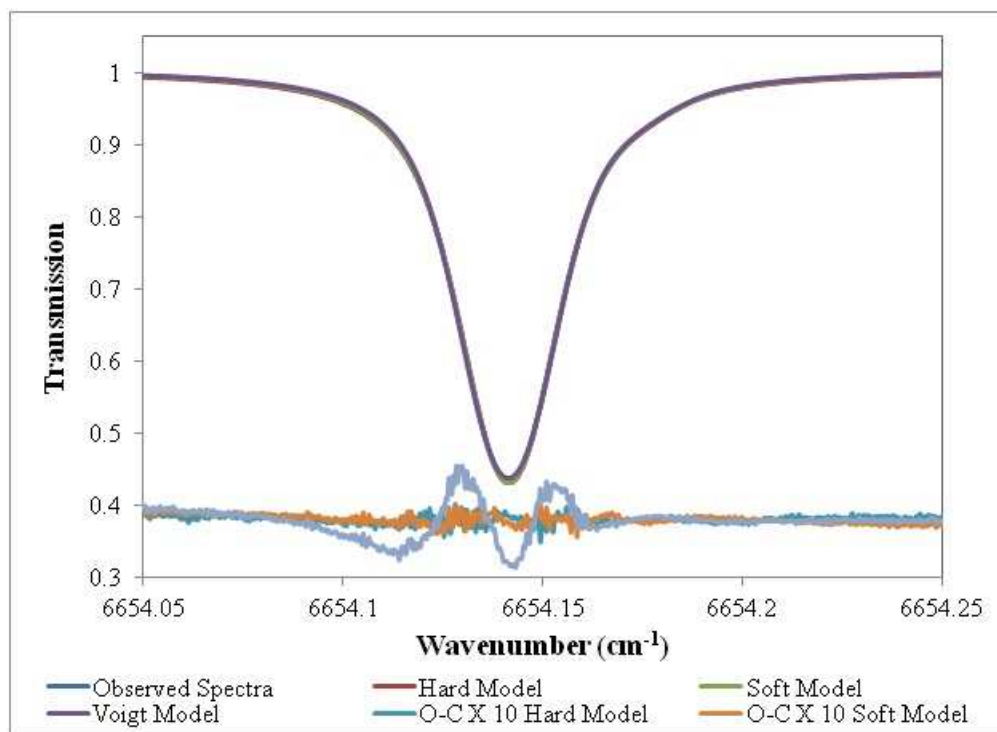


Figure 6-6: Observed and calculated spectra for the R(13) transition of the $\nu_1 + \nu_2 + \nu_4 + \nu_5$ band of C_2H_2 . Here the residuals have been vertically shifted and magnified for easier comparison [112].

To complete a careful examination of the temperature dependence for self- shift, self-broadening and narrowing coefficients, spectra were recorded for the R(0) to R(19) transitions of the $\nu_1 + \nu_2 + \nu_4 + \nu_5$ band using C_2H_2 provided by Praxair with a quoted purity of 99.6 %. For each line, spectra were recorded at six separate pressures: 10, 25, 40, 65, 90, and 115 Torr and at seven different temperatures: 213, 233, 253, 273, 293, 313 and 333 K. Table 6-8 shows the experimental conditions for each scan completed.

Table 6-8: Experimental conditions (each scan takes approximately 3.5 hrs).

Lines Scanned	Average Cell Temperature (K)	Temperature Deviation During scan (K)	Average Chamber Gradient (K/m)	Average Pressure During Scan (Torr)	Pressure Deviation During Scan (Torr)
R19 to R0	214.09	0.91	1.14	22.829	0.012
R19 to R0	214.18	0.86	1.11	36.939	0.016
R19 to R0	214.33	1.06	1.39	9.623	0.002
R19 to R0	233.46	0.41	0.49	40.189	0.012
R19 to R0	233.68	0.54	0.65	10.465	0.003
R19 to R0	233.73	0.53	0.65	24.866	0.001
R19 to R0	253.17	0.25	0.28	43.520	0.007
R19 to R0	253.24	0.29	0.32	26.908	0.005
R19 to R0	253.24	0.26	0.29	11.318	0.001
R19 to R0	272.81	0.14	0.05	10.342	0.001
R19 to R0	272.85	0.17	0.15	25.330	0.004
R19 to R0	272.93	0.16	0.21	40.635	0.002
R19 to R0	292.81	0.17	0.06	43.547	0.001
R19 to R0	292.82	0.16	0.07	27.149	0.001
R19 to R0	292.83	0.17	0.07	11.089	0.001
R19 to R0	312.80	0.19	0.03	40.482	0.003
R19 to R0	312.81	0.20	0.03	9.505	0.001
R19 to R0	312.82	0.20	0.05	24.261	0.001
R19 to R0	332.53	0.24	-0.11	42.992	0.001
R19 to R0	332.53	0.24	-0.11	10.093	0.001
R19 to R0	332.58	0.22	-0.06	25.774	0.002

The line parameters were obtained by using a weighted multispectrum analysis software [87]. Multispectrum fits were performed on spectra of varying pressures that were recorded at the same set temperature. Through the use of a non-linear least squares fitting routine, the line parameters were optimized by minimizing the residual. The initial parameter values for self- broadening and shift used in the fitting procedure were taken from Refs. [111] and [21].

Although the effects due to line mixing are not clearly evident at the pressures studied here, line mixing effects have been included in the line shape model. In the weak line-mixing regime, the spectral lines are slightly asymmetric. Therefore, the line asymmetry was handled in the same manner as outlined in Section 6.2.4 using the line mixing coefficients presented in that section for the individual transitions.

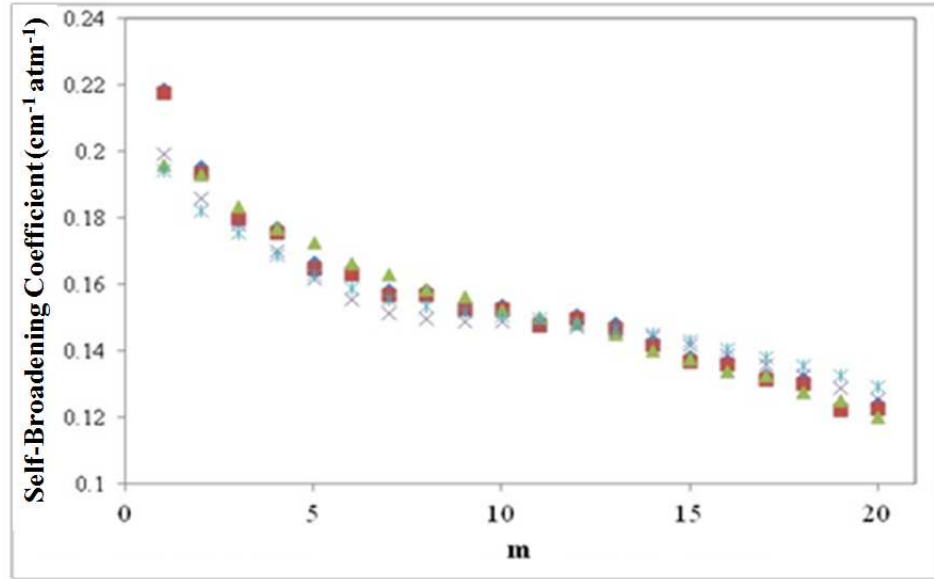
6.3.3. Self –broadening

Using equation 6-5 we the temperature dependence exponents of the self-broadening coefficients were determined. Table 6-9 shows the self-broadening coefficients that were obtained for both the Soft and Hard collision models at the temperature of 293 K. The table also shows the retrieved temperature dependence exponents n .

Figure 6-7 shows the self-broadening coefficients that were obtained from spectra recorded at 293 K. The results indicate very close agreement with both theoretical calculations published by Bouanich and Predoi-Cross [117] and our previous analysis [111] using a Voigt profile. A further comparison to many of the preceding studies is given in Figure 6-8. It is clear from this figure that the self-broadening coefficient determined at 293 K from present measurements are in agreement with the majority of the results reported in the last decade or so.

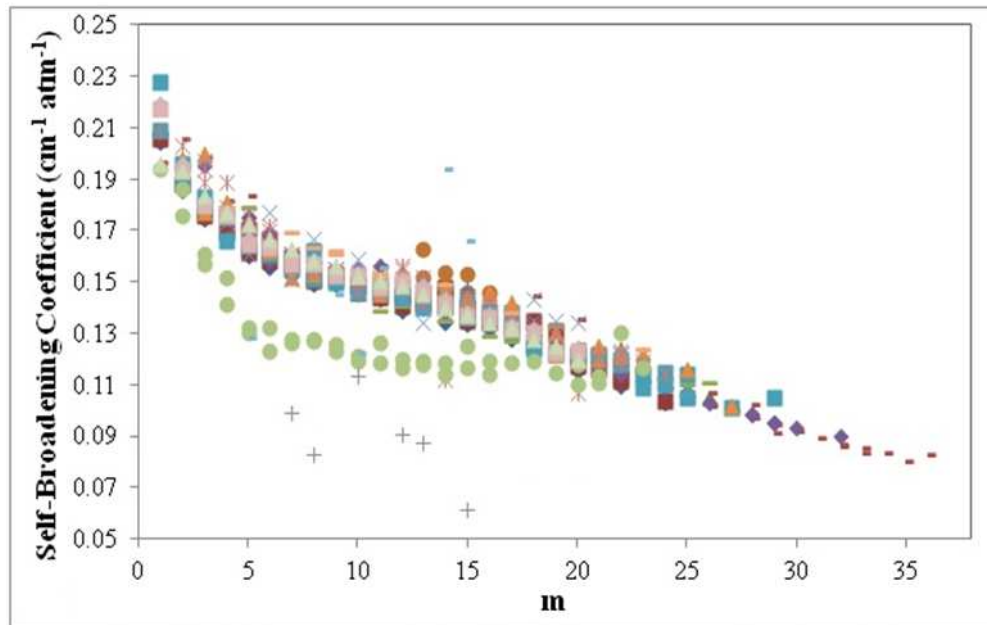
Table 6-9: Self Broadening coefficients at 293 K and temperature dependence exponents n for both the Soft and Hard collision line shape models [112].

Retrieved self-broadening coefficients ($\text{cm}^{-1} \text{atm}^{-1}$) at 293 K and their temperature dependence exponents (unit-less)					
Line	m	Soft γ_0	Soft n	Hard γ_0	Hard n
R(0)	1	0.219(2)	0.63(7)	0.218(2)	0.65(7)
R(1)	2	0.196(2)	0.70(1)	0.194(2)	0.71(1)
R(2)	3	0.182(2)	0.77(3)	0.180(2)	0.78(3)
R(3)	4	0.177(2)	0.65(1)	0.176(2)	0.66(1)
R(4)	5	0.167(2)	0.69(1)	0.165(2)	0.70(1)
R(5)	6	0.165(2)	0.68(2)	0.163(2)	0.70(1)
R(6)	7	0.159(2)	0.72(2)	0.157(2)	0.73(2)
R(7)	8	0.158(2)	0.68(1)	0.157(2)	0.69(1)
R(8)	9	0.154(2)	0.70(1)	0.153(2)	0.71(1)
R(9)	10	0.154(2)	0.71(2)	0.153(2)	0.72(2)
R(10)	11	0.150(1)	0.72(2)	0.148(1)	0.74(2)
R(11)	12	0.151(2)	0.68(1)	0.150(1)	0.69(1)
R(12)	13	0.148(1)	0.64(1)	0.147(1)	0.65(1)
R(13)	14	0.143(1)	0.64(1)	0.142(1)	0.65(1)
R(14)	15	0.138(1)	0.66(2)	0.137(1)	0.67(2)
R(15)	16	0.137(1)	0.61(1)	0.136(1)	0.62(1)
R(16)	17	0.133(1)	0.60(2)	0.132(1)	0.62(2)
R(17)	18	0.132(1)	0.51(1)	0.130(1)	0.56(1)
R(18)	19	0.124(1)	0.59(2)	0.122(1)	0.60(1)
R(19)	20	0.124(1)	0.56(2)	0.123(1)	0.57(2)



- ◆ Present Work: Soft collision (293 K) [112]
- ▲ Present Work: Voigt [111]
- ✱ Bouanich and Predoi-Cross (DV) [117]
- Present Work: Hard collision [112]
- ✕ Bouanich and Predoi-Cross (MV) [117]

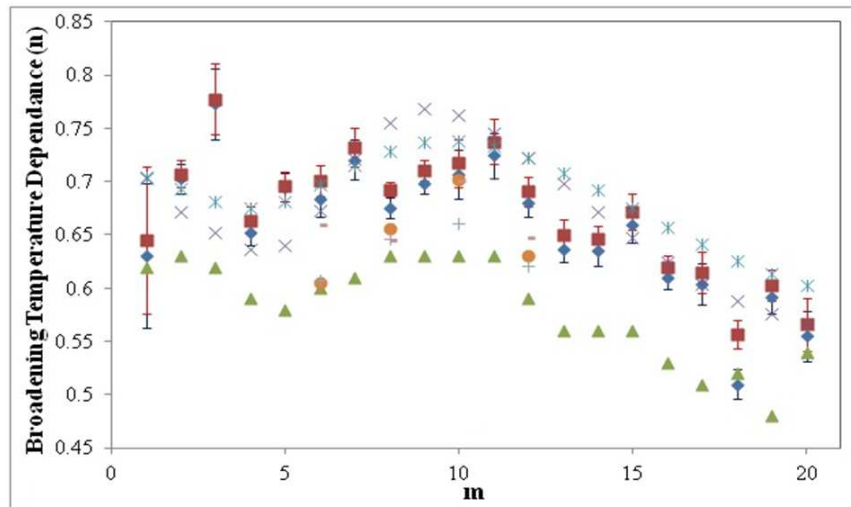
Figure 6-7: Self Broadening Coefficients at 293 K [112].



- ◆ v_4+v_5 Voigt Ref. [18]
- v_4+v_5 Hard Ref. [18]
- ▲ v_1+v_3 Ref. [15]
- ✕ v_1+v_3 Voigt Ref. [20]
- ✱ v_1+v_3 Hard Ref. [20]
- $v_1+v_3+v_4-v_4$ Ref. [15]
- + $v_1+v_3+v_5-v_5$ Ref. [15]
- $3v_5$ Ref. [17]
- $2v_4+v_5$ I Ref. [17]
- ◆ $2v_4+v_5$ II Ref. [17]
- v_2+v_3 Ref. [19]
- ▲ $v_1+(2v_4+v_5)$ I Ref. [19]
- ✱ $v_2+v_3+v_4$ Ref. [19]
- ✕ $v_1+v_3-v_4$ Ref. [19]
- v_1+3v_3 Ref. [13]
- + v_1+3v_3 Ref. [12]
- v_1+3v_3 Ref. [14]
- v_1+3v_3 Ref. [16]
- $v_1+v_2+v_4+v_5$ Voigt Ref. [111]
- ◆ $v_1+v_2+v_4+v_5$ SDV Ref. [111]

Figure 6-8: Comparison of self-broadening coefficients from previous studies [112].

The general trend of the temperature dependence exponents can be seen in Figure 6-9. It was found that for the Soft and Hard collision models we had on average larger values for n than those obtained from [111]. It was also found that there was good agreement with the semi-classical calculations reported by Bouanich and Predoi-Cross [117]. Figure 6-9 also indicates that the Voigt results presented in section 6.2 and found in Ref. [111] match well with Voigt results obtained by Dyne *et al.* [115]. However the results from the Soft and Hard collision profiles do not agree as well. The results obtained by Dyne *et al.* [115] for the Soft and Hard profiles were found to be in close agreement with their results using the Voigt profile. A similar result when comparing the three different line shape models should also appear when studying this data set. This is not the case from our observed results for the temperature dependence exponents. The slightly increased values of n may be due to the determination of the narrowing parameter. Therefore, a direct comparison of the present Soft and Hard collision line shape results to those of Dyne *et al.* [115] may not be appropriate.



◆ Present Work Soft collision [112] ■ Present Work Hard collision [112]
▲ Present Work Voigt [111] × Bouanich and Predoi-Cross (MV) [117]
✱ Bouanich and Predoi-Cross (DV) [117] ● Dhyne *et al.* Ref. [115]

Figure 6-9: Temperature dependence coefficients n obtained from equation 6-5 [112].

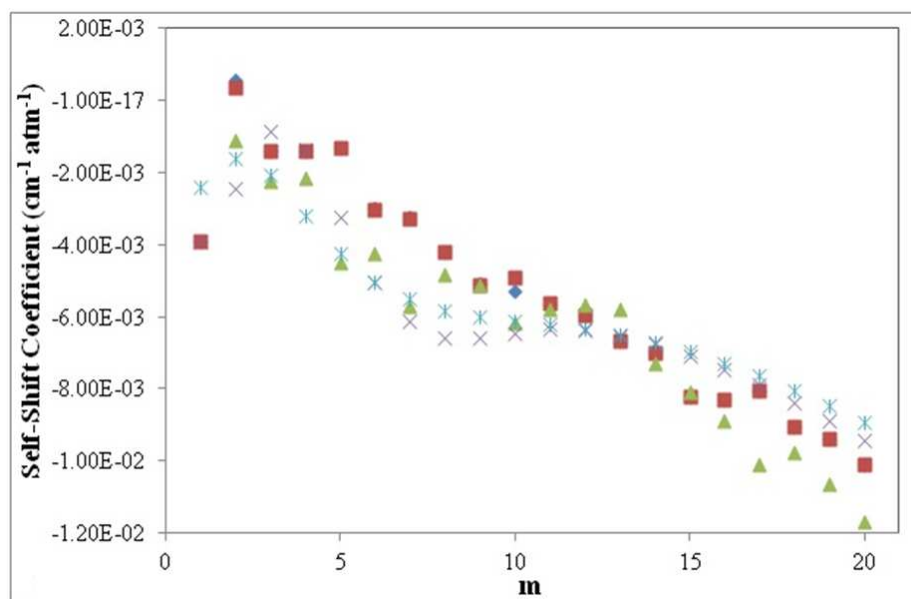
6.3.4. Self-induced pressure shift

The self-shift coefficients δ and their temperature dependent coefficients/exponents δ' and n' were determined using equations 6-6 and 6-7 respectively. Table 6-10 and Figure 6-10 show the self-shift coefficients obtained from both the Soft collision and the Hard collision line shape models for spectra recorded at 293 K. Figure 6-10 shows a good agreement with the semi-classical calculations obtained by Bouanich and Predoi-Cross [117] and with the results presented in section 6.2 using a Voigt profile.

Table 6-10: Self-shift coefficients at 293 K and the corresponding temperature dependent coefficients δ' from both the Soft and Hard collision line shape models [112].

Retrieved self-shifting coefficients ($\text{cm}^{-1} \text{atm}^{-1}$) at 293 K					
Line	m	Soft δ_0 (10^{-3})	δ' (10^{-5})	Hard δ_0 (10^{-3})	δ' (10^{-5})
R(0)	1	-3.9(2)	-5.3(9)	-3.9(2)	-5.3(9)
R(1)	2	0.6(1)	-1.2(3)	0.4(1)	-2.8(2)
R(2)	3	-1.4(1)	-2.8(1)	-1.4(1)	-2.8(1)
R(3)	4	-1.4(1)	0.7(2)	-1.4(1)	0.7(2)
R(4)	5	-1.3(1)	2.4(5)	-1.3(1)	2.4(5)
R(5)	6	-3.0(1)	1.1(1)	-3.0(1)	1.1(1)
R(6)	7	-3.2(1)	1.1(1)	-3.3(1)	1.1(1)
R(7)	8	-4.2(2)	1.6(2)	-4.2(2)	1.6(2)
R(8)	9	-5.1(2)	1.2(2)	-5.1(2)	1.2(2)
R(9)	10	-5.3(2)	3.8(5)	-4.9(2)	4.2(5)
R(10)	11	-5.6(3)	2.8(4)	-5.6(3)	2.8(4)
R(11)	12	-6.0(3)	2.9(2)	-6.0(3)	2.9(2)
R(12)	13	-6.7(3)	3.0(3)	-6.7(3)	3.0(3)
R(13)	14	-7.0(3)	3.6(2)	-7.0(3)	3.6(2)
R(14)	15	-8.2(4)	2.8(4)	-8.2(4)	2.8(4)
R(15)	16	-8.3(4)	4.2(3)	-8.3(4)	4.2(3)
R(16)	17	-8.1(4)	4.3(4)	-8.1(4)	4.3(4)
R(17)	18	-9.1(4)	5.7(5)	-9.1(4)	5.7(5)
R(18)	19	-9.4(4)	3.0(3)	-9.4(4)	2.9(3)
R(19)	20	-10.1(5)	4.9(2)	-10.1(5)	4.9(2)

The self-shift temperature dependent coefficient δ' is given in Table 6-10 and in Figure 6-11. The figure indicates that the δ' does have a rotational dependence. A similar dependence was observed using a Voigt profile in our previous work [111], but has also been determined in theoretical calculations performed by Bouanich and Predoi-Cross [117]. It is important to note that an attempt was made to try and incorporate a second order expression ($\delta''(T)$) as proposed by Bouanich and Predoi-Cross [117], but it was found that the error in shift coefficients were too large to make an accurate assessment of the proposed δ'' term .



- ◆ Present Work Soft collision (293 K) [112]
- ▲ Present Work Voigt [111]
- ✱ Bouanich and Predoi-Cross (DV) [117]
- Present Work Hard collision [112]
- ✕ Bouanich and Predoi-Cross (MV) [117]

Figure 6-10: Self-shift coefficients obtained from spectra recorded at 293 K [112].

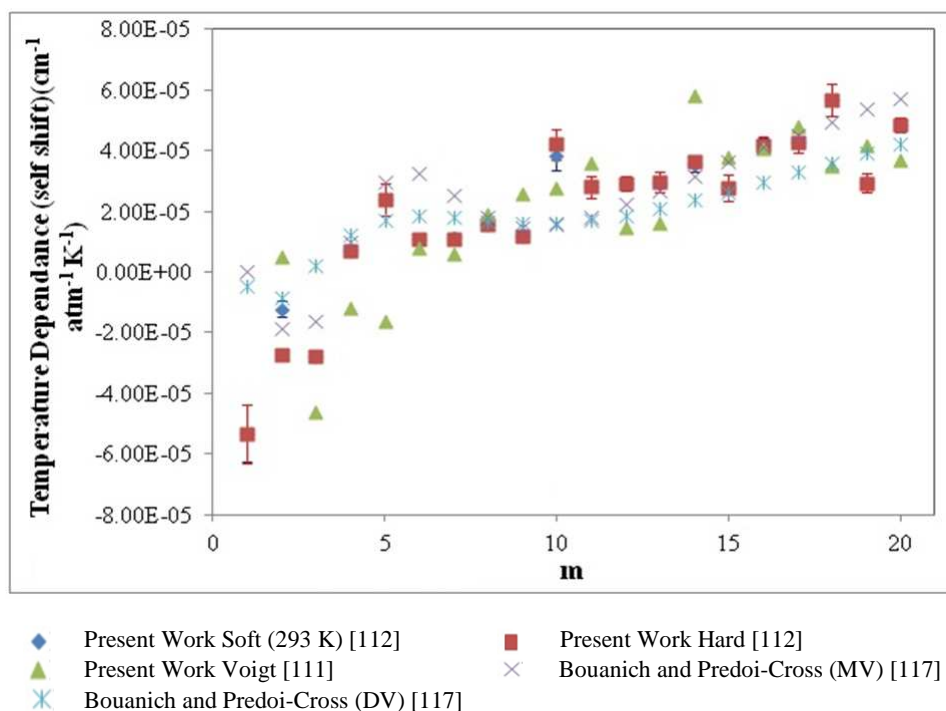


Figure 6-11: Temperature dependence term δ' obtained from equation 6-7 [112].

6.3.5. Self-collisional narrowing

Building on the work published by both Herregodts *et al.* [13] and Valipour and Zimmermann [16], the narrowing coefficients were measured for both Soft and Hard collision models. Gas pressures in the initial recorded spectra ranged from 100 Torr down to 10 Torr and were obtained in the temperature range 213 to 333 K. By carefully examining the pressure dependence of the narrowing coefficient, it was determined that only those spectra in the 40 to 10 Torr were within the Dicke narrowing regime. From these spectra, the temperature dependence of the narrowing coefficients was determined.

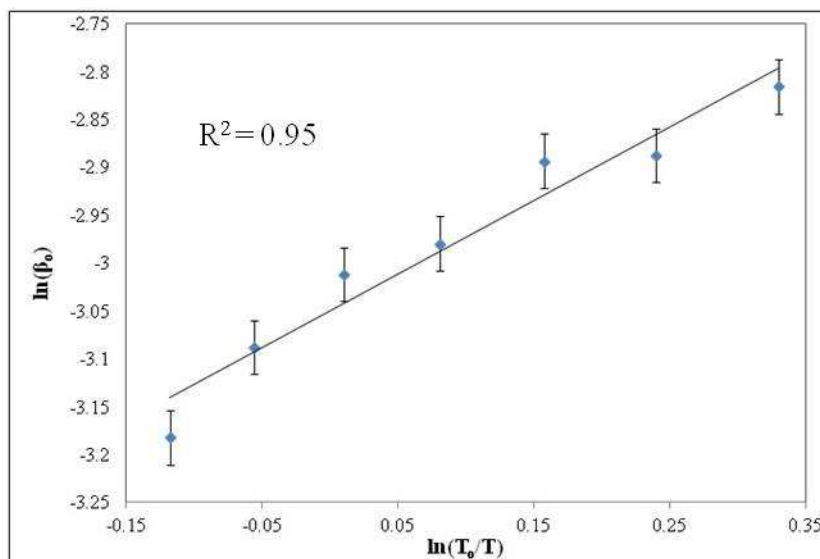


Figure 6-12: Plot showing the collisional narrowing vs. temperature for the R(11) transition in the $\nu_1+\nu_2+\nu_4+\nu_5$ band of C_2H_2 [112].

Recent work by Li *et al.* [118] who studied the collisional narrowing in water vapor spectra have concluded that the temperature dependence of narrowing coefficients is similar to that of the temperature dependence of broadening coefficients. Figure 6-12 depicts the log of the narrowing coefficient for the R(11) transition and its relation to temperature. The figure indicates that there is indeed a linear dependence similar to those observed for the broadening coefficients. Based upon this observation, and also the work by Li *et al.* [118] the following expression was used to describe the temperature dependence of the narrowing coefficients:

$$\beta(p, T) = p\beta^o(p_o, T_o) \left[\frac{T_o}{T} \right]^{n'}, \quad 6-10$$

where the reference pressure p_o and temperature T_o are defined the same manner as for equations 6-5 and 6-7, β^o is the retrieved self-narrowing coefficient at the reference pressure p_o and reference temperature T_o , β is the measured self-narrowing coefficient of

the spectral line, and p is the total sample pressure in atmospheres, and n' is the temperature dependence exponent of the self-narrowing coefficient.

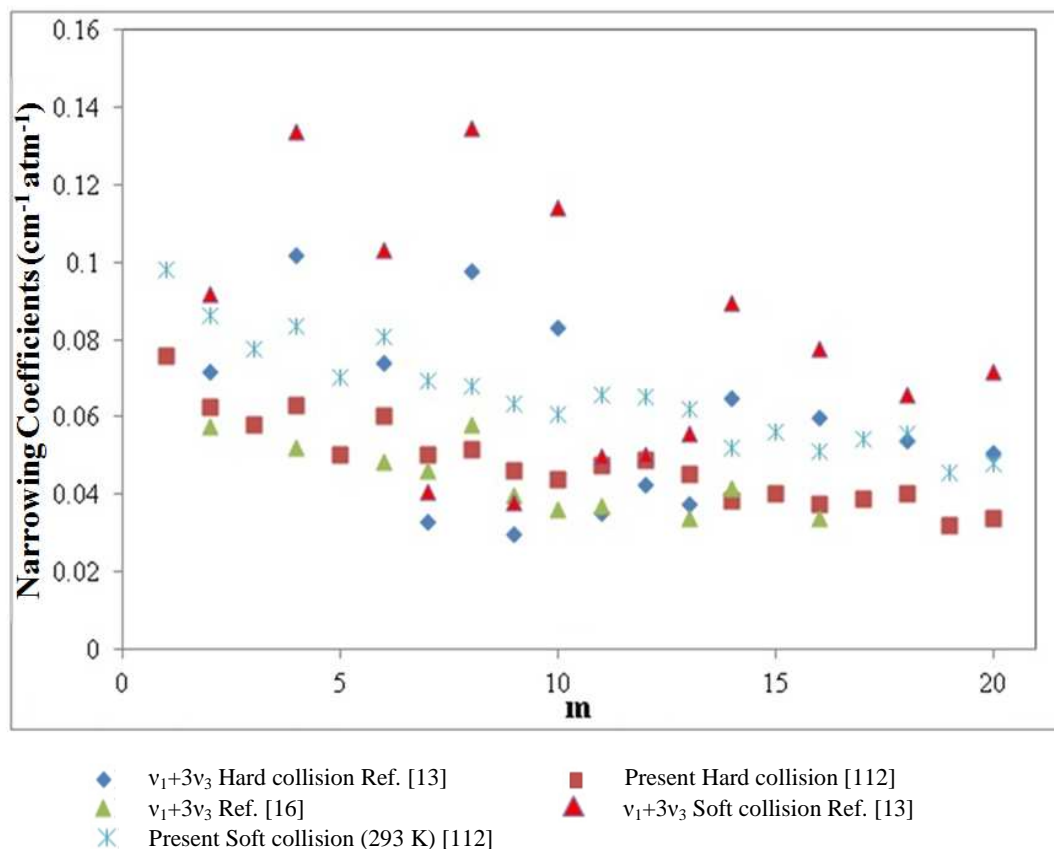


Figure 6-13: Collisional narrowing coefficients obtained from multispectral fitting of spectra recorded at 293 K in the $\nu_1+\nu_2+\nu_4+\nu_5$ band of C_2H_2 [112].

Table 6-11 and Figure 6-13 show the collisional narrowing coefficients obtained from spectra recorded at 293 K. From the figure one can identify that there is in fact a small rotational dependence associated with the narrowing coefficient. A similar trend was also observed by Valipour and Zimmermann [16] for the $\nu_1+3\nu_3$ band. From Figure 6-13 the observed narrowing coefficients for the hard collision model agree well with those of Valipour and Zimmermann [16], but are on average slightly lower than those obtained by Herregodts *et al.* [13].

Table 6-11: Self-collisional narrowing coefficients at 293 K and their temperature dependence exponents n' for the soft and hard collision line shape models [112].

Retrieved narrowing coefficients ($\text{cm}^{-1} \text{atm}^{-1}$) at 293 K					
Line	m	Soft β_o	n'	Hard β_o	n'
R(0)	1	0.099(3)	-0.5(2)	0.076(2)	2.4(2)
R(1)	2	0.087(3)	1.0(1)	0.063(2)	1.1(1)
R(2)	3	0.078(2)	1.5(2)	0.058(2)	1.6(2)
R(3)	4	0.084(3)	0.6(1)	0.063(2)	0.7(1)
R(4)	5	0.070(2)	1.6(3)	0.050(2)	1.7(2)
R(5)	6	0.081(2)	0.5(1)	0.060(2)	0.7(1)
R(6)	7	0.069(2)	0.9(2)	0.050(2)	1.1(2)
R(7)	8	0.068(2)	0.42(2)	0.052(2)	0.6(1)
R(8)	9	0.064(2)	0.7(1)	0.047(1)	0.8(1)
R(9)	10	0.061(2)	0.6(1)	0.044(1)	0.7(1)
R(10)	11	0.066(2)	0.8(2)	0.048(1)	0.7(2)
R(11)	12	0.065(2)	0.6(1)	0.049(1)	0.8(1)
R(12)	13	0.062(2)	0.6(1)	0.045(1)	0.7(1)
R(13)	14	0.052(2)	0.6(2)	0.039(1)	0.7(2)
R(14)	15	0.056(2)	0.6(1)	0.040(1)	0.8(1)
R(15)	16	0.051(2)	0.7(1)	0.038(1)	0.8(1)
R(16)	17	0.054(2)	0.7(1)	0.039(1)	0.9(1)
R(17)	18	0.056(2)	0.4(1)	0.040(1)	0.8(2)
R(18)	19	0.046(1)	0.6(1)	0.032(1)	0.7(1)
R(19)	20	0.048(1)	0.8(2)	0.034(1)	0.9(2)

It was observed by Herregodts et al. [13] that the Soft collision model gave larger narrowing coefficients than the Hard collision model. However, due to the signal-to-noise ratio of their experiment, they were unable to identify which model better described the experimental results. This same trend was also observed in this recorded spectra. However, even with the much higher signal-to-noise ratio obtained with the TDL system it was difficult to justify the choice of one model over the other. It was found from the residuals of many fits using both models that there was no substantial difference between the two models and, therefore, no specific model could be preferred.

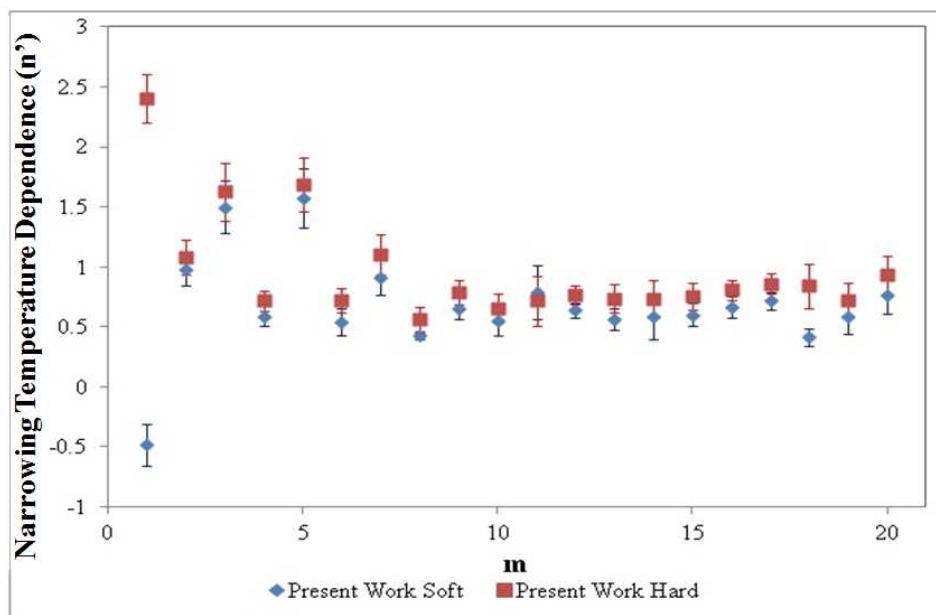


Figure 6-14: Narrowing temperature dependence coefficient n' obtained from equation 6-10 [112].

The temperature dependence term n' from equation 6-10 was also determined and is presented in Table 6-11 and shown in Figure 6-14. The temperature dependence exponents n' determined from both models were found to be similar. The largest difference in n' was found for the R(0) transition and is most likely due to the low intensity of the transition. The larger variations in n' that are seen for transitions R(0) to R(10) may be the result of undefined neighbouring spectral features. Similarly, unidentified features were also observed by Li *et al.* [20] in this spectral region and can be attributed to unassigned hot bands with weak absorption features. Every attempt was made to incorporate these features into the fitting routine. However, without more information, the spectral parameters used may not have been the ideal for these unknown transitions.

6.3.6. Diffusion coefficients

Herregodts *et al.* [13] found that the values they had obtained agreed well with the dynamic friction coefficient $\beta^o_{diff} = 37.8(3) \times 10^{-3} \text{ cm}^{-1}/\text{atm}$ experimentally determined by Mueller and Cahill [119]. Based on the relative agreement of the present data to both Valipour and Zimmermann [16] and Herregodts *et al.* [13] results the narrowing parameter β^o has been equated to the dynamic friction coefficient β^o_{diff} in an attempt to investigate the diffusion coefficient and its temperature dependence. The dynamic friction coefficient β^o_{diff} can be determined by the following equation [118, 120]:

$$\beta^o_{diff} = \frac{KT}{2\pi M c D_{11}}, \quad 6-11$$

Here, K is the Boltzmann constant, T the temperature in Kelvin, M the mass of acetylene molecule, c the speed of light and D_{11} is the Self Diffusion coefficient for acetylene.

The diffusion coefficient for any gas may be obtained in a general sense using the following equation 6-12 [121]:

$$D = 2.628 * 10^{-3} \left[\frac{\sqrt{T^3/M}}{p\sigma^2} \right]_{\tau} (\text{cm}^2/\text{sec}), \quad 6-12$$

where M is the molecular weight, T the temperature in Kelvin, p the pressure in atmospheres and σ the molecular diameter in angstroms (for acetylene $\sigma = 4.221\text{\AA}$ [122] was used).

Using equation 6-11, the experimentally determined diffusion coefficients have been compared to the values obtained from equation 6-12. Figure 6-15 shows the results of this comparison for three different transitions. It can be seen that both the experimental

results and the theoretically calculated values using the equations show similar slopes with temperature. This indicates a good agreement between the estimated diffusion coefficients' temperature dependence and what are actually observed. Also seen in the figure are the results obtained by Mueller and Cahill [119] and they agree quite well with the results obtained using equations 6-11 and 6-12. We can also see from the same figure that the diffusion coefficient does in fact have a rotational dependence. It has been found that as m increases, so does the value of the diffusion coefficient. Figure 6-16 shows the diffusion coefficients and the rotational dependence obtained from spectra recorded at 293K.

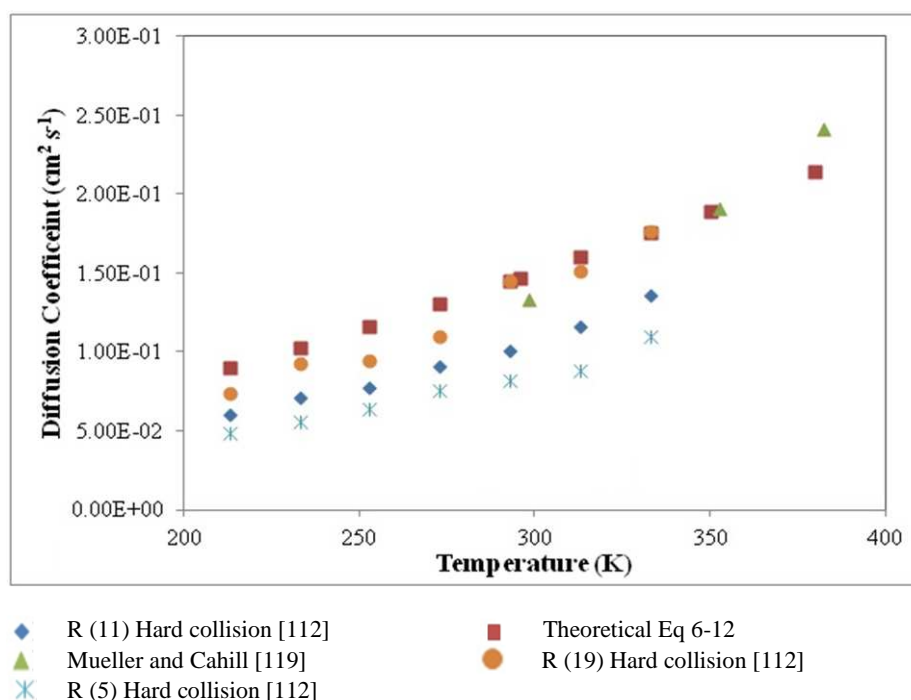


Figure 6-15: Comparison of diffusion coefficients. The diffusion coefficients determined for R(19), R(13) and R(11) were obtained through the use of equation 6-11. The Theoretical values were calculated from equation 6-12 [112].

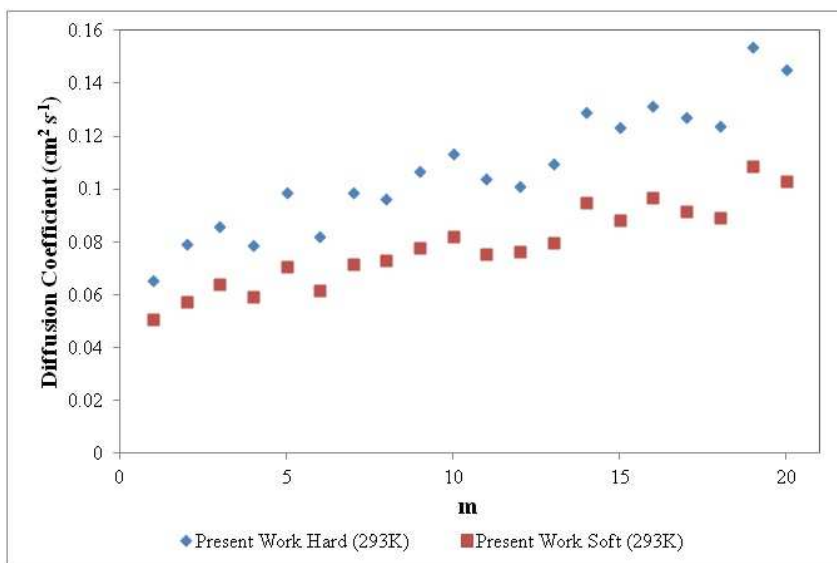


Figure 6-16: Experimentally determined Diffusion coefficients obtained from retrieved β_o at 293K [112].

6.4. Low pressure line shape study of nitrogen perturbed acetylene transitions in the $\nu_1+\nu_3$ band over a range of temperatures.

6.4.1. Introduction

Six nitrogen perturbed transitions of acetylene in the $\nu_1+\nu_3$ absorption band have been recorded using the TDLS described in Chapter 3. The goal was to obtain an improved understanding of both the broadening and narrowing effects of low pressure acetylene infrared transitions broadened with nitrogen gas. For this C_2H_2 spectra were analyzed using a hard collision (Rautian) profile for five different sample temperatures (213 - 333 K) and pressures (5-40 Torr). From these analyses the N_2 -broadening and N_2 -narrowing coefficients were determined to retrieve their temperature dependences. The

experimentally measured narrowing coefficients have been used to estimate the nitrogen diffusion coefficients (D_{12}). The broadening coefficients and their corresponding temperature dependence exponents have been compared to those calculated by S. Ivanov, O. Buzykin, and F. Thibault using a classical impact approach on an *ab initio* potential energy surface (details of this analysis can be found in [113]).

Table 6-12 shows a summary of the studies previously reported on nitrogen broadened acetylene transitions. From this table, it is clear that most of the information used here are from room temperature measurements [9, 15, 16, 123-130]. However, there have been a handful of studies that were carried out at other temperature ranges [107, 111, 112, 131-136]. Proper knowledge of the temperature dependences of the collisional broadening and narrowing coefficients are important in the correct interpretation of atmospheric data as most regions of the atmosphere are not at a constant temperature. Therefore, understanding the temperature dependence exponents of pressure broadening, shift and narrowing can improve radiative transfer models in interpreting remote sensing observations accurately.

Proper choice of spectral line shapes is also vital to improving the understanding of these transitions. It has been found that the Voigt profile, thought easy to fit, does not always provide the most accurate results [13, 16, 111, 112, 125, 127, 133, 134, 136]. This is even more important when considering a low pressure gas when collisional narrowing of the Doppler profile known as “Dicke narrowing” takes place [137]. The work presented here adopts the use of the hard collision (Rautian) line-shape profile as discussed in Chapter 2 and Ref. [47] to measure the temperature dependence of the N₂-broadening and narrowing coefficients.

Table 6-12: Summary of prior studies of acetylene bands broadened by N₂.

Vibrational Band	Broadener	Temperatures (K)	Assignment range	Ref.
ν_5	N ₂ , O ₂	297	P(29)-R(25)	[123]
ν_5	N ₂ , O ₂	297	P(35)-R(34)	[128]
ν_5	H ₂ , N ₂ , He, Ar	147-295	P(8)-R(21)	[131]
ν_5	H ₂ , N ₂ , He, Ar	296	R(3)-R(34)	[129]
ν_5	N ₂	173.4	P(29)-R(28)	[132]
$\nu_4+\nu_5-\nu_4$	N ₂ , He	296	Q(1)-Q(35)	[130]
$2\nu_5-\nu_5$	N ₂ , He	296	Q(1)-Q(35)	[130]
$\nu_4+\nu_5-\nu_4$	N ₂ , He	183.2, 198.2	Q(1)-Q(35)	[107]
$2\nu_5-\nu_5$	N ₂ , He	183.2, 198.2	Q(1)-Q(35)	[107]
$\nu_4+\nu_5$	N ₂ , air	296	P(31)-R(20)	[124]
$\nu_4+\nu_5$	N ₂	173.2-273.2	P(1)-R(23)	[133]
$\nu_4+\nu_5$	N ₂	298	P(17)-R(22)	[125]
$\nu_4+\nu_5$	N ₂	173.2-298.2	R(11)-P(23)	[134]
$\nu_1+\nu_3$	H ₂ , N ₂ , D ₂ , air	295	P(31)-R(27)	[126]
$\nu_1+\nu_3$	C ₂ H ₂ , N ₂	296	P(11)	[127]
$\nu_1+\nu_3$	N ₂	195, 373, 473	P(25)-R(25)	[135]
$\nu_1+\nu_3$	N ₂ , O ₂ , CO ₂	296	P(26)-P(22)	[15]
$\nu_1+\nu_3$	N ₂	213-333	P(31)-R(33)	[136]
$\nu_1+\nu_5$	C ₂ H ₂ , N ₂ , Ar	296	R(0)-R(7), Q(7)-Q(29)	[9]
$\nu_1+3\nu_3$	N ₂ , O ₂ , He, Ar, Ne, Kr, Xe	298	P(17)-R(22)	[16]

6.4.2. Experiment and analysis overview

The spectra of six transitions, P(21), P(19), P(16), R(21), R(19) and R(16) belonging to the $\nu_1+\nu_3$ combination band of acetylene were recorded. The gas sample used for the reference chamber was pure C_2H_2 provided by Praxair with a quoted purity of 99.6 %. The gas samples kept inside the temperature controlled chamber was also provided by Praxair and was quoted as being 9.94 % C_2H_2 with the remaining being N_2 gas. Low pressure tests on the P(11) transition in the $\nu_1+\nu_3$ band showed that the concentration was within 0.5% of the quoted value.

The spectra were recorded at the following set temperatures: 213, 253, 296, 313, and 333 K. For each set temperature spectra were recorded at 40, 30, 20, 10 and 5 Torr. Table 6-13 shows the experimental details for the R(21) transition with the other five transitions recorded with similar pressures and temperatures.

Table 6-13: Experimental conditions for the R(21) transition [113]. The uncertainties listed in the table in parenthesis are one standard deviation from the average listed.

Line	Temperature (K)	Pressure (Torr)	# of Recorded Spectra
R(21)	213.9(3)	5.214(5)	4
		10.214(10)	4
		20.270(20)	4
		30.408(30)	4
		42.371(42)	3
	253.4(3)	5.267(5)	4
		10.668(11)	4
		20.131(20)	4
		30.185(30)	4
		40.409(40)	4
	295.8(3)	5.264(5)	4
		10.324(10)	4
		19.839(20)	4
		30.013(30)	4
		40.364(40)	4
	312.7(3)	5.170(5)	4
		10.250(10)	4
		19.910(20)	4
		30.087(30)	4
		39.286(39)	4
332.5(3)	5.499(5)	4	
	10.898(11)	4	
	21.153(21)	4	
	29.983(30)	4	
	40.022(40)	2	

To take into account the Dicke narrowing effect, the soft and hard collision models are often used [45, 47]. Despite the physics leading to these models being very different, it was found for the case of the self-perturbed spectrum of C_2H_2 (Section 6.3 [112]) that there was no substantial difference in the residuals produced from fits of these two line shape functions to that of the experimental lineshape even though they did produce slightly different narrowing parameters. Generally, the choice of which line shape function to fit to the experimental lineshape comes down to the masses of the perturber and radiator, and as was seen for the self-perturbed case (Section 6.3,[112])

either lineshape function was preferable over the other. For the case of the N₂ perturbed spectrum of C₂H₂ it was decided to only make use of an un-correlated hard collision Rautian line shape function as the mass of N₂ and C₂H₂ are very similar. Therefore, fitting the experimental line shape using the Galatry line shape function was assumed to add no extra value to the analysis. Figure 6-17 shows the spectra of the P(16) line of the $\nu_1+\nu_3$ band measured at 40 Torr. In this figure one can see that when fitting with a Voigt profile a 'w'-type residual is observed, which is indicative of the broadening in the Dicke narrowing regime. It is clearly shown that once the data is fitted using a diffusion profile such as the Rautian profile, an improved result is obtained. It was found that for the spectra recorded at 333 K, the percent difference between the broadening coefficients using the Voigt and Rautian lineshape functions was as high as 6 %. This difference in retrieved values diminished along with the temperature as it was observed that at lower temperatures (i.e., 213 K) there was only a 3% difference.

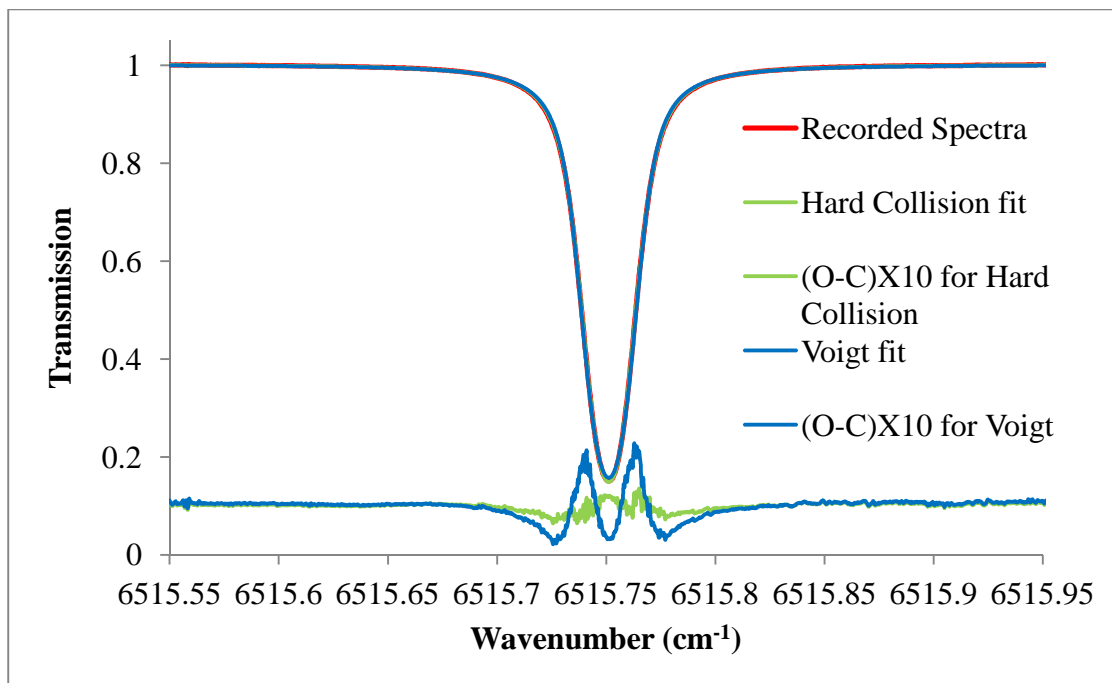


Figure 6-17: Observed and calculated spectra for the P(16) transition of the $\nu_1+\nu_3$ absorption band of C_2H_2 at a pressure of 40 Torr and temperature of 296 K. The residuals have been shifted vertically and magnified for easier comparison [113].

Below are the expressions used to retrieve the temperature dependence exponents for the N_2 -broadened half-width and N_2 -narrowing coefficients:

$$\gamma(p, T) = p \left[\gamma_{N_2}^o(p_o, T_o)(1 - \chi) \left[\frac{T_o}{T} \right]^{n_1} + \gamma_{self}^o(p_o, T_o)\chi \left[\frac{T_o}{T} \right]^{n_2} \right] \text{ and} \quad 6-13$$

$$\beta(p, T) = p \left[\beta_{N_2}^o(p_o, T_o)(1 - \chi) \left[\frac{T_o}{T} \right]^{n'_1} + \beta_{self}^o(p_o, T_o)\chi \left[\frac{T_o}{T} \right]^{n'_2} \right]. \quad 6-14$$

where $\gamma_{N_2}^o$ and $\beta_{N_2}^o$ are the retrieved N_2 -broadened half-width and N_2 -narrowing coefficients at the reference pressure p_o (1 atm) and reference temperature T_o (296 K), γ and β are the measured broadened half-width and narrowing coefficients of the spectral line at the total sample pressure of p and temperature T , the total sample pressure $p = p_{N_2} + p_{self}$ and χ is the ratio of p_{self} to p , and n and n' are the temperature dependence exponents of the pressure-broadened half-width and narrowing coefficients. In equations 6-13 and 6-14, the reference pressure and temperature are $p_o = 1$ atm and $T_o = 296$ K,

respectively. The use of equation 6-14 for the temperature dependence of the narrowing coefficient has been justified by the work of both Li *et al.* [118, 138] and our earlier study of Povey *et al.* [112] (Section 6.3). It is important to note that equations 6-13 and 6-14 are merely approximations that will become less valid with increasing temperatures [53].

The line parameters were obtained by using a weighted multispectrum analysis software [87]. For one set temperature, multispectrum fits were performed on a series of spectra recorded for the different pressures. The software uses a non-linear fitting routine to optimize the line parameters by minimizing the fit residual. For each measured line investigated, a simultaneous fit of the intensity, N₂-broadening and N₂-narrowing was made. The shift was also fit simultaneously. However, due to the low pressures of the sample gas, it was decided not to present the results for the N₂-shifts.

6.4.3. N₂-Broadening of acetylene transitions

Table 6-14 shows the N₂-broadening coefficients measured for all five temperatures. A comparison of the experimental results to those of the theoretically determined line widths provided by S. Ivanov, O. Buzykin, and F. Thibault [113] can be seen in Figure 6-18. From the figure it can be seen that both sets of data agree with each other quite well with a maximum relative difference of no greater than 7 %.

Table 6-14: N₂-Broadening coefficients for five different temperatures obtained using an uncorrelated hard collision Rautian line-shape model [113]. (The normal convention of $m = -J''$ for the P branch and $m = J'' + 1$ for the R branch is used).

Retrieved N ₂ -Broadening Coefficients $\gamma_{N_2}^0$ (cm ⁻¹ atm ⁻¹)							
Line	m	Line Position (cm ⁻¹)	213 K	253 K	296 K	313 K	333 K
P(21)	-21	6501.7047	0.0888(9)	0.0798(8)	0.0708(7)	0.0692(7)	0.0665(7)
P(19)	-19	6507.3982	0.0947(9)	0.0832(8)	0.0769(8)	0.0719(7)	0.0704(7)
P(16)	-16	6515.7516	0.1017(10)	0.0889(9)	0.0774(8)	0.0766(8)	0.0714(7)
R(16)	17	6592.5030	0.0985(10)	0.085(9)	0.0752(8)	0.0727(7)	0.0699(7)
R(19)	20	6598.0774	0.0913(9)	0.0823(8)	0.0739(7)	0.0725(7)	0.0673(7)
R(21)	22	6601.6617	0.0859(9)	0.0768(8)	0.0693(7)	0.0689(7)	0.0676(7)

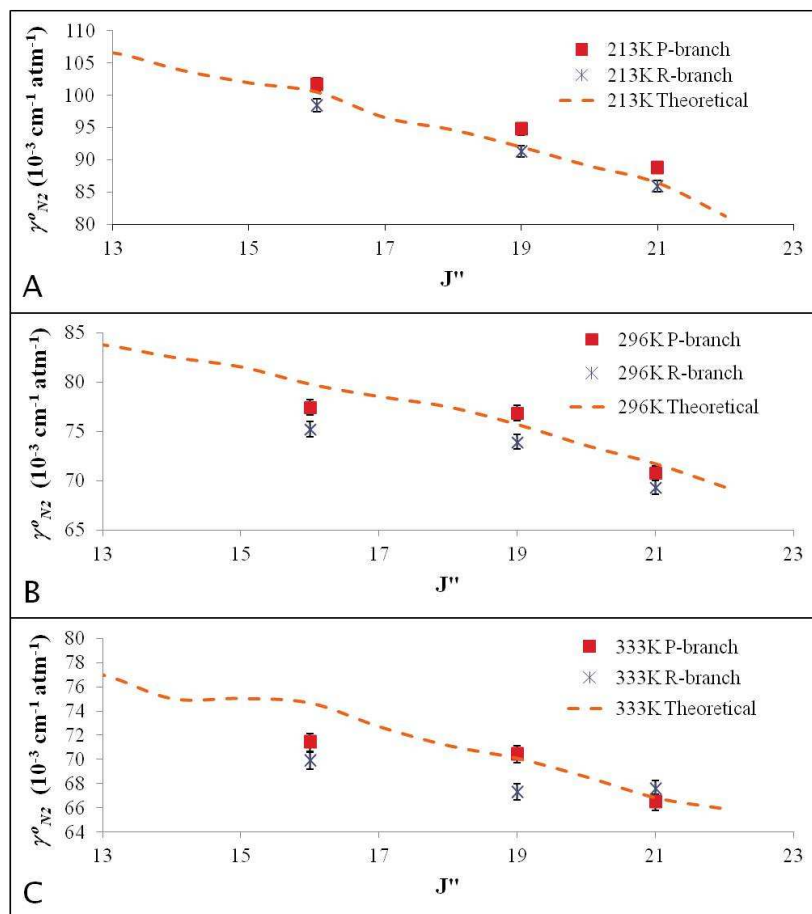


Figure 6-18: Comparison of classically calculated and experimentally determined N₂-broadening coefficients for three different temperatures. In each panel, the line depicts the theoretically determined broadening coefficients [113].

Figure 6-19 shows the results of the room temperature N_2 -broadening coefficients and comparisons with previous measurements reported in the literature. As it can be seen in the figure, the broadening coefficients retrieved in this study agree reasonably well with most of the previous work published to date.

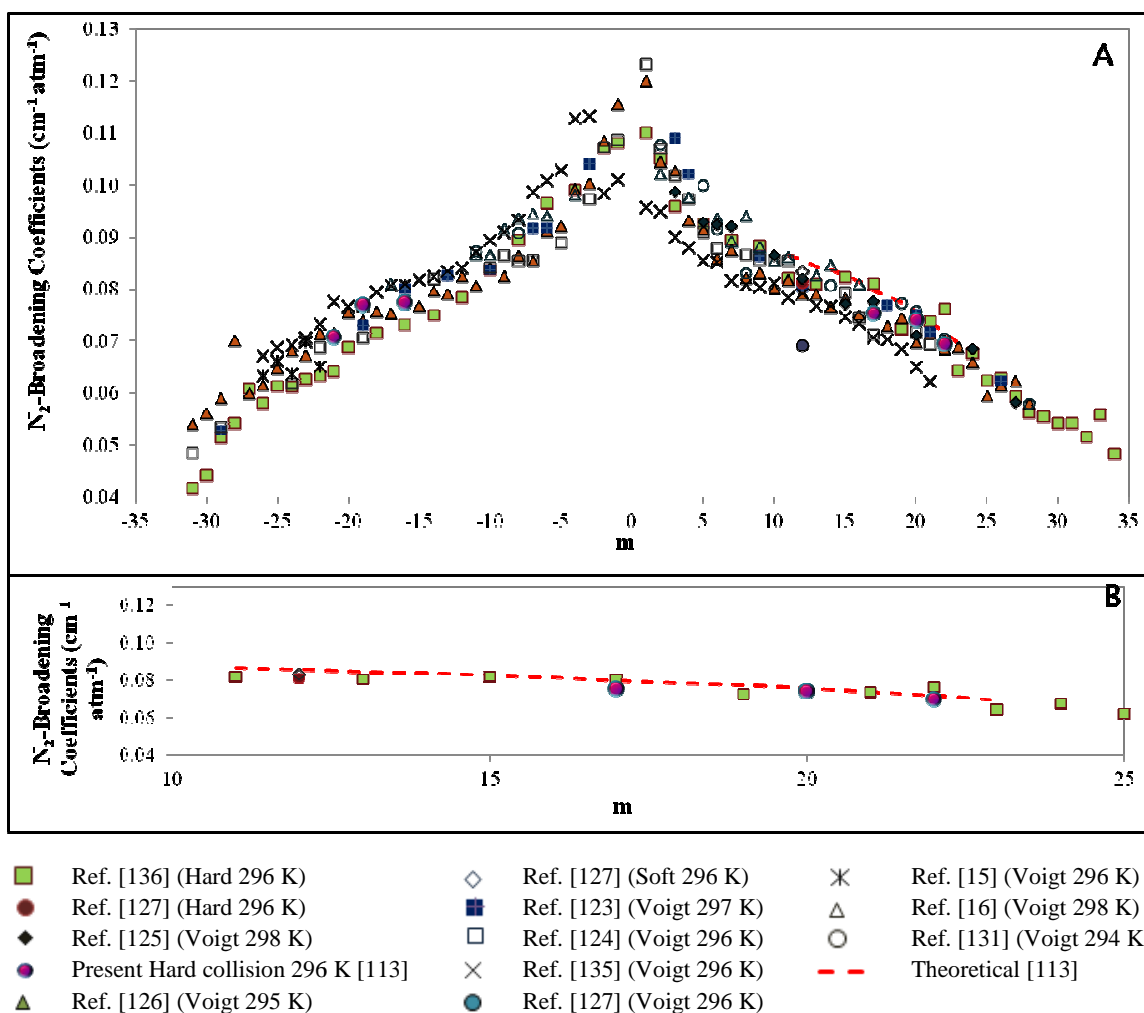


Figure 6-19: Panel A shows a comparison of the present N_2 -broadening coefficients with previous studies. Panel B shows a smaller region between $m=10$ to $m=25$ where only values, obtained from a narrowing model, are compared [113].

Using equation 6-13, the temperature dependence exponents of the N_2 -broadening coefficients were calculated. Both experimentally and theoretically determined N_2 -broadening temperature dependence exponents, n are shown in Table 6-15 and plotted in Figure 6-20. In Figure 6-20, a comparison of the present results with those by Rozario *et*

al. [136] and Campbell *et al.* [135] is shown. The experimentally determined coefficients of N₂- broadening temperature dependence n reasonably compare with previous work done for higher values of the quantum number $|m|$. The figure also indicates that as $|m|$ becomes smaller there is more deviation from both the theoretical work done by S. Ivanov, O. Buzykin, and F. Thibault [113] and that of Campbell *et al.* [135]. However, it is important to note that the work done by Campbell *et al.* [135], where they have smoothed their results, agrees quite well with the proposed theoretical calculations presented in [113]. From Figure 6-20 it can also be seen that for the R-branch transitions there is much better agreement than for the P-branch transitions. This discrepancy is more than likely due to the initial parameters used for the self-narrowing coefficients obtained in Section 6.3 [112]. This has allowed for less error to be introduced in the results obtained for the R-branch transitions. However, for the P-branch transitions, the assumption was made that initial self-narrowing coefficients were similar to those obtained for the R-branch. At this time there is no known published work showing both the m and temperature dependence of the self-narrowing coefficients for P-branch transitions.

Table 6-15: Comparison of theoretical and experimental results obtained for N₂-broadening coefficients at 296 K and their temperature dependence exponents n_l [113].

Retrieved N ₂ -Broadening Coefficients (cm ⁻¹ atm ⁻¹) at 296 K and Determined Temperature Dependence Exponents							
Line	m	Rautian γ_{N_2}	Calculated γ_{N_2}	% Difference	Rautian n_l	Calculated n_l	% Difference
P(21)	-21	0.0708(7)	0.0736	3.77%	0.66(2)	0.57	12.87%
P(19)	-19	0.0769(8)	0.0775	0.80%	0.67(4)	0.60	9.30%
P(16)	-16	0.0774(8)	0.0815	5.02%	0.78(4)	0.67	13.66%
R(16)	17	0.0752(8)	0.0798	5.73%	0.77(2)	0.67	12.94%
R(19)	20	0.0739(7)	0.0757	2.35%	0.66(4)	0.60	7.97%
R(21)	22	0.0693(7)	0.0717	3.37%	0.55(5)	0.57	3.35%

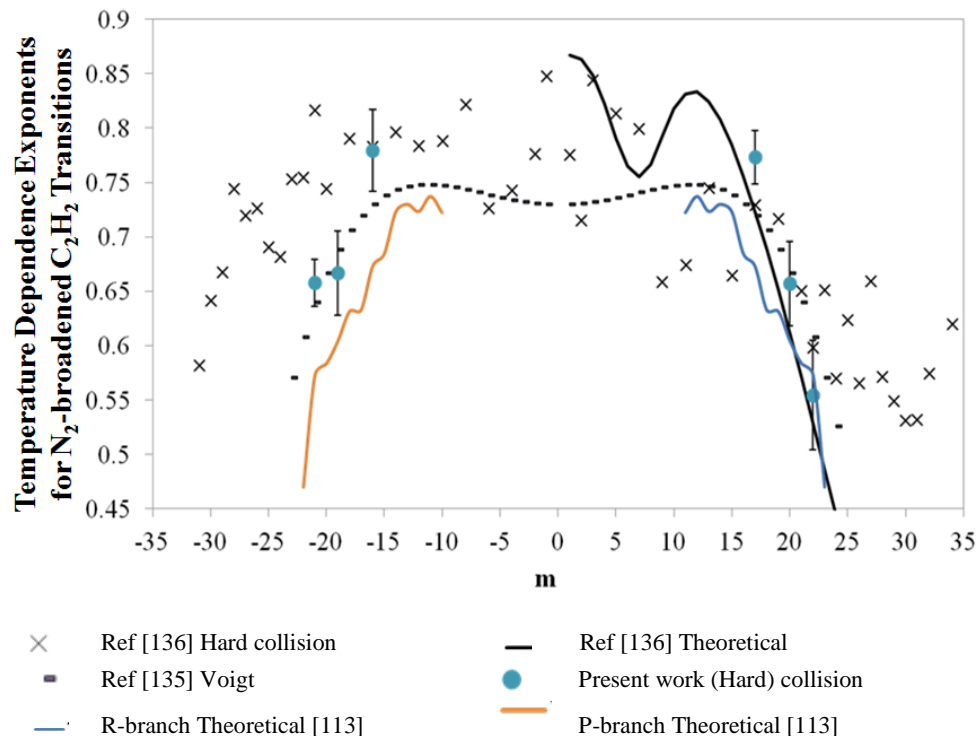


Figure 6-20: Temperature dependence exponents n_l obtained from equation 6-13 [113].

6.4.4. N₂-collisional narrowing of acetylene transitions

In the previous Section 6.3 [112] it was discussed that only transitions recorded at pressures below 40 Torr were strictly in the Dicke narrowing regime. Therefore, only spectra recorded at 40 Torr and lower were obtained for this analysis. Figure 6-21 shows the relationship of the pressure dependent narrowing coefficient for the P(16) line of the $\nu_1+\nu_3$ band at 296 K plotted against the N₂-partial pressure of the temperature controlled cell. It is clear from the figure that once again there is a linear relationship between the N₂-partial pressure and the Narrowing coefficient obtained. This justifies the use of a diffusional line model for the examination of the narrowing effects in this pressure region.

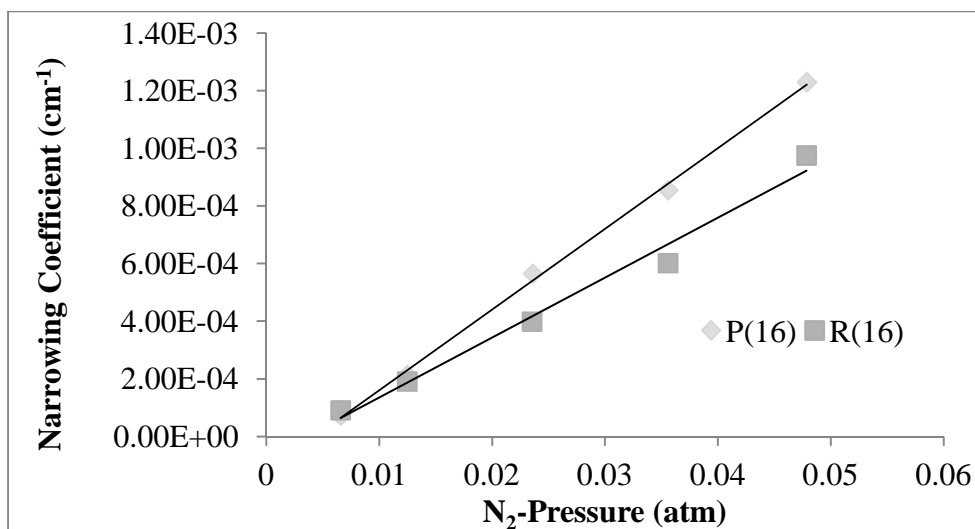
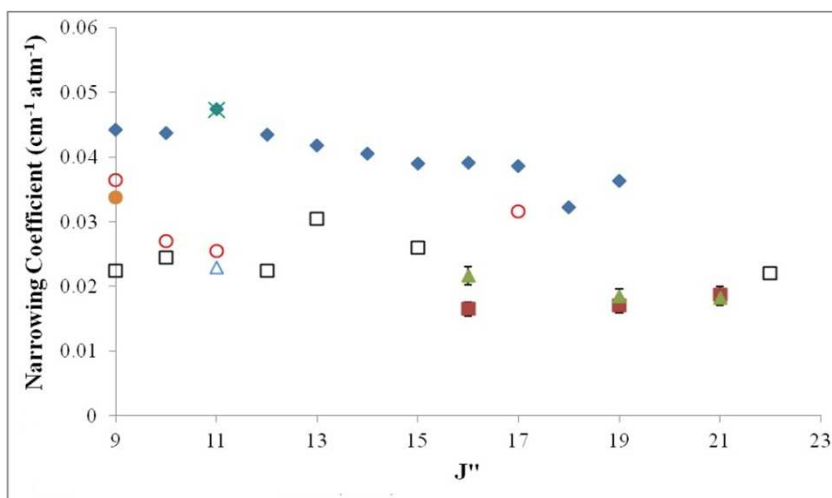


Figure 6-21: The pressure dependent narrowing coefficient β_{N_2} for the P(16) and R(16) transitions at 296 K as they vary with the N_2 pressure [113].

Table 6-16 shows the N_2 -narrowing coefficients obtained from fitting the line shape with the hard collision (Rautian) profile. The room temperature N_2 -narrowing coefficients from Table 6-16 are compared in Figure 6-22 to the values obtained for both self- and N_2 -narrowing coefficients reported in Section 6.3 [112], McRaven *et al.* [127], Dhyne *et al.* [133, 134] and Valipour and Zimmermann [16]. From the figure it can be observed that all studies report similar results. Each of the previous studies that measured both self- and N_2 -narrowing effects [16, 127] reported the N_2 -narrowing coefficients to be smaller than the self-narrowing coefficients. This is also what was observed when comparing the results of Section 6.3.5 [112] with what is presented here.

Table 6-16: N₂-Narrowing coefficients for the five recorded temperatures using an un-correlated hard collision Rautian line-shape model. The last column shows the temperature dependence terms obtained from the data in the table and equation 6-14 [113].

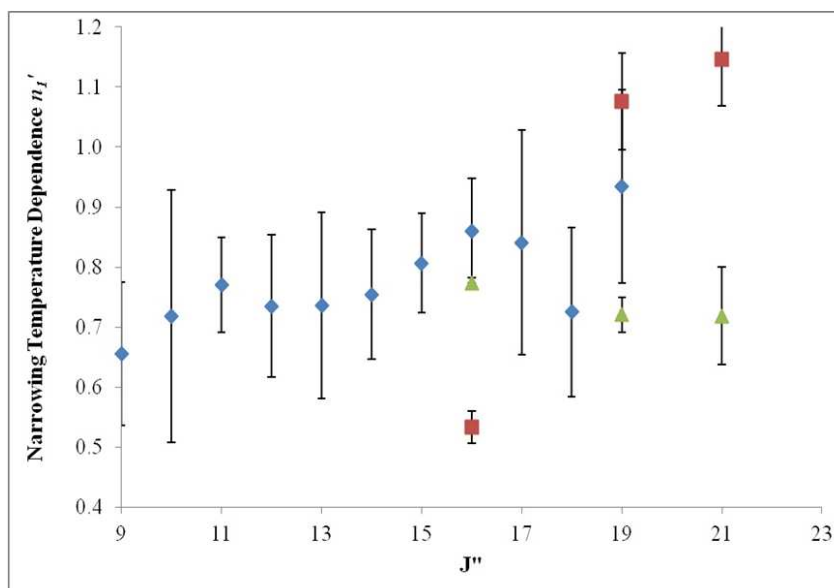
Retrieved N ₂ -Narrowing Coefficients $\beta^o_{N_2}$ (cm ⁻¹ atm ⁻¹) and Temperature Dependence n_I'							
Line	m	213 K	253 K	296 K	313 K	333 K	n_I'
P(21)	-21	0.0279(9)	0.0225(7)	0.0182(6)	0.0177(6)	0.017(5)	1.146(78)
P(19)	-19	0.0273(9)	0.0232(7)	0.0184(6)	0.018(6)	0.0173(6)	1.076(81)
P(16)	-16	0.0256(8)	0.0239(8)	0.0217(7)	0.021(7)	0.0203(6)	0.533(26)
R(16)	17	0.0212(7)	0.0186(6)	0.0165(5)	0.0157(5)	0.015(5)	0.773(9)
R(19)	20	0.0211(7)	0.0188(6)	0.017(5)	0.016(5)	0.0153(5)	0.721(29)
R(21)	22	0.0225(7)	0.0209(7)	0.0187(6)	0.0173(6)	0.0163(5)	0.719(82)



- ◆ Ref [112] Self-Narrowing (296 K)
- ▲ N₂-Narrowing P-branch (296 K)
- △ Ref [127] N₂-Narrowing P(11)
- Ref [16] N₂-Narrowing P-branch (298 K)
- N₂-Narrowing R-branch (296 K)
- × Ref [127] Self-Narrowing P(11)
- Ref [133, 134] N₂-Narrowing R(9)
- Ref [16] N₂-Narrowing R-branch (298 K)

Figure 6-22: Comparison of the N₂-Narrowing coefficients obtained at 296 K to previous work [113].

The exponents n_1' for temperature dependence of N_2 -narrowing are given in Table 6-16. These temperature dependence exponents are plotted in Figure 6-23 along with self-narrowing temperature dependence exponents from Section 6.3.5 [112]. From the figure it can be seen that the measured temperature dependence exponent is very similar and for the most part they agree to within one standard deviation of each other.



◆ Ref [112] Self-Narrowing (296 K) ■ N_2 -Narrowing P-branch (296 K)
 ▲ N_2 -Narrowing R-branch (296 K)

Figure 6-23: Narrowing temperature dependence coefficient n_1' obtained from equation 6-14. The diamonds show the results from Section 6.3.5 [112] with self-narrowing coefficients [113].

6.4.5. Diffusion coefficients

Using the same approach that was taken in Section 6.3.6 [112], the narrowing parameter $\beta^o_{N_2}$ was equated to the dynamic friction coefficient β^o_{diff} in an attempt to estimate the nitrogen diffusion coefficient and its temperature dependence. The dynamic friction coefficient for nitrogen β^o_{diff,N_2} can be expressed by equation 6-11 with D_{11} being replaced with D_{12} .

The mass diffusion coefficient for a gas mixture can be estimated in general using the following equation [121, 139]:

$$D_{12} = \frac{2.628 \cdot 10^{-3}}{p \sigma_{12}^2 \Omega_{12}^{(1,1)}(T_{12})} \sqrt{T^3 \frac{(M_1 + M_2)}{2M_1 M_2}}, \quad [cm^2/sec], \quad 6-15$$

where M_1 and M_2 are the molecular weights of C_2H_2 and N_2 respectively, T is the temperature in Kelvin, p is the pressure in atmospheres, T_{12} is the reduced temperature equal to KT/ϵ_{12} , ϵ_{12} is the depth of the isotropic potential, and σ_{12} is the finite distance at which the intermolecular isotropic potential is zero. From the *ab initio* PES [140] values of $\epsilon_{12} = 88.8 \text{ cm}^{-1}$ and $\sigma_{12} = 4.015 \text{ \AA}$ were deduced and used. Finally, $\Omega_{12}^{(1,1)}$ is a dimensionless reduced collision integral, a function of the reduced temperature; values are tabulated in [121].

Using the measured $\beta_{N_2}^o$ narrowing coefficients in equation 6-11 the D_{12} coefficients were calculated for all the temperatures investigated and are presented in Table 6-17. The temperature dependence of the nitrogen diffusion coefficient was determined using equation 6-15 and is plotted in Figure 6-24. A comparison of the experimentally estimated, through equation 6-11, nitrogen-diffusion coefficients to those obtained by equation 6-15 show a similar trend in the temperature dependence. However, unlike in the previous Section 6.3.6 [112] where it was determined that the diffusion coefficients were slightly lower than those obtained theoretically, now the values are slightly larger than what was found using equation 6-15. This result indicates that $\beta_{diff}^o > \beta_{N_2}^o$ which implies that there is less narrowing as expected on the basis $\beta_{diff}^o = \beta_{N_2}^o$. Such a result was also found in the work done by Wehr *et al.* [141] for the CO-Ar system. Also

it is expected that for the P- and R-branch transitions, the diffusion coefficients should be similar (for a given m or J'' value). Figure 6-24 does in fact this for the P(21) and R(21) transition. The fact that this is not observed between the P(16) and R(16) as well as the P(19) and R(19) may in fact be due to neighbouring spectral features that are not properly accounted for as there are many weak transitions in this spectral region. However, it does indicate the need for a closer inspection of both self- and N_2 - narrowing coefficients for both P- and R-branch transitions on a broader scale than what is presented here.

Table 6-17: Estimated N_2 -Diffusion coefficients obtained from equation 6-15. For the values obtained at 296 K a percent difference was calculated ($|\text{theoretical-experimental}|/\text{experimental}$) [113].

Retrieved N_2 -Diffusion Coefficients D_{12} ($\text{cm}^2 \text{sec}^{-1}$)							
Line	m	213 K	253 K	296 K	% Difference	313 K	333 K
P(21)	-21	0.129(4)	0.190(6)	0.275(9)	43.37%	0.300(10)	0.331(11)
P(19)	-19	0.132(4)	0.185(6)	0.272(9)	42.74%	0.295(9)	0.326(10)
P(16)	-16	0.141(5)	0.179(6)	0.232(7)	32.77%	0.253(8)	0.278(9)
R(16)	17	0.170(5)	0.231(7)	0.304(10)	48.73%	0.338(11)	0.376(12)
R(19)	20	0.171(5)	0.228(7)	0.295(9)	47.22%	0.332(11)	0.370(12)
R(21)	22	0.160(5)	0.206(7)	0.268(9)	41.82%	0.307(10)	0.345(11)

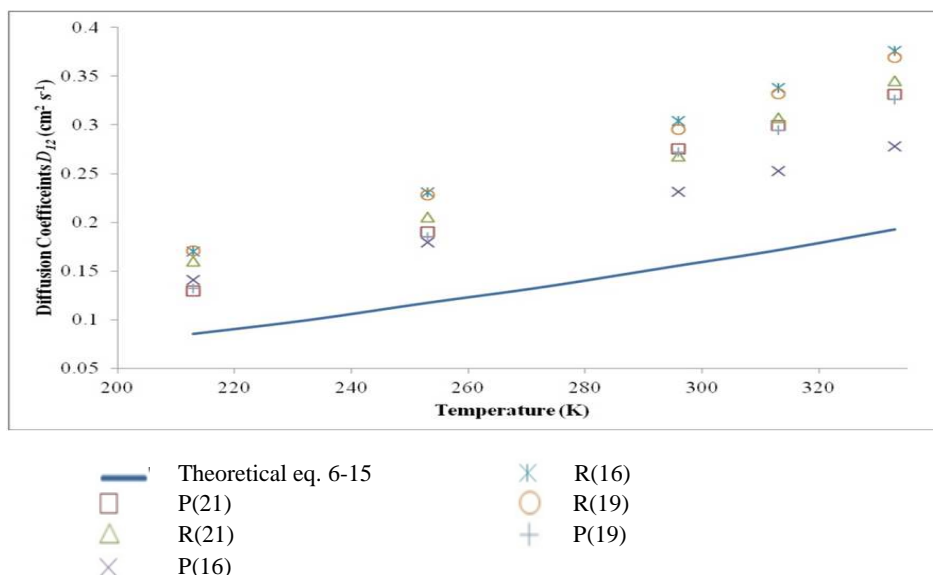


Figure 6-24: Estimated diffusion coefficients obtained from retrieved experimental $\beta_{N_2}^o$ and equation 6-15 [113].

Moreover, our comparison between the binary diffusion coefficients as given by equation 6-15 and the effective (or optical) diffusion coefficients retrieved using line shape analysis cannot be completely satisfactory for the following reasons. Firstly, equation 6-15 is only a first order approximation [121, 142]. Secondly, paraphrasing Varghese and Hanson [143], “the two parameters (the mass diffusion constant and the effective diffusion coefficient) appear in different contexts in the theory and hence do not have the same physical significance...”. More recently, Wehr *et al.* [141] have also pointed out that both coefficients are related to (or take into account) a different collisional mechanism. (In addition, many studies found large discrepancies between these two kinds of coefficients, see Refs. in [141].) Therefore, one can only expect a rough agreement between these coefficients and such spectroscopic analysis can only be considered as an estimation within an order of magnitude of the true binary diffusion coefficient.

6.5. Conclusion

In this chapter three independent studies have been presented. The first two studies presented in Sections 6.2 and 6.3 both dealt with the analysis of pure acetylene gas and presented very similar findings for self- broadening and self-induced pressure-shift coefficients. It was also found that the inclusion of a narrowing profile did indeed improve the spectral fit for low pressure acetylene. The third study presented in Section 6.4 covered the topic of low pressure acetylene perturbed by Nitrogen. The line shape parameters obtained in this section agreed quite well with the results found in previous works and more recent theoretical calculations by S. Ivanov, O. Buzykin, and F. Thibault [113].

It was found in Section 6.2 that at ~ 100 Torr the spectral line shape with either the Voigt or speed dependant Voigt could not adequately fit the observed spectrum. It was later found in Section 6.3 that Dicke narrowing could only be examined up to pressures of 40 Torr. This breakup in the pressure regime is very interesting as it indicates that in the range 40 to 100 Torr a more comprehensive understanding of how the speed dependence and collisional narrowing might contribute to the correct line shape information. At this time for the studies presented here this was not feasible with the capability of the available software.

Another interesting observation comes from the determination of the diffusion coefficients presented in Sections 6.3.6 and 6.4.5. It was found that for the acetylene self-broadened measurements the kinetic diffusion coefficients observed in [119] compared quite well with the optical diffusion coefficients obtained in the present study while in

the case of the N₂-broadened acetylene a larger discrepancy was observed. Further investigation into possible reasons for this might be warranted.

Chapter 7: Experimental setup of a Greenhouse Gas Monitoring System (GGMS)

7.1. Introduction

As stated in the Section 1.5 N_2O is 300 times more potent as a green-house gas than CO_2 . This high potency is a major driving force for current research to understand where this gas comes from and how human agricultural activities alter concentrations in the atmosphere. Therefore the development of a detector system that can measure N_2O near what are considered to be local sources of this gas will give great insight into the influence agriculture has on local N_2O concentrations.

The current known concentration of N_2O in the Earth's atmosphere is approximately 314 ppb [144]. This corresponds to about 3.14 mTorr of N_2O in 100 Torr of air. Therefore in order to properly identify this trace gas the system used must be able to measure observable transitions of N_2O under these conditions.

Presented within this chapter is a system that has been developed to address this issue. The system has been designed to measure the P(12), P(13) and P(14) lines of the $4v_1+2v_2$ band of N_2O . This is a weaker combination but it is very isolated and can be observed with the spectrometer system described here. The following sections will outline the setup and performance of the Green-house Gas Monitoring System (GGMS).

7.2. System Overview

7.2.1. Introduction

The overall setup of the GGMS is shown in Figure 7-1 and 7-2. The present setup incorporates an Aerodyne Research, Inc. AMAC-200 astigmatic Herriot cell. This Herriot cell allows for the laser light to travel a distance of 213 meters, offering an ideal path length for low molecular concentration measurements. The system uses a Vortex 6000 laser system provided by New Focus with an operating wavelength range of 1591.12 to 1591.83 nm. A second HeNe laser is used for alignment purposes. The light produced by the laser system is focused onto three separate detectors. The first detector is a Nirvana detector (purchased from New focus) connected directly to the laser diode via fiber optics. This detector is used to record the laser's background signal. The second beam passes through a fiber optics system to a Thor Labs SA200-12B Fabry Perot interferometer. The interferometer's fringe pattern is used to generate the frequency scale after spectral scans have been completed in much the same way as outlined in Section 4.4.2 for the tunable diode laser spectrometer. Finally, the third detector records the signal of the light that has traversed the AMAC-200 Herriot cell.

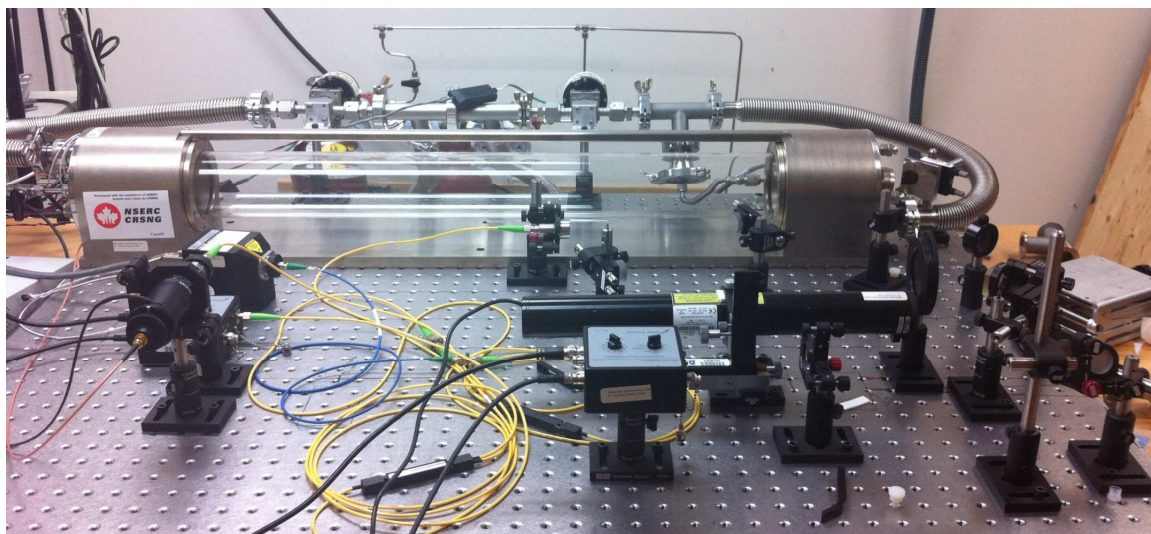


Figure 7-1: Visual overview of the experimental setup of the GGMS.

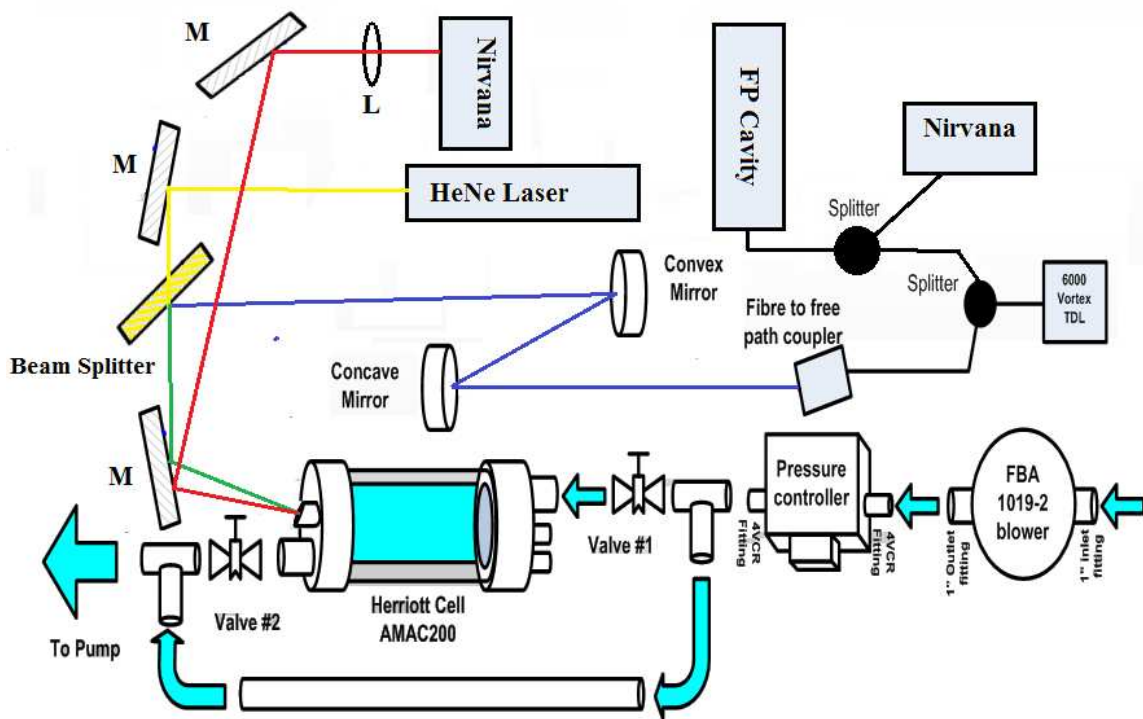


Figure 7-2: Schematic overview of the GGMS system. M indicates where mirrors are placed and L indicates a lens.

The temperature of the gas in the system is measured using a platinum resistance thermometer (PRT) mounted and positioned inside the cell, next to one of the gas inlet ports. The temperature of the PRT is monitored using a LakeShore 330 temperature controller. The pressure of the system is controlled by four instrument components. The first one is the MKS 690A capacitance manometer, which records the pressure of the gas within the chamber using a MKS 670 signal conditioner. The second one is a MKS 640 pressure controller which is used to regulate the pressure within the chamber through the use of a MKS type 246 controller. The third component is a VRC model 200-7.0. A rotary pump is used to generate the vacuum in the system. Finally, a FBA 1019-2 blower is placed on the inlet side of the pressure controller as seen in Figure 7-2. These four components allow for the pressure of the gas to be regulated and maintained at set values.

The system is monitored and controlled using a NI-USB 6229 DAQ system in conjunction with the Labview software. The DAQ system is used to open and close the control valves seen in Figure 7-2, turn on the vacuum pump, blower and the pressure control unit. Once the system is in operation, the DAQ system is used to ramp the laser system and records the signals produced by the three detectors.

7.2.2. Leak rate

The AMAC-200 gas cell was evacuated and tested for any potential leaks beyond what was reported by the manufacturer. Using a turbo molecular pump, the AMAC-200 gas cell was evacuated for several days to guarantee a minimum base pressure. After obtaining a good base pressure, the cell was isolated from the vacuum system. Figure 7-3 shows the leak rate determined over the course of a 10-minute interval after this isolation.

From this figure it can be seen that the leak rate obtained for the system was 0.1158 mTorr/min, better than the manufacturer's quoted leak rate of 0.8 mTorr/min. Therefore, the system was found to be operating well within its stated leak rate and no external leaks were detected.

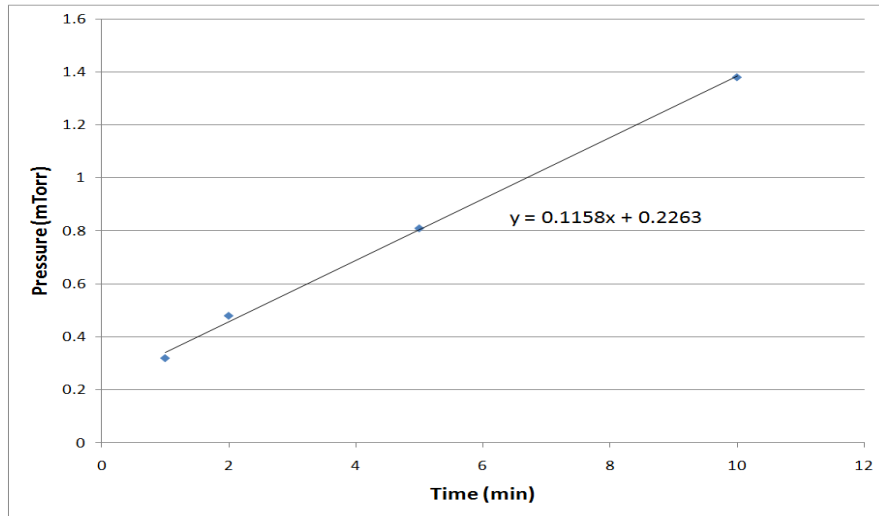


Figure 7-3: Measured leak rate for the AMAC-200 gas cell.

7.2.3. Generating air flow

For field measurements it is important to guarantee that the air within the system is actually being pumped through the gas cell. Early measurements using this system indicated that when the blower, vacuum pump and pressure controller were working together an adequate flow through the cell, was not achieved. This was in fact due to the conductance of the system. Originally, the system had the input and output directly connected using 1 inch T- type fittings. This allowed for maximum conductance along the direct path of inlet to outlet, therefore the air would not flow directly through the chamber. To compensate for this, a 1/4-inch tube was placed between the inlet and outlet

of the system (Figure 7-4 shows this tube in place). The result of including this tube was to produce a conductance of 0.8078 (P) (L/s) along the direction of flow, while the conductance through the cell is approximately 13.059 (P) (L/s). This indicates that the path of least resistance is now through the cell, thus allowing for the proper recycling of the gas inside the chamber.

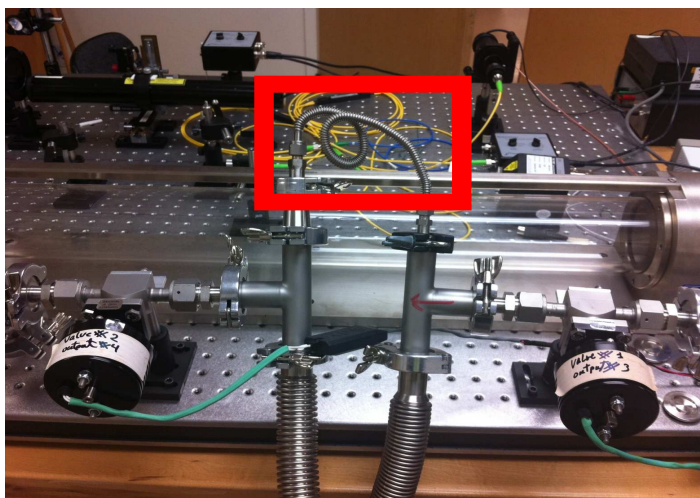


Figure 7-4: Image depicts the reduced conductance along the direct path to the vacuum line.

7.2.4. Fabry Perot cavity

As described in Section 3.3.4, the fringe spacing for this Fabry Perot interferometer needs validated. By measuring the wavelength for all of the peaks from 8 piezo scans using the 1500 WA EXFO wavemeter, the average fringe spacing was determined to be $0.04962 \pm 0.00070 \text{ cm}^{-1}$. This is very close to the manufacturer's stated spacing of 0.05 cm^{-1} .

Table 7-1: Retrieved line positions for P(12), P(13) and P(14) lines of the $4\nu_1+2\nu_2$ band of N_2O .

File name	Line Position (cm^{-1})			# of scans
	P(14)	P(13)	P(12)	
test9Transmission	6282.550653	6283.520180	6284.528333	1
test10Transmission	6282.577355	6283.520381	6284.501073	1
test11Transmission	6282.550340	6283.519991	6284.527814	50
test12Transmission	6282.550557	6283.520025	6284.527637	20
test13Transmission	6282.550401	6283.519929	6284.527522	10
HITRAN [21]	6282.514460	6283.520480	6284.520480	
average	6282.550432	6283.519982	6284.527658	
Position difference (cm^{-1})	-0.035972	0.000498	-0.007178	

Table 7-1 shows line positions retrieved using the “Wprofit.exe” software [87] with spectra recorded on the GGMS and calibrated with the Fabry Perot fringes. The line position of the P (13) transition was used from HITRAN [21] to calibrate the spectra as supported by the high level of agreement observed for this transition. The P (13) line is the most important transition here as it is situated in the center of the lasers scan range while P (12) and P (14) are at either end and in some cases may not be observed depending on how the laser is scanned.

7.3. Measuring Signals

7.3.1. Introduction

The software used to record the data obtained for this experiment was developed using the Labview programming language. The experimental setup can be seen in Figure 7-2 and the control software front panel is shown in Figure 7-5. The control software has been designed to read all the relevant signals and produces a transmission profile as an output. The experimental design incorporates the use of a function generator along with

triggering features built within the Labview environment in order to record single piezo scans of the laser system.

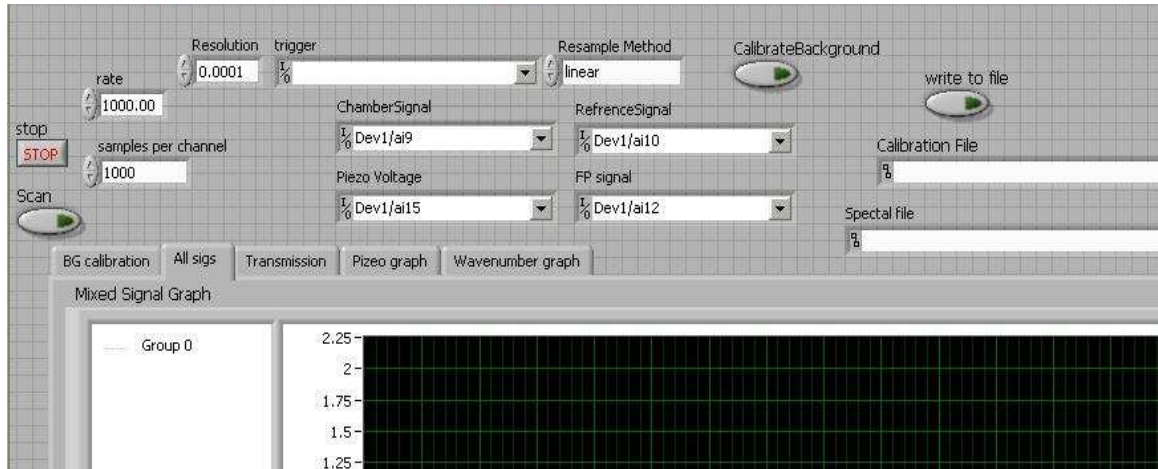


Figure 7-5: Screen shot of the “TriggeredMeasuring.vi” VI used to measure spectra with the GGMS.

Scans of the system are completed by applying a saw tooth signal produced by a Global Specialties 20 MHz function generator to the frequency modulation port on the Vortex laser controller. The Vortex laser system is very similar to Velocity laser system presented in 3.2.2 with the major difference being the absence of a stepping motor in the Vortex system. The applied voltage is varied from -2.3V to 2.3V in order to cover the full range of the piezo device within the laser head. The signal applied to the Vortex laser controller can be seen in Figure 7-6 as the dark blue trace. The frequency of the piezo modulation can be set reliably between 1 to 5 Hz, while each channel of the national instruments DAQ card can be sampled up to a rate of 70 KHz. This allows for high-resolution measurements to be acquired in a very short scan time. The frequency of the piezo modulation is related to the two controls shown in Figure 7-5 “rate” (which controls the sampling rate of the DAQ card) and “samples per channel” (which controls

how many samples are recorded for a single cycle of the saw tooth function) by the following expression.

$$\text{Samples per channel} = \frac{\text{Rate}}{\text{Frequency}} \quad 7-1$$

Therefore, the resolution of the spectra will depend on the number of samples recorded for a complete piezo scan. Therefore, careful selection of the sampling rate and modulation frequency is required.

7.3.2. Measuring transmission spectra

An example of the recorded data for one complete scan of the laser system can be seen in Figure 7-6. As seen in the figure, two important signals are recorded. The first is the “Background Signal” produced by the laser light traveling directly to one of the Nirvana detectors and the other is the “Gas Chamber Signal” produce by the light that has traversed the 213 meters through the long path achieved via the Herriot cell to the second Nirvana detector.

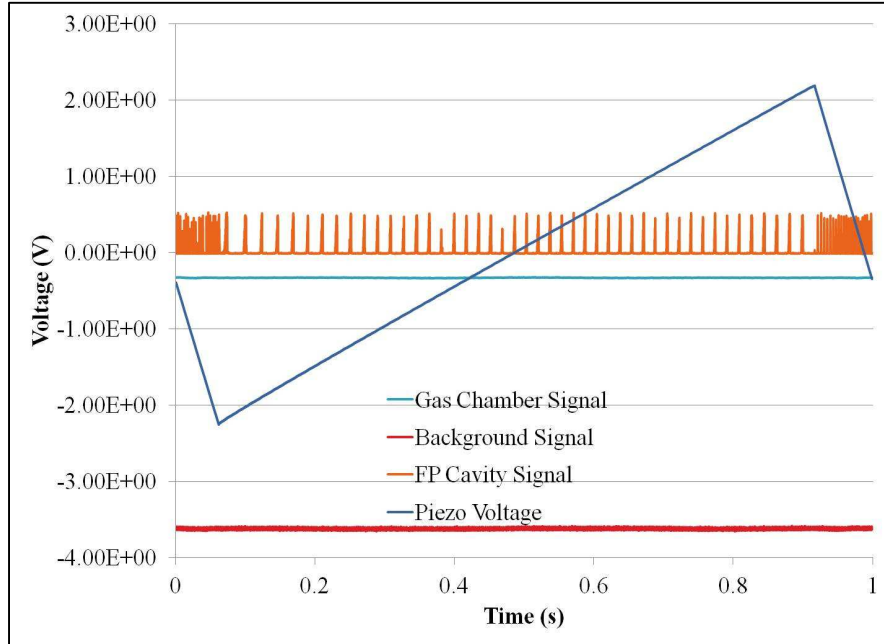


Figure 7-6: Example of the signals recorded using the GGMS setup.

In order to produce a transmission profile, the software has been designed to record a calibration file. The calibration file is produced by evacuating the chamber and then selecting the “Scan” button with the “CalibrateBackground” control turned on (see Figure 7-5). This will record all the necessary signals to produce the calibration file. The calibration file is created by taking the two low-pressure signals measured and generates a ratio that is called the calibration signal. The following equation shows how the calibration signal is produced from the two signals.

$$Calibration\ Signal = \frac{Gas\ Chamber\ Signal\ (p \approx 0)}{Background\ Signal\ (p \approx 0)} \quad 7-2$$

Once this calibration signal has been determined, the chamber can be filled with the gas and the resulting measurements can produce transmission spectra. The transmission spectrum is generated by creating a background signal from the reference signal as shown in the following equation:

$$\text{Background} = \frac{\text{Background Signal (p)}}{\text{Calibration Signal}} \quad 7-3$$

By dividing the Gas Chamber Signal by the new Background signal the transmission spectrum is obtained as follows:

$$\text{Transmission} = \frac{\text{Gas Chamber Signal (p)}}{\text{Background}} \quad 7-4$$

Once the transmission spectrum has been produced, the time scale is converted into a wavenumber scale using the Fabry Perot peaks in much the same way as described in Section 4.4.2. This only produces a relative wavenumber scale. To calibrate the actual wavenumber scale, a measured transition is selected and used to shift the scale accordingly; the HITRAN08 [21] database is used to do this. Figure 7-7 shows an example of a single transmission spectrum. It is clear from the figure that there is quite a bit of noise. To deal with this noise, signal averaging has been included within the “TriggeredMeasuring.vi” VI and will be discussed next.

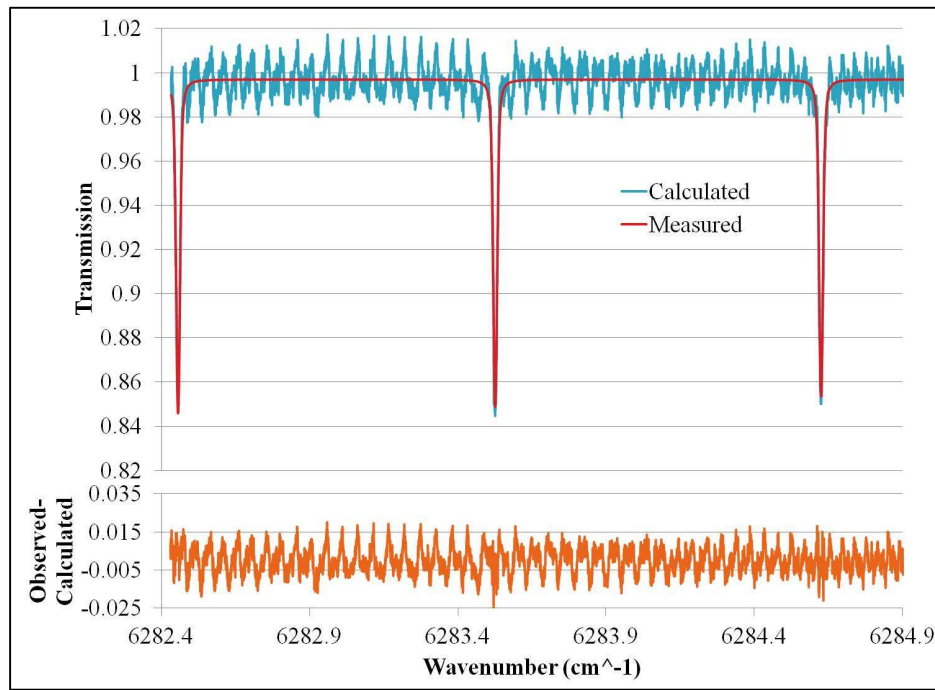


Figure 7-7: Spectra generated from a single scan of the GGMS system.

7.3.3. Signal averaging

To improve the poor signal-to-noise ratio seen in Figure 7-7, the averaging of the scans was performed. Table 7-2 shows the results of performing several different averaging numbers. It is clearly obvious and not unexpected that the more averaging that is completed, the better the signal to noise ratio will be. Figure 7-8 shows the difference between completing one scan versus using the average of 50 scans. It is clear that the noise is considerably reduced as more spectral features are observed in the averaged spectrum. However, it is also important to consider the temporal impact that averaging a large number of scans might have on the resulting spectra. This temporal component will need to be tested in the field through the use of the Allan variance [145].

Table 7-2: Summary of the changes observed in the signal to noise ratio in relation to the number of scans averaged.

# of Scans Averaged	1	5	10	20	50
Average S/N	150.8013	418.1971	598.1395	855.5968	1302.115

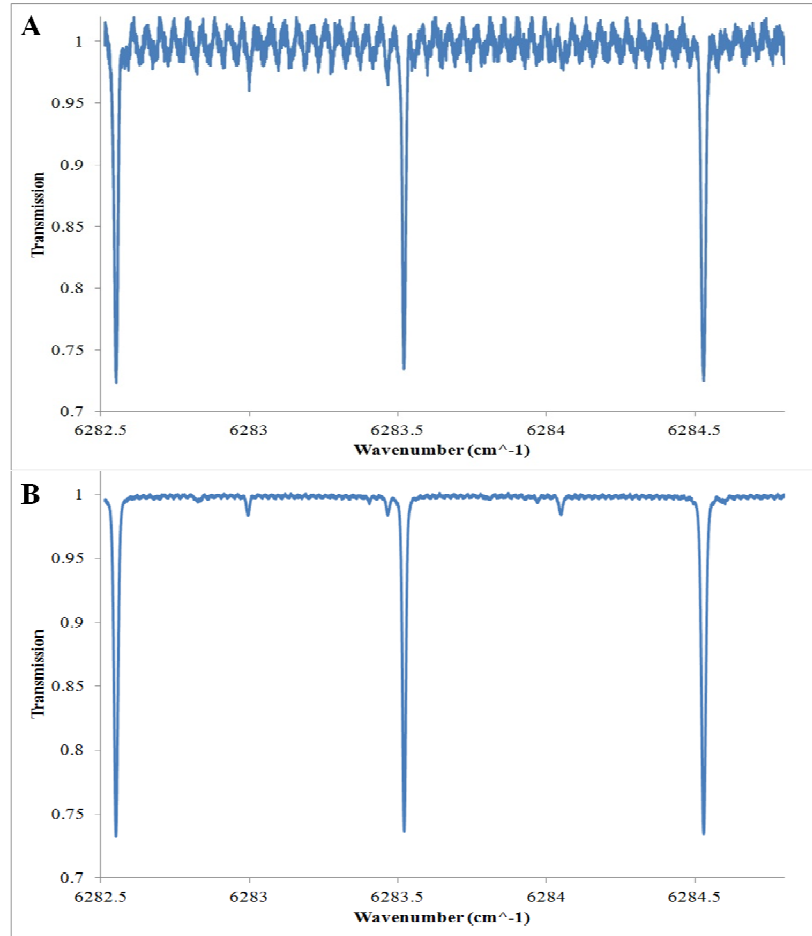


Figure 7-8: Example of N₂O recorded spectra when (A) single scan is performed and (B) 50 scans are averaged together.

7.4. Verifying the Optical Alignment of the cell

The alignment of the astigmatic Herriot cell can be very challenging even if you can see the beam. In the case where infrared radiation is used, the degree of difficulty grows substantially. Several tricks can be used to make the alignment process easier. From Figure 7-2 it can be seen that there is a HeNe laser inside the system. This laser is directed onto a beam splitter in an effort to produce a co-linear beam that contains both the infra-red beam and the HeNe beam. Once the two beams are correctly overlapped, then the input mirror can be adjusted until the ideal spot pattern is formed. An example of the proper spot pattern is shown in Figure 7-9.

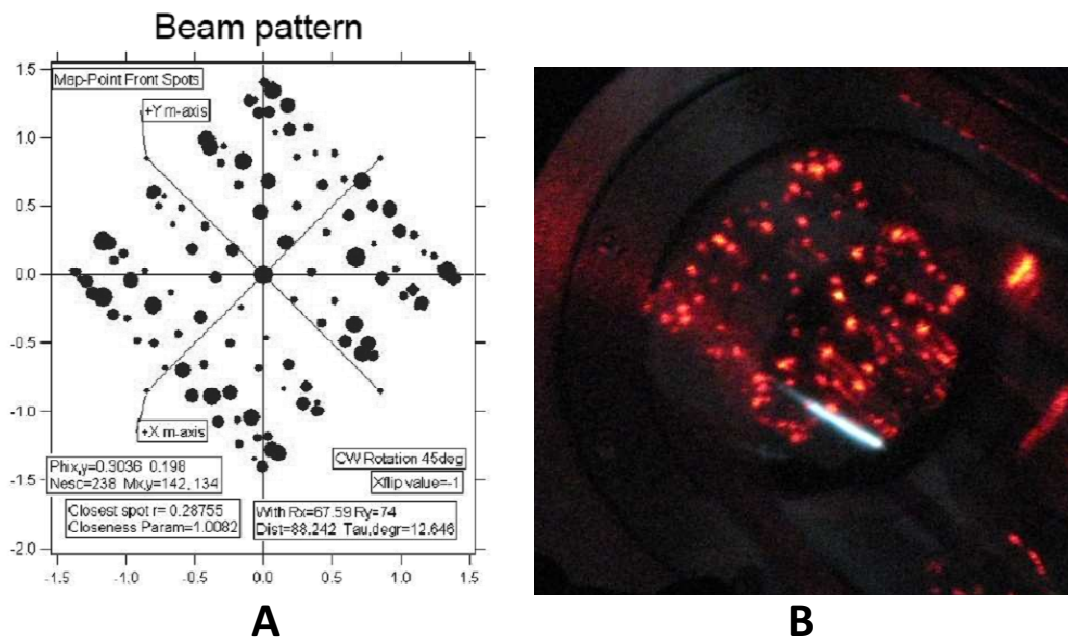


Figure 7-9: Visual spot pattern produced from proper alignment, (A) shows the spot pattern provided by Aerodyne Research inc. and (B) shows the spot pattern produced by the HeNe trace beam after completing the alignment.

Once the ideal spot pattern is found with the HeNe beam, the cell's output signal is monitored with the Nirvana detector while the directing mirrors are adjusted slowly until an optimal signal is achieved. After finding the optimal signal, scans are performed to record spectra at known pressures, concentrations and temperatures?. These spectra were then compared to simulated spectra generated from the line parameters listed in the HITRAN08 [21] database and the assumed pathlength of 213 m (same as the pathlength of the Herriot cell). Two examples of these simulations are shown for 10.7 Torr and 140 mTorr in Figure 7-10 and Figure 7-11, respectively. It is clear from these figures that the two spectra do line up really well with each other. This result indicates that the optimal path length of 213 m has been achieved.

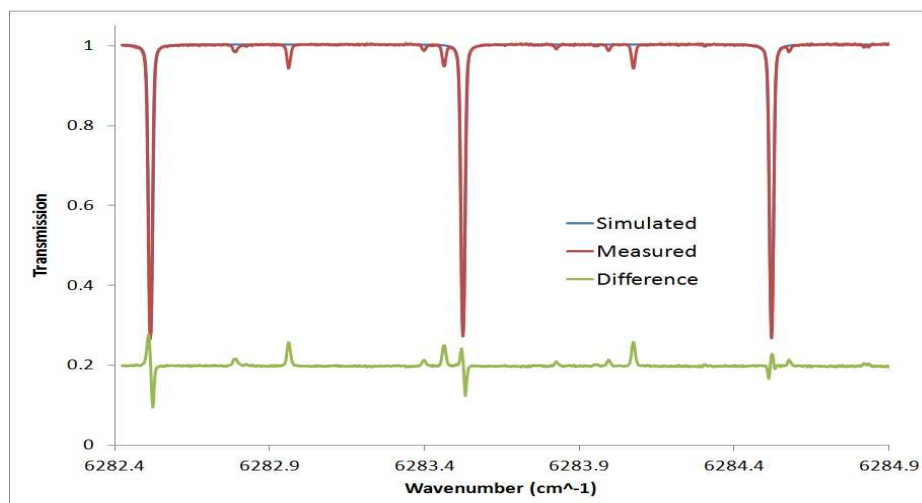


Figure 7-10: Comparison of N₂O gas at 10.7 Torr (one single spectrum) measured with the GGMS against HITRAN [21] simulated spectra.

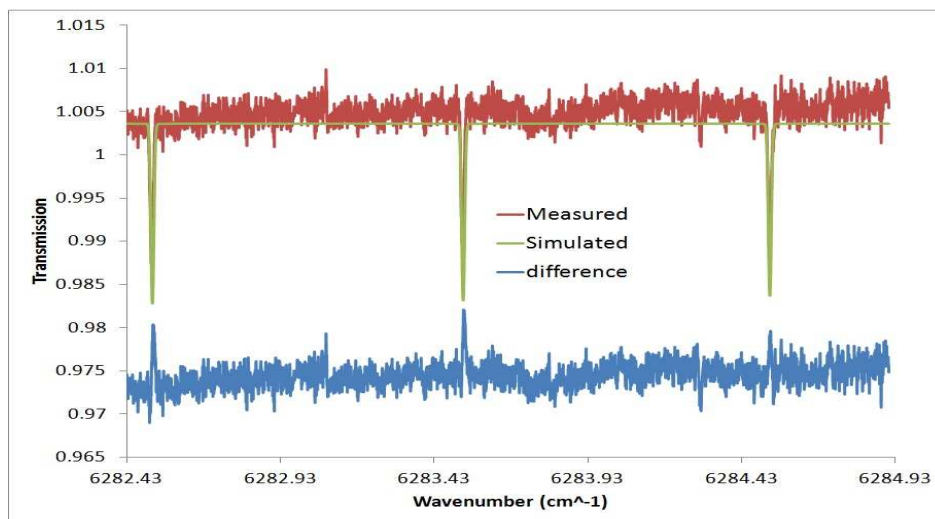


Figure 7-11: Comparison of N₂O gas at 140 mTorr measured (one single spectrum) with the GGMS against HITRAN [21] simulated spectra.

7.5. Spectral Analysis

Data analysis using programs such as the one developed by Dr. Daniel Hurtmans [87] has been up until this point more than adequate. However, with the desire to run this system in the field in an automated fashion, a new program had to be written to allow for concentration retrievals to be made from the spectra recorded by the GGMS. Figure 7-12 and Figure 7-13 show the program called “ProfileFit.vi”. It has been developed to allow for multiple lines to be fit simultaneously using a non-linear least squares fitting routine. The program allows the user to fit for intensity, molar fraction (concentration), narrowing, line center, self- and foreign- broadening and pressure-induced shift. It currently can fit the Doppler, Lorentz, Voigt and Hard Rautian line shape models outlined in Section 2.4.

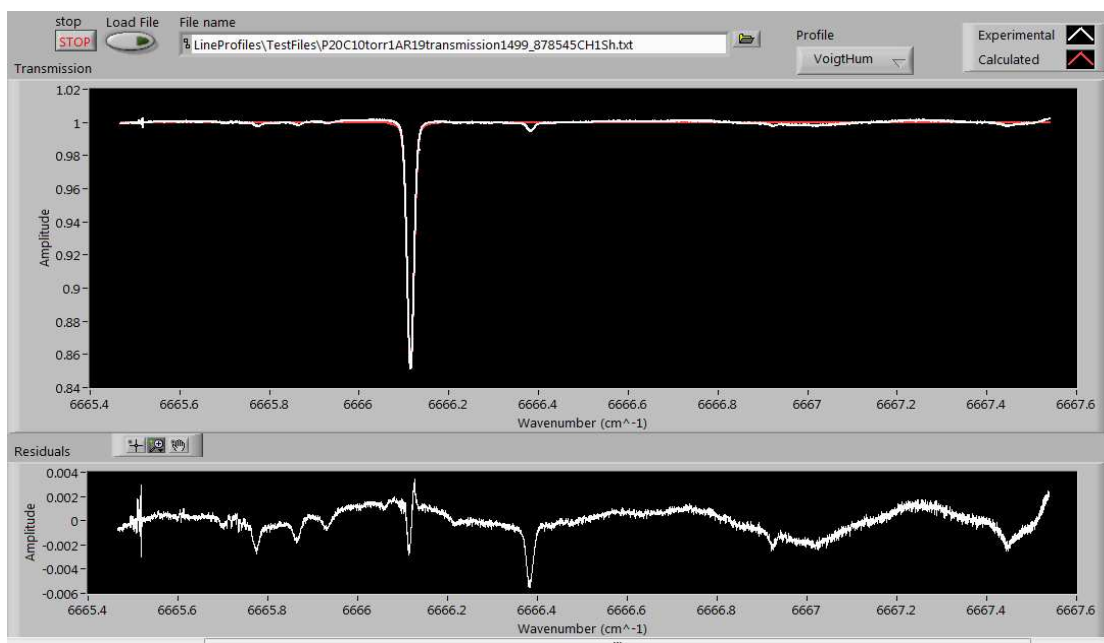


Figure 7-12: Example spectra of the R(19) line in the $\nu_1+\nu_2+\nu_4+\nu_5$ band of C_2H_2 fit with a Voigt profile from the “ProfileFit.vi” VI.

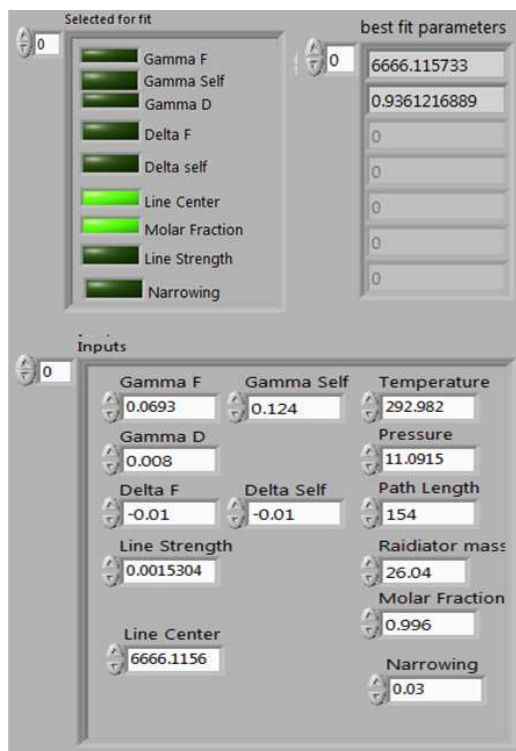


Figure 7-13: Controls and Indicators for the “ProfileFit.vi” VI. Gamma denotes the broadening values, Delta the shift with the F representing foreign. Gamma D is the Doppler width. The Inputs cluster contains the initial values and spectral information like pressure and temperature. The best fit parameters are directly related to the Boolean controls in the cluster select to fit.

The “ProfileFit.vi” program was tested for accuracy against the “Wprofit.exe” program to validate the quality of the retrieved parameters. Table 7-3 shows the results of examining three individual spectra recorded for the R(19) line of the $\nu_1+\nu_2+\nu_4+\nu_5$ band of C_2H_2 when fit using the Voigt profile. The table indicates reasonably good agreement with the two programs. The average values calculated from this analysis show the best overall agreement. Another important finding from the table is that the variations in the retrieved parameters for the “ProfileFit.vi” program are quite small from one spectrum to another. This indicates a higher degree of stability with the Voigt approximation made in this program.

Table 7-3: Comparison of retrieved line shape parameters using the Voigt profile in “Wproffit.exe” [87] and “ProfileFit.vi”. The isolated R(19) line of the $\nu_1+\nu_2+\nu_4+\nu_5$ band of C_2H_2 was used to compare values.^a For positions the differences between the two retrieved positions are listed.

Program	Wproffit.exe	ProfileFit.vi	% Difference ^a
P20C10Torr1AR19transmission1499_878545CH1Sh			
Position (cm ⁻¹)	6666.11552	6666.11573	0.00022
broadening (cm ⁻¹ atm ⁻¹)	0.09001	0.09405	4.48%
Intensity (cm ⁻¹ atm ⁻¹)	0.00141	0.00141	0.55%
P20C10Torr1AR19transmission1499_928545CH1Sh			
Position (cm ⁻¹)	6666.11552	6666.11571	0.00018
broadening (cm ⁻¹ atm ⁻¹)	0.10160	0.09400	7.48%
Intensity (cm ⁻¹ atm ⁻¹)	0.00146	0.00141	3.69%
P20C10Torr1AR19transmission1499_978545CH1Sh			
Position (cm ⁻¹)	6666.11548	6666.11569	0.00021
broadening (cm ⁻¹ atm ⁻¹)	0.09037	0.09460	4.69%
Intensity (cm ⁻¹ atm ⁻¹)	0.00143	0.00140	1.77%
Average Values			
Position (cm ⁻¹)	6666.11551	6666.11571	0.00020
broadening (cm ⁻¹ atm ⁻¹)	0.09399	0.09422	0.24%
Intensity (cm ⁻¹ atm ⁻¹)	0.00143	0.00141	2.02%

7.6. Conclusion

This chapter presents a detailed introductory picture of the GGMS. The system is in the final stages for laboratory testing and setup. The remaining features to be completed are the optimization of the signal-to-noise ratio so that the lowest possible concentration limit can be obtained, and the development of an enclosure to keep it safe while operating in the field.

As an interesting side note to this detection system is its detection capability to identify several CO₂ transitions in the 1.59 μm spectral range if present in high enough

concentrations. It may therefore be possible for this system to be used to monitor exhaust products from conventional combustion engines.

Chapter 8: Conclusion

8.1. Closing Remarks

The purpose of the work presented here has been the development of methods and techniques that can be used to improve how spectra are measured. Through the development of high-resolution techniques it is hoped that improved line shape parameters can be measured in the laboratory with the sole purpose of improving spectral databases like HITRAN and GIESA. The improvements made to these databases will hopefully lead to the improved accuracy of future remote sounding experiments.

The work contained in this thesis has been based strictly on select rovibrational bands in the infrared spectra of linear polyatomic molecules such as C_2H_2 , CO_2 and N_2O . These types of molecules are some of the most important ones as they offer a window into more complicated systems. By understanding the physics and chemistry behind the rotation-vibration spectra of these simpler molecules one probably can obtain greater insight into the knowledge that will affect the spectral line shapes of more complex molecules.

Chapter 2 focused solely on the theoretical aspects that describe how spectra are observed. The information presented in this chapter is vital to understanding how spectroscopic analysis is performed. The information presented there was used to produce all of the work presented in Chapters 5, 6 and 7.

A complete description of the experimental system used to record and analyze the spectra for acetylene was presented in Chapters 3 and 4. They outline the entire process

taken to generate high resolution spectra. Also a detailed description of determining the measurement uncertainties was provided for each of the retrieved spectral line parameters. Understanding and correcting such errors are vital in justifying the validity of the data obtained by any system.

Chapter 5 outlines the detailed analysis done on line mixing in CO₂. Using known broadening coefficients, two methods were employed to obtain the line mixing coefficients and their temperature dependence exponents. This information is critical in improving remote based measurements of CO₂ in planetary atmospheres as slight asymmetries in the spectra measured due to line mixing need to be accounted for. When ignored retrieved concentrations will have a much larger associated error.

The line shape analysis presented in Chapter 6 was completed using the software developed by Dr. Hurtmans [87]. The data presented in this chapter include the two combination bands $\nu_1+\nu_3$ and $\nu_1+\nu_2+\nu_4+\nu_5$ of acetylene. Both of these bands are $\Sigma \leftarrow \Sigma$ bands with a vibrational angular momentum of $\ell = 0$ thus only giving rise to P and R branches. The results of analysing the data from this work was shown to agree quite well with previous studies reported in the literature and also presenting new insight into the temperature dependence of the line shape parameters. Furthermore the detailed analysis of Dicke narrowing in these two bands will hopefully aid in future studies of this molecule.

Chapter 7 describes the initial development of a green-house gas monitoring system. An overview and the quality of recorded spectra are presented with a description of the methods used to obtain high resolution spectra. Also presented is the program

“ProfileFit.vi” which has been compared to the “Wproffit.exe” developed by Dr. Hurtmans [87]. The comparison indicates that the program will be able to reliably obtain concentrations for the trace gas molecules using spectra recorded by the system.

8.2. Future Work

Simulated line mixing in CO₂ offers a great way to improve the retrieval of concentrations from remote-based measurements. However, with any model confirmation from experimental data is very important. Therefore, it would be ideal if the line mixing coefficients presented in Chapter 5 could be confirmed experimentally for all the temperatures presented. It is important to note that it is expected that there are differences in the retrieved spectral line parameters as the complete description of the relaxation matrix depends on both the pressure broadening and pressure-induced shift coefficients. The pressure-induced shift is generally ignored so that a tractable solution can be found. Any observed systematic difference observed may offer insight into the effects related to ignoring the pressure-induced shift from the general solution.

Future work for the field instrument would be testing the system at a remote location. The final steps needed to complete this task include the development of a thermally isolated enclosure for the entire system and final testing and setup of the signal averaging and processing. Once completed N₂O levels at designated locations could be examined and a comprehensive time study could be completed. This could potentially identify the impact of agriculture on the local N₂O concentrations and also give a seasonal picture of how the concentration of N₂O fluctuates throughout the year.

With regards to acetylene spectrum analysis, more complex work involving different perturbing species could improve our understanding of line-shape parameters obtained using the various models presented in this work. By adjusting the mass ratio of the radiator and the perturber a more detailed analysis of the Dicke narrowing pressure regime could be investigated. It may also be possible to understand the correlation between the speed dependence and Dicke narrowing by carefully examining spectra in different pressure regimes. That is speed dependence could be tested for spectra with pressures over 200 Torr. Then using the information obtained from this analysis, speed dependence could be fixed while Dicke narrowing is fit for low pressure spectra at 100 Torr or lower. This type of work would require the development of more sophisticated fitting software, but would be enlightening on the physical mechanisms observed in these spectra.

Bibliography

- [1] R.N. Hall, R.O. Carlson, T.J. Soltys, G.E. Fenner, J.D. Kingsley, *Coherent Light Emission from Gaas Junctions*. Physical Review Letters **9**, 366-& (1962).
- [2] A.A. Madej, A.J. Alcock, A. Czajkowski, J.E. Bernard, S. Chepurov, *Accurate absolute reference frequencies from 1511 to 1545 nm of the $\nu(1)+\nu(3)$ band of (C₂H₂)-C-12 determined with laser frequency comb interval measurements*. Journal of the Optical Society of America B-Optical Physics **23**, 2200-2208 (2006).
- [3] A. Coustenis, R.K. Achterberg, B.J. Conrath, D.E. Jennings, A. Marten, D. Gautier, C.A. Nixon, F.M. Flasar, N.A. Teanby, B. Bezard, R.E. Samuelson, R.C. Carlson, E. Lellouch, G.L. Bjoraker, P.N. Romani, F.W. Taylor, P.G.J. Irwin, T. Fouchet, A. Hubert, G.S. Orton, V.G. Kunde, S. Vinatier, J. Mondellini, M.M. Abbas, R. Courtin, *The composition of Titan's stratosphere from Cassini/CIRS mid-infrared spectra*. Icarus **189**, 35-62 (2007).
- [4] T.Y. Brooke, A.T. Tokunaga, H.A. Weaver, J. Crovisier, D. BockeleeMorvan, D. Crisp, *Detection of acetylene in the infrared spectrum of comet Hyakutake*. Nature **383**, 606-608 (1996).
- [5] P. Varanasi, B.R.P. Bangaru, *INTENSITY AND HALF-WIDTH MEASUREMENTS IN 1.525 MUM BAND OF ACETYLENE*. Journal of Quantitative Spectroscopy & Radiative Transfer **15**, 267-273 (1975).
- [6] J.S. Wong, *Pressure Broadening of Single Vibrational-Rotational Transitions of Acetylene at $Nu=5$* . Journal of Molecular Spectroscopy **82**, 449-451 (1980).
- [7] D. Lambot, A. Olivier, G. Blanquet, J. Walrand, J.P. Bouanich, *Diode-Laser Measurements of Collisional Line Broadening in the Upsilon-5 Band of C₂h₂*. Journal of Quantitative Spectroscopy & Radiative Transfer **45**, 145-155 (1991).
- [8] D. Lambot, J.C. Populaire, J. Walrand, G. Blanquet, J.P. Bouanich, *Diode-Laser Measurements of Self-Broadening Coefficients in the Upsilon(5)-Band of C₂h₂ at Low-Temperature*. Journal of Molecular Spectroscopy **165**, 1-11 (1994).
- [9] A.S. Pine, *Self-Broadening, N₂-Broadening and Ar-Broadening and Line Mixing in Hcn and C₂h₂*. Journal of Quantitative Spectroscopy & Radiative Transfer **50**, 149-166 (1993).
- [10] A. Lucchesini, M. DeRosa, D. Pelliccia, A. Ciucci, C. Gabbanini, S. Gozzini, *Diode laser spectroscopy of overtone bands of acetylene*. Applied Physics B-Lasers and Optics **63**, 277-282 (1996).
- [11] R. Georges, D. VanderVorst, M. Herman, D. Hurtmans, *Ar and self-pressure broadening coefficient of the R(11), 5 nu(3) line of (C₂H₂)-C-12*. Journal of Molecular Spectroscopy **185**, 187-188 (1997).
- [12] D. Biswas, B. Ray, S. Dutta, P.N. Ghosh, *Diode laser spectroscopic measurement of line shape of (nu(1)+3 nu(3)) band transitions of acetylene*. Applied Physics B-Lasers and Optics **68**, 1125-1130 (1999).
- [13] F. Herregodts, D. Hurtmans, J. Vander Auwera, M. Herman, *Laser spectroscopy of the nu(1)+3 nu(3) absorption band in (C₂H₂)-C-12. I. Pressure broadening and absolute line intensity measurements*. Journal of Chemical Physics **111**, 7954-7960 (1999).
- [14] C. Yelleswarapu, A. Sharma, *Pressure-induced self-broadening and frequency shift measurements of absorption lines of acetylene using tunable diode laser absorption*

- spectroscopy*. Journal of Quantitative Spectroscopy & Radiative Transfer **69**, 151-158 (2001).
- [15] P. Minutolo, C. Corsi, F. D'Amato, M. De Rosa, *Self- and foreign-broadening and shift coefficients for C₂H₂ lines at 1.54 μ m*. European Physical Journal D **17**, 175-179 (2001).
- [16] H. Valipour, D. Zimmermann, *Investigation of J dependence of line shift, line broadening, and line narrowing coefficients in the $\nu(1)+3 \nu(3)$ absorption band of acetylene*. Journal of Chemical Physics **114**, 3535-3545 (2001).
- [17] D. Jacquemart, J.Y. Mandin, V. Dana, L. Regalia-Jarlot, X. Thomas, P. Von der Heyden, *Multispectrum fitting measurements of line parameters for 5- μ m cold bands of acetylene*. Journal of Quantitative Spectroscopy & Radiative Transfer **75**, 397-422 (2002).
- [18] M. Lepere, G. Blanquet, J. Walrand, J.P. Bouanich, M. Herman, J.V. Auwera, *Self-broadening coefficients and absolute line intensities in the $\nu(4)+\nu(5)$ band of acetylene*. Journal of Molecular Spectroscopy **242**, 25-30 (2007).
- [19] O.M. Lyulin, D. Jacquemart, N. Lacombe, V.I. Perevalov, J.Y. Mandin, *Line parameters of acetylene in the 1.9 and 1.7micron spectral regions*. Journal of Quantitative Spectroscopy & Radiative Transfer **109**, 1856-1874 (2008).
- [20] J.S. Li, G. Durry, J. Cousin, L. Joly, B. Parvitte, V. Zeninari, *Self-broadening coefficients and positions of acetylene around 1.533 μ m studied by high-resolution diode laser absorption spectrometry*. Journal of Quantitative Spectroscopy & Radiative Transfer **111**, 2332-2340 (2010).
- [21] L.S. Rothman, I.E. Gordon, A. Barbe, D.C. Benner, P.E. Bernath, M. Birk, V. Boudon, L.R. Brown, A. Campargue, J.P. Champion, K. Chance, L.H. Coudert, V. Dana, V.M. Devi, S. Fally, J.M. Flaud, R.R. Gamache, A. Goldman, D. Jacquemart, I. Kleiner, N. Lacombe, W.J. Lafferty, J.Y. Mandin, S.T. Massie, S.N. Mikhailenko, C.E. Miller, N. Moazzen-Ahmadi, O.V. Naumenko, A.V. Nikitin, J. Orphal, V.I. Perevalov, A. Perrin, A. Predoi-Cross, C.P. Rinsland, M. Rotger, M. Simeckova, M.A.H. Smith, K. Sung, S.A. Tashkun, J. Tennyson, R.A. Toth, A.C. Vandaele, J. Vander Auwera, *The HITRAN 2008 molecular spectroscopic database*. Journal of Quantitative Spectroscopy & Radiative Transfer **110**, 533-572 (2009).
- [22] N. Jacquinet-Husson, N.A. Scott, A. Chedina, L. Crepeau, R. Armante, V. Capelle, J. Orphal, A. Coustenis, C. Boone, N. Poulet-Crovisier, A. Barbee, M. Birk, L.R. Brown, C. Camy-Peyret, C. Claveau, K. Chance, N. Christidis, C. Clerbaux, P.F. Coheur, V. Dana, L. Daumont, M.R. De Backer-Barilly, G. Di Lonardo, J.M. Flaud, A. Goldman, A. Hamdouni, M. Hess, M.D. Hurley, D. Jacquemart, I. Kleiner, P. Kopke, J.Y. Mandin, S. Massie, S. Mikhailenko, V. Nemtchinov, A. Nikitin, D. Newnham, A. Perrin, V.I. Perevalov, S. Pinnock, L. Regalia-Jarlot, C.P. Rinsland, A. Rublev, F. Schreier, L. Schult, K.M. Smith, S.A. Tashkun, J.L. Teffo, R.A. Toth, V.G. Tyuterev, J.V. Auwera, P. Varanasi, G. Wagner, *The GEISA spectroscopic database: Current and future archive for Earth and planetary atmosphere studies*. Journal of Quantitative Spectroscopy & Radiative Transfer **109**, 1043-1059 (2008).
- [23] C.P. Rinsland, M.A.H. Smith, J.M. Russell, J.H. Park, C.B. Farmer, *STRATOSPHERIC MEASUREMENTS OF CONTINUOUS ABSORPTION NEAR 2400 CM⁻¹*. Applied Optics **20**, 4167-4171 (1981).
- [24] D. Spankuch, Atmos. Res **23**, 244-323 (1989).

- [25] D.P. Edwards, L.L. Strow, *SPECTRAL-LINE SHAPE CONSIDERATIONS FOR LIMB TEMPERATURE SOUNDERS*. Journal of Geophysical Research-Atmospheres **96**, 20859-20868 (1991).
- [26] B. Funke, G.P. Stiller, T. Von Clarmann, G. Echle, H. Fischer, *CO₂ line mixing in MIPAS limb emission spectra and its influence on retrieval of atmospheric parameters*. Journal of Quantitative Spectroscopy & Radiative Transfer **59**, 215-230 (1998).
- [27] R. Rodrigues, K.W. Jucks, N. Lacombe, G. Blanquet, J. Walrand, W.A. Traub, B. Khalil, R. Le Doucen, A. Valentin, C. Camy-Peyret, L. Bonamy, J.M. Hartmann, *Model, software, and database for computation of line-mixing effects in infrared Q branches of atmospheric CO₂ - I. Symmetric isotopomers*. Journal of Quantitative Spectroscopy & Radiative Transfer **61**, 153-184 (1999).
- [28] L.L. Strow, S.E. Hannon, S. De Souza-Machado, H.E. Motteler, D. Tobin, *An overview of the AIRS radiative transfer model*. Ieee Transactions on Geoscience and Remote Sensing **41**, 303-313 (2003).
- [29] F. Niro, C. Boulet, J.M. Hartmann, *Spectra calculations in central and wing regions of CO₂IR bands between 10 and 20 μ m. I: model and laboratory measurements*. Journal of Quantitative Spectroscopy & Radiative Transfer **88**, 483-498 (2004).
- [30] F. Niro, T. von Clarmann, K. Jucks, J.M. Hartmann, *Spectra bands calculations in central and wing regions of CO₂IR between 10 and 20 μ m. III: atmospheric emission spectra*. Journal of Quantitative Spectroscopy & Radiative Transfer **90**, 61-76 (2005).
- [31] V.M. Devi, D.C. Benner, L.R. Brown, C.E. Miller, R.A. Toth, *Line mixing and speed dependence in CO₂ at 6348 cm^{-1} : Positions, intensities, and air- and self-broadening derived with constrained multispectrum analysis*. Journal of Molecular Spectroscopy **242**, 90-117 (2007).
- [32] V.M. Devi, D.C. Benner, L.R. Brown, C.E. Miller, R.A. Toth, *Line mixing and speed dependence in CO₂ at 6227.9 cm^{-1} Constrained multispectrum analysis of intensities and line shapes in the 30013 \leftarrow 00001 band*. Journal of Molecular Spectroscopy **245**, 52-80 (2007).
- [33] A. Predoi-Cross, W. Liu, C. Holladay, A.V. Unni, I. Schofield, A.R.W. McKellar, D. Hurtmans, *Line profile study of transitions in the 30012 \leftarrow 00001 and 30013 \leftarrow 00001 bands of carbon dioxide perturbed by air*. Journal of Molecular Spectroscopy **246**, 98-112 (2007).
- [34] A. Predoi-Cross, A. Unni, W. Liu, I. Schofield, C. Holladay, A.R.W. McKellar, D. Hurtmans, *Line shape parameters measurement and computations for self-broadened carbon dioxide transitions in the 30012 \leftarrow 00001 and 30013 \leftarrow 00001 bands, line mixing, and speed dependence*. Journal of Molecular Spectroscopy **245**, 34-51 (2007).
- [35] A. Predoi-Cross, A.R.W. McKellar, D.C. Benner, V.M. Devi, R.R. Gamache, C.E. Miller, R.A. Toth, L.R. Brown, *Temperature dependences for air-broadened Lorentz half-width and pressure shift coefficients in the 30013 \leftarrow 00001 and 30012 \leftarrow 00001 bands of CO₂ near 1600 nm*. Canadian Journal of Physics **87**, 517-535 (2009).
- [36] S.A. Montzka, et al., *Controlled substances and other source gases*. In: *Scientific Assessment of Ozone Depletion: 2002*. World Meteorological Organization Geneva, pp. 1.1-1.83 (2003).

- [37] E.G. Estupinan, Georgia Institute of Technology, Atlanta, Georgia, USA, 2001.
- [38] C.R. Flechard, P. Ambus, U. Skiba, R.M. Rees, A. Hensen, A. van Amstel, A. van den Pol-van Dasselaar, J.-F. Soussana, M. Jones, J. Clifton-Brown, A. Raschi, L. Horvath, A. Neftel, M. Jocher, C. Ammann, J. Leifeld, J. Fuhrer, P. Calanca, E. Thalman, K. Pilegaard, C. Di Marco, C. Campbell, E. Nemitz, K.J. Hargreaves, P.D. Levy, B.C. Ball, S.K. Jones, W.C.M. van de Bulk, T. Groot, M. Blom, R. Dominguez, G. Kasper, V. Allard, E. Ceschia, P. Laville, P. Cellier, C. Henault, F. Bizouard, M. Abdalla, M. Williams, S. Baronti, F. Berretti, B. Grosz, *Effects of climate and management intensity on nitrous oxide emissions in grassland systems across Europe*. *Agricultural, Ecosystems and Environment* **121**, 135-152 (2007).
- [39] J.M. Hollas, *Modern Spectroscopy*, 4th Edition. 2004.
- [40] J.-M. Hartmann, C. Boulet, D. Robert, *Collisional Effects on Molecular Spectra*. Elsevier, 2008.
- [41] P. Joubert, X. Bruet, J. Bonamy, D. Robert, F. Chaussard, X. Michaut, R. Saint-Loup, H. Berger, *H₂ vibrational spectral signatures in binary and ternary mixtures: theoretical model, simulation and application to CARS thermometry in high pressure flames*. *Comptes Rendus de l'Academie des Sciences Series IV Physics* **2**, 989 (2001).
- [42] P.R. Berman, *Speed-Dependent Collisional Width and Shift Parameters in Spectral Profiles*. *Journal of Quantitative Spectroscopy & Radiative Transfer* **12**, 1331-& (1972).
- [43] F. Rohart, L. Nguyen, J. Buldyreva, J.M. Colmont, G. Wlodarczak, *Lineshapes of the 172 and 602 GHz rotational transitions of (HCN)-N-15*. *Journal of Molecular Spectroscopy* **246**, 213-227 (2007).
- [44] S. Chandrasekhar, *Stochastic problems in physics and astronomy*. *Reviews of Modern Physics* **15**, 0001-0089 (1943).
- [45] L. Galatry, *Simultaneous Effect of Doppler and Foreign Gas Broadening on Spectral Lines*. *Physical Review* **122**, 1218 (1961).
- [46] M. Nelkin, A. Ghatak, *Simple Binary Collision Model for Van Hoves Gs(R,T)*. *Physical Review a-General Physics* **135**, A4-& (1964).
- [47] S.G. Rautian, I.I. Sobelman, *Effect of Collisions on Doppler Broadening of Spectral Lines*. *Soviet Physics Uspekhi-Ussr* **9**, 701-& (1967).
- [48] P.W. Anderson, *Pressure Broadening in the Microwave and Infra-Red Regions*. *Physical Review* **76**, 647-661 (1949).
- [49] C.J. Tsao, B. Curnutte, *Line-Widths of Pressure-Broadened Spectral Lines*. *Journal of Quantitative Spectroscopy & Radiative Transfer* **2**, 41-91 (1962).
- [50] G. Birnbaum, *Microwave pressure broadening and its application to intermolecular forces*. *Advances in Chemical Physics: Intermolecular Forces, Volume 12* 487-548 (2007).
- [51] T. Nakazawa, M. Tanaka, *Intensities, Half-Widths and Shapes of Spectral-Lines in the Fundamental-Band of Co at Low-Temperatures*. *Journal of Quantitative Spectroscopy & Radiative Transfer* **28**, 471-480 (1982).
- [52] M.F. Lemoal, F. Severin, *N-2 and H-2 Broadening Parameters in the Fundamental-Band of Co*. *Journal of Quantitative Spectroscopy & Radiative Transfer* **35**, 145-152 (1986).
- [53] J. Bonamy, D. Robert, C. Boulet, *Simplified Models for the Temperature-Dependence of Linewidths at Elevated-Temperatures and Applications to Co Broadened*

- by Ar and N₂. *Journal of Quantitative Spectroscopy & Radiative Transfer* **31**, 23-34 (1984).
- [54] T. Drascher, T.F. Giesen, T.Y. Wang, N. Schmucker, R. Schieder, G. Winnewisser, P. Joubert, J. Bonamy, *Temperature-dependent line shift and broadening of CO infrared transitions*. *Journal of Molecular Spectroscopy* **192**, 268-276 (1998).
- [55] T.A. Brunner, D. Prichard, in: K.P. Lawley, *Advances in Chemical Physics*, volume 50: Dynamics of the excited state. John Wiley and Sons, Ltd, 1982.
- [56] A. Levy, N. Lacombe, C. Chackerian, in: K. Narahari Rao, *Spectroscopy of the Earth's Atmosphere and of the Interstellar Medium*. Academic Press, New York, 1992.
- [57] T.H. Maiman, *Stimulated Optical Radiation in Ruby*. *Nature* **187**, 493-494 (1960).
- [58] N.G. Basov, O.N. Krokhin, Y.M. Popov, *Production of Negative-Temperature States in P-N Junctions of Degenerate Semiconductors*. *Soviet Physics JETP-USSR* **13**, 1320-1321 (1961).
- [59] M.G.A. Bernard, G. Duraffourg, *Laser Conditions in Semiconductors*. *Physica Status Solidi* **1**, 699-703 (1961).
- [60] N. Holonyak, S.F. Bevacqua, *Coherent (Visible) Light Emission from Ga(As1-Xpx) Junctions*. *Applied Physics Letters* **1**, 82-83 (1962).
- [61] M.I. Nathan, W.P. Dumke, G. Burns, F.H. Dill, G. Lasher, *Stimulated Emission of Radiation from GaAs P-N Junctions*. *Applied Physics Letters* **1**, 62-64 (1962).
- [62] C. Ye, *Tunable External Cavity Diode Lasers*. 2004 ed.; World Scientific Publishing, Danvers, 2004.
- [63] M.G. Littman, *Single-Mode Operation of Grazing-Incidence Pulsed Dye-Laser*. *Optics Letters* **3**, 138-140 (1978).
- [64] M.G. Littman, H.J. Metcalf, *Spectrally Narrow Pulsed Dye-Laser without Beam Expander*. *Bulletin of the American Physical Society* **23**, 75-75 (1978).
- [65] K. Liu, M.G. Littman, *Novel Geometry for Single-Mode Scanning of Tunable Lasers*. *Optics Letters* **6**, 117-118 (1981).
- [66] M.G. Littman, *Single-Mode Pulsed Tunable Dye-Laser*. *Applied Optics* **23**, 4465-4468 (1984).
- [67] K.C. Harvey, C.J. Myatt, *External-Cavity Diode-Laser Using a Grazing-Incidence Diffraction Grating*. *Optics Letters* **16**, 910-912 (1991).
- [68] T. Day, F. Luecke, M. Brownell, *Continuously tunable diode lasers*. *Lasers and Optonics* 15-17 (1993).
- [69] T. Day, M. Brownell, I.F. Wu, *Widely Tunable External Cavity Diode Lasers. Laser Frequency Stabilization and Noise Reduction* **2378**, 35-41 256 (1995).
- [70] D. Mondelain, C. Camy-Peyret, A.W. Mantz, E. Tang, A. Valentin, *Performance of a Herriott cell, designed for variable temperatures between 296 and 20 K*. *Journal of Molecular Spectroscopy* **241**, 18-25 (2007).
- [71] Z. El Helou, B. Erba, S. Churassy, G. Wannous, M. Neri, R. Bacis, E. Boursey, *Design and performance of a low-temperature-multi-pass-cell for absorbance measurements of atmospheric gases. Application to ozone*. *Journal of Quantitative Spectroscopy & Radiative Transfer* **101**, 119-128 (2006).
- [72] A.R.W. Mckellar, *Long-path equilibrium IR spectra of weakly bound complexes at low temperatures*. *Faraday Discussions* **97**, 69-80 (1994).

- [73] A.R.W. Mckellar, J.K.G. Watson, B.J. Howard, *The No Dimer - N-15 Isotopic Infrared-Spectra, Line-Widths, and Force-Field*. *Molecular Physics* **86**, 273-286 (1995).
- [74] J. Ballard, K. Strong, J.J. Remedios, M. Page, W.B. Johnston, *A Coolable Long Path Absorption Cell for Laboratory Spectroscopic Studies of Gases*. *Journal of Quantitative Spectroscopy & Radiative Transfer* **52**, 677-691 (1994).
- [75] K. Strong, F.W. Taylor, S.B. Calcutt, J.J. Remedios, J. Ballard, *Spectral Parameters of Self-Broadened and Hydrogen-Broadened Methane from 2000 Cm(-1) to 9500 Cm(-1) for Remote Sounding of the Atmosphere of Jupiter*. *Journal of Quantitative Spectroscopy & Radiative Transfer* **50**, 363-429 (1993).
- [76] D. Newnham, J. Ballard, M. Page, *Doppler-Limited Spectroscopy at Cryogenic Temperatures - Application of Collisional Cooling*. *Review of Scientific Instruments* **66**, 4475-4481 (1995).
- [77] K.M. Smith, D.A. Newnham, *Near-infrared absorption cross sections and integrated absorption intensities of molecular oxygen (O-2, O-2-O-2, and O-2-N-2)*. *Journal of Geophysical Research-Atmospheres* **105**, 7383-7396 (2000).
- [78] R.A. McPheat, D.A. Newnham, R.G. Williams, J. Ballard, *Large-volume, coolable spectroscopic cell for aerosol studies*. *Applied Optics* **40**, 6581-6586 (2001).
- [79] Y. Abebe, C.D. Ball, F.C. De Lucia, A.W. Mantz, *Spatial mapping of collisionally cooled carbon monoxide molecules in a cold cell*. *Spectrochimica Acta Part a-Molecular and Biomolecular Spectroscopy* **55**, 1957-1966 (1999).
- [80] A. Valentin, A. Henry, C. Claveau, C. Camy-Peyret, D. Hurtmans, A.W. Mantz, *Development of a stabilized low temperature infrared absorption cell for use in low temperature and collisional cooling experiments*. *Spectrochimica Acta Part a-Molecular and Biomolecular Spectroscopy* **60**, 3477-3482 (2004).
- [81] M.A.H. Smith, C.P. Rinsland, V.M. Devi, D.C. Benner, *Temperature-Dependence of Broadening and Shifts of Methane Lines in the Nu(4) Band*. *Spectrochimica Acta Part a-Molecular and Biomolecular Spectroscopy* **48**, 1257-1272 (1992).
- [82] M.W.P. Cann, *An Optical Absorption Cell with Variable Path Length and Temperature*. *Review of Scientific Instruments* **40**, 595-& (1969).
- [83] R.D. Schaeffer, J.C. Sproul, J. Oconnell, C. Vanvloten, A.W. Mantz, *Multipass Absorption Cell Designed for High-Temperature Uhv Operation*. *Applied Optics* **28**, 1710-1713 (1989).
- [84] R.E. Shetter, J.A. Davidson, C.A. Cantrell, J.G. Calvert, *Temperature Variable Long Path Cell for Absorption-Measurements*. *Review of Scientific Instruments* **58**, 1427-1428 (1987).
- [85] A. Predoi-Cross, C. Hnatovsky, K. Strong, J.R. Drummond, D.C. Benner, *Temperature dependence of self- and N-2-broadening and pressure-induced shifts in the 3 <- 0 band of CO*. *Journal of Molecular Structure* **695**, 269-286 (2004).
- [86] V.S.I. Sprakel, M.C. Feiters, R.J.M. Nolte, P.M.F.M. Hombergen, A. Groenen, H.J.R. De Haas, *A cell for combined UV-visible and x-ray absorption spectroscopy studies under low-temperature and air exclusion conditions*. *Review of Scientific Instruments* **73**, 2994-2998 (2002).
- [87] D. Hurtmans, G. Dufour, W. Bell, A. Henry, A. Valentin, C. Camy-Peyret, *Line intensity of R(0) and R(3) of the (CH4)-C-12 2 nu(3) band from diode laser spectroscopy*. *Journal of Molecular Spectroscopy* **215**, 128-133 (2002).

- [88] C. Povey, A. Predoi-Cross, *Computations of temperature dependences for line shape parameters in the 30012 \leftarrow 00001 and 30013 \leftarrow 00001 bands of pure CO(2)*. Journal of Molecular Spectroscopy **257**, 187-199 (2009).
- [89] L.L. Strow, B.M. Gentry, *ROTATIONAL COLLISIONAL NARROWING IN AN INFRARED CO₂ Q-BRANCH STUDIED WITH A TUNABLE-DIODE LASER*. Journal of Chemical Physics **84**, 1149-1156 (1986).
- [90] T. Huet, N. Lacome, A. Levy, *LINE MIXING EFFECTS IN THE Q BRANCH OF THE 10-DEGREES-O -01 10 TRANSITION OF CO₂*. Journal of Molecular Spectroscopy **138**, 141-161 (1989).
- [91] L. Bonamy, J. Bonamy, S. Temkin, D. Robert, J.M. Hartmann, *STATE-TO-STATE ROTATIONAL CROSS-SECTIONS IN VIBRATIONAL-MODES - APPLICATION TO THE INFRARED Q-BRANCH PROFILE FOR THE (11 10)I -(00 (0)0) (CO₂)-C-12-O-16 BENDING BAND*. Journal of Chemical Physics **98**, 3747-3753 (1993).
- [92] N.N. Filippov, M.V. Tonkov, *SEMICLASSICAL ANALYSIS OF LINE MIXING IN THE INFRARED BANDS OF CO AND CO₂*. Journal of Quantitative Spectroscopy & Radiative Transfer **50**, 111-125 (1993).
- [93] M. Margottinmaclou, F. Ratchet, C. Boulet, A. Henry, A. Valentin, *Q-BRANCH LINE MIXING EFFECTS IN THE (20(0)0)(I) -01(1)0 AND(12(2)0)(I) -01(1)0 BANDS OF CARBON-DIOXIDE*. Journal of Molecular Spectroscopy **172**, 1-15 (1995).
- [94] M.V. Tonkov, J. Boissoles, R. LeDoucen, B. Khalil, F. Thibault, *Q-branch shapes of CO₂ spectrum in 15 μ m region: Experiment*. Journal of Quantitative Spectroscopy & Radiative Transfer **55**, 321-334 (1996).
- [95] R. Berman, P. Duggan, P.M. Sinclair, A.D. May, J.R. Drummond, *Direct measurements of line-mixing coefficients in the $\nu(1)+\nu(2)Q$ branch of CO₂*. Journal of Molecular Spectroscopy **182**, 350-363 (1997).
- [96] A. Predoi-Cross, C.Y. Luo, R. Berman, J.R. Drummond, A.D. May, *Line strengths, self-broadening, and line mixing in the 20(0)0 \leftarrow 01(1)0 (Sigma \leftarrow Pi) Q branch of carbon dioxide*. Journal of Chemical Physics **112**, 8367-8377 (2000).
- [97] A. Predoi-Cross, A.D. May, A. Vitcu, J.R. Drummond, J.M. Hartmann, C. Boulet, *Broadening and line mixing in the 20 (0)0 \leftarrow 01 (1)0, 11 (1)0 \leftarrow 00 (0)0 and 12 (2)0 \leftarrow 01 (1)0 Q branches of carbon dioxide: Experimental results and energy-corrected sudden modeling*. Journal of Chemical Physics **120**, 10520-10529 (2004).
- [98] J.M. Hartmann, C. Boulet, M. Margottinmaclou, F. Ratchet, B. Khalil, F. Thibault, J. Boissoles, *SIMPLE MODELING OF Q-BRANCH ABSORPTION .1. THEORETICAL-MODEL AND APPLICATION TO CO₂ AND N₂O*. Journal of Quantitative Spectroscopy & Radiative Transfer **54**, 705-722 (1995).
- [99] S. Green, *PRESSURE BROADENING AND LINE COUPLING IN BENDING BANDS OF CO₂*. Journal of Chemical Physics **90**, 3603-3614 (1989).
- [100] B. Gentry, L.L. Strow, *LINE MIXING IN A N-2-BROADENED CO₂Q BRANCH OBSERVED WITH A TUNABLE DIODE-LASER*. Journal of Chemical Physics **86**, 5722-5730 (1987).
- [101] M.V. Tonkov, N.N. Filippov, Y.M. Timofeyev, A.V. Polyakov, *A simple model of the line mixing effect for atmospheric applications: Theoretical background and comparison with experimental profiles*. Journal of Quantitative Spectroscopy & Radiative Transfer **56**, 783-795 (1996).

- [102] A. Predoi-Cross, Y.I. Baranov, *Lineshape modeling of inter-branch intensity transfer in the $20(0)0 \leftarrow 01(1)0$, $11(1)0 \leftarrow 00(0)0$ and $12(2)0 \leftarrow 01(1)0$ Q-branches of carbon dioxide*. Journal of Molecular Structure **742**, 77-82 (2005).
- [103] L. Bonamy, F. Emond, *ROTATIONAL-ANGULAR-MOMENTUM RELAXATION MECHANISMS IN THE ENERGY-CORRECTED-SUDDEN SCALING THEORY*. Physical Review A **51**, 1235-1240 (1995).
- [104] J.M. Hartmann, C. Boulet, *LINE MIXING AND FINITE DURATION OF COLLISION EFFECTS IN PURE CO₂ INFRARED-SPECTRA - FITTING AND SCALING ANALYSIS*. Journal of Chemical Physics **94**, 6406-6419 (1991).
- [105] J.P. Bouanich, R. Rodrigues, C. Boulet, *LINE MIXING EFFECTS IN THE $1-0$ AND $2-0$ CO BANDS PERTURBED BY CO AND N₂ FROM LOW TO HIGH-DENSITIES*. Journal of Quantitative Spectroscopy & Radiative Transfer **54**, 683-693 (1995).
- [106] J.P. Bouanich, J.M. Hartmann, G. Blanquet, J. Walrand, D. Bermejo, J.L. Domenech, *Line-mixing effects in He- and N₂-broadened Sigma \leftarrow II infrared Q branches of N₂O*. Journal of Chemical Physics **109**, 6684-6690 (1998).
- [107] G. Blanquet, J. Walrand, J.P. Bouanich, *Line-mixing effects in He- and N₂-broadened Q branches of C₂H₂ at low temperatures*. Journal of Molecular Spectroscopy **210**, 1-7 (2001).
- [108] S. Haddad, F. Thibault, P.M. Flaud, H. Aroui, J.M. Hartmann, *Experimental and theoretical study of line mixing in NH₃ spectra. I. Scaling analysis of parallel bands perturbed by He*. Journal of Chemical Physics **116**, 7544-7557 (2002).
- [109] A. Predoi-Cross, W. Liu, R.-J. Murphy, A.R.W. Mckellar, D. Hurtmans, The 20th International Conference on High Resolution Molecular Spectroscopy, Prague, Czech Republic, September, 2008, Talk M6.
- [110] Available From: <<http://library.wolfram.com/infocenter/MathSource/5344>>.
- [111] C. Povey, A. Predoi-Cross, D.R. Hurtmans, *Line shape study of acetylene transitions in the $\nu(1) + \nu(2) + \nu(4) + \nu(5)$ band over a range of temperatures*. Journal of Molecular Spectroscopy **268**, 177-188 (2011).
- [112] C. Povey, A. Predoi-Cross, D.R. Hurtmans, *Low-pressure line shape study of acetylene transitions in the $\nu 1 + \nu 2 + \nu 4 + \nu 5$ band over a range of temperatures*. Molecular Physics **110**, 2633-2644 (2012).
- [113] C. Povey, M. Guillourel-Obregon, A. Predoi-Cross, S. Ivanov, O. Buzykin, F. Thibault, *Low pressure line shape study of nitrogen-perturbed acetylene transitions in the $\nu 1 + \nu 3$ band over a range of temperatures I*. Canadian Journal of Physics (2013).
- [114] M. Herman, *The acetylene ground state saga*. Molecular Physics **105**, 2217-2241 (2007).
- [115] M. Dhyne, P. Joubert, J.C. Populaire, M. Lepere, *Self-collisional broadening and shift coefficients of lines in the $\nu(4) + \nu(5)$ band of (12)C(2)H(2) from 173.2 to 298.2 K by diode-laser spectroscopy*. Journal of Quantitative Spectroscopy & Radiative Transfer **112**, 969-979 (2011).
- [116] J.Y. Wang, P. Ehlers, I. Silander, O. Axner, *Dicke narrowing in the dispersion mode of detection and in noise-immune cavity-enhanced optical heterodyne molecular spectroscopy-theory and experimental verification*. Journal of the Optical Society of America B-Optical Physics **28**, 2390-2401 (2011).

- [117] J.P. Bouanich, A. Predoi-Cross, *Theoretical calculations for line-broadening and pressure-shifting in the $\nu(1) + \nu(2) + \nu(4) + \nu(5)$ band of acetylene over a range of temperatures*. *Molecular Physics* **109**, 2071-2081 (2011).
- [118] H. Li, A. Farooq, J.B. Jeffries, R.K. Hanson, *Near-infrared diode laser absorption sensor for rapid measurements of temperature and water vapor in a shock tube*. *Applied Physics B-Lasers and Optics* **89**, 407-416 (2007).
- [119] C.R. Mueller, R.W. Cahill, *MASS SPECTROMETRIC MEASUREMENT OF DIFFUSION COEFFICIENTS*. *Journal of Chemical Physics* **40**, 651 (1964).
- [120] M. Lepere, A. Henry, A. Valentin, C. Camy-Peyret, *Diode-laser spectroscopy: Line profiles of H₂O in the region of 1.39 μ m*. *Journal of Molecular Spectroscopy* **208**, 25-31 (2001).
- [121] J.O. Hirschfelder, C.F. Curtiss, R.B. Bird, Wiley-Interscience, 1964, p 1280.
- [122] T. Titani, *Chemical Society of Japan* **5**, (1930).
- [123] D. Lambot, G. Blanquet, J.P. Bouanich, *Diode-Laser Measurements of Collisional Broadening in the ν_5 Band of C₂H₂ Perturbed by O₂ and N₂*. *Journal of Molecular Spectroscopy* **136**, 86-92 (1989).
- [124] V.M. Devi, D.C. Benner, C.P. Rinsland, M.A.H. Smith, B.D. Sidney, *Tunable Diode-Laser Measurements of N₂- and Air-Broadened Halfwidths - Lines in the $(\nu_4 + \nu_5)_0$ Band of (C₂H₂)-C-12 near 7.4 μ m*. *Journal of Molecular Spectroscopy* **114**, 49-53 (1985).
- [125] L. Fissiaux, M. Dhyne, M. Lepere, *Diode-laser spectroscopy: Pressure dependence of N₂-broadening coefficients of lines in the $\nu(4) + \nu(5)$ band of C₂H₂*. *Journal of Molecular Spectroscopy* **254**, 10-15 (2009).
- [126] S.W. Arteaga, C.M. Bejger, J.L. Gerecke, J.L. Hardwick, Z.T. Martin, J. Mayo, E.A. McIlhattan, J.M.F. Moreau, M.J. Pilkenton, M.J. Polston, B.T. Robertson, E.N. Wolf, *Line broadening and shift coefficients of acetylene at 1550 nm*. *Journal of Molecular Spectroscopy* **243**, 253-266 (2007).
- [127] C.P. McRaven, M.J. Cich, G.V. Lopez, T.J. Sears, D. Hurtmans, A.W. Mantz, *Frequency comb-referenced measurements of self- and nitrogen-broadening in the $\nu(1) + \nu(3)$ band of acetylene*. *Journal of Molecular Spectroscopy* **266**, 43-51 (2011).
- [128] J.P. Bouanich, D. Lambot, G. Blanquet, J. Walrand, *N₂-Broadening and O₂-Broadening Coefficients of C₂H₂ ν_5 Lines*. *Journal of Molecular Spectroscopy* **140**, 195-213 (1990).
- [129] A. Babay, M. Ibrahimi, V. Lemaire, B. Lemoine, F. Rohart, J.P. Bouanich, *Line frequency shifting in the $\nu(5)$ band of C₂H₂*. *Journal of Quantitative Spectroscopy & Radiative Transfer* **59**, 195-202 (1998).
- [130] J.P. Bouanich, G. Blanquet, J. Walrand, *Line-mixing effects in He- and N₂-broadened $\sigma \leftarrow \pi$ infrared Q branches of C₂H₂*. *Journal of Molecular Spectroscopy* **203**, 41-48 (2000).
- [131] P. Varanasi, *Intensity and Linewidth Measurements in the 13.7 μ m Fundamental Bands of (C₂H₂)-C-12 and (C₁₃H₂)-C-12 at Planetary Atmospheric Temperatures*. *Journal of Quantitative Spectroscopy & Radiative Transfer* **47**, 263-274 (1992).
- [132] J.P. Bouanich, G. Blanquet, J.C. Populaire, J. Walrand, *Nitrogen broadening of acetylene lines in the $\nu(5)$ band at low temperature*. *Journal of Molecular Spectroscopy* **190**, 7-14 (1998).

- [133] M. Dhyne, L. Fissiaux, J.C. Populaire, M. Lepere, *Temperature dependence of the N-2-broadening coefficients of acetylene*. Journal of Quantitative Spectroscopy & Radiative Transfer **110**, 358-366 (2009).
- [134] M. Dhyne, P. Joubert, J.C. Populaire, M. Lepere, *Collisional broadening and shift coefficients of lines in the $\nu(4) + \nu(5)$ band of (C₂H₂)-C-12 diluted in N-2 from low to room temperatures*. Journal of Quantitative Spectroscopy & Radiative Transfer **111**, 973-989 (2010).
- [135] N.T. Campbell, J.D. Cook, B.A. Coombs, E.P. Fuller, J.L. Hardwick, S.M. Hurley, L.K. Ho, P.A. Kovac, E.J. Robertson, E.N. Senning, J.K. Utterback, R.S. Wiser, *Temperature dependence of pressure broadening and shifts of acetylene at 1550 nm by N-2*. Molecular Physics **109**, 2199-2208 (2011).
- [136] H. Rozario, J. Garber, C. Povey, D. Hurtmans, J. Buldyreva, A. Predoi-Cross, *Experimental and theoretical study of N₂-broadened acetylene line parameters in the $\nu_1 + \nu_3$ band over a range of temperatures*. Molecular Physics **110**, 2645-2663 (2012).
- [137] R.H. Dicke, *THE EFFECT OF COLLISIONS UPON THE DOPPLER WIDTH OF SPECTRAL LINES*. Physical Review **89**, 472-473 (1953).
- [138] H. Li, A. Farooq, J.B. Jeffries, R.K. Hanson, *Diode laser measurements of temperature-dependent collisional-narrowing and broadening parameters of Ar-perturbed H₂O transitions at 1391.7 and 1397.8 nm*. Journal of Quantitative Spectroscopy & Radiative Transfer **109**, 132-143 (2008).
- [139] F. Thibault, A.W. Mantz, C. Claveau, A. Henry, A. Valentin, D. Hurtmans, *Broadening of the R(0) and P(2) lines in the (CO)-C-13 fundamental by helium atoms from 300 K down to 12 K: Measurements and comparison with close-coupling calculations*. Journal of Molecular Spectroscopy **246**, 118-125 (2007).
- [140] F. Thibault, O. Vieuxmaire, T. Sizun, B. Bussery-Honvault, Molecular Physics **110**, 2761-2771 (2012).
- [141] R. Wehr, R. Ciurylo, A. Vitcu, F. Thibault, J.R. Drummond, A.D. May, *Dicke-narrowed spectral line shapes of CO in Ar: Experimental results and a revised interpretation*. Journal of Molecular Spectroscopy **235**, 54-68 (2006).
- [142] F.R.W. McCourt, J.J.M. Beenaker, W.E. Köhler, I. Kučšer, *Non equilibrium phenomena in polyatomic gases*. Clarendon Press, Oxford, 1990.
- [143] P.L. Varghese, R.K. Hanson, *Collisional Narrowing Effects on Spectral-Line Shapes Measured at High-Resolution*. Applied Optics **23**, 2376-2385 (1984).
- [144] H. Waechter, M.W. Sigrist, *Mid-infrared laser spectroscopic determination of isotope ratios of N₂O at trace levels using wavelength modulation and balanced path length detection*. Applied Physics B-Lasers and Optics **87**, 539-546 (2007).
- [145] P. Werle, R. Mucke, F. Slemr, *The Limits of Signal Averaging in Atmospheric Trace-Gas Monitoring by Tunable Diode-Laser Absorption-Spectroscopy (Tdlas)*. Applied Physics B-Photophysics and Laser Chemistry **57**, 131-139 (1993).